SYNTHESIS, CHARACTERIZATION AND IRRADIATION OF FULLERENE BASED METAL NANOCOMPOSITES

Ph.D. Thesis

POOJA SHARMA
ID No. 2014RPY9008

DEPARTMENT OF PHYSICS
MALAVIYA NATIONAL INSTITUTE OF TECHNOLOGY JAIPUR

June, 2019

Synthesis, Characterization and Irradiation of Fullerene Based Metal Nanocomposites

Submitted in

fulfillment of the requirements for the degree of

Doctor of Philosophy

by

Pooja Sharma
ID:2014RPY9008

Under the Supervision of

Dr. Rahul Singhal
Prof. M.K. Banerjee

DEPARTMENT OF PHYSICS
MALAVIYA NATIONAL INSTITUTE OF TECHNOLOGY JAIPUR,

June, 2019

This work is dedicated to my beloved sister and brother, Asha and Harimohan Sharma for their eternal love

DECLARATION

I, **Pooja Sharma** declare that this thesis titled **"SYNTHESIS, CHARACTERIZATION AND IRRADIATION OF FULLERENE BASED METAL NANOCOMPOSITES"** and the work presented in it is my own. The work has been carried out under the supervision of Dr. Rahul Singhal and Prof. M.K. Banerjee, I confirm that:

- This work was done wholly or mainly while in candidature for a research degree at this university.

- Where any part of this thesis has previously been submitted for a degree or any other qualification at this university or any other institution, has been clearly stated.

- Where I have consulted the published work of others, this is always clearly attributed.

- Where I have quoted from the work of others, the source is always given. With the exception of such quotations, this thesis is entirely my own work.

- I have acknowledged all main sources of help.

- Where the thesis is based on work done by myself, jointly with others, I have made clear exactly what was done by others and what I have contributed myself.

Date:

Pooja Sharma

(2014RPY9008)

CERTIFICATE

This is to certify that the thesis entitled **"SYNTHESIS, CHARACTERIZATION AND IRRADIATION OF FULLERENE BASED METAL NANOCOMPOSITES"** being submitted by **Ms. Pooja Sharma (ID: 2014RPY9008)** is a bonafide research work carried out under my supervision and guidance in fulfillment of the requirement for the award of the degree of **Doctor of Philosophy** in the department of **Physics**, Malaviya National Institute of Technology, Jaipur, India. The matter embodied in this thesis is original and has not been submitted to any other University or Institute for the award of any other degree.

Place: Jaipur
Date :

Dr. Rahul Singhal	**Prof. M. K. Banerjee**
Assistant Professor	Former MOS Chair Professor
Department of Physics	Department of Metallurgical and
MNIT, Jaipur	Material Engineering
	Presently Visiting Faculty
	Materials Research Center
	MNIT, Jaipur

ACKNOWLEDGEMENT

It is a great honor for me to record my sincere gratitude to Dr. Rahul Singhal under whose supervision I have carried out my Ph.D. work on **"Synthesis, Characterization and Irradiation of Fullerene Based Metal Nanocomposites"** Dr. Rahul Singhal has been very careful in guiding me aright throughout my research work. But for his kind attitude towards me it would be impossible for me to accomplish this task. During my entire research work, Dr. Singhal has encouraged me to take up the challenges of working in unknown situation and it is the inspiration from his end that has enabled me to complete my work. I am greatly indebted to my supervisor, Dr. Rahul Singhal for the affection he showered on me and for the scope he opened for me to acquire gainful experience not only in reputed organization of our country but also in famous research laboratories in other countries. I feel myself highly fortunate to secure the chance of working with Dr. Rahul Singhal. In my opinion my association with him has enriched my knowledge quite significantly. I am overwhelmed to observe the enormous patience of my supervisor in rectifying my errors wherever I made as a learner. I express my deep respect to Dr. Rahul Singhal for what he has done for me.

I would like to express my sincere gratitude to my co-supervisor, Prof. M.K. Banerjee, Chair Professor, Department of Metallurgical and Material Engineering for their continuous support, guidance and motivation. It would never have been possible for me to take this work to completion without their incredible support and encouragement. I am grateful to him for the long discussions that helped me sort out the technical details of my research work.

It is a great pleasure to acknowledge help and guidance received from Dr. D.K. Avasthi, former Director of Material Science Group, IUAC, New Delhi and presently Director of Amity Institute of Nanotechnology, Amity University, Uttar Pradesh. Dr. Avasthi is globally accepted an accomplished scientist and it is anybody's fortune to come in contact with a great personality like him. I am sincerely proud for being treated so affectionately by Dr. D.K. Avasthi. He has been very kind in making me learn a lot and has been quite sympathetic to me all throughout my research work. In this context, it is also my pleasant duty to acknowledge with deep respect the guidance and support of Dr. Suresh Chand (Chief Scientist, National Physical Lab, New Delhi) offered to me during my Ph. D. work. Dr. Suresh Chand has been very

Contextually, I record the bewildering support, my friend Ms. Sonam Parashar has been providing me. Her help in right time makes me remember that "a friend in need is a friend indeed".

At this time of completion of my long cherished Ph. D. work my inner self is always reminded of the great inspiration and encouragement I received from Late Dr. Praveen Aghamkar in the formative period of research career. Without his blessings I could have reached this landmark in no way. I record my deepest respect to Dr. Aghamkar.

It is my moral dictate to keep on record the affection, support and inspiration from my elder brother Mr. Harimohan Sharma. The inspiration received from my beloved sister Mrs. Asha has been the major source of motivation in accomplishment of this task. I will be erred if I do not mention the contribution of my younger brother, Mr. Sharad Sharma who has given me a very pleasant company in my distressed hours.

Last but not the least, I record my deepest respect to beloved parents who have been mentoring me in the most pleasing manner till date.

Pooja Sharma

ABSTRACT

The present research work entitled **"Synthesis, Characterization and Irradiation of Fullerene Based Metal Nanocomposites"** envisages the study on the feasibility of using fullerenes, one of the most emerging functional materials as a matrix for the reinforcement of metal nanoparticles. Fullerene matrix nanoparticles embedded composites are found to exhibit surface plasmon resonance (SPR) by virtue of which a significant enhancement of absorbance of the material become possible; the bi-functional property of matrix and metal nanoparticles in a single material makes it highly beneficial and applicable for different optical devices, thereby making it poised for emergence as a lucrative energy material.

Understanding that the performance of optical absorbance of nanocomposites is highly influenced by the host microstructure, it has appeared important to monitor the structural conditions of fullerene as matrix material when subjected to such treatments as considered useful for enhancement of SPR due to noble metal particles in nanocomposites. It is further known that ion beam irradiation is most effective in alteration of SPR behavior of nanoparticles of noble metals like Au and Ag. So the present study in chapter 4.1 has contemplated to explore the effect of heavy ion beam irradiation (90 MeV Ni ion) on fullerene C_{60} thin film. As expected the damage of fullerenes has been fluence dependent and that ion tracks of determinable diameter could be formed by such irradiation.

In view of the fact that elaborate studies on fullerene C_{70} is till due to be reported in literature, the present research work in chapter 4.2 has investigated and reported the effect of irradiation by different ions viz. 90 MeV Si, 55 MeV Si, 90 MeV Ni and 125 MeV Au on fullerene C_{70} thin films. Based on the results of the above ion beams of different electronic energy loss (S_e), the damage cross section has been calculated for each ion beam, compiled and a relationship between damage cross section and electronic energy loss is developed which is supposed to be beneficial in estimating the value of damage cross section for any unknown situation of electronic energy loss within the range of present study.

Although the potential of nanoparticles of gold and silver as reinforcement in fullerene C_{60} and C_{70} has been amply researched, the potential of copper is yet to

receive due research attention in spite of its advantage of interesting mechanical properties, high electrical conductivity, favorable catalytic properties, appropriate melting point, high stability and high natural abundance in nature. Hence, the present thesis work has reported (chapter 5.1) the results of investigation on the incorporation of copper nanoparticles in fullerene C_{60} matrix subjected to irradiation by low energy ion beams (100 keV Ag ion, 350 keV Ar ion). As a corollary of low energy 100 keV Ag ion irradiation study the widening of absorption range could be observed due to hybridization of copper nanoparticles induced SPR and that due to Ag ions getting implanted within in the silicon substrate. The low cost of Cu over Ag and Au makes it more attractive for applications in various fields of optics, electronics, solar energy conservation, sensors, lubricants and sliding electrical contacts. Effect of high energy (120 MeV Ag) ion irradiation on Cu (18 at. %)-C_{60} has implicitly demonstrated (chapter 5.2) the enhancement of SPR band intensity due to copper nanoparticles; the concurrent growth of copper nanoparticles at increasing fluences has caused a shift in the position of SPR band.

The chapter 6 of present study has addressed the research questions related to Cu-C_{70} nanocomposite thin films under ion irradiation of various energies. The low energy ion beam irradiation (350 keV Ar ion) of Cu (10 at.%)-C_{70} nanocomposite thin films have been able to exhibit SPR band due to copper only after irradiation at fluence of 1×10^{15} ions/cm^2. The SPR band increases its intensity with increasing fluence and got shifted towards lower wavelength side. This is in contrast with the pristine which has not exhibited any SPR due to copper presumably due to its low concentration. The similar behavior was also exhibited by this composite subjected to high energy ion beam irradiation (120 MeV Ag ion) with the exception that SPR could be obtained only at a higher fluence like 3×10^{13} ions/cm^2. Since any fluence higher than 3×10^{13} ions/cm^2 has not been employed in the present study it is not possible to be conclusive if it would also exhibit a blue shift with still increasing fluence, which, it seems would occur most likely. However, the studies in chapter 6 clearly authenticates that both the concentration of embedded nanoparticles and the change in optical properties of irradiated fullerenes are responsible for determining the intensity and the position of SPR due to copper in fullerene C_{70} matrix.

CONTENTS

CAPTIONS OF FIGURES

liquid drop.

LIST OF ABBREVATIONS

SPR	Surface Plasmon Resonance
SHI	Swift Heavy Ion
a-C	Amorphous Carbon
RBS	Rutherford Back Scattering
TEM	Transmission Electron Microscopy
XRD	X-Ray Diffraction
SEM	Scanning Electron Microscopy
AFM	Atomic Force Microscopy
XPS	X-ray Photoelectron Spectroscopy

Chapter 1

Introduction

1.1 Third allotropic form of carbon-Fullerenes:

The existence of polyhedral carbon cluster and its properties was first predicted as early as 1970's. Finally the fullerene, the closed hollow cage was discovered in 1985 by Richard Smalley, Robert Curl, James Heath, Sean O'Brien, and Harold Kroto at Rice University; while studying the mass spectrograph of graphite vapour, the group observed some distinctive peaks analogous to mass 720 with a clue to the existence of a unique molecule of 60 carbon atoms [1].
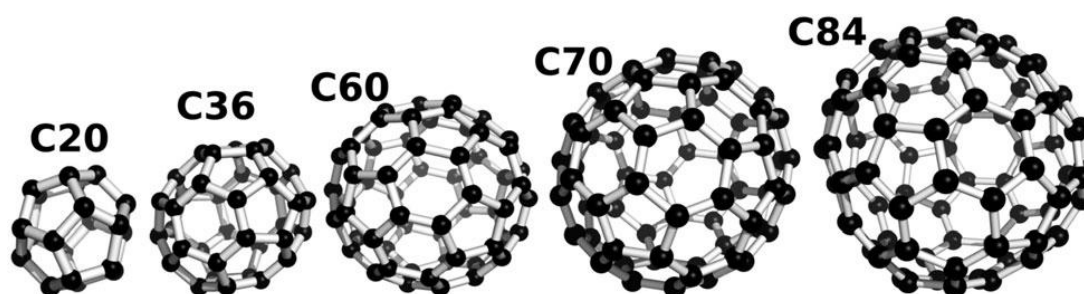
Figure 1.1 Geometric structures of different order of fullerenes.

Kroto et al. [1] have reported that this molecule of 60 carbon atoms could readily be formed with extraordinary stability. Its structure was visualized from the design of geodesic domes due to the architect, Buckminster Fuller; accordingly this unique molecule was named as Buckminster fullerene C_{60}. Owing to this remarkable discovery, Richard Smalley, Robert Curl and Harold Kroto were awarded Nobel Prize in 1996. It was further observed that there was a less intense peak corresponding to mass 840 hinting the existence of one more molecule, C_{70} in fullerene family. Similarly other fullerenes C_{20}, C_{36}, C_{70}, C_{80}, and C_{84} etc were also discovered. C_{20} is the smallest member molecule in fullerene family. The geometric structures of different fullerenes are shown in figure 2.1 [3]. Zhang et al [3] demonstrated the geometrical structures of all even fullerenes from C_{20} to C_{70} with the aid of tight binding molecular dynamics.

It was also reported that only fullerene C_{60} and C_{70} are of the high symmetry structures of high stability [3]. Existence of fullerenes comprising of higher number of carbon atoms is also documented in literatures [4-5].

1.2 Characteristics of fullerenes:

The properties of this unique material are essentially determined by the stereography, symmetry and the number of atoms in fullerene structure. Fullerene molecules are known to be composed of carbon atoms interconnected in pentagonal and hexagonal

rings. Kroto et al. [1] have confirmed the cage structure of fullerenes which is composed of carbon atom and in which each of carbon atoms on the cage surface is bonded to three neighboring carbon atoms with sp^2 hybridization. The suffix "ene" signifies that each carbon atom in fullerene is covalently bonded with three other carbon atoms and hence there will be double bonds present in fullerene structure. In general a molecule composed of only carbon atoms belongs to fullerene even though they may exhibit different shapes, such as spherical, ellipsoidal or tubular; quite often they are known as Buckyball cluster, nanotube, megatubes, polymers and nano onions. Thus, the tubular shaped fullerenes are called carbon nanotubes [2, 6-9].

1.2.1 Structure of fullerene C_{60} and C_{70}:

❍ The fullerene resembles graphitic structure as far as hexagonal carbon rings are concerned but it differs from a typical graphite structure by a way of containing a considerable portion of pentagonal rings in its structure [1]. The most abundant fullerene is C_{60} which has 60 sp^2 hybridized carbon atoms. It is arranged in the configuration of 20 hexagons and 12 pentagons obeying the isolated pentagon rule that is pentagons must not share the edges. In fullerene structure, carbon atoms do not have any dangling (free) bonds. In fullerene C_{60}, the measured value of hexagon-hexagon bond length is 1.46 Å and that of hexagon-pentagon is 1.40 Å. That results in a three dimensional spherical structure of diameter ~7.1 Å [9-10]. Besides C_{60}, C_{70} has the most abundant yield in the production of fullerenes.

❍ The structure of C_{70} molecule is more complex than that of C_{60}. The addition of 10 carbon atoms around the equatorial plane of C_{60} molecule has the equivalence of inserting a strap of five hexagons. Accordingly, C_{70} molecule exhibits an ellipsoidal form consisting of 25 hexagons and 12 pentagons, with a rugby ball shape. The symmetry of C_{70} molecule is D_{5h}. In C_{70} molecule, there are five non-equivalent carbon sites and eight distinct bond lengths. These bond lengths are experimentally determined by neutron inelastic scattering (NIS) and are found to range from 1.356 Å to 1.475 Å. However, in most cases the lengths of single and double bond, 1.40 Å and 1.46 Å are considered [11].

1.2.2 Symmetry and phase transition in C_{60} and C_{70}:

With the aid of nuclear magnetic resonance study (NMR), icosahedral symmetry in C_{60} molecules can be observed [12]. The symmetry operations in icosahedra of a C_{60} molecule are rather interesting. The symmetry of this structure is described by 12 fivefold axes, 20 threefold axes and 15 twofold axes passing respectively through the

centers of the pentagonal faces, hexagonal faces, and the edges joining two hexagons. Compounded by inversion operations, the 60 rotational symmetry results in 120 symmetry operations in the icosahedral point group I_{h77}. C_{60} molecules of I_h symmetry is most prominent in respect of possessing the maximum degree of symmetry so far known for any existing molecule.

In contrast, C_{70} molecule bears a lower symmetry, D_{5h} without having inversion. This leads to 53 Raman active modes in accordance with selection rules [12-13]. Due to paucity of experimental data the assignment of Raman active modes are not certain although theoretical calculation with the help of DFT (Density functional theory) has predicted the possible modes [14].

The phase transition behavior of fullerenes is as follows:

❍ The phase transition study on C_{60} by differential scanning calorimetry (DSC) has shown that there is a phase transition involving orientation ordering [15-17]. The observed change in enthalpy by a magnitude of 6.98 kJ mol^{-1} is indicative of first order phase transition. The earlier researchers have observed a discontinuous change in cell volume across phase transition to imply that the phase transition is a first order transition.

❍ C_{70} molecule is ellipsoidal in shape with the presence of characteristic major and minor axes. C_{70} exhibit two different phase transitions involving rotation around both the axes in sequence as the temperature is lowered [18-19]. Molecular Dynamics simulations by a combined LJ and partial charge potential model. has indicated that high temperature structure of C_{70} is in general face centered cubic (fcc). Upon cooling, a low symmetry structure results by way of a rhombohedral to monoclinic phase transition [20]. Similarly, the high temperature structure (440 K) of C_{70} is fcc. An elongated molecule can exhibit fcc structure only if it is orientationally disordered; this makes averse molecular density to correspond to a sphere. However the spinning of the molecules along the two axes at different rates are also instrumental in describing the structure of the molecule. Two different phase transitions are seen to occur at 276 K and 337 K [21]. It is anticipated that changes in temperature and pressure or irradiation of the fullerene molecule can bring about significant alteration in its structure.

1.2.3 Optical behavior:

The highest occupied molecular orbital (HOMO) in C_{60} molecule belongs to a five-fold degenerate h_u level. Likewise, the lowest unoccupied molecular orbital (LUMO)

levels are respectively the t_{1u} and t_{1g} levels. In the solid state, these HOMO and LUMO give rise to the valence and conduction bands separated by a 1.7 eV band gap [22]. Optical absorption spectra of C_{70} occur over a wide range from 0.6 to 6.5 eV via optical transmission spectroscopy. The spectra records different band positions with onset of a weak band at about 700 nm, followed by a series of very weak peaks at 656 nm, 612 nm, 568 and 527 nm superimposed on a gradually rising continuum leading to a stronger but broad peak at 499 nm [22].

There is unique characteristic of fullerene in having a large number of conjugated pi electrons. Since fullerene molecules are comprised of only carbon atoms, any residual IR absorption is seemingly improbable [1, 23-25]. The non linear optical properties of fullerenes have been elaborately studied by a number of researchers [26-30]; evidence of off-resonant and resonant third-order nonlinear optical polarizabilities was provided in the above studies and values of nonlinear optical polarizabilities for C_{60} and C_{70} were observed to be 10^{-33} esu and 10^{-32} esu, respectively.

1.2.4 Some other physical and chemical behavior of fullerenes:

❍ As fullerene molecule is highly electronegative, it readily forms compounds with electron donating atoms, the most common examples being alkali metals [31]. This reaction leads to creation of an interesting class of compounds known as alkali-doped fullerides, wherein alkali metal atoms fill in the space between Buckyballs and donate valence electron to the neighboring carbon atom. For potassium or rubidium, the resultant compounds become superconductors, and they can conduct electric current without any resistance, below the temperatures 20-40 K [32].

❍ If buckyballs are given to combine with a reactant which is capable to donate its electrons to the carbon molecules, the resultant compound can exhibit ferromagnetic behavior when heated to above 16 K from a preceding state of cooling. This is the lone organic magnet which can work at such high temperature [33].

❍ Since its discovery in 1985, it has been a belief that the absence of dangling bonds in Fullerene C_{60} makes it highly non reactive; implicit was the thought that this material C_{60} will become earth abundant owing principally to its immunity to chemical destruction. However, it has been found that a fullerene can undergo chemical reaction with a number of species viz. oxygen, hydrogen, fluorine, chlorine and bromine [34].

1.3 Applications of fullerenes:

Due to its unique properties fullerene is considered to be a potential candidate for various applications. Besides excellent optical properties and electronic properties, the hollow shape of fullerene poses it as an attractive material in biomedical engineering. It bears enormous potential for use in solar cells, sensors and optoelectronic devices.

❍ Due to high electron affinity and superior charge transfer ability, fullerenes are the best suited electron acceptor material for the solar cells. The properties like deep lying LUMO that makes this molecule highly electron affinitive, negative charge stabilization by fullerene molecules and the high electron mobility of C_{60} taken together make fullerene, the best electron acceptor material [35-39]. Not only in organic solar cells, fullerenes are also a good candidate for perovskite solar cells [39-42].

❍ Fullerenes have the property of allowing light of wavelengths below a threshold value. This makes it useful as optical limiter by being capable of transmitting light of constant wavelength band. This feature is used for applications in eye sensors [43-44].

❍ Fullerenes and its compounds can be used in sensor electronics to produce humidity sensors and isostatic pressure sensors which are based on high electron affinity of fullerenes. [45].

❍ Due to high electron affinity, the application of fullerene in electron transport is possible more in the form of single molecule rather than collection of molecules [46].

❍ The curved structure of fullerene envisages the presence of partial sp^3 bonding which makes fullerene suitable for application as a precursor to diamond, produced by subjecting fullerene at high pressure at the ambient temperatures to make abundant presence of sp^3 as in a typical diamond structure [47].

❍ The use of fullerenes in hydrogen storage is possible due to its structure which makes hydrogenation and dehydrogenation possible reversibly by conversion of C=C bond into C-C. Moreover, C_{60} is a stable phase in hydrogen atmosphere and is amenable for sensing hydrogen or some other low molecular weight gases by preferential disruption bonds [43].

1.4 Nanocomposites:

In general, composites can be defined as a combination of one or more discontinuous phase (called reinforcement or reinforcing material) embedded in a continuous phase

(matrix) [48]. When the small nanoparticles are reinforced in a matrix which may be made of metals, polymers or ceramics, the nanocomposite are said to have produced [49]. Nanocomposites have fascinating properties for which it finds wide area of applications. Nanocomposite thin films have been found to very efficient with modified properties. In a nanocomposite thin film quite often the resultant properties differ from those of matrix or the constituent reinforcement. Hence the incorporation of nanoparticles not only preserves the matrix properties but also new properties of nanoparticles [50]. The excellent properties of nanocomposite thin films are due to higher surface area to volume ratio of reinforcing nanoparticles; therefore, in a small weight percentage of lighter nanoparticles like carbon nanotube, fullerene etc. the interfacial area becomes quite large (due to high volume percent of nanoscale material) which helps to enhance the mechanical and many a times physical properties of the nanocomposites [51]. The drastic change in physical and chemical properties takes place on changing the dimension of reinforcement to nano scale. Hence all the physical and chemical properties related to the size of embedded nanoparticles makes the nanocomposite thin films modified and open for different application areas [23-54].
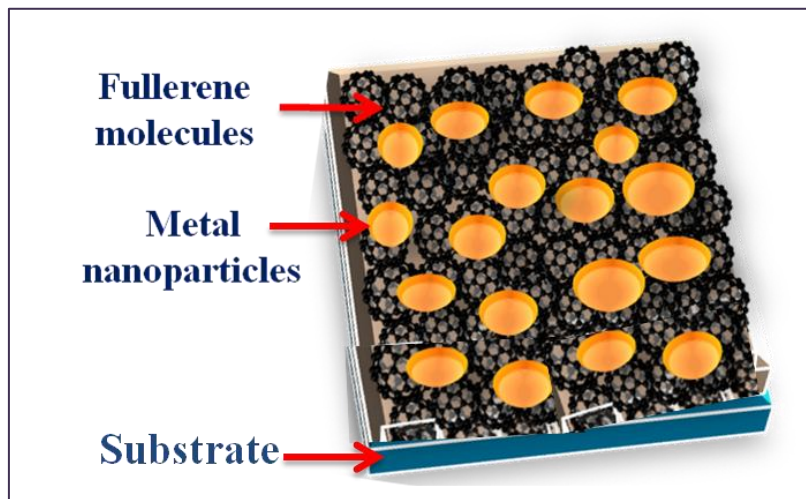
Figure1.2 Schematic of fullerene based metal nanocomposite thin film.

The effect of noble metal nanoparticles in the matrix is manifested by overall improvement of nanocompoaite thin film where reinforcing nanoparticles have different mechanical, physical, chemical, electronic, optical and magnetic properties from the bulk material. Incorporation of nanoparticles in thin films has emerged as an attractive area of exploration for various industrial applications [55]. The loading of

nanoparticles in thin film govern the mechanical, electrical, electronic, magnetic, chemical and optical properties of nanocomposites. The origin of the modification in properties lies in the interfacial structure. But for a smooth and coherent interface the adequate improvement in physical properties becomes difficult. In view of the current scientific interest in the development of new energy materials specifically for solar cells, a lot of research efforts are being exerted on the creation of new generation nanocomposite thin films by reinforcing metal nanoparticles in matrix of fullerenes (C_{60} or C_{70}) due to its excellent physical properties [56-59].

1.5 Surface plasmon resonance (SPR):

When nanocomposites with certain metallic nanoclusters (typically Au, Ag, Cu and Pt) are exposed to light, they exhibit a strong interaction of the oscillating electromagnetic field of light with the free electrons of the metal nanoparticles [60]. This gives rise to certain absorption maximum at a particular wavelength in the corresponding optical absorption spectra due to photon induced oscillation of the electron charge density. This oscillation of the surface electrons is called surface plasmon resonance (SPR) in the case of thin films, or particle plasmon resonance (PPR) for nanoparticles. Figure 2.2 shows the schematic of surface plasmon resonance in metal nanoparticles [61-62].
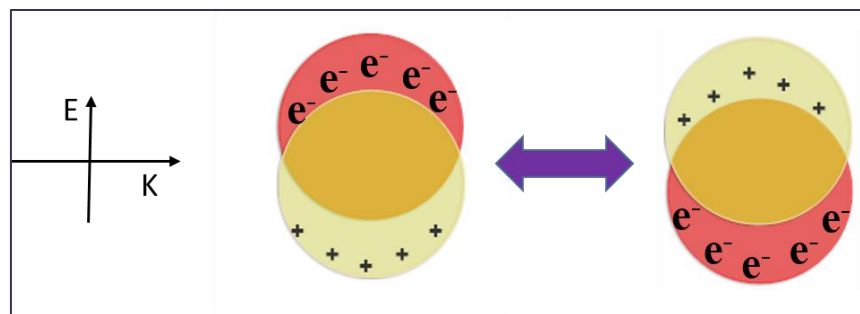
Figure 1.3 Schematic representation of SPR in nanoparticles.

As stated earlier, the electric vector of the electromagnetic radiation falling on the nanocomposite thin films interacts strongly with the electrons of metal nanoparticles resulting in an oscillatory motion of a specific frequency, commonly called SPR frequency when the frequency of oscillation becomes resonating with the frequency of incident radiation. The oscillation of electrons leads to polarization in surrounding medium; the polarization acts in opposition to the restoring force and shifts SPR band to higher wavelength.

The peak intensity and peak position of the SPR spectrum is dependent on various factors such as shape of the nanoparticles, size of the nanoparticles, and interparticle separation and surrounding material around the nanoparticles ie. Matrix [63-64].

A number of means which can enhance the magnitude and tune the position of SPR are stated to be the varying atomic fraction of nanoparticles embedded in matrix, annealing temperature of thin film, alteration of refractive index of matrix material and also chemical composition of the thin films [63-69].

The energy position of the SPR peak can be predicted by using the following equation of Mie theory [55]. As per Mie theory, extinction cross-section coefficient (σ_{ext}) for spherical particles is enough low, such that they don't polarize each other; it is expressed by the equation

$$\sigma_{ext} = 9\frac{\omega}{c}\varepsilon_m^{3/2}V_o\left[\frac{\varepsilon_2(\omega)}{\{\varepsilon_1(\omega)+2\varepsilon_m\}^2 + \varepsilon_2^{2}(\omega)}\right] \tag{1.1}$$

Where, V_o is the volume fraction and ω is the applied optical frequency. $\varepsilon(\omega) = \varepsilon_1(\omega) + i\epsilon_2(\omega)$ is the dielectric constant of metal and $\varepsilon_m(\omega)$ = dielectric constant of embedding matrix.

In the present study, fullerene is the host matrix, which has complex dielectric constant given by

$$\epsilon_m = \epsilon'_m - j\epsilon''_m \tag{1.2}$$

Where ϵ'_m is real part and ϵ''_m is imaginary part of dielectric constant of fullerene. According Kataura's optical data, imaginary part of the dielectric constant in the visible and near IR region is related to the absorption. So it is very important to consider this; it however, makes the calculation for dielectric constant very complex. But the complex part approaches to zero for the wavelength range above 420 nm. Hence, in the present case, the imaginary part has negligible influence on the absorption in the visible and IR region. So this imaginary part is neglected and the dielectric constant is taken to result from the real part only.

Now, the complex dielectric function of metal can be expressed by Drude free carrier contribution for ($\omega\tau \gg 1$) and an interband contribution:

$$\varepsilon(\omega) = 1 - \frac{\omega_p^2}{\omega^2} + i\frac{\omega_p^2}{\omega^2\tau} + \varepsilon_{inter} \tag{1.3}$$

Where ω_p is Drude bulk plasma frequency which is given by $\mathscr{O}_p = \sqrt{\dfrac{ne^2}{\varepsilon_o m_e}}$, n = free electron density of metal, e is electronic charge, m_e is the mass of e and ε_{inter} denotes interband transition term

With the replacement, $\omega = \dfrac{2\pi c}{\lambda}$, it follows

$$\varepsilon_1(\lambda) = 1 + \varepsilon_{inter} - \frac{\omega_p^2}{4\pi^2 c^2}\lambda^2 \tag{1.4}$$

$$\varepsilon_2(\lambda) = \frac{\omega_p^2}{8\pi^3 c^3 \tau}\lambda^3 \tag{1.5}$$

Here λ is the free space wavelength of light. From the above expression $\varepsilon_1(\lambda)$ is seen to vary linearly with λ^2 , and the same occurs for $\varepsilon_2(\lambda)/\lambda$. Here $\varepsilon_2(\lambda)$ has dependency on relaxation time (τ) hence it will rise with temperature as relaxation time is anticipated to decline with temperature.

From above discussion it seems that the SPR energy not only depends on the shape and size but also depends on the dielectric constant of the matrix. For the maximum value of the σ_{ext} , the denominator of equation (1) has to be minimum and this gives $\varepsilon_1(\omega) + 2\varepsilon_m = 0$; this is known as Frohlich condition which, when coupled with dipole mode presents its maximum.

By considering the Drude free electron term and above condition, the resonance frequency is given:

$$\omega = \frac{\omega_p}{\sqrt{(1+2\varepsilon_m)}} \tag{1.6}$$

The above equation clearly indicates that with the decrease of dielectric constant of host matrix (ε_m), the resonance frequency (ω) increases and so there is a blue shift in the UV-visible absorption studies.

1.6 Ion irradiation:

Ion irradiation is a unique tool to modify the properties of a material and has occupied valuable place in elaborating different properties of materials for different application in material science. The explanation about the non equilibrium process of interaction

of ion beam with a solid [70] follows from the fact that during the passage of ion through a solid material, two distinct processes take place:

(i)   Process related to nuclear energy loss; S_n

(ii)   Process related to electronic energy loss; S_e.

These two losses dominate at different energy range of the incident ion. The nuclear energy loss (S_n), dominates at low energy (~ 1 keV/amu) whereas electronic energy loss (S_e) dominates at high energy (~ 1 MeV/amu or more) [71].

1.6.1 Matter-ion interaction:

❍ Whenever fast moving ions pass through any solid there is a loss of energy due to interaction with target nuclei; this is called nuclear energy loss, S_n. This phenomenon normally takes place at low energy of ion beams preferably below 0.1 MeV/u. It is obvious that there will be significant change in angular scattering of projectile. This implies that the direction of incident beam remains no longer intact and material alteration resulting from displacement cascades is rather isotropic [70-71].

❍ Likewise interaction with electrons leads to the excitation of target atom and even the target atoms may be ionized. This phenomenon will maintain the original beam direction and normally takes place at ion energy levels in excess of 1 MeV/u. Thus it may be visualized that an electron gas is generated around the moving ions of straight trajectories. Efficient coupling between electron gas and atoms of the solid can raise the local temperature to a very high value within a few pico seconds; subsequent re-solidification at the fast rate (within 100ps) leads to amorphization of material, thereby forming what is known as ion track [71].

❍ These nanostructured amorphous materials are aligned along the beam direction and can find enormous practical applications as described elsewhere [72-74]. When the velocity of heavy ions is equal to or higher than velocity of Bohr electron, the concerned high energy heavy ions are termed as swift heavy ions (SHI). In case of SHI, S_e is about two orders of magnitude higher than S_n. While passing through insulators, SHI are found to bring about defect annealing, clustering of point defects and generation of columnar type of defects. This entails the possibility of using SHI for defects engineering in materials. Defect engineering is influenced by the parameters of ion beam, energy of the beam and quantum of energy deposited per unit length i.e. fluence [75-77]. Following the passage of SHI, the solid assumes its equilibrium state with modifications at the

surface and the bulk which are decided by the electrical, thermal and structural properties of the target material, the type of ion and parameters of irradiation.

1.6.2 Models:

SHI induced ion track formation is generally explained by two existing models viz. Coulomb Explosion model and Thermal Spike model.

1.6.2.1 Thermal spike model:

Initially propounded [78-79] to explain ion track formation in thin films under the action of high energy particles (viz. ion beam irradiation), thermal spike model witnessed development of its quantitative aspect due to Izui et al.[80]. It was proposed that sharing of energy between the electrons takes place within about 10^{-15} s; the energy of electron gets transferred to the atoms through interaction between electrons and atoms in time span of 5×10^{-13} s. Afterwards the model was further developed, to put forward explanation for the track formation in insulators; in consideration of hydrodynamics of energy propagation in so understood electron fluid and ionic fluid two equations were proposed [81]. Further development of a transient thermal model could explain the phase transformation of Si surfaces taking place after femto second (fs) laser irradiation. Moreover, fs pulse technique enables supply of energy to the electronic carriers earlier than the usual time required for exchange of energy with the lattice. So irradiation of high energy beam envisages creation of extremely hot carrier gas in an otherwise colder lattice [82]. This gives rise to increase in the lattice temperature due mainly to the electron–atom interaction. This thermalization event takes place within 10^{-14} s and becomes less with increase in the quantum of deposited energy [80]. The electron cools down by transferring energy to the colder electrons, thereby enhancing the electron–atom interaction with concurrent rise in lattice temperature [83-85].

Thus heavy ion irradiation can cause phase transformations that are thermally activated. The associated increase in lattice temperature is two-step process [86-87] viz.

❍ Thermalization of the deposited energy by electron–electron interaction.

❍ Transfer of energy to the lattice via electron–atom interaction.

The electron-atom system does not attain equilibrium and so the variation of temperatures of the lattice and the electron system with position and time, T and Te respectively, are expressed by coupled second order differential equations.

$$\rho C_e (T_e) \frac{dT_e}{dt} = \frac{d}{dr} \left[K_e(T_e) \frac{dT_e}{dr} \right] + \frac{K_e (T_e)}{r} \frac{dT_e}{dr} - g(T_e - T) + A(r) \qquad (1.7)$$

$$\rho C (T) \frac{dT}{dt} = \frac{d}{dr} \left[K(T) \frac{dT}{dr} \right] + \frac{K(T)}{r} \frac{dT}{dr} - g(T_e - T) \qquad (1.8)$$

where C_e, C and K_e, K are the specific heat and thermal conductivity for the electronic system and lattice, respectively, ρ is the material density, A(r) is the energy brought on the electronic system in a time t and r is the radius of cylindrical geometry with the heavy ion path as the axis. A(r) can be defined as $\iint 2\pi r A(r,t)dr\, dt = S_e$. The electron–phonon coupling factor g is given by:

$$g = \pi^4 \frac{(K_g n_e s)^2}{18 K_B T} \qquad (1.9)$$

Where K_B is the Boltzmann's constant, n_e is the electron density and s is the speed of sound in the metal.

Solution of differential equations gives the value of lattice temperature T(r,t) as function of position and time. The temperature maximum of the lattice for a specific radius r of ion path is dependent upon a critical value called electron stopping energy, S_e. It is obvious that the increase in temperature of electron system continues till the energy deposition time, $\sim 10^{-15}$ sec. Electron–phonon interaction becomes dominant for increasing the temperature of the lattice and as high a temperature as$\sim 10^4$ K may be attained at equilibrium which is normally attained after a mean time of the order of 10^{-12} sec. It may be noted that beyond a specific value of Se, temperature of the lattice becomes higher than the melting of the lattice, Tm within a cylindrical mass of radius r_m which is known as latent track having a dimension of a few nm. Subsequently the temperature of the systems starts decreasing and the rate of fall of temperature is decided by the thermal conductivity. Meanwhile molten phase is quenched at a rate of approximately 10^{15} K/sec. Diffusion in molten track plays the major role in mixing the constituents at the interface [88].

1.6.2.2 Coulomb explosion model:

Coulomb Explosion Model advocates the formation of a cylinder of ionized atoms due to the passage of the ion through matter. The electron-electron interaction is operative to effect the sharing of the electron excitation energy within the electron systems. This gives rise to the formation of latent tracks [88-89]. In fact, Coulomb Explosion model is better applicable for insulating materials. This is because electronic mean free path in metals is quite large, and therefore, the excitation energy is effectively utilized for warming up the system as a whole without resort to much

atomic movement. However, the defect production by electronic energy loss Se is explained by some researchers with the aid of this model [90] on the basis of assumption that a mean ionization degree D is possessed by all the atoms within a cylindrical mass of radius r_o. It is surmised that a uniform space charge ρ is responsible for generating an electric field E, which, within a time τ of the order of plasmon lifetime $\sim 10^{-14}$ creates an impulsive field on each of ionized atoms; this gives rise to a maximum recoil energy given by,

$$E_r \propto \left(\frac{D^2\tau}{r_0^3}\right)^2 \qquad (1.10)$$

It means that mechanism involved in the model deals with the direct, sudden and coherent energy transfer with respect to time and position. In general the magnitude of recoil energy derived in this way is very small, ~ 0.1 eV against the critical displacement energy, 10–20 eV; nevertheless, the energy transfer being coherent, can cause the effective atomic displacements. The description pertains to bulk material and not for the case of interfaces where the cylindrical region along ion trajectory is not conceivable [83, 91].

The finite magnitude of atomic impulsive forces normal to the interface acts in favor of atomic mixing. However, as time progresses, these ionic spikes in $\sim 10^{-14}$ sec are masked by the thermal spike at $\sim 10^{-12}$ sec; the enhanced lattice temperature due to thermal spikes act in opposition to the previous atomic displacement by Coulomb Explosion. Ultimately thermal spikes dominate and lead damage process [88-91].

1.6.3 Role of ion irradiation:

Low and high energy ion beams find immense applications in material science and biological sciences. Ion beam techniques are very powerful tools in thin film technology due to its high flexibility and easy amenability to control technologically important parameters. In general, the modification of materials achieved by energetic ions irradiation may take place in form of (i) doping through ion implantation at low doses (mainly in semiconductors) (ii) Ion beam synthesis by forming buried layers or precipitates of new metastable compounds by implantation of doses exceeding the solubility limit; (iii) ion beam mixing that is mixing of interfaces and growth of layers by Ion beam assisted deposition [88].
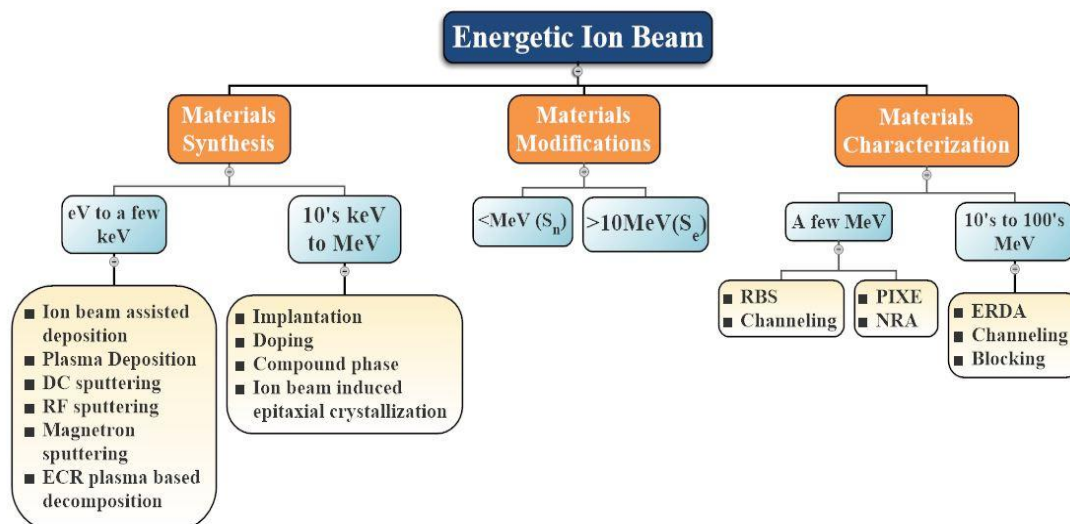
Figure 1.4 Schematic presentation of use of ion beam irradiation.

The structural and chemical modifications achieved by ion irradiation are important for physical and physicomechanical properties of materials in bulk or thin film form and can be suitably tailored to invoke new functionalities of high technological merits [86]. Energetic ion beam can be used in material science for material synthesis, material modification as well as materials characterizations [92]. In general, ion beams to eV to few keV can be used for different deposition techniques such as plasma deposition, DC sputtering and RF sputtering whereas the energetic ion beam of 10 keV to MeV is used for implantation and doping in materials (figure 1.3). Ion beams irradiation is a technique that works at atomic level. The electronic energy loss S_e can create the defects as well as anneal the defects. This may lead to phase transformation and particle growth. The density of defects is dependent on energy of ion beam as well as on the fluence of the beam. Swift heavy ion irradiation can result in the formation of long, linear nanoscale tracks in a broad range of materials, and such swift heavy ion tracks are exploited in a number of applications in nanoscience [93].

1.7 Objectives in the present thesis work:

❍ To probe into the role of fluence levels on structural changes in C_{60} upon irradiation by high energy swift heavy ion.

❍ To observe the effect of different energy ion beam irradiation on fullerene C_{70} thin films to observe the effect of different values of electronic energy loss on damage cross section.

○ To observe the effect of low energy ion beam irradiation effect on Copper-fullerene C_{60} nanocomposite thin films.

○ To observe the effect of high energy ion beam irradiation effect on Copper-fullerene C_{60} nanocomposite thin films.

○ To observe the effect of low energy ion beam irradiation effect on Copper-fullerene C_{70} nanocomposite thin films.

○ To observe the effect of high energy ion beam irradiation effect on Copper-fullerene C_{70} nanocomposite thin films.

1.8 Motivation of the thesis problem:

○ The fullerenes are the emerging functional material because of their excellent property and being based on carbon, one of the most abundant elements in nature. Due to its inherent high electron affinity property, fullerenes are treated as useful electron acceptor material in solar cells [35-39]. Noble metals (Au, Ag) exhibit the amazing property of Surface Plasmon Resonance (SPR) which modifies the optical properties of nanomaterial [60-62]. However, the frequency of SPR band is strongly dependent on nature of host matrix, shape and size of nanoparticles [63-69]. Ion track formation modifies the optical and electrical properties of irradiated fullerene C_{60}. The fascinating properties and the potential of fullerene C_{60} as the host matrix of metal embedded nanocomposite, seems to be a great motivation to study the possible modification of fullerene C_{60} as host material upon irradiation by high energy ion beam over a wide fluence range from 1×10^{9}-3×10^{13} ions/cm^{2}

○ Fullerene C_{70} having different structure and stability as compared to fullerene C_{60} is expected to show different SPR behavior due to irradiation by ion beam. Swift heavy ions (SHI) are used to engineer the fullerene C_{70} properties for engineering application. Because of its higher refractive index (~2.3) in comparison to fullerene C_{60} (~2.1), fullerene C_{70} matrix can give better SPR tuning of nanocomposites [35-39]. Non-availability of authentic data stimulates to take up studies on the possible modification in characteristics of fullerene C_{70} upon irradiation by ion beams of different energies.

○ Functional relationship between damage cross-section and electronic energy loss values due to ion beam irradiation of fullerene C_{60} has been developed by earlier workers [94]; this relationship enables to calculate the radius of the damaged cylindrical zone for any value of electronic energy loss in fullerene C_{60} irradiated

by ion beams of different energies. A Similar study on the effect of irradiating fullerene C_{70} thin films with ion beams of different energies is thought to be a step forward towards developing the quantitative relationship between damage cross section in fullerene C_{70} and electronic energy loss secured by ion beam of different energy.

❍ Fullerenes are chosen as the host matrix material in metal reinforced nanocomposites for solar cell application. It demands a broad absorption band for effective utilization of sunlight. Heavy ion irradiation is useful to enhance and tune SPR spectra of fullerene noble metal nanocomposites, In the light of above; the present study aims to induce SPR in such a way that most of visible region can be utilized for use in optoelectronics and organic solar cell. For this, nanoparticles of group 11 elements viz. Cu and Ag with respective SPR peak positions within ~410-450 nm and ~550 - 600 nm [61] are chosen. It appears that implantation of Ag ion (whose SPR peak lies at the lowest wavelength among these three elements) in Cu-C_{60} nanocomposite may yield a wide coverage within the visible band for SPR to take place. Thus, the present approach of exploring synergistic SPR enhancement in C_{60} nanocomposites with binary and ternary reinforcement of nanoparticles of group 11 elements seems to open a new vista in plasmonic research.

❍ It still remains a question if irradiation of fullerene by low energy heavy ions has identical impact on the structural transformation as that of high energy ion beam irradiation. In fact, the effect of low energy ion beam irradiation on the characteristics of Cu metal reinforced fullerene-based nanocomposites is not well studied till date. At higher doses of low energy heavy ion irradiation, nuclear collision becomes perceptible and leads to the formation of amorphized carbon, whereas at low doses photo polymerization of fractal molecules are produced by disintegration of fullerene molecules due to nuclear collisions [95-97]. In contrast, electronic energy deposition may lead a series of collisions, exponentially related with the fluence and tantamount to collision cascades; at low doses its density is not high enough to destroy all the molecules of fullerenes. This scenario of fullerene molecule under ion irradiation by low energy heavy ions, entices to conduct the study on modifications in structure and optical properties of Cu-C_{60} nanocomposites after irradiation by 350 keV Ar ion beam.

○ With a view to the possible widening of SPR band in Cu embedded fullerene C_{60}, it is aimed to observe the influence of SHI irradiation on SPR response of copper-C_{60} nanocomposites so that the system becomes cost effective. It motivates to conduct study the effect of irradiation of copper-C_{60} nanocomposites by high energy heavy ions like 120 MeV Ag ion.

○ The power conversion efficiency of C_{70} is 25% higher than that of C_{60}. The efficiency of organic solar cells based on fullerene C_{70} matrix can be further enhanced by incorporating metal nanoparticles for SPR enhancement. Copper is less expensive, abundant, and possesses high thermal and electrical conductivity. Moreover, copper shows similar absorption characteristic (SPR) property to those of Ag and Au. Moreover, it is least studied till date. So, it seems worthy to study the effect of irradiation on Cu - C_{70} nanocomposite by low energy heavy ions viz. 350 keV Ar; it is especially important as the low energy ion beam can produce sufficient atomic defects to promote electronic energy loss. Se for 350 keV Ar ion is smaller than the threshold for ion track creation. Therefore, it further motivates to probe into the possible structural and property modifications in the nanocomposite thin films which will be decided by nuclear energy loss, S_n, leading to collision cascades.

○ Discussion on the results of experiments with low energy ion beam irradiated (350 keV Ar) Cu-C_{70} nanocomposite thin films has been presented in last chapter. It is a matter of scientific interest to explore if high energy heavy ion beam (120 MeV Ag) irradiation produces any other interesting results. Moreover, it is important to understand the effect of such high energy ion beam irradiation on the characteristic growth of nanoparticles and the concurrent change in refractive index of fullerene C_{70}. So, the irradiation study on copper-C_{70} nanocomposite thin film is taken up.

1.9 Organization of thesis:

Chapter 1:

In this chapter, general introduction about fullerene, fullerene based metal nanocomposites and the work carried out in the Ph.D. thesis has been dealt. The importance of fullerene as a matrix of fullerene-based metal nanocomposites, their advantage is introduced in this chapter. Especially, research question on Cu–C_{60}/C_{70} nanocomposites are narrated. In the end, the motivation, objective for the work undertaken, the methodology adopted and the results are given in brief.

Chapter 2:

This chapter covers the concise review of the literature on fullerene matrix, metal incorporated fullerene based nanocomposite thin film and effect of ion irradiation on the fullerene matrix and its nanocomposite thin films. Emphasis has been given on elaboration of previous studies on influence of ion irradiation on the different properties of fullerene matrix and thin films of metal fullerene nanocomposites; further, description on structure property correlation of fullerene matrix metal reinforced nanocomposites has been elaborated.

Chapter 3:

In this chapter a detailed description about the experimental methods used for the present investigation is furnished; a brief review of the principles of techniques used in the present work is presented. Moreover, the chapter includes description about the raw materials used for the current research, the details of various experimental techniques used, experimental conditions employed and the parameters fixed for individual experimentation. The methods adopted for the synthesis of C_{60}, C_{70}, Cu-C_{60} and Cu-C_{70} nanocomposites thin films are narrated, and the implication of selection of specific fabrication parameters is also discussed. Details about the methodology adopted for various characterization techniques like Raman spectroscopy, Rutherford beam scattering (RBS), UV-visible absorption optical spectroscopy, Scanning Electron Microscopy (SEM), Atomic force Microscopy (AFM), Transmission Electron Microscopy (TEM), X-ray Photoelectron spectroscopy (XPS) and two probe electron conductivity measurements are clearly narrated.

Chapter 4:

This Chapter deals with the study on the effect of high energy ion beam irradiation on the characteristics of fullerene C_{60} and C_{70}, which are subsequently taken as the target matrix material of metal embedded nanocomposite thin films for solar cell applications. Chapter 4 is divided into two sections named, here after termed as section 4.1 and section 4.2.

Section 4.1 describes the results of study on the modifications in structure and properties of fullerene C_{60} after irradiation by 90 MeV Ni ion beam for various fluences from 1×10^{9} to 3×10^{13} ions/cm^2. Structure and property characterization are done by Raman spectroscopy, UV-visible absorption spectroscopy, atomic force microscopy and Rutherford backscattering technique. Damage caused to C_{60} has been assessed by following the already established technique. Transformation of fullerene

to amorphous carbon state has also been monitored. The results are elaborately discussed.

Section 4.2 deals with the information about which are quite scarce in literature. Four different types of ion beam of different energies are used to irradiate C_{70} thin film. These are 90 MeV Si ion, 55 MeV Si ion, 90 MeV Ni ion and 125 MeV Au ions. Each type of high energy ion beam of varying energy produces different degree of damage to C_{70} fullerene. The characteristic electronic energy loss associated with irradiation by a specific ion beam decides the damage cross section and hence attempts are made in this section to map the damage cross section against the electronic energy loss. This may help in determining possible damage cross section for particular electronic energy loss characterizing a specific ion irradiation for predetermined fluence. Different characterization techniques are used to understand the structural changes and the associated changes in absorption behavior of C_{70} for each type of irradiation. Moreover surface studies are also done to correlate the bulk and surface structures with the optical property of fullerene C_{70} which is the major point of interest, in terms of the major objective of the thesis work which is to explore applicability of fullerene based metal nanocomposites in organic solar cells. The results of the effect of individual ion irradiation were correlated at the end of section.

Chapter 5:

Chapter 5 deals with the effect of irradiation on the structure and properties of copper-C_{60} nanocomposites; both high and low energy ions beams are used for the study. This work is stimulated by the encouraging results of experiments done by others on the noble metal (Au and Ag) embedded fullerene C_{60} based nanocomposites. This chapter is divided into two sections as 5.1and 5.2.

The section, 5.1, is comprised of two studies; the effect of irradiation by 100 keV Ag ions (section 5.1.1) and 350 keV Ar ion (5.1.2) are described;

In the first section, 5.1.1, study on the effect of irradiation by 100 keV Ag ions over fluence range from 1×10^{14} to 3×10^{16}, on the structure and over fluence range from 1×10^{14} to 3×10^{16}, on the structure and properties of Cu-C_{60} has been described. Cu-C_{60} nanocomposite thin films synthesized by co-deposition restive heating method was given to contain about 13at% Cu at film thickness of ~28 nm as determined by Rutherford backscattering spectroscopy (RBS) analysis. Being of low energy, Ag ions got implanted and influenced the SPR due to copper which is reported. Structural

modifications due to ion irradiation are analyzed by Raman, and Transmission Electron Microscopy (TEM). Raman spectroscopy study reveals the transformation of fullerene C_{60} into amorphous carbon (a-C) with increasing fluence. TEM showed the enlargement of copper particles with increasing fluence. Reports on Atomic force microscopy (AFM) study as well the detection of bond formation in the nanocomposite by XPS study is also made in this section.

This section 5.1.2 discusses the report of study on the effect of low energy ion beam irradiation upon Cu-C_{60} nano composite; in the present case 350 keV Ar ion beam for the fluence ranging from 1×10^{13} to 3×10^{16} ions/cm^2 was used for irradiating copper-C_{60} nano composite whose copper concentration was determined to be 18at% at a thickness of 32nm. Choice of Ar ion is inherited from similar experiments with Au/Ag embedded- fullerene matrix composites. Characterization by TEM verified the growth of copper particles; it is observed from UV-visible spectroscopy that there is a red shift in SPR due to copper, the cause of which was assigned to particle growth at high fluence.

Section 5.2 discusses the effect of irradiation on the characteristics of Cu-C_{60} nano composite whose film thickness is 32nm and copper content has been 18at% as measured by RBS technique. The thin film is irradiated with high energy 120MeV Ag ion beam. Absorption spectroscopy study reveals that irradiation enhances SPR band due to copper, initially positioned at 622nm at pristine nanocomposite and then undergoing 11nm red shift at higher fluence. This stems from copper particle coarsening at increasing fluence which is as evidenced by TEM and XRD results. Raman spectroscopy confirms the transformation of fullerene to amorphous state; the existence of copper oxide in irradiated sample is ruled out by the XPS study, although the XRD profile recorded oxide peak in the pristine, diminishing at increasing fluence in irradiated sample.

Chapter 6:

Chapter 6 deals with the effect of irradiation on the structure and properties of copper-C_{70} nanocomposites; both high and low energy ions beams are used for the study. This work is stimulated by the encouraging results of experiments done by others on the noble metal (Au and Ag) embedded fullerene C_{60} based nanocomposites. This chapter is divided into two sections as 6.1 and 6.2.

In the first section, 6.1, the nanocomposite thin films of Cu-C_{70} are deposited by thermal co-evaporation on glass, silicon and TEM grids. The thickness of deposited

thin films (10 at. % Cu-C_{70}) is measured to be is ~30 nm by Rutherford backscattering spectrometry (RBS). The thin films irradiated with low energy heavy ion, 350 keV Ar ion at different fluences ranging from 1×10^{13} to 3×10^{16} ions/cm^2 have been characterized; optical properties and structural study are done by UV-visible absorption spectroscopy, Raman spectroscopy, transmission electron microscopy (TEM), atomic force microscopy (AFM) and X-ray photoelectron spectroscopy (XPS).

Section 6.2, Cu (10%) C_{70} nanocomposite films of thickness around 30 nm are deposited by thermal co-evaporation on glass, silicon and TEM grids. These thin films were irradiated with 120 MeV Ag ions at different fluences ranging from 1×10^{12} to 3×10^{13} ions/cm^2. The modifications in the optical properties and structure have been examined by UV-visible absorption spectroscopy, Raman spectroscopy, transmission electron microscopy (TEM).

REFERENCES

[1]   H.W. Kroto, J.R. Heath, S.C. Obrien, R.F. Curl and R.E. Smalley, C_{60}: Buckminsterfullerene, *Nature*, 318 (1985) 162-163.

[2]   P.D.Q. Huy and M.S. Li, Binding of fullerenes to amyloid beta fibrils: size matters, *Phys. Chem. Chem. Phys.,* 16 (2014) 20030.

[3]   B.L. Zhang, C.Z. Wang, K.M. Ho, C.H. Xu, and C.T. Chan, The geometry of small fullerene cages: C_{20} to C_{70}, *J. Chern. Phys.*, 97 (1992) 5007-5011.

[4]   F. Diederich and R.L. Whetten, Beyond C_{60}: The higher fullerenes, *Acc. Chem. Res.,* 25 (1992) 119-126.

[5]   V.P. Sedov, V.V. Kukorenko, S.V. Kolesnik, V.A. Shilin and Y.S. Grushko, Concentration and separation of higher fullerenes, *Fullerenes, Nanotubes, and Carbon Nanostructures*, 20 (2012) 354-356.

[6]   D.R. Mitchell, R.M. Brown, T.L. Spires, D.K. Romanovicz and R.J. Lagow, The synthesis of megatubes: new dimensions in carbon materials, *Inorg Chem.*, 40 (2001) 2751-2755.

[7]   A.A. Shvartsburg, R.R. Hudgins, R. Gutierrez, G. Jungnickel, T. Frauenheim, et al., Ball-and-chain dimers from a hot fullerene plasma, J Phys Chem A., 103 (1999) 5275-5284.

[8]   N. Sano, H. Wang, M. Chhowalla, I. Alexandrou and G.A.J. Amaratunga, Synthesis of carbon 'Onions' in water, *Nature*, 414 (2001) 506-507.

[9]   S. Iijima, Helical microtubules of graphitic carbon, *Nature*, 354 (1991) 56-58.

[10]   M.S. Dresselhaus, G. Dresselhaus and P.C. Eklund, Science of Fullerenes an Carbon Nanotubes, Academic Press, California 1996.

[11]   A.V. Nilolaev, T.J.S. Dennis, K. Prassides and A.K. Soper, Molecular structure of the C_{70} fullerene, *Chem. Phys. Lett.*, 223 (1994) 143-148.

[12]   M.S. Dresselhaus, G. Dresselhaus and P.C. Eklund, Fullerenes, *Journal of Materials Research*, 8 (1993) 2054-2097.

[13]   P. Diwan and A. Bharadwaj, The nanoscope *Encyclopedia of Nano science and Nanotecnology*, Pentagon Press, Nanomedicine (2005) 156 pages.

[14]   X.Q. Wang, C.Z. Wang and K.M. Ho, Vibrational modes in C_{70}:A first-principles study, Phys. Rev. B, 51 (8656) 1995.

[15]   A. Dworkin. H. Szwarc, S. Leach, J.P. Hare, T.J.S. Dennis et. al, C.R. Acad. Sci. (Paris), 312 U(1991) 979. 1941.

[16] J.S. Tse, D.D. Klug, D.A. Wilkinson and Y.P. Handa, Phase transitions in solid C_{60}, *Chem. Phys. Lett.*, 183(1991) 387-390.

[17] P.A. Heiney, J.E. Fischer, A.R. Mcghie, W.J. Romanow, A.M. Denenstein et al., Orientational ordering transition in solid C_{60}, *Phys. Rev. Lerr.*, 66 (1991) 2911-2914.

[18] P.A. Heiney, G.B.M. Vaughan, J.E. Fischer, N. Coustel, D.E. Cox et al., Discontinuous volume change at the orientational-ordering transition in solid C_{60}, *Phys. Rev. B*, 45 (1992) 4544-4547.

[19] W.I.F. David, R.M. Ibberson, T.J.S. Dennis, J.P. Hare and K. Prassides, Structural phase transitions in the fullerene C_{60}, *Europhysics Letters*, 18 (1992) 219-225.

[20] M. Sprik, A. Cheng and M.L. Klein, Orientational ordering in solid C_{70}: Predictions from computer simulation, *Phys. Rev. Lett.* , 69 (1992) 1660-1663.

[21] G.B.M. Vaughan, P.A. Heiney, J.E. Fischer, D.E. Luzzi, D.A. Ricketts-Foot et al., Orientational disorder in solvent-free solid $C_{70,}$ Science, 254 (1991) 1350.

[22] M.S. Dresselhaus, G. Dresselhaus, A.M. Rao and P.C. Eklund, Optical properties of C_{60} and related materials, *Synthetic Metals*, 78 (1996) 313-325.

[23] W. Zhou, S. Xie, S. Qian, T. Zhou, R. Zhao and G. Wang, Optical absorption spectra of C_{70} thin films, *J. Appl. Phys.*, 80 (1996) 459-463.

[24] W. Krätschmer, L.D. Lamb, K. Fostiropoulos and D.R. Huffman, Solid C_{60}: a new form of carbon, *Nature* 347 (1990) 354-358

[25] A.F. Hebard, M.J. Rosseinsky, R.C. Haddon, D.W. Murphy, S.H. Glarum, T.T. M. Palstra, A.P. Ramirez and A.R. Kortan, Superconductivity at 18 K in potassium-doped C_{60}, Nature, 350 (1991) 600-601.

[26] Y. Wang and L.T.Cheng, Nonlinear optical properties of fullerenes and charge-transfer complexes of fullerenes, *J. Phys. Chem.*, 96 (1992) 1530-1532.

[27] Z. Shuai and J.L. Bredas, Electronic structure and nonlinear optical properties of the fullerenes C_{60} and C_{70}: A valence-effective-Hamiltonian study, *Phys. Rev. B*, 46 (1992) 16135-16141.

[28] S.R. Flom, R.G.S. Pong, F.J. Bartoli and Z.H. Kafafi , Resonant nonlinear optical response of the fullerenes C_{60} and C_{70}, *Phys. Rev. B*, 46 (1992) 15598-15601.

[29] D. Neher, G.I. Stegeman, F.A. Tinker and N. Peyghambarian, Nonlinear optical response of C_{60} and $C_{70,}$ *Opt. Lett.*, 17 (1992) 1491-1493.

[30] F. Kajzar, C. Taliani, R. Danieli, S. Rossini, and R. Zamboni, Dispersion of Third-Harmonic-Generation Optical Susceptibility in C_{70} Thin Films, *Phys. Rev. Lett*., 73 (1994) 1617-1620.

[31] R.C. Haddon, A.F. Hebard, M.J. Rosseinsky, D.W. Murphy, S.J. Duclos et al., Conducting films of C_{60} and C_{70} by alkali-metal doping, *Nature*, 350 (1991) 320-322.

[32] A.F. Hebard, M.J. Rosseinsky, R.C. Haddon, D.W. Murphy, S.H. Glarum et al., Superconductivity at 18 K in potassium-doped C_{60}, *Nature*, 350(1991) 600

[33] P.M. Allemand, K.C. Khemani, A. Koch, F. Wudl, K. Holczer et al., Organic molecular soft ferromagnetism in a fullerene C_{60}, *Scienc*e, 253 (1991) 301-303.

[34] X. Zhao, A. Striolo and P.T. Cummings, C_{60} Binds to and Deforms Nucleotides, *Biophys J*., 89 (2005) 3856-3862.

[35] P.M. Allemand, A. Koch, F. Wudl et al., Two different fullerenes have the same cyclic voltammetry, *J. Am. Chem. Soc.,* 113 (1991) 1050-1051.

[36] S. Gunes, H. Neugebauer and N.S. Sariciftci, Conjugated Polymer-Based Organic Solar Cells, *Chem. Rev.*, 107 (2007) 1324-1338.

[37] T. B. Singh, N. Marjanovic, G.J. Matt, S. Gunes, N.S. Sariciftci et al., High-mobility *n*-channel organic field-effect transistors based on epitaxially grown C_{60} films, *Org. Electron.*, 6 (2005) 105-110.

[38] M.T. Rispens, A. Meetsma, R. Rittberger, C.J. Brabec, N.S. Sariciftci and J.C. Hummelen, Influence of the solvent on the crystal structure of PCBM and the efficiency of MDMO-PPV:PCBM 'plastic' solar cells, *Chem. Commun*., 0 (2003) 2116 -2118.

[39] W. Ma, C. Yang, X. Gong, K. Lee and A.J. Heeger, Thermally stable, efficient polymer solar cells with nanoscale control of the interpenetrating network morphology, *Adv. Funct. Mater*., 15 (2005)1617-1622.

[40] A.H. Ip, L.N Quan, M.M. Adachi, J. J. Mcdowell, J. Xu et al., A two-step route to planar perovskite cells exhibiting reduced hysteresis, *Appl. Phys. Lett*., 106 (2015) 143902-1-4.

[41] W. Ke, D. Zhao, C. Xiao, C. Wang, A. J. Cimaroli, C. R. Grice et al., Cooperative tin oxide fullerene electron selective layers for high-performance planar perovskite solar cells, *J. Mater. Chem. A*, (2016) 1-28.

[42] W. Ke, D. Zhao, C.R. Grice, A.J. Cimaroli, J. Ge et al., Efficient planar perovskite solar cells using room-temperature vacuum-processed C_{60} electron selective layers, *J. Mater. Chem. A*, 3 (2015) 17971-17976.

[43] J.C. Withers, R.O. Loutfy and T.P. Lowe, Fullerene commercial vision, *Fullerene Science and Technology*, 5 (1997) 1-31.

[44] J.R. Heflin, S. Wang, D. Marciu, C. Figura and R. Yordanov, Optical limiting of C6o, C_{60} charge-transfer complexes, and higher fullerenes from 532 to 750 nm, *Proceedings of Fullerenes and Photonics II SPIE*, 2530 (1995) 176-187.

[45] A.S. Berdinsky, Y.V. Shevtsov, A.V. Okotrub, S.V. Trubin, L.T. Chadderton et al., Sensor properties of fullerene films and fullerene compounds with iodine, *Chemistry for Sustainable Development 8*, (2000) 141-146.

[46] D.M. Guldi, B.M. Illescas, C.M. Atienza, M. Wielopolskia and N. Martín, Fullerene for organic electronics, *Chemical Society Reviews*, 38 (2009) 1587-1597.

[47] H. Imahori and Y. Sakat, Donor-linked fullerenes: photo induced electron transfer and its potential application, *Advanced Materials, 9 (1997)* 537-546.

[48] J.M. Berthelot, Composite materials: mechanical behaviour and structural analysis, Mechanical Engineering Series, Springer, (1998).

[49] C. Dupas, P. Houdy and M. Lahmani, Nanosciences, nanotechnologies and nanophysics. Springer, New York, (2006).

[50] W.L Barnes, A. Dereux, T.W. Ebbesen, Surface plasmon sub wavelength optics, *Nature*, Aug 14 (2003) 824-30.

[51] S.A. Maier, P.G. Kik, H.A. Atwater, S. Meltzer, E. Harel et al., Local detection of electromagnetic energy transport below the diffraction limit in metal nanoparticle plasmon waveguides, *Nat Mater*, 2(2003) 229-232.

[52] J. Reithmaier, P. Petkov, W. Kulisch and C. Popov, Nanostructured materials for advanced technological applications, *Springer Science & Business Media, Technology & Engineering*, (2009) 547.

[53] J.R. Krenn, Nanoparticle waveguides: watching energy transfer, *Nature Materials*, 2 (2003) 210-211.

[54] GP. Wiederrecht, Near-field optical imaging of noble metal nanoparticles, *Eur Phys J Appl Phys,* 28 (2004) 3-18.

[55] U. Kreibig and M. Vollmer, Optical Properties of Metal Clusters, Springer Series in Materials Science, 25 (1995).

[56]   R. Singhal, J.C. Pivin and D.K. Avasthi, Ion beam irradiation-induced tuning of SPR of Au nanoparticles in fullerene C_{70} matrix: Dependence of energy loss, *J. Nanoparticle Res*. 15 (2013) 1-10.

[57]   R. Singhal, D.C. Agarwal, S. Mohapatra, Y.K. Mishra, D. Kabiraj et al.*,* Synthesis and characterizations of silver fullerene C_{70} nanocomposite, *Applied Physics Letters,* 93 (2008) 103114.

[58]   R. Singhal, D.C. Agarwal, Y.K. Mishra, D. Kabiraj, G. Mattei et al., Synthesis, characterizations, and thermal induced structural transformation of silver-fullerene C_{60} nanocomposite thin films for applications in optical devices, *J. Appl. Phys*. 107 (2010) 2-7.

[59]   R. Singhal, D.C. Agarwal, Y.K. Mishra *et al.,* Swift heavy ion induced modifications of optical and microstructural properties of silver–fullerene C_{60} nanocomposite, *Nucl. Instr. and Meth. B,* 267 (2009) 1349-1352.

[60]   K.L. Kelly, E. Coronado, L.L. Zhao and G.C. Schatz, The optical properties of metal nanoparticles: the influence of size, shape, and dielectric environment, *J. Phys. Chem. B,* 107 (2003) 668-677.

[61]   E. Hutter and J.H. Fendler, Exploitation of localized surface plasmon resonance, *Adv. Mater.*, 16 (2004) 1685-1706.

[62]   L.L. Beecroft and C.K. Ober, Nanocomposite materials for optical applications, *Chem. Mater.*, 9 (1997) 1302–1317.

[63]   X. Huang and M.A. El-Sayed, Gold nanoparticles: Optical properties and implementations in cancer diagnosis and photothermal, *Journal of Advanced Research,* 1 (2010) 13-28.

[64]   Y.K. Mishra, S. Mohapatra, R. Singhal, D.K. Avasthi, D.C. Agarwal and S.B. Ogale, Au-ZnO: A tunable localized surface plasmonic nanocomposite, *Appl. Phys. Lett.*, 92 (2008) 043107.

[65]   Y.K. Mishra, D.K. Avasthi, P.K. Kulriya, F. Singh, D. Kabiraj et al., Controlled growth of gold nanoparticles induced by ion irradiation: An *in situ* x-ray diffraction study, Appl. Phys. Lett., 90 (2007) 073110.

[66]   M.C. Ridhway, R. Giulian, D.J. Sprouster, P. Kluth, L.L. Araujo et al., Role of thermodynamics in the shape transformation of embedded metal nanoparticles induced by swift heavy-ion irradiation, *Phys. Rev. Lett.,* 106 (2011) 095505.

[67]   T. Lee, N.K. Min, H.W. Lee, J.N. Jang, D.H. Lee et al., The deposition of amorphous carbon thin films for hard mask applications by reactive particle beam assisted sputtering process, *Thin Solid Films*, 517 (2009) 3999-4002.

[68]   J.W. Arbogast, A.P. Darmanyan, C.S. Foote, Y. Rubin, F.N. Diederich, M.M. Alvarez, J. Anz and R.L. Whetten, Photophysical properties of sixty atom carbon molecule (C_{60}), *J. Phys. Chem.,* 95 (1991) 11-12.

[69]   G. Xu, M. Tazawa, P. Jin and S. Nakao, Surface plasmon resonance of sputtered Ag films: substrate and mass thickness dependence, *Appl. Phys. A: Mater. Sci. Process.*, 80 (2005) 1535.

[70]   A.V. Krasheninnikov and K. Nordlund, Ion and electron irradiation-induced effects in nanostructured materials, Journal of Applied Physics 107 (2010) 071301.

[71]   S. Klaumunzer, Modification of nanostructures by high-energy ion beams, *Nucl. Instr. and Meth. B*, 244 (2006) 1-7.

[72]   D. Fink, P.S. Alegaonkar, A.V. Petrov, M. Wilhelm, P. Szimkowiak et al., High energy ion beam irradiation of polymers for electronic applications, *Nucl. Instr. and Meth. B*, 236 (2005) 11.

[73]   Z. Siwy, P. Apel, D. Baur, D.D. Dobrev, Y.E. Korchev et al., Preparation of synthetic nanopores with transport properties analogous to biological channels, *Surf. Sci.,* 532 (2003) 1061-1066.

[74]   J. Chen and R. Konenkamp, Vertical nanowire transistor in flexible polymer foil, *Appl. Phys. Lett.*, 82 (2003) 4782.

[75]   G.K. Mehta, Acceleration based material science research in India, *Journal of Applied Physics*, 107 (2010) 071301.

[76]   S.K. Srivastava and D.K. Avasthi, Swift Heavy Ion-induced Mixing, *Defence Science Journal*, 59 (2009) 425-435.

[77]   D.K. Avasthi and G.K. Mehta, Swift heavy ions for materials engineering and nanostructuring, Springer Series in materials science 145.

[78]   F. Seitz, J.S. Koehler, F. Seitz and D. Turnbull (Eds.), Displacement of atoms during irradiation, *Solid State Physics*, Academic press, New York, 2 (1956) 305.

[79]   K. Markle, Fission-fragment tracks in metal and oxide films, *Phys. Rev. Lett.*, 9 (1962) 150.

[80]   K. Izui, Fission fragment damage in semiconductors and ionic crystals, *J. Phys. Soc. Japan*, 20 (1965) 945.

[81]   R.H. Ritchie and C. Claussen, A core plasma model of charged particle track formation in insulators, *Nucl. Instrum. Methods*, 198 (1982) 133.

[82]   S.J. Lewandowski, E. Paumier, Y. Quéré, R. Soboleswki, M. Toulemonde et al., Observation of transient response of nb superconducting thin film to a single-heavy-ion impact, *Europhysics Lett.,* 6 (1988) 425.

[83]   R.L. Fleischer, P.B. Price and R.M. Walker, Ion explosion spike mechanism for formation of charged particle tracks in solids, Journal of Applied Physics, 36 (1965) 3645.

[84]   G.S. Khara, S.T. Murphy, S.L. Daraszewicz and D.M. Duffy, The influence of the electronic specific heat on swift heavy ion irradiation simulations of silicon, *J. Phys.: Condens. Matter*, 28 (2016) 1-7.

[85]   W. Primak, Experimental Evidence for Thermal Spikes in Radiation Damage, Phys. Rev., 98 (1955) 1854-5.

[86]   M. Toulemonde, C. Trautmann, E. Balanzat, K. Hjort and A. Weidinger, Track formation and fabrication of nanostructures with MeV-ion beams, Nuclear Instruments and Methods in Physics Research B, 216 (2004) 1-8.

[87]   Z.G. Wang, C. Dufour, E. Paumier and M. Toulemonde, The S_e sensitivity of metals under swift-heavy-ion irradiation: a transient thermal process, *J. Phys: Condens. Matter*, 6 (1994) 6733.

[88]   I.P. Jain and G. Agarwal, Ion beam induced surface and interface engineering, *Surface Science Reports*, 66 (2011) 77-172.

[89]   S.O. Kucheyev, H. Timmers, J. Zou, J.S. Williams and C. Jagadish, Lattice damage produced in GaN by swift heavy ions, J. Appl. Phys. 95 (2004) 5360.

[90]   A. Dunlop, D. Lesueur, J. Morillo, J. Dural, R. Spohr and J. Vetter, Atomic displacements and atomic motion induced by electronic excitation in heavy-ion-irradiated amorphous metallic alloys, *Nucl. Instrum. Methods Phys. Res. B,* 48 (1990) 419.

[91]   G. Schiwietz, E. Luderer, G. Xiao and P.L. Grande, Energy dissipation of fast moving heavy ions in matter, *Nucl. Instrum. Methods Phys. Res. B*, 1(2001) 175-177.

[92]   D.K. Avasthi, Modification and characterisation of materials by swift heavy ions, *Defence Science Journal*, 59 (2009) 401-412.

[93]   G.K. Mehta, Materials modification with high energy heavy ions, *Nucl. Instrum. Methods Phys.Res.* A, 382 (1996) 335-342.

[94]   N. Bajwa, A. Ingale, D.K. Avasthi, R. Kumar, A. Tripathi, K. Dharamvir and V.K. Jindal, Role of electron energy loss in modification of C_{60} thin films by swift heavy ions, *J. Appl. Phys.*, 104 (2008) 054306-1-13.

[95]   J. Kastner, H. Kuzmany and L. Palmetshofer, Damage and polymerization by ion bombardment of C_{60}, *Appl Phys Lett*, 65 (1994) 543-545.

[96]   D. Fink, R. Klett, P. Szimkovick, J. Kastner, L. Palmetshofer et al., Ion beam radiation damage of thin fullerene films, *Nucl. Instrum. Methods Phys.Res. B,* 108 (1996) 114-124.

[97]   D. Fink, L.T. Chadderton, J. Vacik, V. Hnatowicz, F.C. Zawislak, M. Behar and P.L. Grande, Damage and sputtering of fullerene by low energy medium and heavy ions, *Nucl. Instrum. Methods Phys.Res. B*, 113 (1996) 244-247.

Chapter 2

Literature Review

2.1 Introduction:

The discovery of fullerenes is believed to be responsible for triggering the nanotechnology revolution. Fullerenes are unique nanostructured materials with extraordinary mechanical, thermal and electrical properties. These properties have inspired the development of nanocomposites with extraordinary properties. The reinforcement of noble metal nanoparticles (Au, Ag and Cu) phase is added with the aim to improve the specific optical property. Among gold silver and copper, Cu nanoparticles get attention in recent times due to its interesting mechanical properties, high electrical conductivity, catalytic properties, appropriate melting point, high stability and high natural abundance in nature. The low cost of Cu over Ag and Au makes Cu nanoparticles attractive for applications in various fields of optics, electronics and solar energy conservation.

In view of the fact that fullerene based nanocomposites has attracted a great research interest for harnessing the potential of fullerene to be employed as new generation energy material, it is taken up as the broad area of the present research work. While lot of excellent research reports are documented in literature, it is no denying that there are many research challenges to surmount for developing fullerene based nanocomposites for optical device applications. The survey of literature is accomplished as a prerequisite for identifying the immediate research questions to address. A brief account of literature review is furnished below:

2.2 Metal nanocomposites thin films, properties and applications:

❍ Jean Marie et al. [1] defines composites as a combination of one or more discontinuous phase (called reinforcement or reinforcing material) embedded in a continuous phase (matrix).

❍ According to Dupas et al. and others [2-3] the small nanoparticles of metals reinforced in a matrix makes the nanocomposite thin film more efficient with modified properties. Hence the incorporation of nanoparticles not only preserves the matrix properties but also new properties of nanoparticles.

❍ Maier et al. [4] also reported that the modified properties of nanocomposite thin films are due to higher surface to volume ratio of reinforcing nanoparticles.

❍ Reithmaier et al. [5] also concluded that a drastic change takes place not only in physical but also in chemical properties of the material or substance on changing its dimension to nano scale. Hence all the physical and chemical properties related

to the size of embedded nanoparticles makes the nanocomposite thin films modified and open for different application areas (Krenn et al. and Wiederrecht et al.) [6-7].

○ Kreibig et al. [8] narrates the effect of noble metal nanoparticles in the matrix. Nanoparticles have different mechanical, physical, chemical, electronic, optical and magnetic properties from the bulk material and hence alter the properties of nanocomposite thin film.

○ Kelly et al. [9] have reported the interaction of the oscillating electromagnetic field of light with the free electrons of the metal nanoparticles. This oscillation of the surface electrons is called surface plasmon resonance (SPR) in the case of thin films, or particle plasmon resonance (PPR) for nanoparticles.

○ E. Hunter et al. [10] reported that when nanocomposites with certain metallic nanoclusters (typically Au, Ag, Cu and Pt) are exposed to light, they exhibit a strong absorption maximum at a particular wavelength due to photon induced oscillation of the electron charge density.

○ Previous report by L.L. Beecroft [11] documented in the literature have shown that the peak intensity and peak position of the SPR spectrum is dependent on various factors such as shape of the nanoparticles, size of the nanoparticles, and interparticle separation and surrounding material around the nanoparticles ie. Matrix.

○ A number of means which can enhance the magnitude and tune the position of SPR are stated to be the varying atomic fraction of nanoparticles embedded in matrix, annealing temperature of thin film, alteration of refractive index of matrix material and also chemical composition of the thin films are reported in literature [12-18].

○ Lee et al. [67 19] studied the effect of size of silver nanoparticles on the SPR. It was observed that with increasing grain size of the nanoparticles, peak position of SPR band also shift to higher wavelength side. Apart from this, the concentration of Ag nanoparticles also contributes towards the position of SPR peak.

○ Amendola et al [20] presented a review on the SPR on gold nanoparticles. They have carried out modeling of the SPR in Au nanoparticles.

○ Takele et al [21] researched on the plasmonic behavior of silver nanaoparticles embedded in different type of matrices such a polymer matrix of Teflon AF, poly (methyl methacrylate) (PMMA) and Nylon 6. As per their observation, the

particle plasmon resonance (PPR) frequency is highly dependent on the volume fraction of Ag. The effect due to the dielectric constant of the surrounding matrix also plays a critical role in tuning of the plasmon peak position.

○ Mathpal et al. [22] investigated the plasmonic behavior of Ag, embedded in glass matrix; over this, Au nanoparticles and titania were co deposited. The effect of annealing was studied and as per observation plasmonic response of both kinds of nanoparticles was found to be affected by the annealing treatment.

2.3 Fullerene based metal nanocomposites:

○ Carbon based nanocomposites containing noble metal nanoparticles are useful in industry due to the bi-functional properties of metal and matrix in single material. These types of materials show superior optical and electrical properties because of high surface-to-volume ratio of nanoparticles and physical properties related to matrix for applications in solar cells, memory devices and optical sensors and bioscience [23-26].

○ F. Banhart [27] reported the effects of irradiation in different carbon nanostructures. As fullerenes are different from the crystalline graphitic structure because of their curved basal planes, it governs specific geometry without the presence of vander wall interaction. This makes them an interesting material for studying the effect of irradiation..

○ Thermally co-deposited fullerene C_{70} nanocomposite thin films with varying composition were studied by Singhal et al. [28]. A red shift from 521 to 581nm in the SPR band position was observed with increasing the concentration of metal in the matrix C_{70}. Maxwell –Garnett theory explained the tuning of the SPR peak in consideration the absorbing nature of the fullerene matrix.

○ However in a recent work, the effect of 120 MeV Ag ion irradiation on thin films of a-C containing Ag nanoparticles has been reported by Singhal et al [29]. UV-visible absorption spectrum has confirmed a 26 nm shift in SPR band produced due to Ag nanoparticles; it was associated with a bi modal growth of nanoparticles. at a particular fluence of 3×10^{13} ions/cm^2. Thermal spike model was employed to explain the growth of nanoparticles.

○ Similar study on irradiation of gold nanoparticles embedded a-C based nanocomposite thin film with 120 MeV Ag ion has been reported by Singhal et al. [30]. The study had included the effect of thermal treatment on the nanocomposites. Both irradiation as well as thermal treatment study recorded blue

shift along with growth of nanoparticles. Percolation of nanoparticles is also observed at a specific temperature 500 °C.

2.4 Ion irradiation effect in fullerene as a matrix and fullerene based metal nanocomposites:

○ The structural modification obtained by irradiation of 189 MeV Ag, 110 MeV N and 50 MeV Si ions at fluences ranging from 1×10^{10} to 1.8×10^{12} ions/cm^2 on fullerene C_{60} thin films have been observed by Lotha et al. [31] . They calculated the ion track radius for each ion irradiation through damage cross section and were found to be of values about 6, 5 and 4 nm, respectively.

○ It is reported by Narumi et al. [32] that ion irradiation (7-MeV 12 C^{2+}) effect on C_{60} thin films results in amorphization of the film at higher fluence and at lower fluence disintegration of C_{60} molecules takes place.

○ Ghosh et al. [33] studied the electron sputtering yield of carbon versus fullerene film thickness under the effect of ion irradiation and observed that with increase in the thickness of the film, the respective yield decreases.

○ He, N and Bi ions at energies from 30 to 800 keV were used to irradiate thin films and the study due to Zawislak et al. [34] led to the inference that the destruction radius is smaller for light ions and is one order of magnitude larger for heavy ions. The above study have further reveled that both the nuclear energy loss and electronic energy loss are responsible for the destruction of C_{60} molecule.

○ Narayana et al [35] demonstrated a comparable study on the effect of irradiation of low and high energy ions on C_{60} thin films with a conclusion that low energy ion is implanted in the film and produces amorphization of the film at fluence 10^{15} ions/cm^2 whereas high energy Ag ion passes through the film and gets embedded in the substrate; moreover, there was no difference in crystallinity up to a fluence 10^{12} ions/cm^2.

○ An investigation due to Kumar et al. [36-38] established the effect of ion irradiation on the modification in properties like electrical transport, electromagnetic, ferromagnetic and infrared properties.

○ Their study on the phase transition of fullerene films by temperature dependent electrical transport measurement could transpire that transition temperature is not significantly influenced by the ion beam, rather broadening of structural phase transition with ion irradiation was noted [36].

○ The C_{60} thin film under ion irradiation produces conducting nanowires at lower fluences and at higher fluence, transforms into amorphous carbon (a-C). This a-C at room temperature shows ferromagnetic behavior; moreover some paramagnetic behavior is also observed in irradiated films due to oxygen oriented defects [37]. Comparative study with low energy and high energy ion irradiation was performed to analyze the effect of collision cascade and electronic excitation on ferromagnetic properties of C_{60} thin films; it was observed that there was an increase in degree of magnetization with increasing fluence of 250 keV Ar and 92 MeV Si ion beam. It therefore appears that high energy ion beam brings about more significant change in magnetization as compared to the lower energy ion beam [38].

○ With the help of Fourier transform infrared (FTIR) spectroscopy, the modification in vibrational properties of C_{60} due to 200 MeV Au ion irradiation was studied by Kumar et al. [39]. All the IR active modes T_{1u} (527, 577, 1183, 1428 cm^{-1}) were affected differently by ion beam, T_{1u} (2) mode being the most sensitive; the radius of ion track for this mode is found to be about 1.35 nm.

○ Bajwa et al. [40] presented the report of an elaborate study on the effect of different ion beams on Fullerene C_{60} thin films over a broad range of fluences 10^{10} to 10^{14} ions/cm^2. Different ions were chosen to vary S_e values within a range of 80 to 1270 eV/Å; a relationship between damage cross section and electronic energy loss was developed. The same researchers presented a phenomenological model for damage cross section and impact of electronic energy loss and nuclear energy loss values on polymerization and destruction of C_{60} molecules; it was reported that the conductivity of the films increases with ion irradiation due to transformation of fullerene into a-C. Scanty reports on C_{70} thin films are available in literature.

○ The effect of 120 MeV Au ion beam irradiation on fullerene C_{70} thin films has been studied by Singhal et al. [41] where it was observed that increasing fluence leads to decreasing optical band gap and resistivity. Amorphization of the C_{70} films was found to have taken place at a fluence of 3×10^{13} ions/cm^2, with the value of calculated radius of ion track being 2.9 nm.

○ A comparative study between C_{60} and C_{70} under 120 MeV Ag ion irradiation has been reported by Singhal et al. [42] who presented 2.5 and 3.5 nm as the calculated radii of ion track in C_{70} and C_{60}, respectively. From Tauc plots

decrement in band gap is observed from 1.98 eV to 1.86 and from 2.28 to 2.16 eV for C_{70} and C_{60}, respectively. For both the films, the amorphization fluence is reported same as 3×10^{13} ions/cm^2 and stability of C_{70} was marginally superior to fullerene C_{60}. Irradiation induced enhancement in grain size in both C_{60} and C_{70} thin films were confirmed by the same authors with the aid of microscopic measurements.

○ As reported by Kumar et al. [43] and Tripathi et al. [44] conducting nanowires could be produced in fullerene C_{60} thin films by ion irradiation at low fluence. Reportedly, the conductivity of nanowires so produced was observed to be seven times higher than that of the surrounding material i.e. fullerene $C_{60.}$ The synthesis of the concerned nanowires was carried out by 120 MeV Au, 180 MeV Ag ions, and 55 MeV Ti ions at low fluence levels ranging from 10^{10} to 5×10^{11} ions/cm^2. Conceptually, the formation of these nanowires in fullerene film due to passage of the ions makes the material amorphous along its path and hence it turns into highly conducting nanowires. At low fluence the overlapping of tracks is less probable and this paves the way of formation of isolated nanowires of 40–100 nm diameter as could be verified by conducting atomic force microscopy (C-AFM) measurements [45].

○ Similarly, such nanowires of fullerene C_{70} of diameter 11-20 nm were produced by Singhal et al. [45] with the aid of 100 MeV Ag ion irradiation. The conductivity of these nanowires increases with increasing fluence.

○ Silver nanoparticles in fullerene C_{60} matrix co deposited via thermal evaporation method were exposed to ion irradiation with 120 MeV Ag ion by Singhal et al [46]. UV-visible absorption analysis has revealed the shift of SPR band by 49 nm in lower wavelength side (blue shift) at the fluence value of 3×10^{13} ions/cm^2. Growth of the silver nanoparticles was also confirmed by the same worker with the help of transmission electron microscopy.

○ Attempts were also made to tune the SPR in Ag nanoparticles reinforced C_{70} nanocomposites [47]. The Ag-C_{70} thin films were irradiated with 120 MeV Ag ion beam; it was observed that there was increase in particle size from 7.0 ± 0.8 to 11.0 ± 0.4 nm and that fullerene matrix transformed into a-C. Moreover, a blue shift by about 100 nm was observed and the shift has been ascribed to the change in local refractive index of the matrix together with the size of thin films.

○ Singhal et al. [48] synthesized the gold nanoparticles embedded nanocomposite thin films and irradiated the same with ion beam of different energies viz.120 MeV Ag, 70 MeV Ni and 60 MeV Si and 350 keV Ar. The results of experiment recorded an appreciable electronic energy loss effect coupled with cascade collision effect due to low energy ion beam irradiation. Raman spectrum confirmed the transformation of the fullerene matrix into a-C and X-ray diffraction (XRD) analysis revealed the increase in particle size with increasing the fluence. For each ion beam irradiation, there is a characterizable SPR peak which depends upon the S_e values of the ion beam. Higher the value of Se, higher tuning is observed. In low energy ion irradiation tuning was also observed but not as much as in the case of high energy ion irradiation.

REFERENCES

[1]   J.M. Berthelot, Composite Materials: mechanical behaviour and Structural Analysis, Mechanical Engineering Series, Springer, (1998).

[2]   C. Dupas, P. Houdy and M. Lahmani, Nanosciences, nanotechnologies and nanophysics. Springer, New York, (2006).

[3]   W.L Barnes, A. Dereux and T.W. Ebbesen, Surface plasmon sub wavelength optics, Nature, Aug 14 (2003) 824-30.

[4]   S.A. Maier, P.G. Kik, H.A. Atwater, S. Meltzer, E. Harel, B. Koel and A.A.G. Requicha Local detection of electromagnetic energy transport below the diffraction limit in metal nanoparticle plasmon waveguides, Nat Mater, 2(2003) 229-232.

[5]   J. Reithmaier, P. Petkov, W. Kulisch and C. Popov, Nanostructured Materials for Advanced Technological Applications, Springer Science & Business Media, Technology & Engineering, (2009) 547.

[6]   J.R. Krenn, Nanoparticle waveguides: watching energy transfer, *Nature Materials*, 2 (2003) 210-211.

[7]   G.P. Wiederrecht, Near-field optical imaging of noble metal nanoparticles, *Eur Phys J Appl Phys,* 28 (2004) 3-18.

[8]   U. Kreibig and M. Vollmer, Optical Properties of Metal Clusters, Springer Series in Materials Science, 25 (1995).

[9]   K.L. Kelly, E. Coronado, L.L. Zhao, and G.C. Schatz, The optical properties of metal nanoparticles: the influence of size, shape, and dielectric environment, *J. Phys. Chem. B,* 107 (2003) 668-677.

[10] E. Hutter and J.H. Fendler, Exploitation of Localized Surface Plasmon Resonance, *Adv. Mater.*, 16 (2004) 1685-1706.

[11] L.L. Beecroft and C.K. Ober, Nanocomposite materials for optical applications, *Chem. Mater.*, 9 (1997) 1302-1317.

[12] X. Huang and M.A. El-Sayed, Gold nanoparticles: optical properties and implementations in cancer diagnosis and photothermal, *Journal of Advanced Research,* 1 (2010) 13-28.

[13] Y.K. Mishra, S. Mohapatra, R. Singhal, D.K. Avasthi, D.C. Agarwal and S.B. Ogale, Au-ZnO: A tunable localized surface plasmonic nanocomposite, *Appl. Phys. Lett.*, 92 (2008) 043107.

[14] Y.K. Mishra, D.K. Avasthi, P.K. Kulriya, F. Singh, D. Kabiraj et al., Appl. Phys. Lett., Controlled growth of gold nanoparticles induced by ion irradiation: An *in situ* x-ray diffraction study, 90 (2007) 073110.

[15] M.C. Ridhway, R. Giulian, D.J. Sprouster, P. Kluth, L.L. Araujo et al., Role of Thermodynamics in the Shape Transformation of Embedded Metal Nanoparticles Induced by Swift Heavy-Ion Irradiation, Phys. Rev. Lett., 106 (2011) 095505.

[16] T. Lee, N.K. Min, H.W. Lee, J.N. Jang, D.H. Lee, M.P. Hong, K.H. Kwon, The deposition of amorphous carbon thin films for hard mask applications by reactive particle beam assisted sputtering process, *Thin Solid Films*, 517 (2009) 3999-4002.

[17] J.W. Arbogast, A.P. Darmanyan, C.S. Foote, Y. Rubin, F.N. Diederich et al., Photophysical properties of sixty atom carbon molecule (C_{60}), *J. Phys. Chem.*, 95 (1991) 11-12

[18] G. Xu, M. Tazawa, P. Jin and S. Nakao, Surface plasmon resonance of sputtered Ag films: substrate and mass thickness dependence, *Appl. Phys. A: Mater. Sci. Process.*, 80 (2005) 1535.

[19] K.C. Lee, S.J Lin, C.H. Lin, C.S. Tsai and Y.J. Lu, Size effect of Ag nanoparticles on surface plasmon resonance, *Surface & Coatings Technology*, 202 (2008) 5339-5342.

[20] V. Amendola, R. Pilot, M. Frasconi1, O. M Marago and M.A. Iatì, Surface plasmon resonance in gold nanoparticles: a review, *J. Phys.: Condens. Matter*, 29 (2017) 203002.

[21] H. Takele, H. Greve, C. Pochstein, V. Zaporojtchenko and F. Faupe, Plasmonic properties of Ag nanoclusters in various polymer matrices, *Nanotechnology*, 17 (2006) 3499-3505.

[22] M.C. Mathpal, A.K. Tripathi, P. Kumar, R. Balasubramaniyan, M.K. Singh et al., Polymorphic transformations and optical properties of graphene-based Ag-doped titania nanostructures, *Phys. Chem. Chem. Phys.*, 16 (2014) 23874-23883.

[23] A. Biswas, O.C. Aktas, U. Schürmann, U. Saeed, V. Zaporojtchenko and F. Faupel, Tunable multiple plasmon resonance wavelengths response from multicomponent polymer-metal nanocomposite systems, *Appl. Phys. Lett.,* 84 (2004) 2655.

[24] S. Korchev, M.J. Bozack, B.L. Slaten, G. Mills, Polymer initiated photogeneration of silver nanoparticles in SPEEK/PVA films: direct metal photo patterning, *J. Am. Chem. Soc.,* 126 (2004), 10-11.

[25] H. Inouye, K. Tanaka, I. Tanahashi, T. Hattori, H. Kanatsuka, Ultrafast optical switching in a silver nanoparticle system, *Jpn. J. Appl. Phys.,* 39 (2000) 5132-5133.

[26] Y. Dirix, C. Bastiaansen, W. Caseri and P. Smith, Oriented pearl necklace arrays of metallic nanoparticles in polymers: a new route to polarization dependent color filters, *Adv. Mater.,* 11 (1999), pp. 223–227.

[27] F. Banhart, Irradiation effects in carbon nanostructures, *Rep. Prog. Phys.,* 62 (1999) 1181-1221.

[28] R. Singhal, D.C. Agarwal, S. Mohapatra, Y.K. Mishra, D. Kabiraj et al., Synthesis and characterizations of silver-fullerene C_{70} nanocomposite, *Applied physics letter,* 93(2008) 103114.

[29] R. Singhal, J.C. Pivin, R. Chandra, D.K. Avasthi, Ion irradiation studies of silver/amorphous carbon nanocomposite thin film, *Surface & Coatings Technology*, 229 (2013) 50-54.

[30] R. Singhal, D. Kabiraj, P.K. Kulriya, J.C. Pivin, R. Chandra and D.K. Avasthi, Blue-Shifted SPR of Au nanoparticles with ordering of carbon by dense ionization and thermal treatment, *Plasmonics,* 8(2013) 295.

[31] S. Lotha, A. Ingale, D.K. Avasthi, V.K. Mittal, S. Mishra, K.C. Rustagi, Gupta, V.N. Kulkarnif and D.T. Khathinga, Effect of heavy ion irradiation on c_{60}, *Solid State Communications*, 111 (1999) 55-60.

[32] K. Narumi and H. Naramoto, Modification of C_{60} thin films by ion irradiation *Surface and Coatings Technology*, 158-159 (2002) 364-367.

[33] S. Ghosh, D.K. Avasthi, A. Tripathi, S.K. Srivastava, S.V.S. Nageswara Rao et al., Studies of electronic sputtering of fullerene under swift heavy ion impact, *Nucl. Instrum. Methods Phys. Res. B,* 190 (2002) 169-172.

[34] C. Zawislak, D.L. Baptista, M. Behar, D. Fink, P.L. Grande et al., Damage of ion irradiated C_{60}, *Nucl. Instrum. Methods Phys. Res. B,* 149 (1999) 336-342.

[35] K.L. Narayana, M.Yamaguchi, N. Dharmarasu, N. Kojima and D. Kanjilal, Low energy ion implantation and high energy heavy ion irradiation in c_{60} films, *Nucl. Instrum. Methods Phys. Res. B,* 178 (2001) 301-304.

[36] A. Kumar, F. Singh, R. Kumar, A. Tripathi, D.K. Avasthi and J.C. Pivin, Electrical transport study of structural phase transitions in C_{60} films and the effect of swift heavy ion irradiation, *Solid State Communications*, 138 (2006) 448-451

[37] A. Kumar, D.K. Avasthi and J.C. Pivin, Electromagnetic properties of ion irradiated C_{60} films, *Surface & Coatings Technology*, 203 (2009) 2703-2706.

[38] A. Kumar, D. K. Avasthi, J. C. Pivin, A. Tripathi, and F. Singh, Ferromagnetism induced by heavy-ion irradiation in fullerene films, *Physical Review B*, 74 (2006) 153409-1-4.

[39] A. Kumar, Fouran Singh, D.K. Avasthi and J.C. Pivin, Infrared studies of swift heavy ion irradiated C_{60} thin films, *Nucl. Instrum. Methods Phys. Res. B,* 244 (2006) 221-224.

[40] N. Bajwa, A. Ingale, D.K. Avasthi, R. Kumar, A. Tripathi, K. Dharamvir and V.K. Jindal, Role of electron energy loss in modification of C_{60} thin films by swift heavy ions, *J. Appl. Phys.*, 104 (2008) 054306-1-13.

[41] R. Singhal, A. Kumar, Y.K. Mishra, S. Mohapatra, J.C. Pivin and D.K. Avasthi, Swift heavy ion induced modifications of fullerene C_{70} thin films, *Nucl. Instrum. Methods Phys. Res. B,* 266 (2008) 3257–3262.

[42] R. Singhal, F. Singh, A. Tripathi and D. K. Avasthi, A comparative study of ion-induced damages in C_{60} and C_{70} fullerenes, *Radiation Effects & Defects in Solids*, 164 (2009) 38–48..

[43] A. Kumar, D.K. Avasthi, A. Tripathi, D. Kabiraj and F. Singh, Synthesis of confined electrically conducting carbon nanowires by heavy ion irradiation of fullerene thin film *Journal of Applied Physics*, 101 (2007) 014308-1-5

[44] A. Tripathi, A. Kumar, D. Kabiraj, S.A. Khan, V. Baranwal and D.K. Avasthi, SHI induced conducting tracks formation in C_{60}, *Nuclear Instruments and Methods in Physics Research B,* 244 (2006) 15-18.

[45] R. Singhal, A. Tripathi and D.K. Avasthi, Synthesis of carbon nanowires by SHI irradiation of fullerene C_{70} thin film, *Adv. Mat. Lett.*, 4 (2013) 413-417.

[46] R. Singhal, D.C. Agarwal, Y.K. Mishra, S. Mohapatra, D.K. Avasthi, et al.*,* Swift heavy ion induced modifications of optical and microstructural properties of silver–fullerene C_{60} nanocomposite, *Nucl. Instrum. Methods Phys. Res. B,,* 267 (2009) 1349-1352

[47] R. Singhal, D.C. Agarwal, Y.K. Mishra, F. Singh, J.C. Pivin, R. Chandra and D.K. Avasthi, Electronic excitation induced tuning of surface plasmon resonance of Ag nanoparticles in fullerene C_{70} matrix, *J. Phys. D: Appl. Physics*, 42(2009) 155103.

[48] R. Singhal, J.C. Pivin and D.K. Avasthi, Ion beam irradiation-induced tuning of SPR of Au nanoparticles in fullerene C_{70} matrix: Dependence of energy loss, *J. Nanoparticle Res*. 15 (2013) 1-10.

Chapter 3

Experimental Techniques

3.1 Thin Film Deposition

Thin Film Deposition [1] is an essential technology nowadays especially when nanotechnology has covered semiconductor industry, for solar panels, CDs, disk drives, and optical devices industries. This technology is used for synthesizing a very thin film (few nm to100µm) or sometimes of a few atoms of thickness on different kind of substrates (glass, quartz, silicon etc.). The same can be used for layered structure by depositing thin film on previously deposited surface. Thin Film Deposition is usually divided into two broad categories:

   ❍ Chemical Deposition
   ❍ Physical Deposition

Chemical deposition process [2], uses a volatile fluid precursor which bring about a chemical change on surfaces for which a coating is left deposited on the surfaces. The use of fluid precursor makes the deposition conformal that is a constant thickness of coating is obtained although even though the interface is uneven. There are different techniques of chemical deposition, such as,

   ❍ Chemical Vapour Deposition

   ❍ Plasma Enhanced Chemical Vapour Deposition

   ❍ Atomic layer Deposition

   ❍ Sol-Gel Method

The chemical deposition is very useful for mono-dispersed and large quantity synthesis but via physical deposition technique the synthesis of highly uniform, nanocrystalline thin films is possible. Physical deposition technique involves coating of surface and is generally used for decorative coating, tool coating etc. In this process, deposition of a material on a substrate is accomplished by involving mechanical, electromechanical or thermodynamic processes after the material is made released from a source. Temperature, pressure and the other conditions fix the quality and quantity of deposition of materials on the chosen substrates..It is fundamentally a vaporization coating process in which the basic mechanism is an atom by atom transfer of material from the solid phase to the vapour phase and back to the solid phase, gradually building a film on the surface to be coated. The thin films produced by this method assume directionality as the depositing particles take up their path in a straight line towards the substrate. The following processes are included in physical deposition.

- Molecular Beam Epitaxy (MBE)
- Sputtering
- Pulse Laser Deposition
- Electrodynamic Deposition
- Thermal Evaporation

The above mentioned techniques under physical deposition process are different and can be elected on the basis of the material to be deposited and further what kind of application is going to fulfil by the deposited thin film [2]. In the present thesis work Thermal Evaporation technique has been adapted to deposit fullerene (C_{60}/C_{70}) and fullerene based metal nanocomposite (Cu-C_{60} andCu-C_{70}) thin films.

3.1.1 Thermal evaporation Technique:

In this technique, the material used for coating is thermally vaporized and then the vaporised material proceeds by potential difference to the substrate with little or no collisions with gas molecules. Due the reasons that high vacuum insures the travel of vaporised molecules over a large distance without having any collisions with the gas molecules (that is large mean free path) in the evaporation chamber normal levels of vacuum maintained within the evaporator range from 10^{-5} to 10^{-9} mbar. Collision with gas molecules causes a directional change of traversing gas molecules and as a result the chance of uniform deposition over the entire surface gets adversely affected. If the pressure within the chamber is less than 10^{-5} mbar, the mean free path becomes shorter and chance of collisions increase. Moreover, a higher purity is obtainable at higher vacuum level. This high vacuum confirms the deposition of thin film with less contamination. In thermal evaporation techniques, the following methods can be applied to heat the material:

- Electron beam heating technique
- Resistive heating technique

In fact, directional resistive evaporation is desirable in cases of nano-fabrications. The depositing materials can be either in the form of elemental atoms of or can be molecules of oxides or nitrides; moreover the substrate material can widely vary semiconductor wafers, optical components, solar cells etc. If the material to be evaporated is contaminated with the impurities of melting point higher than the material itself, there will be little possibility of evaporation of these impurities and hence so the deposited thin film will be more impure. Masking on the substrates is also possible so that the area where deposition of film on the substrate is not required

can be excluded. This technique facilitates monitoring of the deposition rate and it is easy to control this rate too.

With the above advantages of use of this technique, there are some difficulties as well; these are related to problems with deposition of high melting point materials, insurance of uniform heating, rapid change in deposition rate, reactions between the source and the heating container.

The deposition of fullerene and fullerene-based metal nanocomposite thin films has been done via resistive heating thermal evaporation technique which is explained below:

3.1.1.1 Resistive Heating Technique:

In this technique [2], the material is heated to its evaporation point by means of an electrical current passing through a filament or boat (source; thin sheet metal pieces of suitable high temperature metals (such as tungsten) with formed indentations or troughs into which the material is placed) where the source material is placed. The evaporated molecules of the source material travel from source to the substrate (target) where they nucleate together, to coat thin film. Since, the source material is heated to its melting point and is liquid, it is usually located in the bottom of the chamber, often in some sort of upright crucible. The vapour then rises above this bottom source, and the substrates are held inverted in appropriate fixtures at the top of the chamber. The surfaces intended to be coated are thus facing down toward the heated source material to receive their coating. The assembly of the technique is simple and results appropriate for depositing metals and some compounds with low melting temperature.

Preparation of thin films was carried out in the thermal co-evaporator (figure 3.1) available at optical material laboratory, Physics Department, Malaviya National Institute of technology (MNIT), Jaipur. This evaporator is equipped with co deposition facility as it has two boats and can be used to evaporate two materials simultaneously.

For uniform deposition of films, precaution should be taken for the rate of deposition. The rate should be constant for the whole process of deposition. Synthesis of fullerene thin films takes place by directly evaporating the powder of fullerene C_{60}/C_{70}. The powder of the C_{60}/C_{70} was placed in the boat and heated. Different kinds of substrates (glass, quartz and silicon) are placed over the substrate holder which is kept about 12

cm above the boat. Through resistive heating, temperature of the boat makes the material vapourized.
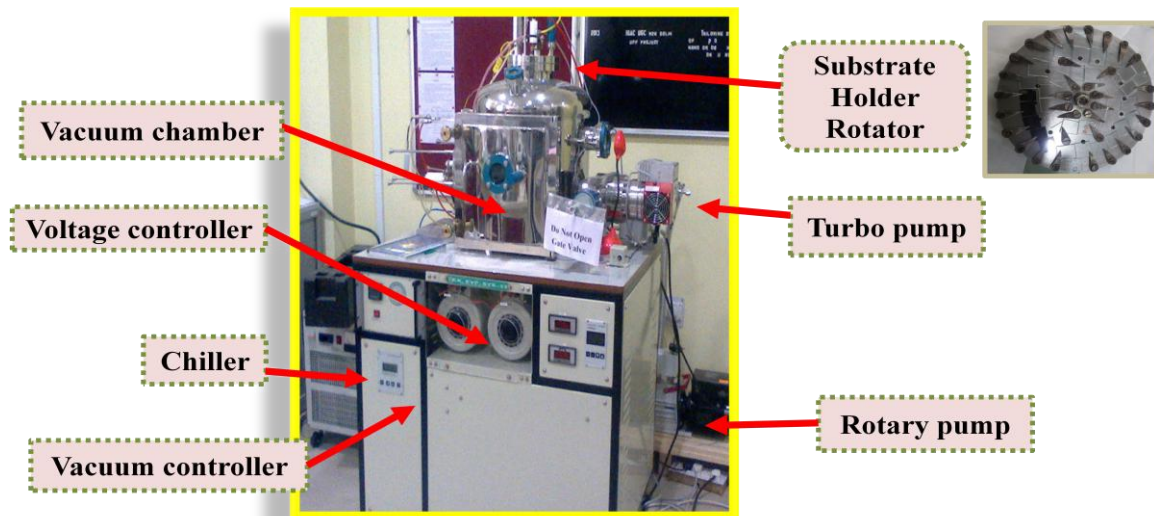
Figure 3.1 Thermal evaporator used in the present study.

Since fullerene C_{60} and C_{70} sublimes at ~800˚C, so it seems that direct deposition of the material takes place on the substrates. For making uniform deposition on each of the substrates, the target holder is kept on rotating throughout the deposition process. For maintaining the rate of deposition, the current is regulated manually and adjusted as per requirement. No substrate heating was required.

For nanocomposite thin film, co-deposition of the materials, fullerene and copper takes place simultaneously. During this co-deposition, both materials fullerene C_{60}/C_{70} powder and copper powder are placed in two tungsten boats in thermal evaporator chamber. First they are evaporated separately one by one for noting the current value and deposition rate value by keeping the mask over the materials placed in different boats. After realizing both the values, actual deposition is started and rate is monitored by taking the joint value of both the rates for each material. The vacuum pressure and rate were monitored and maintained at the specific values for desired uniform nanocomposite thin film deposition. The concentration of the metal content in the film is based on the rate taken for the deposition. During the film deposition, the sample holder was rotated using a DC motor in order to get the uniformity across all the samples in a single deposition.

3.2 Irradiation:

In the present research work, irradiation of samples was done in three different ways: the low energy ion implanter, low energy ion beam irradiation and high energy ion beam irradiation [3]. These facilities are available at Inter University Accelerator Center (IUAC), New Delhi and have been utilized for irradiation of experimental samples. Brief description of each type of facilities used for the purpose is narrated below:

3.2.1 Ion Implantation by Low Energy Ion Implanter:

Impingement of low energy heavy ion bears a strong potential for implantation of ions in thin film samples.
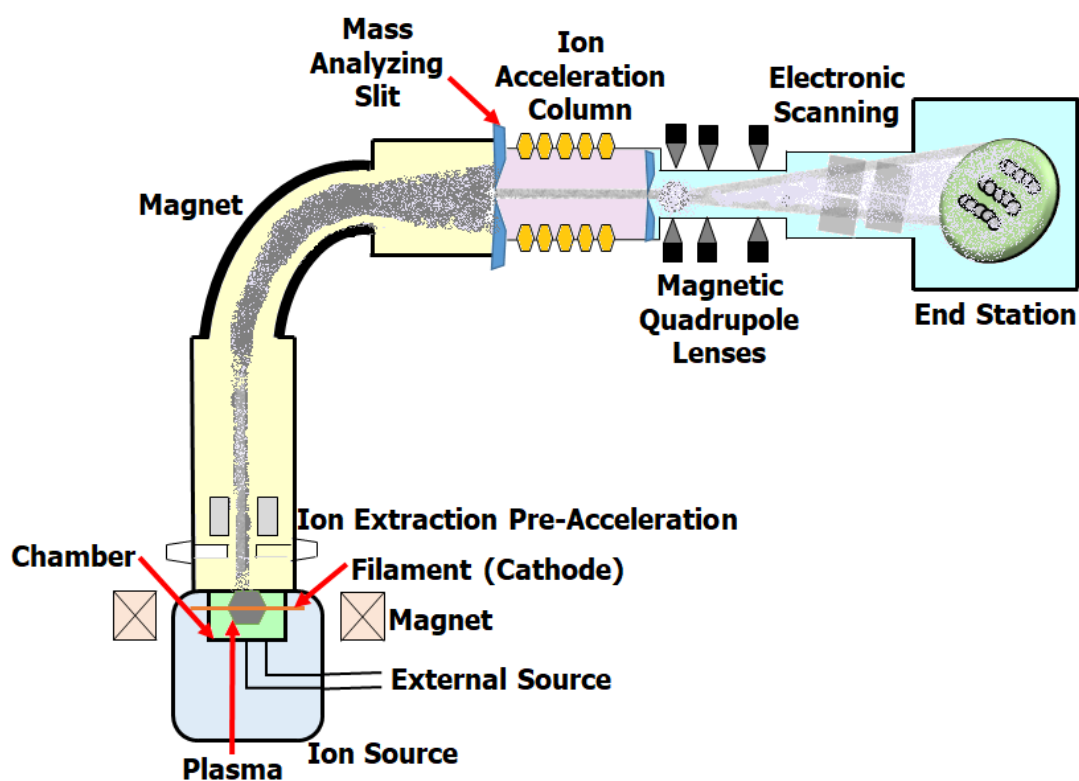
Figure 3.2 Schematic diagram of low energy ion implanter present at IUAC, New Delhi.

This is a reliable way for ion beam irradiation over a large specific area. The ion implanter is a flexible system and is made of sub systems (figure 3.2) like

- ❍ Source of ions
- ❍ Analyzer of mass
- ❍ Accelerator stage
- ❍ Scanning system
- ❍ Chamber to load target

The principles of designs remaining same, the latest version of ion implanter is more versatile in operation, less power consuming for water cooling and capable of

optisimising power consumption equipment size and hard ware requirement of vacuum. In the equipment available at IUAC, New Delhi, there is a provision for ion extraction with the aid of high potential source, 0-500 kV. An additional voltage of 10-30 kV is normally applied to extract the ions which goes through the entrance slit of mass analyzing magnet.

The ion beam, after being mass separated and traversing through the analyzing magnet enters the accelerator tube. Within the accelerator tube the ions get accelerated to acquire the required energy. There is a quadrupole lens which aids in focusing the ion beam passing through the acceleration tube; the focused beam hits the target material in x-y scan direction. The scanning is done along both x and y directions in order that a uniform distribution of ions is secured. The resulting current of the incident beam is measured by Faraday cups around the target.

3.2.2 Low Energy Ion Beam Irradiation:

The low energy ion beam facility (LEIBF) [4] of IUAC, New Delhi has been used for irradiating experimental thin films of present work by 350 keV Ar ion. An electron cyclotron resonance (ECR) constitutes the above facility and is based on a source of ions placed at a high voltage of 200kV. A high current of multiple charged positive ions are obtained from the source (figure 3.3). 10 GHz ECR is used to produce ions. The entire system which includes power supplies, high frequency transmitter etc. is placed on a deck at high voltage. Optical fiber communication system is used for controlling the operation. The accelerator is grounded at the beam line end and the voltage difference between this and high potential deck is responsible to impart the required kinetic energy to the ions. A vacuum of 10^{-6} mbar is maintained through the pumping station which is comprised of turbo molecular pump with a backup rotary pump.

The beam steering is accomplished by electrostatic steerer along with double slit; the control of beam size is also possible with the help of the same. The distribution of ions inside the system can be monitor by a beam profile monitor for both the directions orthogonal to each other. The beam can be stopped by the Faraday cup and there are valves to isolate to two sections of a beam line. Mass analysis is carried out by magnetic analyzer which makes the selection of the required ions possible by the application of pre determined magnetic field. Focusing at the desired spot is made possible by the provision of electric quadrupole-triplet. While tuning the beam, the

beam is focused within a small circular spot and to provide the availability of ions homogenously over the entire area a beam scanner is used.
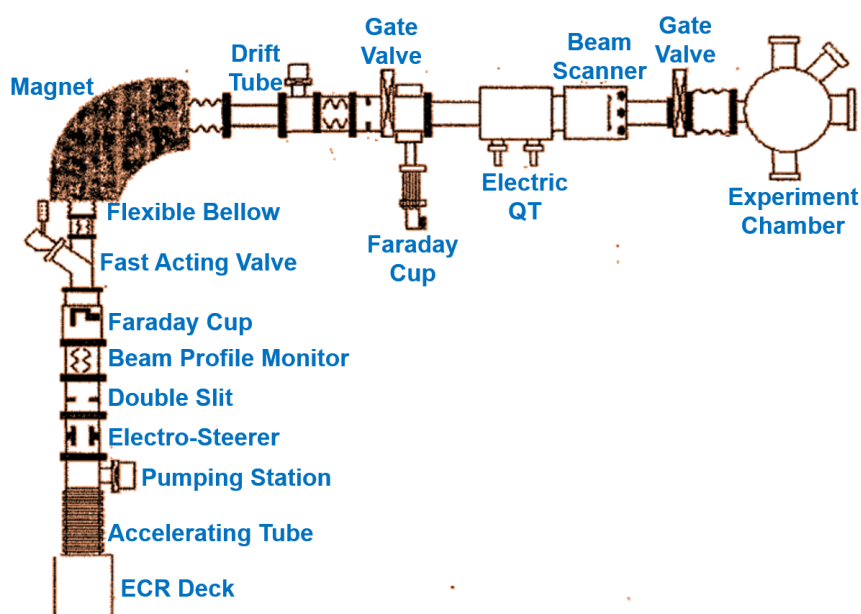
Figure 3.3 Schematic diagram of low energy ion beam irradiation facility (LEBIF) available at IUAC, New Delhi.

The irradiation of the films takes place at high vacuum 10^{-9} mbar. Thin films were mounted on a six or four sided ladder (sample holder) with an arrangement to mount six samples (with marking sample number) on each side (figure 3.4). A copper ladder is used for mounting the samples in the chamber so that flow of heat generated due to ion impingement on the samples can become effective. The ladder was then placed in the chamber.
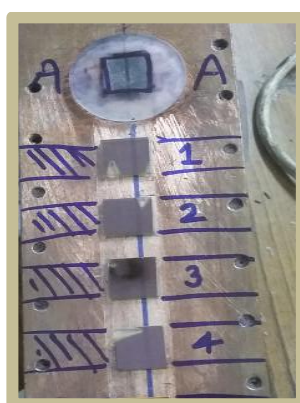
Figure 3.4 Ladder for mounting samples for irradiation.

The ladder was moved vertically up and down to bring the samples into the path of the ion beam for irradiation that is monitored through the screen provided with the camera facing the ladder faces under irradiation. Each marked sample is irradiated

with the required beam at different fluences. The fluences for each sample are calculated on the basis of the beam current in the form of time. The beam is monitored carefully throughout the irradiation so that it remains continued on the sample and covers it properly.

3.2.3 High Energy Ion Beam Irradiation:

The Pelletron accelerator [3] at IUAC New Delhi is able to cause acceleration to any ions ranging from proton to uranium excluding inert gases. The range of energies of accelerated ions extends from a few MeV to 100 MeV (figure 3.5).
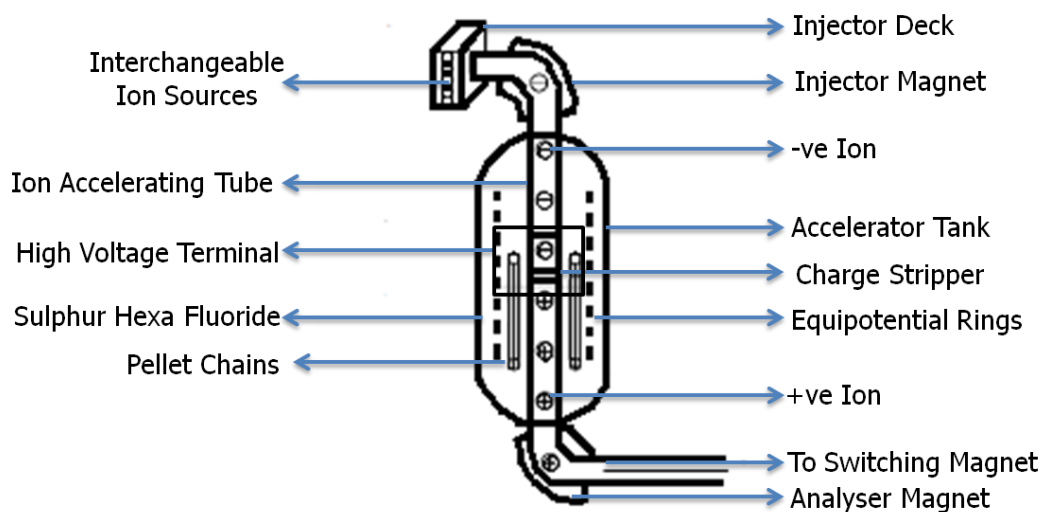
Figure 3.5 Schematic diagram of pelletron accelerator available at IUAC, New Delhi.

A stainless steel tank houses the pelletron; a high voltage terminal is positioned at the middle of the tank and can be charged to high potential. The potential gradient from high voltage to the ground voltage is maintained at the top and bottom of the tank which is filled with an insulating gas, sulphur hexa fluride (SF_6) at 6 to 7 atmospheric pressure. An ion source called Multi Cathode source of Negative Ions by Cesium Sputtering (MC-SNICS) produces negative ions at 250 kV. Mass analysis of ions is carried out by injector magnet (90 degree dipole magnet) which is bent downward. During the passage of negative ions through the accelerating tube towards the positive terminal, sufficient acceleration of ions takes place; the accompanying electron are stripped off by a C-foil or N_2 gas stripper, thereby producing positive ions which are repelled by the positive terminal and get accelerated towards ground. This is repeated twice to accelerate the ions which when comes out off the tank is subjected to selection of specific charge state by the use of magnetic analyzer. The entire beam line is kept under ultra high vacuum. Similar to low energy accelerator the focusing

and beam profiling sterrering magnet, quadrupole triplet magnets and beam profile monitors (BPM).

The energy of ions coming out of accelerator is given by the equation

$$E = [E_D + (1 + q)V_T] \tag{3.1}$$

Where E_D is the potential of the MC-SNICS source at the deck, V_T is the potential at the terminal in MV, q is the charge state of the ion after stripping.

Material science beam line of 15 UD pelletron accelerator (a tandem Van de graft type accelerator) facility [5] available at Inter University Accelerator Center (IUAC), New Delhi has been used for the irradiation of fullerene and fullerene based nanocomposite thin films.

The samples are mounted on the six face sided ladder and placed in the high vacuum chamber for irradiation. The beam energy is fixed at the desired value for the respective ion. Each ladder face is equipped with the quartz on the top of the ladder. Below this crystal, the samples are mounted and marked properly. This quartz crystal is used for profiling the beam that fits to the upcoming samples and covers it properly. As the beam is profiled, then according to the charge state and current, fluence time is calculated as per formula given below

$$T(sec) = \frac{\emptyset \times e \times A}{I} \tag{3.2}$$

Where, $\emptyset$ is the fluence (ions/cm^2), e is the electron charge (C), A is the area (cm^2)of the sample (in our case 1 cm$\times$1 cm) and I is the current of the beam (ampere).

SRIM software has been used to determine the electronic energy loss and nuclear energy loss in the fullerene C_{60} and C_{70} as well as in the Cu nanoparticles embedded fullerene nanocomposite thin films (Cu-C_{60} and Cu-C_{70}). By the use of this software, it is possible to determine ion ranges in one layer which may be composed by one or many elements. Since experimental thin films are chosen as C_{60} and C_{70}, the carbon is chosen by default as the target; as input it is required to put the density value. Density values are taken as 1.65 g/cm^3 for C_{60} and 1.7g/cm^3 for C_{70} thin films. On deciding the unit for output file, (here eV/Å unit is taken), the used ion type and its energy values are provided as input and as a output file we get the values of electronic energy loss and nuclear energy loss as well as projected range that gives idea about the depth up to which ions will travel. In case of compound thin film such as Cu-fullerene thin film, concentration of both elements Cu and C are taken from their measured composition and density is calculated on the weight fraction basis for the constituent

phases. Finally, the output data gives us the information of the S_e, S_n and the projected range. By changing the ions and their energies, it is possible to obtain different set of values of S_e, S_n and the projected range. This is discussed in later section.

3.3 Characterizations:

Various characterization techniques are used for the analysis of different properties of the fullerene (C_{60} & C_{70}) matrix; fullerene based metal nanocomposites and modification of these properties under the effect of irradiation

3.3.1 UV-visible Absorption Spectroscopy:

UV-visible absorption spectroscopy is best suited characterization technique for determination of the absorption spectrum of the material in solution or deposited thin film. This spectroscopy is based on the principle that when a sample is illuminated with a source of light, the absorption of a particular wavelength can take place only when the energy of incident photon is equal to the energy difference in energy between two energy states for transition of electrons in the molecules of the material. This UV-visible absorption spectrometer makes possible to measure the degree of absorption of incident light of different wavelengths and provides a spectrum known as UV-visible absorption spectrum of the concerned sample [6].

The intensity of the absorbed light continuously decreases (exponentially) on passing through the sample. This can be explained with the help of Beer-Lambert Law,

$$A = \in cl \tag{3.3}$$

Here $\in$, is the coefficient of molar excitation, that is a constant for the absorbing sample, c is the concentration of the sample and l is the path length of light through the sample (In case of thin film it is the value of the thickness of the deposited thin film) and A is the absorption of and can be given as

$$A = A_0 log\left(\frac{I_0}{I}\right) \tag{3.4}$$

Where, I_0 is the incident light intensity and I is the transmitted light intensity. The ratio of $\frac{I_0}{I}$ is called the transmittance, T.

The instrumentation of UV-visible absorption spectrograph is composed of two lamps (deuterium lamp and Halogen lamp for UV and visible light), a series of mirrors, monochromator, beam splitter and detector (figure 3.6).
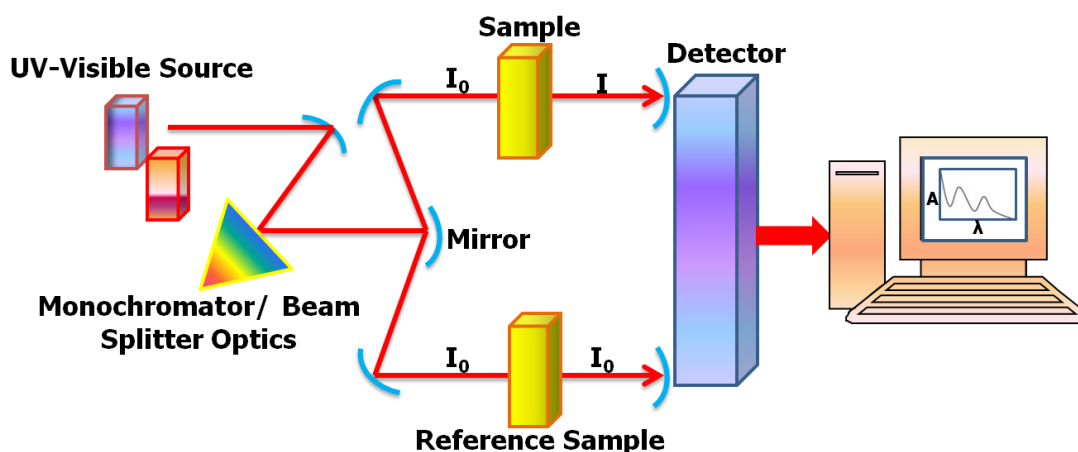
Figure 3.6 Schematic diagram of UV-visible absorption spectrometer.

The spectrometer covers the wavelength within the range of 200-1000 nm [7]. The monochromator changes the small bands of radiation and sends it to beam splitter that splits the beam in two parts; one is sent to the sample and other is sent through the reference sample (background data). The detector measures the difference between the intensities of transmitted light (I) and incident light (I_0) and transmits it to the recorder and spectrum is displayed in the form of absorption versus wavelength on the computer screen.

In present study, LAMBDA 750 (Perkin Elmer) UV-Visible NIR Spectrophotometer instrument is used for recording the UV-visible absorption spectrum of the fullerene and fullerene based metal nanocomposite thin film. The UV-visible absorption spectra of pristine and Si ion irradiated samples have been recorded by using a U-3300 UV-visible spectrometer by Hitachi at IUAC, New Delhi.

3.3.2 Raman Spectroscopy:

Raman scattering occurs with a change in vibrational, rotational or electronic energy of a molecule. Raman spectroscopy is most responsive to highly symmetric covalent bonds with little or no natural dipole moment. Hence carbon material will be the best suited samples for being structurally characterized by this spectroscopy. Thus, Raman spectroscopy provides substantive structural information of fullerene thin films. The carbon-carbon bonds that make up these materials fit this criterion perfectly and as a result Raman spectroscopy is highly sensitive to carbon nanostructures and able to provide information about their structure. All the allotropes of carbon, diamond, graphite, grapheme, fullerene and carbon nanotubes are made of carbon atoms with C-C bonds of different orientation; hence these materials are highly amenable to structural characterization by Raman spectroscopic technique.

On illuminating the diatomic molecule with a monochromatic light, the induced dipole moment of the diatomic molecule starts oscillating in accordance with the electric vector of the incident light [8-9]. The interaction of incident light with a molecule can be expressed by the equation 3.5, as below

$$P = (\alpha_0 E_0 \cos 2\pi v_1 t) + \frac{1}{2} E_0 x \frac{\partial \alpha}{\partial x} [\cos 2\pi (v_0 + v_1) t + cos 2\pi (v_0 - v_1) t] \quad (3.5)$$

Here, α is the polarizability of the molecule, α_0 denotes no interaction of light, x is the inter nuclear distance, E_0, the incident electric field, E is the electric vector of the source, v_0 is the frequency of incident light, v_1 is time dependent frequency of vibration and t is the corresponding time. The first term which represents absence of the interaction of molecule with incident light leads to emission of light with no change in frequency and is referred as Rayleigh scattering as shown in energy level diagram (figure 3.7).

The other two terms in the above equation defines the change in polarizability with x and results in two scattering bands known as Raman scattering bands (figure 3.7). Those are Stokes and anti-stokes scattering bands and are categorized on the basis of frequency difference between emitted light and incident light. After scattering, the scattered light having frequencies lower than the incident light is termed as Stokes lines while those with higher frequencies are known as anti-stokes lines.
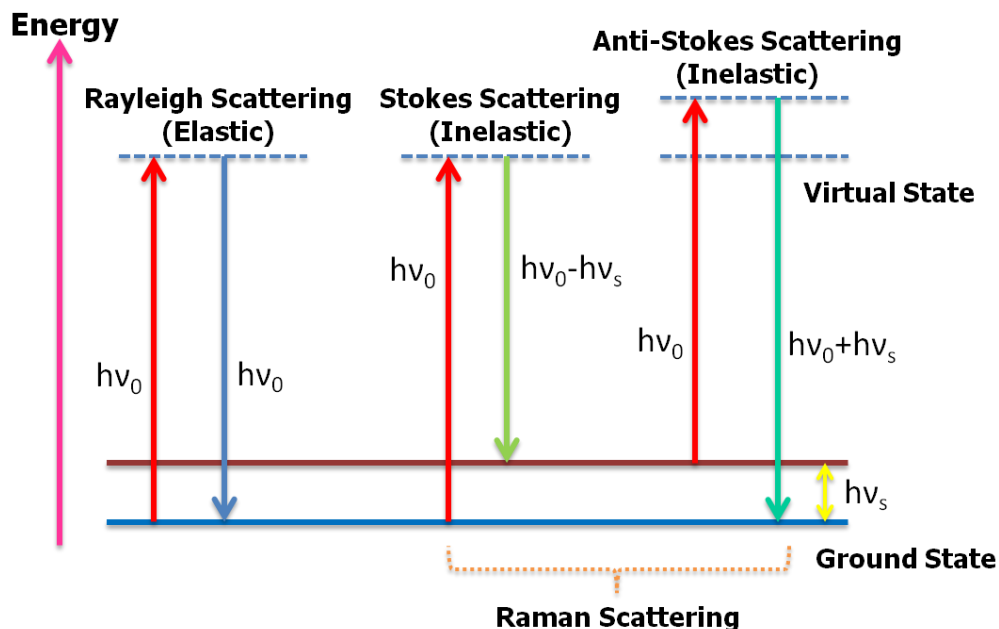
Figure 3.7 Raman scattering energy level diagram.

Raman instrumentation is composed of an illuminating source which is usually a laser source, a spectrograph and a detector. The laser light illuminates the sample and as a

result generation of scattered Raman photons takes place; these pass through the spectrograph and the photons with altered frequency are separated and collected at the CCD detector. The recorded intensity of Raman signals as a function of wavelength (Raman spectrum) can be seen on a computer screen as shown in figure 3.8.
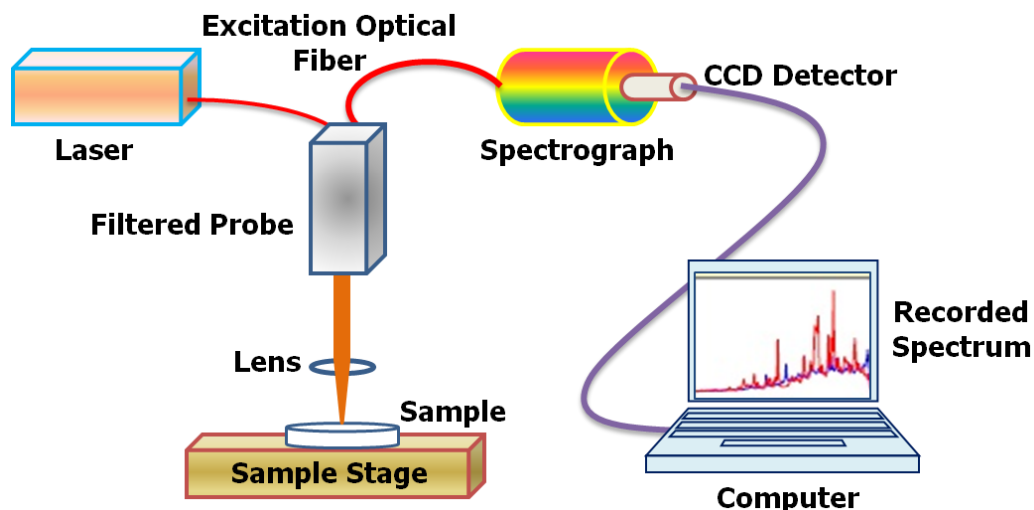
Figure 3.8 Schematic diagram of Raman spectrometer.

Raman spectroscopy is capable of discerning even a slight change in orientation of C-C bonds and becomes very valuable tool for characterization of carbon nanomaterials. Raman spectra is recorded for fullerene C_{60} , fullerene C_{70}, Cu-C_{60} and Cu-C_{70} nanocomposite thin films in the range 200-1800 cm^{-1} using AIRIX STR 500 Raman spectrograph at room temperature available at Material research center in Malaviya National Institute of technology, Jaipur. The Ar ion laser used with excitation wavelength at 532 nm at minimum power (~1mW, 50 × objective) to avoid heating effect. Raman spectra of the pristine and 90 MeV Ni ion irradiated thin films were measured using LABRAM Raman spectrometer in a range of 200-1800 cm^{-1} at room temperature. The Ar ion laser excitation at 488 nm (~1 mW, 50×objective) was used which is available at UGC-DAE Consortium for Scientific Research, Indore Centre. Raman data of pristine and irradiated films with 55 MeV Si ion beam were recorded with a Renishaw in-via Raman microscope using an Ar ion laser excitation at 514 nm at room temperature. To avoid any heating effects, the laser beam was focused at very low power (<1mW, 20×objective).

3.3.3 Rutherford beam scattering (RBS):

Rutherford backscattering (RBS) technique is one of the most precise characterization techniques to determine the film thickness and the concerned atomic species with their concentration in the film. Rutherford back scattering (RBS) [10-11] is the best

ion scattering technique to determine the composition, thickness and depth distribution of the film.
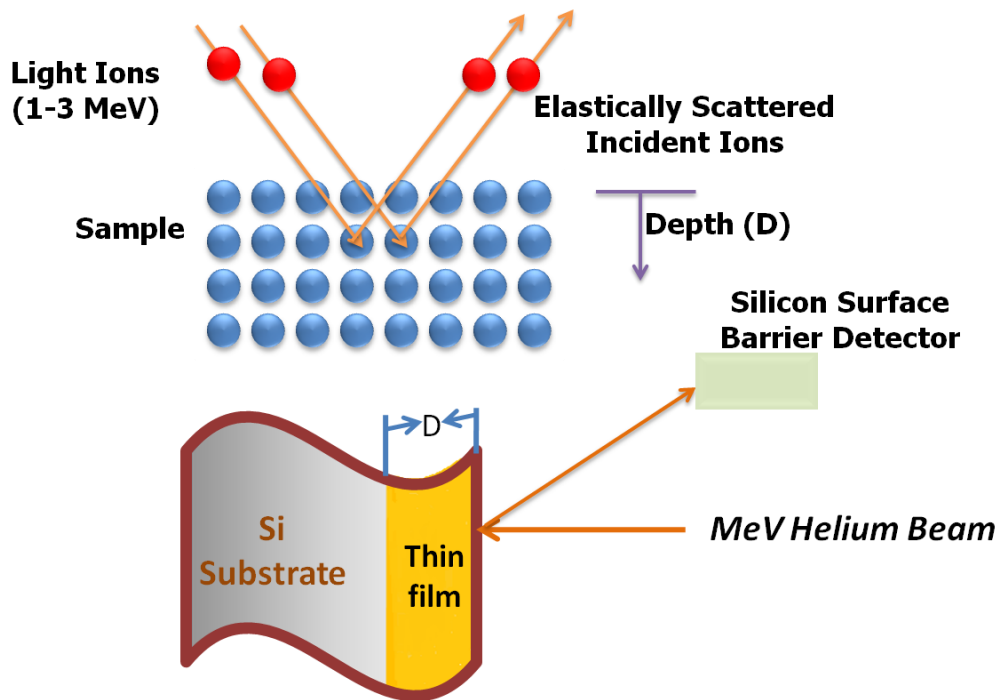
Figure 3.9 Schematic diagram of Rutherford backscattering process.

It is typically the method of choice for quantitative compositional analysis of thin films used for semiconductors, optical coating and other applications where composition and thickness of the film plays very crucial role. The $4He^{2+}$ (alpha particles) beam of energy 2.000 MeV with charge ~15 μC is used to record the spectrum (figure 3.9) [12].

The energy of the backscattered particles depends upon both the kinematic factor and energy loss factor. The number of backscattered ions is directly dependent on the concentration of the given element. This is based on the classical scattering of α-particles from different nuclei in a distinct and well understood way. Surface barrier detector measure the number and energy of ions backscattered after colliding with atoms of the sample enabling us to determine atomic mass and elemental concentration versus depth below the surface. Rutherford Backscattering Spectrometry (RBS) facility with 1.7 Million Volt Pelletron accelerator at IUAC, New Delhi has been used to characterize both matrix and nanocomposite thin films.

3.3.4 X-ray diffraction (XRD):

XRD is a very important experimental technique that has long been used to address all issues related to the crystal structure of solids, including determination of lattice

constants and geometry, identification of unknown materials, orientation of single crystals, preferred orientation of polycrystals, defects, stresses, etc. [13]. In XRD, a collimated beam of X-rays, with a wavelength typically ranging from 0.7 to 2A˚, is incident on a specimen and is diffracted by the crystalline phases (figure 3,10) in the specimen according to Bragg's law:

$$\lambda = 2D \sin\theta \qquad\qquad (3.6)$$

$$n(\lambda) = 2D\sin\theta$$

$$AB = D\sin\theta = BC \therefore ABC = 2D\sin\theta$$
$$A'B' = 2D\sin\theta = B'C' \therefore A'B'C' = 2ABC = 4D\sin\theta$$
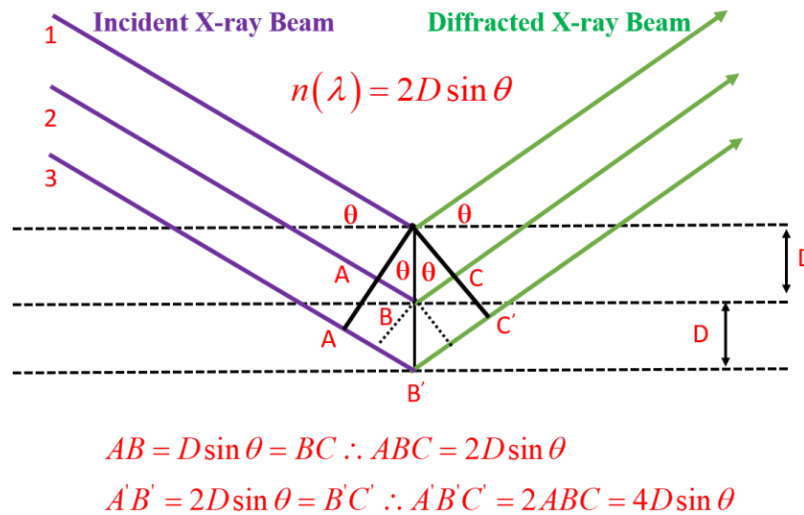
Figure 3.10 Ray diagram of reflection of X-rays.

Where D is the spacing between atomic planes in the crystalline phase and λ is the **X-ray wavelength**. The direction of the diffracted X-rays is measured as a function of the diffraction angle 2θ and the specimen's orientation. It depends upon the size and shape of the crystals. However, the intensity of a diffracted beam is determined by the position of atoms within the unit cell. Depending upon the structure factor, the characteristic diffraction pattern of a particular crystal structure is evolved. This diffraction pattern is used to identify the specimen's crystalline phases and to measure its structural properties.

Diffraction peak positions are accurately measured with XRD, which makes it the best method for characterizing homogenous and inhomogeneous strains. Homogenous or uniform elastic strains shift the diffraction peak positions. From the shift in the peak positions, one can calculate the change in d- spacing, which is the result of the change of lattice constants under the strain. Inhomogeneous strain varies from crystallite to crystallite or within a single crystallite and this causes a broadening of the diffraction peaks that increase with sin θ. Peak broadening is also caused by the finite size of crystallites, but here the broadening is independent of sin θ. When both

crystallite size and inhomogeneous strain contribute to the peak width, these can be separately determined by careful analysis of peak shapes.

If there is no inhomogeneous strain, the crystallite size, d, can be estimated from the peak width with the Scherrer's formula

$$d = \frac{K\lambda}{\beta cos\theta} \tag{3.7}$$

Where λ is the X-ray wavelength, β is the full width of half maximum (FWHM) of diffraction curve and k is the Scherrer's constant of the order of 0.9 for usual crystal. However, one should be alert to the fact that the nanoparticles often form twinned structures; therefore, Scherrer's formula may produce results different from the true particle sizes. In addition, X-ray diffraction provides onlythe collective information of the particle sizes and usually required a sizable amount of powder. It should be noted that since the estimation would work only for very small particles, this technique is very useful in characterizing nanoparticles. Similarly, the film thickness of the epitaxial and highly textured thin films can also be estimated with XRD.

One of the disadvantages of XRD, compared to electron diffraction, is the low intensity of diffracted X-rays, particularly for low-Z materials. XRD is more sensitive to high-z materials, and for low-Z materials, neutron or electron diffraction is more suitable. Typical intensities for electron diffraction are ~108 times larger than for XRD. Because of small diffraction intensities, XRD generally requires large specimens and the information acquired is an average over a large amount of materials.

Information related to the crystallinity of the samples of fullerene thin films is collected with the help of X-ray Diffraction study conducted with XRD at Elettra Synchrotron Lab, Trieste, Italy in MCX beam line at a glancing angle of 0.5°. Bruker D8 Diffractometer was used to record the diffraction pattern of pristine and irradiated nanocomposite thin films.

3.3.5 Scanning Electron Microscope (SEM)

SEM is a type of electron microscope that creates various images by focusing a high energy beam of electrons onto the surface of a sample and detecting signals from the interaction of the incident electron with the sample's surface [14]. SEM images have greater depth of field (curved surfaces are resolved properly) yielding a characteristic

3D appearance useful for understanding the surface structure of a sample. Magnification is of order 10,000 X and resolution 10 nm.
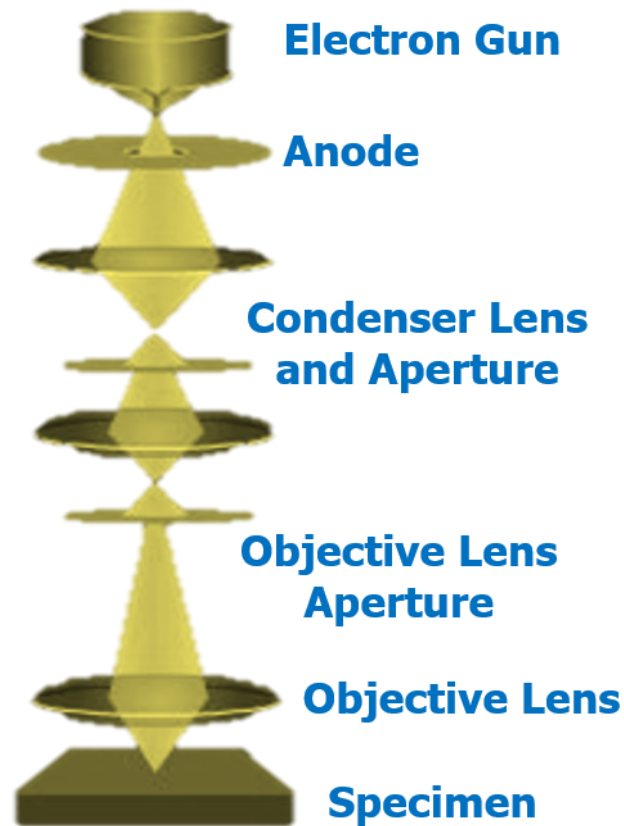
Figure 3.11 Presenting the optics of Scanning electron microscope.

A stream of electrons is emitted by the electron gun and accelerated towards the specimen using positive electric potential (figure 3.11). The stream is confined and focused using metal apertures and magnetic lenses into a thin focused monochromatic beam. The beam is focused onto the sample using a magnetic lens. Interactions occur inside the irradiated sample affecting the electron beam.

SEM is used to find the topological morphology of micro-nano structure along with shape and size of phases in material. For nonconductive samples, sputter coater is used to deposit a few nano meter (2-3 nm) coating of Au/Pt material and once it become conductive, the sample can be analyzed in high resolution mode. The technical specification and resolution of the aforesaid FESEM model is 1nm at 30KV acceleration voltage. The sample was first placed on the stub through an adhesive carbon tape and then put into the sputter coater to make thin film around 2 to 3 nm gold layer. After coating, the sample was placed into the FESEM chamber, the chamber vacuum was kept at around 3×10^{-3} Pa. Sample micrograph were taken on 15 KV with spot size of 2.5 nm. The samples were scanned at the various places to check

the uniformity of the sample; while doing the FESEM, the EDS spectra have also been taken.

Nova Nano FE-SEM 450 (FEI) installed in Material Research Center, MNIT, Jaipur and SEM images were recorded on MIRA IILMH Field Emission Scanning Electron Microscope (TESCAN make at IUAC, New Delhi) having resolution of 1.5 nm at 25 kV. The observed images provide the information regarding the particle morphology and the particle size can also be calculated by this technique.

3.3.6 Transmission Electron Microscopy (TEM):

Transmission electron microscopy (TEM) is a microscopic technique whereby a beam of electrons is transmitted through an ultra thin specimen, interacting with the specimen as it passes through. An image is formed due to the interaction of the electrons transmitted through the specimen; the image is magnified and focused onto an imaging device, such as a florescent screen, on a layer of photographic film, or to be detected by a sensor (figure 3.12). TEMs [15] are capable of imaging at a significantly higher resolution than light microscopes, owing to the small de-Broglie wavelength of electrons. This enables the instrument to be able to examine fine details even as small as a single column of atoms, which is tens of thousands of times smaller than the smallest resolvable object in a light microscope.

Applications for this method include the identification of lattice defects in crystals. It is also possible to observe the defect particle interaction and the substructure within a material.

If the sample is oriented so that one particular plane is only slightly tilted away from the strongest diffracting angle, any distortion of the crystal plane that locally tilts the plane to the Bragg angle will produce particularly strong contrast variations; however, defects that produce only displacement of atoms and do not tilt the crystal to the Bragg angle will not produce strong contrast. TEM specimens are required to be at most hundreds of nanometers thick; preparation of TEM specimens is specific to the material under analysis and the desired information to obtain from the specimen.
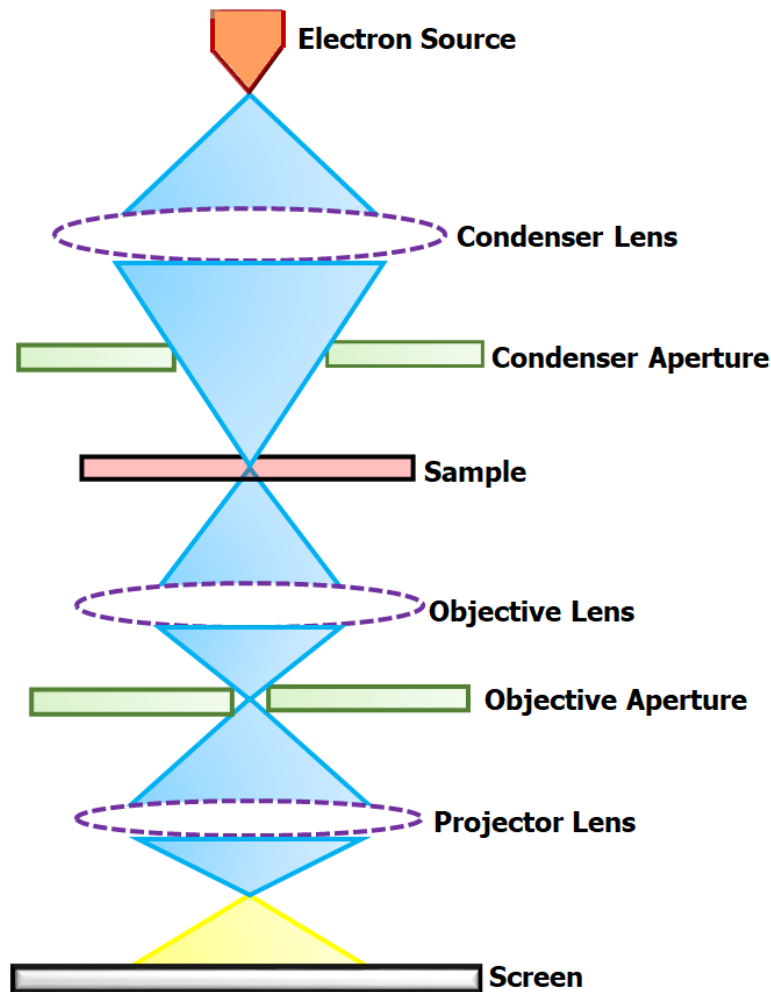
Figure 3.12 Ray diagram of optics of Transmission electron microscope.

Many materials require extensive sample preparation to produce a sample thin enough to be electron transparent, which makes TEM analysis a relatively time-consuming process with a low throughput of samples.

As stated earlier, electron microscopes are the instrument which use the high energy electrons to characterize the material at very fine scale and provides information regarding microstructures (Topography), shape and size of the second phase particles (morphology), the compound made of different elements and their relative amount (composition) and crystallography information of the thin films. TEM provides the information regarding crystal structure and microstructure via electron diffraction pattern and imaging technique. Tecnai G 2 20 (FEI) S-Twin is a 200 kV transmission electron microscope available at MRC, MNIT, Jaipur has been used to characterize the films.

3.3.7 Atomic Force Microscopy (AFM):

In an Atomic Force Microscope the imaging (more accurately the information about the topography) of a surface is done based on the modulation of interaction forces between two atoms. Using an atomic force microscope (AFM) [16-17], it is possible to measure the roughness of a sample surface at a high resolution, to distinguish samples based on its mechanical properties (for example, hardness and roughness); in addition, AFM is used to perform a micro fabrication of a sample (for example, an atomic manipulation).This is a versatile technique with wide range of resolution and can be used to study a wide variety of samples (i.e. plastic, metals, glasses, semiconductors, and biological samples such as the walls of cells and bacteria) with ease of least sample preparation. The measurements can be taken in air and hence no vacuum is required to perform this characterization. With these advantages there is such limitations like it cannot give atomic scale resolution and the physical probe used in AFM imaging is not ideally sharp. As a consequence, an AFM image does not reflect the true sample topography, but rather represents the interaction of the probe with the sample surface.

AFM provides a 3D profile of the surface on a nanoscale, by measuring *forces* between a sharp probe (<10 nm) and the surface at a very short distance (0.2-10 nm probe-sample separation). The probe is supported on a flexible cantilever. The AFM tip "gently" touches the surface and records the small force between the probe and the surface.

The probe is placed at the end of a cantilever (which one can think as a spring). The amount of force between the probe and sample is dependent on the *spring constant* (stiffness of the cantilever) and the distance between the probe and the sample surface. This force can be described by using Hooke's Law:

$$F = -kx \qquad (3.8)$$

Where, F = Force, k = spring constant (typically ~ 0.1-1 N/m) and x = cantilever deflection.

AFM is configured by the following elements:

(i) Cantilever: Small spring-like cantilever rests on the support by means of a piezoelectric element so as to oscillate the cantilever.

(ii) Sharp tip which is fixed to the open end of a cantilever

(iii)Detector- configured to detect the deflection and motion of the cantilever

(iv)Sample for measurement by AFM as mounted on Sample stage.

(v) xyz-drive which permits sample and sample stage to be displaced in x, y, and z directions with respect to a tip apex.

(vi) Controllers further comprising z-Feedback loop.

When the sample has concavity and convexity, the distance between the probe and the sample varies in accordance with the concavity and convexity while scanning of the sample along x-y direction (without height regulation in z-direction).
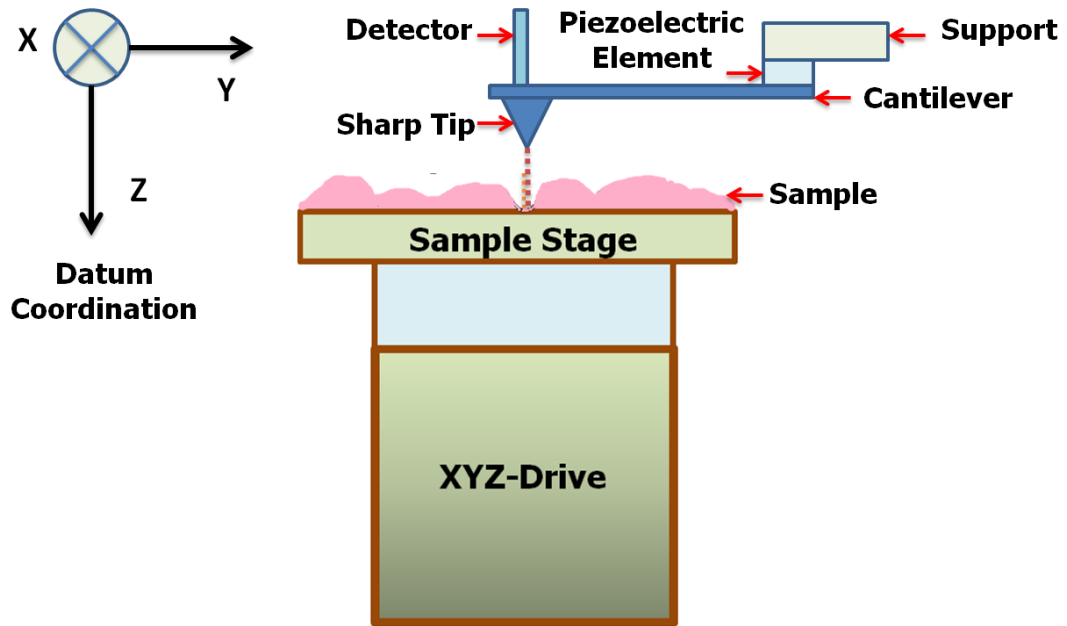
Figure 3.13 Schematic of AFM setup.

Operation mode of Image formation of the AFM are generally classified into two groups from the viewpoint of whether or not it uses z-Feedback loop to maintain the tip-sample distance for preserving the motions of the cantilever. First one (does not use z-Feedback loop) is said to be "constant height mode". Second one (using z-Feedback loop), said to be "constant XX mode" (XX is something which kept by z-Feedback loop). AFM operation is usually described as one of three modes, according to the nature of the tip motion: Contact mode, Tapping mode and Non-contact mode [17]. In the present study, each thin film sample was recorded through scan assist mode at different areas of the film and two dimensional and three dimensional images were taken. Further the roughness of the films was measured by taking average roughness values of the observed data for each film. The surface morphology of samples was recorded by Bruker AFM Analyzer available at Material Research

Center, MNIT, Jaipur and on Veeco Digital Multimode Scanning Probe Microscopy with Nanoscope IIIa in tapping mode available at IUAC, New Delhi.

3.3.8 Conductivity Measurements:

According to Ohm's law, for constant mechanical stress and temperature, the potential difference (V) across the ends of the conductor is given as V=IR

Where I, current flowing through the conductor and R is the resistance of the conductor. Resistance is dimension dependent quantity and is given by

$$R = \rho \frac{l}{A}$$ (3.10)

Where l is the length of the conductor, A is the cross sectional area and ρ is the resistivity of the conductor. The resistivity of a sample is measured by two methods known as two probe method and four probe method.
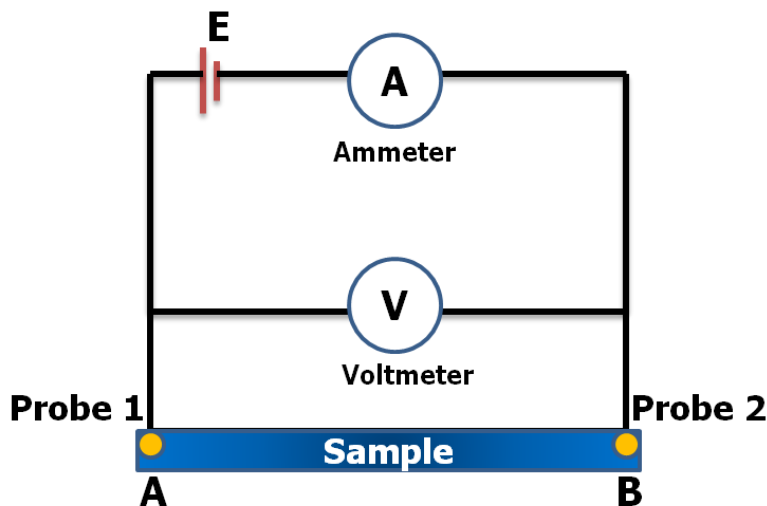
Figure 3.14 Two probe method to measure the resistivity of the sample.

In two probe method (figure 3.14), the resistivity ρ can be measured by passing the constant current through the sample (length l and area A) via two probes A and B with the aid of a battery; the current is measured with the ammeter. By measuring voltage drop across the sample with the aid of voltmeter, the resistivity is given by

$$\rho = \frac{I}{V} \frac{l}{A}$$ (3.11)

In four probe method (figure 3.15) [18], the setup consists of four equally spaced tungsten metal tips with finite radius. Each tip is supported by springs at the end to minimize sample damage during probing. A high impedance current source is used to supply current through the outer two probes; a voltmeter measures the voltage across the inner two probes to determine the resistivity of the sample.

Any unwanted voltage drop due to contact resistance is excluded because of presence of high impedance voltmeter which prohibits the inner probes t to draw any current in the circuit. The electric current carried through the two outer probes, set up an electric field in the sample.

High Impedance Voltmeter

V

Probes

d   d   d

Sample

A

Constant Current Power Supply

+   −
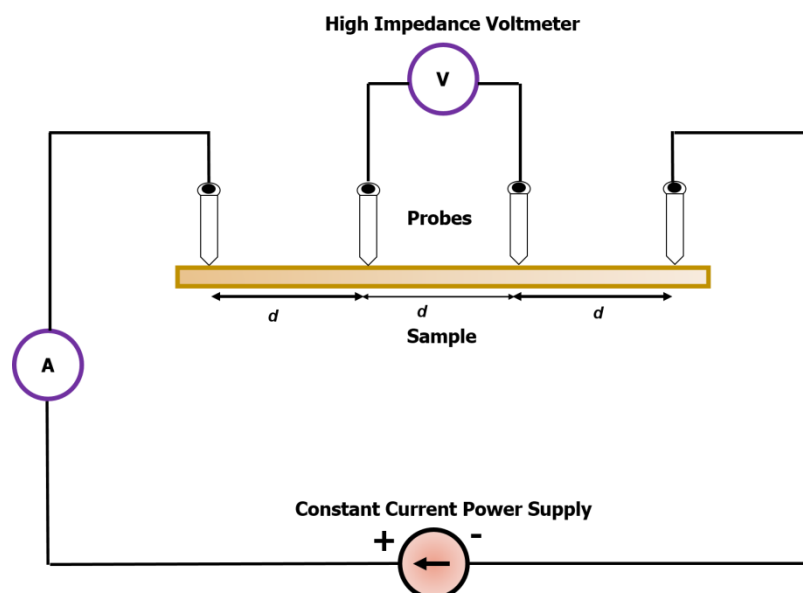
Figure 3.15 Four probe method to measure the resistivity of the sample.

In the present study, electrical characterization was done on Semiconductor Device analyzer (B1500A from Agilent) with probe station (Microxact USA) available at Material research Center, MNIT, Jaipur. For I-V characteristics, ohmic contacts were made on the thin film with the gold coated tungsten tip. Since the resistivity of the fullerene films is very high, two probe method was performed for the I-V measurement of fullerene and fullerene based nanocomposite thin films. The tips (two probes) were landed on a sample in collinear fashion with fixed distance to avoid the error during the measurement. In I-V characteristics the voltage sweep range was fixed to the -5V to +5V while having a voltage of 10mV per step. There is a provision to put some delay and holding time as well in each step to avoid any sharp fluctuation during the measurements. I-V curves were taken at various parts of thin film sample to cross check the consistency of results.

3.3.9 X-ray Photoelectron Spectroscopy (XPS):

XPS is a highly surface-sensitive and non-destructive characterization technique widely used to investigate the chemical constitution and chemical bonding state of elements in the materials [19]. This technique is based on the principle of

photoelectric effect. On exposing the sample to X-rays photon beam, electrons get ejected (figure 3.16) from the inner shell with certain kinetic energy, given by

$$KE = h\nu - BE - \phi \tag{3.12}$$

Where KE is the kinetic energy of the ejected electron, $h\nu$ is the energy of the incident X-ray photon beam, ϕ is the work function and BE is the binding energy.

This emitted electron with certain kinetic energy is analyzed to confirm the electronic structure and chemical composition. With the ejection of electrons, excitation takes place; as a result the electrons from higher orbital (say L shell) jumps into the K orbital to fill the vacant state created due to emitted electrons (figure 3.16). The difference in energy between L and K orbitals is conserved by the emission of electromagnetic radiation (in the form of photons) and Auger electrons.
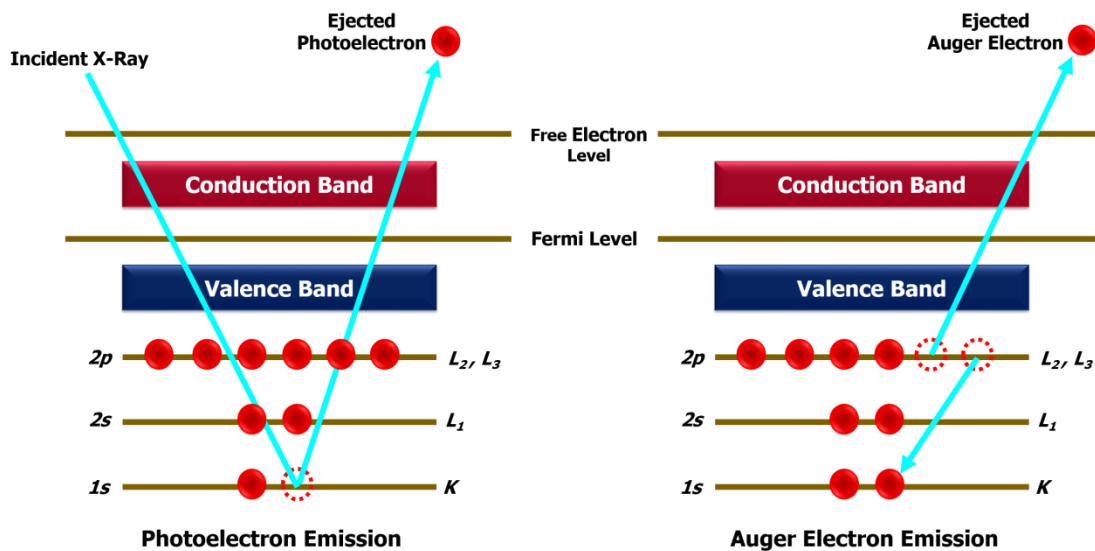
Figure 3.16 Ray diagram of emission of photoelectron and Auger electron on exposing the sample to X-ray photon beam.

In some cases, due to the need for conservation of energy perceptible number of electrons of L shell may absorb the energy difference and got ejected as Auger electron of higher yield. The energy expression can be given as

$$KE = E_K - E_{L2} - E_{L3} \tag{3.13}$$

The analyzer measures the kinetic energy of all emitted electrons (emitted photoelectrons and Auger electrons) and the resultant spectrum includes the contribution of both type of emitted electrons.

The working of the XPS includes the steps as: the sample is exposed with mono energetic X-ray beam (Al Kα or Mg Kα). Theses incident X-ray photons penetrate up to a depth of a few μm of the sample and provide information only of the surface (1-

10 nm). The entire setup is kept under ultrahigh vacuum for elimination of unwanted surface contamination. All the emitted electrons are analyzed with hemispherical electron analyzer. The recorded spectrum can be seen on the computer screen.

The present study envisages the determination of chemical composition and element states of the samples, particularly the elemental state of the Cu in the fullerene based copper nanocomposite thin films The certain peaks corresponding to the binding energy C, Cu and O, confirms the presence of these elements on the surface of the films. XPS data has been recorded with Omicron nanotechnology XPS system from Oxford instruments (model- ESCA+) available at Material research Center, MNIT, Jaipur. This consists of an ultra-high vacuum chamber attached with a monochromatic Al-Kα radiation source of energy 1486.7 eV and a 124 mm hemispherical electron analyzer.

REFERENCES

[1]   J.L Vossen and W. Kern, Thin film processes II, Academic Press, New York (1991).

[2]   D.A. Glocker and S.I. Shah, Handbook of Thin Film Process Technology, CRC Press, Taylor & Francis, London New York (1998).

[3]   D. Kanjilal, S. Chopra, M.M. Narayanan, I.S. Iyer, V. Jha, R. Joshi and S.K. Datta, Testing and operation of the 15UD Pelletron at NSC, *Nuclear Instruments and Methods in Physics Research A,* 328 (1993) 97-100.

[4]   D. Kanjilal, T. Madhu, G. Rodrigues, U.K. Rao, C.P. Safvan and A.Roy, Development of low energy ion beam facility at NSC, *Ind. J. Pure Appl. Phys.*, 39 (2001) 25-28.

[5]   J.P. Singh , R. Singh, S. Ghosh, A. Tripathi, D. Kabiraj, S. Gupta, et al., Swift heavy ion-based materials science research at NSC, *Nuclear Instruments and Methods in Physics Research B,* 156 (1999) 206-211.

[6]   D.L. Pavia, G.M. Lampman and G.S. Kriz, Introduction to Spectroscopy, 2nd Ed. Harcourt Brace College, New York, (1994).

[7]   N.V. Tkacheno, Optical Spectroscopy Methods and instrumentations, Amsterdam Elsevier Publications, (2006).

[8]   S. Wartewig, IR and Raman Spectroscopy: Fundamental Processing Wiley-Vch Verlag GmbH & Co. KGaA, Weinheim, (2003).

[9]   P. Larkin, Infrared and Raman Spectroscopy; Principles and Spectral Interpretation, Elsevier Science, (2011).

[10] H. Goldstein, Classical Mechanics, Addison-Wesley, Reading, MA (1959).

[11] H. Kumar, Y.K. Mishra, S. Mohapatra, D. Kabiraj, J.C. Pivin, S. Ghosh and D.K. Avasthi, Compositional analysis of atom beam co-sputtered metal–silica nanocomposites by Rutherford backscattering spectrometry*, Nucl. Instr. and Meth. in Phys. Res. B*, 266 (2008) 1511-1516.

[12] W. K. Chu, J. W. Mayer and M. A. Nico let, Backscattering Spectrometry, Academic Press, New York (1978).

[13] B. D. Cullity, Elements of X-ray Diffraction, second edition, Addission-Wesley Publishing Company (1978).

[14] J.I. Goldstein**,** Practical Scanning Electron Microscopy, Practical Scanning Electron Microscopy, Plenum Press, New York (1975).

[15] D. B. Williams and C. B. Carter, Transmission Electron Microscopy, A textbook for Materials Science, Plenum (1996).

[16] W.R. Bowen, N. Hilal, Process Engineering, Introduction to AFM for Improved Processes and Products, Butterworth-Heinemann (1991).

[17] B. Voigtlaender, Scanning Probe Microscopy, Atomic Force Microscopy and Scanning Tunneling Microscopy, *Nano Science and Technology,* (2015).

[18] S.B Kjeldby, O.M. Evenstad, S.P. Cooil and J.W. Wells, Probing dimensionality using a simplified 4-probe method, *Journal of Physics: Condensed Matter*, 29 (2017) 39.

[19] J.F. Watts, J. Wolstenholme, An Introduction to Surface Analysis by XPS and AES, (2003) ISBN 0-470-84713-1

Chapter 4

Effect of Ion Irradiation on the Structure and Properties of Fullerene C_{60} and C_{70} as a Matrix of Metal Reinforced Nanocomposites

4.1 Effect of Ion Irradiation on the Structure and Properties of Fullerene C_{60} as a Matrix of Metal Reinforced Nanocomposites.

Due to high electron affinity property [1], fullerene is used as electron acceptor material in solar cells. Enhancement of its absorbance may be possible by the incorporation of metal nano particles in fullerene matrix; it is reported that noble metals (Au, Ag) exhibit an amazing property of Surface Plasmon Resonance (SPR) [2] which appreciably modifies the optical properties of nanomaterial. A number of studies carried out so far have reported the occurrence of particle induced SPR in metal embedded fullerene nanocomposites with the use of different methods, such as annealing of thin films at different temperatures, irradiating with ions at different fluences and taking different compositions of embedded metals that is embedded [3-6]. However, the frequency of SPR band so formed is strongly dependent on nature of host matrix.

It is known that irradiation with high energy ion forms ion tracks having much higher conductivity than the surrounding material. [7]. Ion track formation modifies the optical and electrical properties of fullerene C_{60}. Increasing fluence of ion irradiation leads to a decrease in optical band gap of fullerenes [8-12]. While polymerization of fullerene C_{60} takes place at lower fluences, fullerene C_{60} undergoes considerable destruction at higher fluence. Maeyoshi et al discussed in detail the Chain polymerization reaction responsible for the polymerization in C_{60} by the single particle nanofabrication technique (SPNT) [13]. Formation of ion track confirms the transformation of fullerene into amorphous carbon within the narrow circular region. This interesting feature can be utilized to form carbon nanowires. Due to fascinating properties, fullerene C_{60} has been widely studied for the modification of its properties upon ion irradiation with different ion beams (O, Ni and Au) under a wide range of fluences, 10^{10} to 10^{14} ions/cm^2. [12].

Aiming at development of a suitable metal embedded nanocomposite for organic solar cell, it appears of special interest to probe into the effect of host matrix properties under situation of ion irradiation. To meet this objective, investigation on the possible modification of fullerene C_{60} as host material upon irradiation by 90 MeV Ni ion beam over a wide fluence range from 1×10^9-3×10^{13} ions/cm^2 is essential. The modifications of different properties such as optical, structural, electrical and morphological are examined by UV-visible absorbance spectroscopy, Raman Microscopy, I-V measurement and Atomic Force Microscopy (AFM), so as to gather

the scientific knowledge about the exact role of ion irradiation on the modification of fullerene C_{60} over range of fluences which enables the observation of polymerization at low fluences and amorphization at high fluences.

Summarily, the study aims at observing the effects of ion irradiation on optical, structural, electrical and morphological properties of fullerene C_{60} which is a potential target matrix of metal embedded nanocomposite for solar cell application.

4.1.1 Experimental Details:

Fullerene C_{60} powder was placed in the evaporation chamber in the tungsten boat. The substrates were mounted on the substrate holder. Then masking was duly done. In deposition of C_{60} thin film, the initial vacuum inside the deposition chamber was kept at $\sim 2.3 \times 10^{-6}$ mbar. During deposition process the vacuum was maintained at about 7.2×10^{-6} mbar. The current through the boat was increased slowly up to the point where the thickness monitor shows deposition rate. The deposition rate was adjusted to a rate about 0.15 Å/sec to be maintained for uniform deposition. As the desired rate is obtained at about 47 A current, the mask over the substrates is removed and the substrates are now ready for deposition. The deposition rate was adjusted through rotating the voltage knob. When the thickness of the film reached the value of 150 nm, the process of deposition was stopped slowly by putting off the voltage. On completion of the deposition, the vacuum was recorded to be about 4.7×10^{-6} mbar. The thin films were irradiated with fluences in the range of 1×10^9 to 3×10^{13} ions/cm^2.

To examine the effect of ion irradiation on the optical properties of the thin films, the UV-visible absorbance spectra of the pristine and 90 MeV Ni ion irradiated C60 thin films has been recorded by using a U-3300 UV-visible spectrometer by Hitachi. Raman spectra of the pristine and ion irradiated fullerene C_{60} films were recorded in the range 200-1800 cm^{-1} using AIRIX STR 500 Raman spectrograph at room temperature. AFM images were recorded by Bruker AFM Analyzer. Conductivity measurements are performed with Agilent Semiconductor device analyzer. The XRD pattern of pristine fullerene C_{60} thin films and that irradiated with 90 MeV Ni ion beam at low fluence were measured at Elettra Synchrotron Lab, Trieste, Italy in MCX beam line at a glancing angle of 0.5˚. The C-AFM measurements were performed on the irradiated and pristine samples using the instrument Nanoscope III a SPM in IUAC, New Delhi.

4.1.2 Results & Discussions:

4.1.2.1 Rutherford Back Scattering Analysis:

Rutherford backscattering (RBS) technique [13] is one of the most precise characterization techniques to determine the film thickness, atomic species and their concentration in the film. This is based on the classical scattering of α-particles from different nuclei in a distinct and well understood way.

Figure 4.1 represents Rutherford backscattering (RBS) spectrum of a C_{60} pristine sample on Si substrate along with the Rutherford Universal Manipulation Program (RUMP) [14] simulated spectrum (solid line).
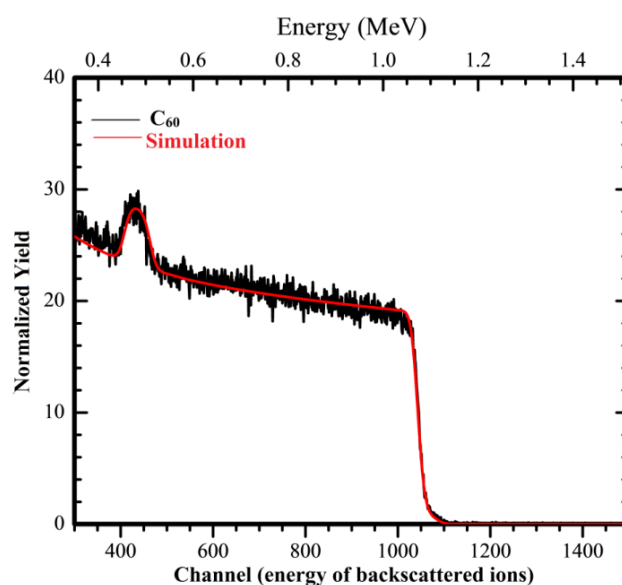
Figure 4.1 RBS spectrum (black line) of a C_{60} pristine sample on Si substrate along with RUMP simulated spectrum.

The plateau region in figure 4.1 represents the Si substrate and fullerene C_{60} hump overrides it. The film thickness was obtained in the units of atoms/cm^2 which was converted into nanometer using the density of the fullerene C_{60} thin film. The estimated thickness of fullerene C_{60} film observed by this simulation is about ~120 nm.

4.1.2.2 Raman Analysis:

In order to determine the irradiation effect on the structure of fullerene C_{60} thin films, Raman analysis has been performed on fullerene C_{60} pristine and 90 MeV Ni ion irradiated thin films with wide range of fluences from 1×10^9 to 3×10^{13} ions/cm^2. Here the analysis of results is divided into two parts to demonstrate the clear picture of effect of ion irradiation on fullerene C_{60} at low fluences (1×10^9-1×10^{11} ions/cm^2) as well as on high fluences (1×10^{12}- 3×10^{13} ions/ cm^2).

Polymerization of C_{60} thin films at low fluence (1×10^9 to 1×10^{11} ions/cm^2):

Raman spectroscopic observations for the fluence range 1×10^9-1×10^{11} ions/cm^2 is presented in figure 4.2. A_g internal mode (centered at 1468 cm^{-1}) is seen to occur in the range 1445-1480 cm^{-1}. After irradiation with fluence 1×10^9 ions/cm^2, the A_g mode starts getting broadened, that is a new shoulder arises in the pristine Raman peak (1468 cm^{-1}). This raised shoulder centered at 1463 cm^{-1} in the peak first increases with fluence and then starts to decrease (1×10^{10} ion/cm^2) and finally completely disappears (1×10^{11} ions /cm^2) as shown by deconvolution of the most intense peak centered at 1468 cm^{-1} in figure 4.2. Along with this, peaks at 1457 and 1451 cm^{-1} are also observed and are presumably due to the specific interaction between the ion species involved and the fullerene C_{60} structure [12] This asymmetry in the A_g mode is best observed with combination of two peaks, one around 1463 cm^{-1} and the other practically remaining at the same position 1468 cm^{-1}. This asymmetry can be attributed to the polymerization at the lower fluences. Hence the mode at 1463 cm^{-1} is the signature of polymerization due to ion irradiation [15].
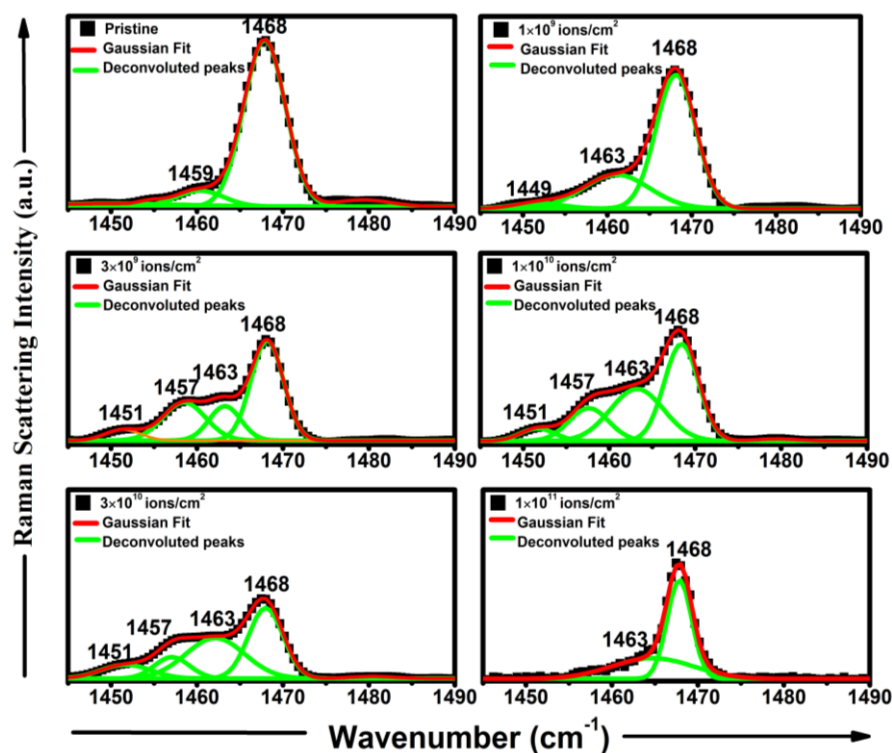
Figure 4.2 Irradiation-induced damage with 90 MeV Ni ions in fullerene C_{60} thin films at low fluences.

It may be further noted that as the fluence is increased the main peak intensity decreases, which may be due to (i) polymerization of fullerene C_{60} molecules (ii) the fragmentation (decrease in C_{60} molecules) of C_{60} molecule.

Amorphization of C_{60} thin films at higher fluence (1×10^{12} to 3×10^{13} ions/cm^2):

The second part is the effect of higher fluences (1×10^{12} - 3×10^{13} ions/cm^2) on this particular A_g mode. Figure 4.3 shows the Raman spectra of the C_{60} thin films at higher fluences (1×10^{12} - 3×10^{13} ions/cm^2).
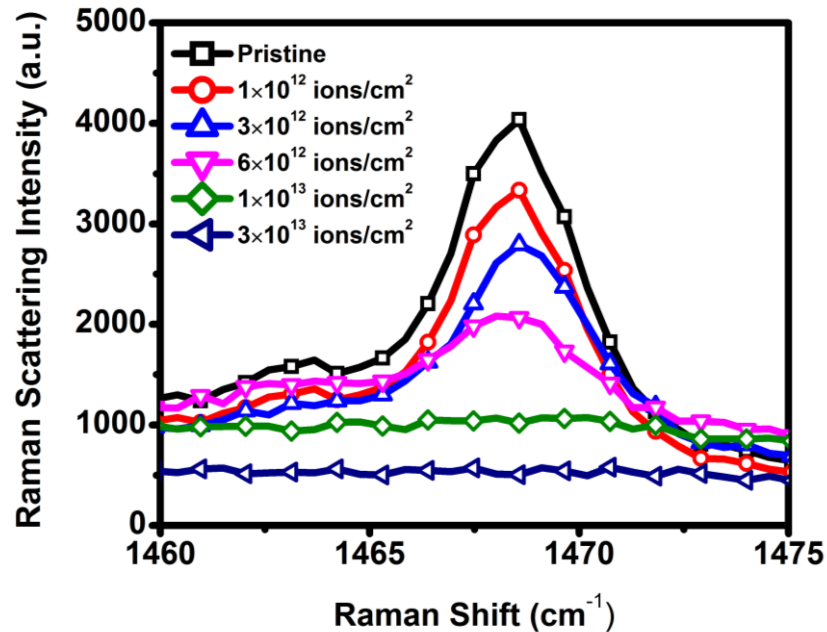
Figure 4.3 Irradiation-induced damage with 90 MeV Ni ions in fullerene C_{60} thin films at high fluences

The intensity of the Raman mode decreases with the increase in fluence and the mode disappears completely at the fluence $\sim 3 \times 10^{13}$ ions/cm^2 to imply that the fullerene has been transformed into a-C [11].

Calculation of diameter of ion track:

Figure 4.4 can be used to determine the modifications of fullerene structure by ion irradiation with 90 MeV Ni ion beam. Damage cross section is calculated by using the classical formula [12], which has been based on the assumption that a single ion can produce damage in the form of amorphization. The classical formula is given by equation (1).

$$N(\phi) = N_o exp(-\sigma \, \phi) \tag{4.1}$$

Where, N (ϕ) = areal density of fullerene C_{70} molecules remaining after ion irradiation at a fluence ϕ, N_0 = areal density of pristine fullerene C_{70} and σ = cross section of damage in fullerene by ion irradiation for a single ion impact.

We can rewrite the equation (1) as

$$\frac{N(\phi)}{N_o} = exp(-\sigma \phi) \tag{4.2}$$

$$ln\left(\frac{N(\phi)}{N_o}\right) = -\sigma \phi \tag{4.3}$$

Equation 4.3 is used to approximate the value of damage cross-section (σ) by evaluating the slope of the curve between $ln\left(\frac{N(\phi)}{N_o}\right)$ and ϕ.
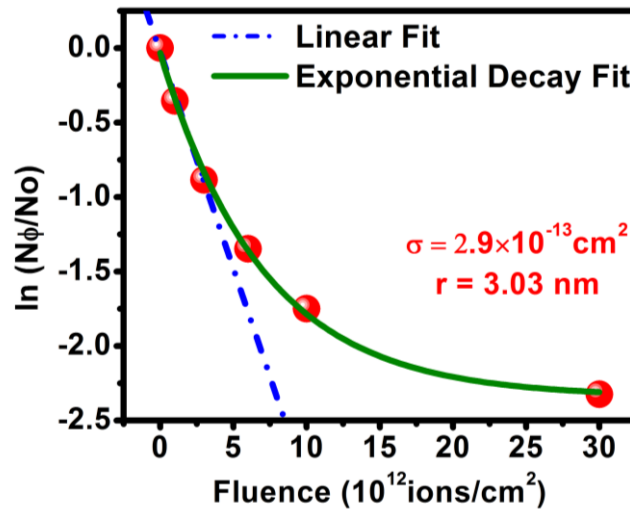
Figure 4.4 Curves between normalized integral area (area under Raman mode of irradiated film divided by that of pristine film) at different fluences of 90 MeV Ni ion beam.

The value of the damaged cross section (σ), can be used to calculate the radius of ion track (r)

$$\sigma = \pi r^2 \tag{4.4}$$

Area under the curve for each of the fluence is approximated to calculate the damage cross section and ion track radius from the above mention equations.

Figure 4.4 depicts the graph of normalized integral area of peak centered at 1468 cm^{-1} with the variation of fluence (ϕ). The deposition of energy results in two slopes in the graph. The deposition of energy takes place in two ways, one at lower value of fluence where the formation of ion tracks takes place (which are far apart from each other) and second at higher value of fluence where ion tracks are very close and

overlapped to each other. The slope gets changed at the start of overlapping of ion tracks formed by the irradiation of 90 MeV Ni ion beam. From equation (1) the damage cross-section (σ) can be calculated and it comes out to be $\sim 2.9 \times 10^{-13}$ cm^2. From this damage cross section, the radius (r) calculated by using the equation (3) is $\sim$ 3.03 nm.

4.1.2.3 UV-visible absorption spectroscopic analysis:

UV-visible absorbance spectra of pristine and irradiated with 90 MeV Ni ion beam with fluence range from 1×10^9 to 3×10^{13} ions/cm^2 are recorded from 300 nm to 800 nm (figure 4.5-a).
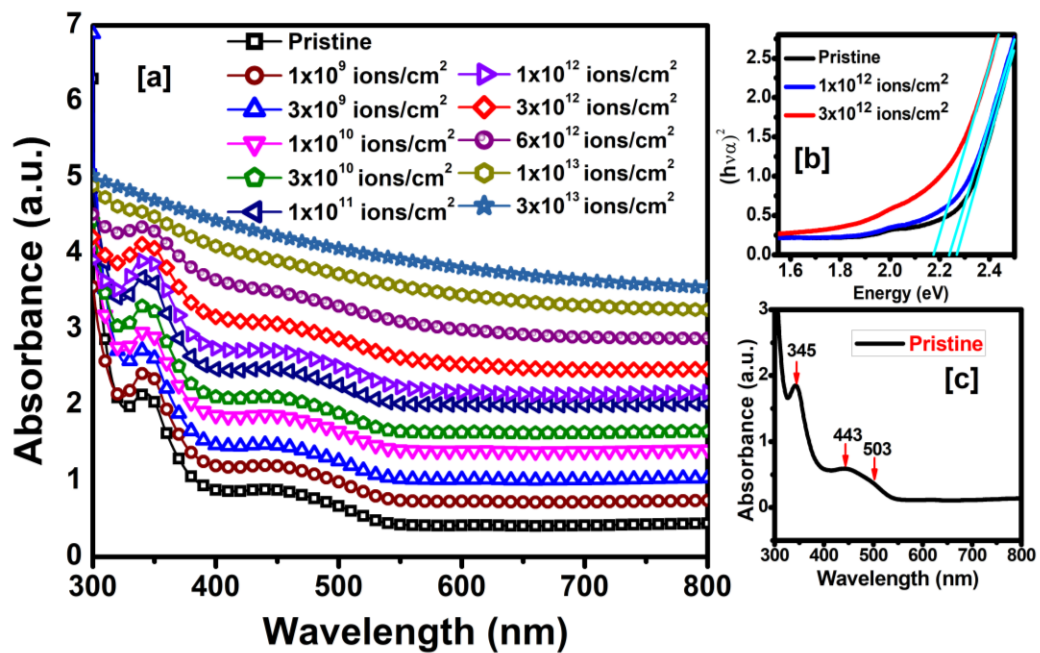
Figure 4.5 (a) UV-visible absorbance spectra of pristine and 90 MeV Ni ion irradiated fullerene C$_{60}$ films (b) Tauc plots of pristine and 90 MeV Ni ion irradiated fullerene C$_{60}$ films (c) UV-visible absorbance spectrum of pristine fullerene C$_{60}$ thin film.

The absorbance spectrum of pristine fullerene C$_{60}$ (figure 4.5-c) has two weak bands at 503 nm and 443 nm with an intense peak at 345 nm. This peak at 345 nm arises due to interband transition among the π orbitals. Figure 4.5(a) clearly reveals that the absorbance peaks disappear with the increase in fluence. Figure 4.5(b) shows the variation in band gap due to irradiation and it has been found that the band gap decreases from 2.26 - 2.17 eV with the fluence.

The band gap is measured up to fluence 6×10^{12} ions/cm^2; after it, absorbance edge gets disappeared and thus reveals the complete transformation of the fullerene C$_{60}$ in a-C which results in a very narrow band gap.

4.1.2.4 Conductivity measurement:

In order to determine the change in resistivity for confirmation of transformation of fullerene into a-C at higher fluence, conductivity measurement has been performed for the pristine and 90 MeV Ni ion irradiated thin films. For resistivity measurement, the two-probe method was used, because the resistances of the pristine and irradiated samples were very high. Figure 4.6(a) demonstrates the curves between the current and the voltage for the pristine and 90 MeV Ni ion irradiated thin films at fluence $1\times10^{12}, 3\times10^{12}, 6\times10^{12}, 1\times10^{13}$ and 3×10^{13} ions/cm^2.
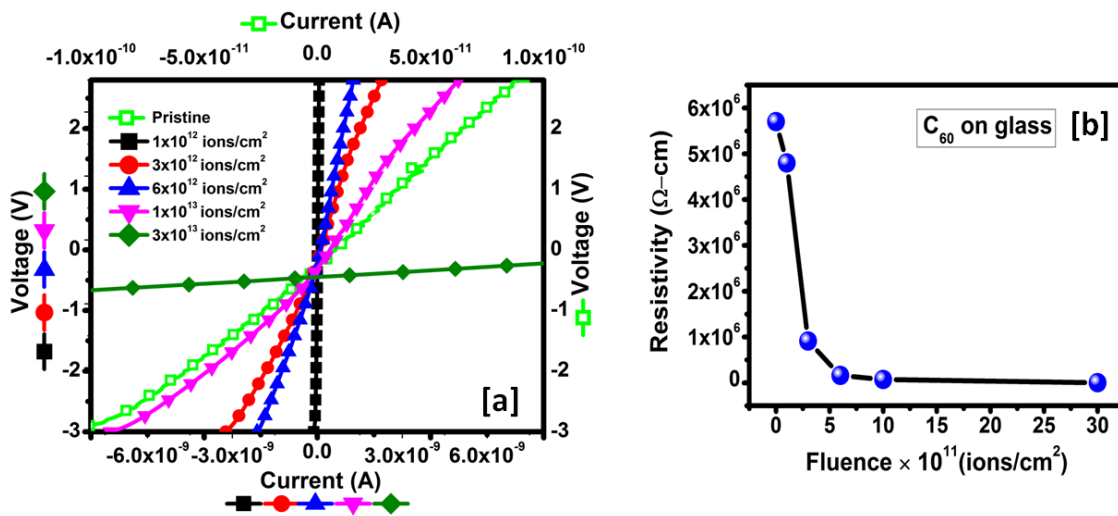
Figure 4.6 (a) I-V plots of pristine and irradiated fullerene C$_{60}$ thin films with 90 MeV Ni ion beam at different fluence on glass substrate (b) Resistivity vs. fluence plot of pristine and irradiated fullerene C$_{60}$ thin films.

The resistivity of the samples is approximated by determining the value of the resistance from the curves shown in figure 4.6(b). The resistivity of pristine is found to be ~ 0.57×10^7 Ω-cm. Decrease in resistivity from the value of pristine to that film irradiated at highest fluence is observed as tabulated in table 4.1 and also plotted in figure 4.6 (b); the results are in agreement with the earlier reports.

Table 4.1 Resistivity of pristine and 90 MeV Ni ion irradiated fullerene C$_{60}$ film at different fluences.

Fluence(ions/cm^2)	Resistivity (Ω-cm)
Pristine	0.57×10^7
1×10^{12}	0.48×10^7
3×10^{12}	0.91×10^6
6×10^{12}	0.16×10^6
1×10^{13}	0.73×10^5
3×10^{13}	0.39×10^4

As the fluence increases the resistivity of the thin films decreases that is the conductivity of the thin films increases and this is due to the formation of increasing number of ion tracks/conducting tracks [16-17].

4.1.2.5 Surface analysis:

AFM measurements have been performed to analyze the surface morphology of pristine and irradiated fullerene C_{60} thin films. Three dimensional (3-D) images of pristine and irradiated fullerene C_{60} thin films at low fluences 1×10^9 to 1×10^{11} ions/cm^2 are shown in figure 4.7.
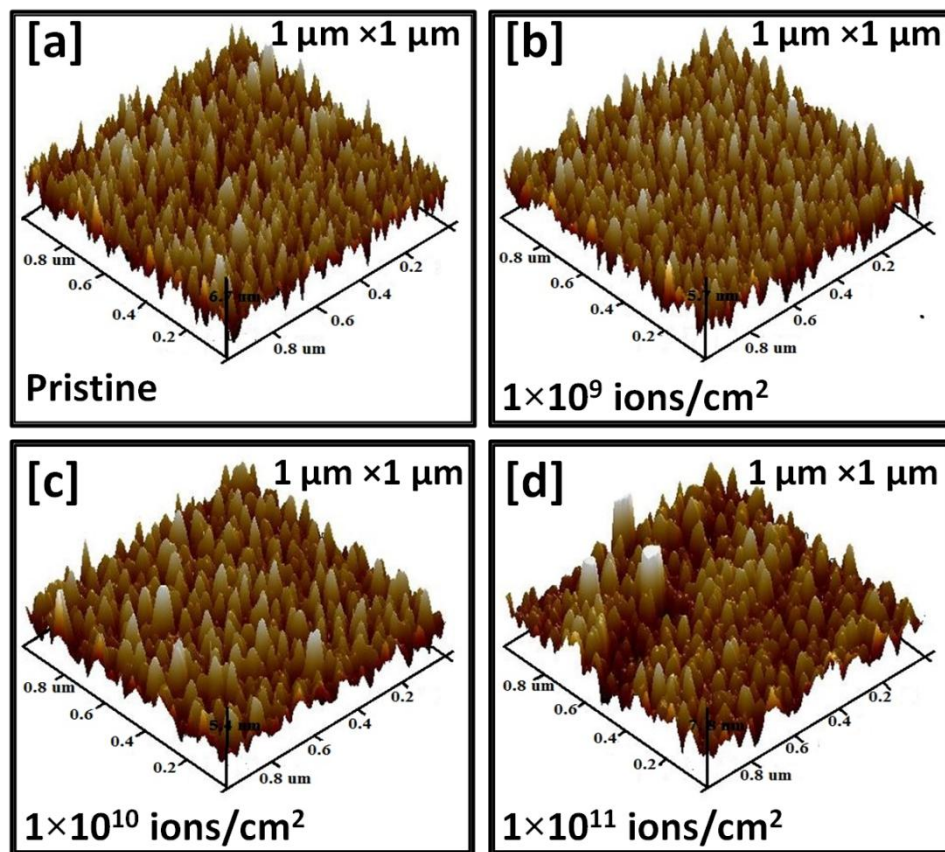
Figure 4.7 AFM 3-D images of pristine and 90 MeV Ni ion irradiated fullerene C_{60} films at low fluences.

AFM images also recorded for the fullerene C_{60} thin films irradiated at high fluence 1×10^{12}, 3×10^{12}, 1×10^{13} and 3×10^{13} ions/cm^2 are shown in figure 4.8. With increasing fluence of 90 MeV Ni ions, particles size is seen to increase. Calculated roughness values for pristine and irradiated films at fluences 1×10^9, 1×10^{10}, 1×10^{11}, 1×10^{12}, 3×10^{12}, 1×10^{13} and 3×10^{13} ions/cm^2 are tabulated in table 4.2.
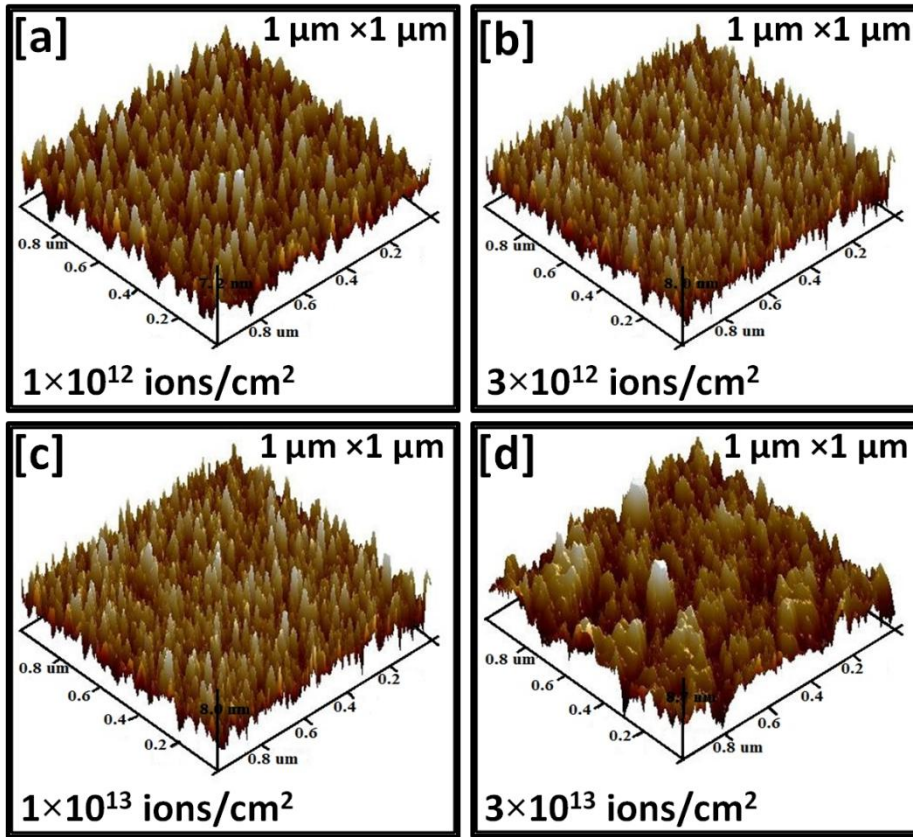
Figure 4.8 AFM 3-D images of 90 MeV Ni ion irradiated fullerene C_{60} films at high fluences.

From the table 4.2, it is observed that there is significant change in roughness at low fluences and that is due to sputtering taking place at the surface. The increased roughness value with increasing fluence originates from the impact of SHI ion causing a high degree of damage on the surface.

Table 4.2 Roughness of pristine and 90 MeV Ni ion irradiated fullerene C_{60} film at different fluences.

Fluence (ions/cm^2)	Roughness (nm)
Pristine	1.47
1×10^9	1.65
1×10^{10}	1.88
1×10^{11}	1.92
1×10^{12}	2.05
3×10^{12}	2.09
1×10^{13}	2.24
3×10^{13}	2.33

At higher fluences the damage occurring in thin film reaches a steady state as observed in figure 4.9.
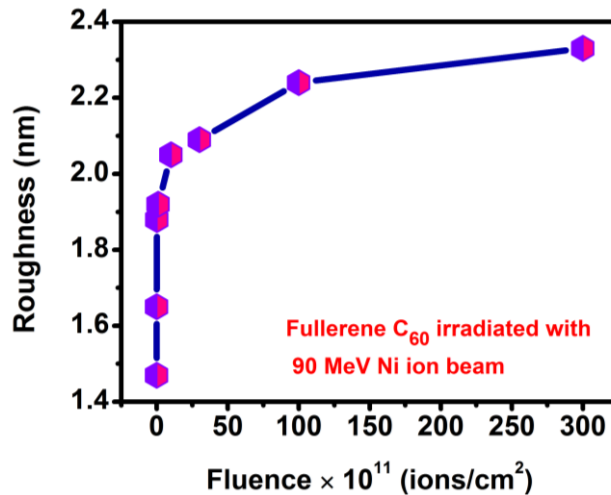
Figure 4.9 Roughness vs. fluence plot of pristine and irradiated fullerene C_{60} thin films with 90 MeV Ni ion beam.

4.1.2.6 XRD analysis:

Figure 4.10 represents the XRD pattern of pristine fullerene C_{60} thin film and irradiated ones at low fluence from 1×10^9, 3×10^9, 1×10^{10}, 3×10^{10} and 1×10^{11} ions/cm^2. Fullerene C_{60} has poor crystallinity.
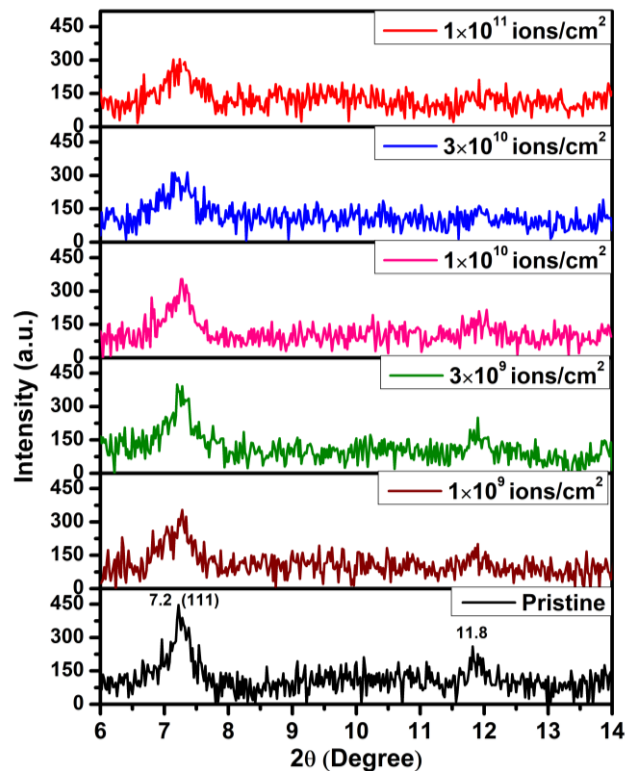
Figure 4.10 XRD patterns of pristine and irradiated fullerene C_{60} thin films.

In the XRD of C_{60}, the highest intensity peak is indexed as (111); as per information available in JCPDS file, manifestation of x-ray diffraction of C_{60} is envisaged through generation peaks in accordance with FCC, Orthorhombic or Monoclinic; While use of

Cu Kα yields highest intensity peak for a FCC structure at 10^0, it is much higher for the other two crystal types [(020) of Orthorhombic at 20^0 and (313) of Monoclinic at 41.66^0]. Since the observed highest intensity peak occurs at 7.20^0, the other two structures are reasoned out; since in the present experiment done in a Synchrotron, a higher energy beam (higher than Cu Kα) is used, 2θ is shifted to a lower value. It is therefore concluded that FCC arrangement has dominated in the present case with appearance of (111) peak. In contrast, in case of C_{70}, the possibility of HCP and Tetragonal arrangements cannot be ruled out if the highest intensity peak occurs at much higher 2θ value (1.5 times than C_{60}). However, it is unlikely that such a great shift in 2θ is plausible. Rather FCC arrangement is better appreciated with a highest intensity peak for (220); else (110) of either of the HCP and Tetragonal arrangements is to be given consideration. However, following the observation in the present investigation, it is conjectured that (111) reflection occurs in C_{60}, whereas it is (220) for C_{70}. Its most intense peak at ~7.2° corresponds to (111) plane is shown in graph. As higher fluence the peak intensity is seem to decrease. This may be attributed to the destruction of C_{60} molecules due to effect of irradiation as explained by the decrease in the intensity of A_g mode peak of the films with irradiation.

At fluence 3×10^9 ions/cm^2, the increase in peak is due to polymerization that take place at this fluence. Further decrease in peak with increase in fluence may be due to the fact that structural damage overrides the effect of polymerization. Thus XRD results are harmonious with Raman results.

4.2 To Observe the Effect of Different Energy Ion Beam Irradiation on Fullerene C_{70} Thin Films: Dependence of Electronic Energy Loss

Swift heavy ion (SHI) irradiation is a unique tool that has extensively been used in the present days to engineer the properties of the materials. It has been observed that SHI irradiation induces drastic changes in the chemical and physical properties of carbon materials. Reports have been found in the literature on the irradiation of fullerene C_{60} films with SHI having energy 1 MeV/nucleon or more, which results in the breaking of fullerene molecules, a polymerization at low fluences (1×10^{11} ions/cm^2) and a transformation into amorphous carbon at high fluence [15,18-20]. However polymerization or amorphization of fullerene C_{70} is expected to depend upon the energy of the irradiated beam; in view of non availability of authentic data, it is of immediate interest to explore the possible modification in characteristics of fullerene C_{70} under the action of different energies. In this investigation results or experiments with four different ion beams (90 MeV Si, 55 MeV Si, 90 MeV Ni and 125 MeV Au) have been reported. Bajwa et al. [11] reported a comparative study using several different electronic energy loss values on the modification of C_{60} fullerene films by swift heavy ion irradiation with electronic energy loss (S_e) values ranging from 80 to 1270 eV/Å and fluence values from 1×10^{10} to 1×10^{14} ions/cm^2. To vary the S_e values, different ions and energies were chosen. A correlation between the energy deposition in fullerene C_{60} and modification produced by this energy deposition in C_{60} films was proposed. A relation between damage cross-section and electronic energy loss values was obtained by these workers; the functional relationship can help in calculating the radius of the damaged cylindrical zone for any value of electronic energy loss. The model also provides a behavior of polymer formation and fragmentation of C_{60} fullerene with increasing S_e. In contrast till date, there is no such well developed model on this behavior of fullerene C_{70}.

On the basis of above understanding it appears prudent to focus the present study with the objective to formulate an authentic data relating electronic energy loss and damage cross-section which is hitherto unavailable for C_{70} fullerene. It is reasonable to presume that if a relationship between electronic energy loss and damage cross-section is established, it will help one to determine the damage cross - section for any value of electronic energy loss.

To obtain one such useful data, fullerene C_{70} is irradiated with 90 MeV Si ion beam which describes the induced modification through electronic excitation. To add to data point, the effect of ion irradiation on fullerene C_{70} thin film using 55 MeV Si ions has been investigated; the magnitude of damage cross section for the used electronic energy loss has been determined. By taking into consideration of above, the fullerene C_{70} thin films have been irradiated with 90 MeV Ni ion too at different fluences to secure a similar data point, Apart from examining the effect of energy deposition in the developed thin films and the approximation of the damage cross-section for 90 MeV Si, 55 MeV Si and 90 MeV Ni ion beam irradiation in fullerene C_{70}, this study is also important to understand the applicability of fullerene C_{70} thin films in radiation zones such as in space or near reactors [21].

Over and above ion beam irradiation of C_{70} fullerene by 90 MeV Si, 55 MeV Si and 90 MeV Ni ions and calculation of damage cross section corresponding to different electron energy losses, the effect of ion beam irradiation with 125 MeV Au ion beam on fullerene C_{70} thin films is a step forward towards developing the quantitative relation between damage cross section in fullerene C_{70} and electronic energy loss secured by varying quality of ion beam of different energy. Imperatively swift heavy ion irradiation on fullerene C_{70} brings about significant changes in its structural optical and other physical properties. Changes in these properties are dependent on the beam and the fluence. It is therefore pertinent to investigate the SHI irradiation induced modification in properties of C_{70} fullerene thin films. Such property changes are monitored mainly by UV-visible absorption spectroscopy and Raman Spectroscopy, although other studies are also taken resort to reinforce the observation on property modifications of C_{70} under ion irradiation by 90, 55 MeV Si, 90 MeV Ni and 125 MeV Au ion.

Study on fullerene C_{70} matrix has a bearing on SPR tuning as the refractive index of C_{70} is higher (~2.3) in comparison to fullerene C_{60} (~2.1) and this results in better tuning of SPR [5]. In the previous section it has been stated that particle induced SPR is exhibited by noble metal (Au, Ag), embedded in fullerene C_{60} matrix and that leads to significant modifications in the optical properties of nanomaterial [2].

It is clear that till date, these studies are mainly concerned with the metal atom embedded fullerene C_{60} nanocomposites [3-6]. Since the frequency of SPR band depends on the nature of host matrix and also since information relating to SPR in C_{70} band nanocomposites is rare in literature, it is considered important to gather

knowledge about the possible modifications in characteristic of C_{70} upon irradiation by SHI as a prelude to further studies on the SPR behavior in SHI irradiated metal atom reinforced C_{70} matrix nanocomposite.

4.2.1 Experimental details:

4.2.1.1 Methods of preparation, irradiation by 90 MeV Si ion and characterization of C_{70} thin films.

High purity C_{70} fullerene powder (99.9+ %, Alfa Aesar) was evaporated using a tungsten boat filament in a high vacuum chamber at base pressure, about 7×10^{-6} and 3.7×10^{-5} torr, before and during deposition respectively. The deposition was carried out at a uniform rate of ~ 0.2 Å s^{-1}. Fullerene C_{70} thin films were irradiated with 90 MeV Si ion. The fluence range varies from 1×10^{12} to 6×10^{13} ions cm^{-2}. S_e and S_n were estimated to be $\sim 2.26 \times 10^2$ and $\sim 1.65 \times 10^{-1}$ eV/Å, respectively. The projected range is about 33.3 μm, for the C_{70} thin films in case of 90 MeV Si ions.

Micro-Raman data of pristine and irradiated films with 90 MeV Si ion beam were recorded using AIRIX STR 500 Raman spectrograph.. The surface morphology of samples was performed on Veeco Digital Multimode Scanning Probe Microscopy with Nanoscope IIIa in tapping mode. The contact angle measurements for water drop were performed using KRUSS set-up at IUAC New Delhi.

4.2.1.2 Methods of preparation, irradiation by 55 MeV Si ion and characterization of C_{70} thin film

The vacuum before starting the evaporation recorded $\sim 1.9 \times 10^6$ mbar and maintained at about 5.6×10^6 mbar. During deposition, the rate was maintained at about 0.20 Å/s during the deposition by adjusting the current value to 40-45 A.

The deposited fullerene C_{70} thin films were irradiated by 55 MeV Si ion beam at different fluences 1×10^{12}, 3×10^{12}, 1×10^{13} and 3×10^{13} ions/cm^2. The charge state of the beam was +4 and the current of the beam was 2 pnA. For 55 MeV Si ions, electronic energy loss (S_e) and nuclear energy loss (S_n) are about $\sim 2.7 \times 10^2$ eV/Å and 2.5×10^1 eV/Å respectively, with a projected range ~ 19.25.

The resistive heating method has been used to deposit the fullerene C_{70} thin films of thickness ~ 150 nm on glass substrates by evaporating fullerene C_{70} and the process of the irradiation of deposited films is described in chapter 3. Micro-Raman data of pristine and irradiated films were recorded with a Renishaw in-Via Raman microscope using an Ar ion laser excitation at 514 nm at room temperature The UV-visible absorption spectra of pristine and Si ion irradiated samples have been recorded

by using a U-3300 UV-visible spectrometer by Hitachi. For surface analysis of the thin films AFM images were recorded by Bruker AFM Analyzer.

4.2.1 .3 Methods of preparation, irradiation by 90 MeV Ni ion and characterization of C_{70} thin film

The vacuum before starting the evaporation recorded ~1.9×10^6 mbar and maintained at about 5.6×10^6 mbar. During deposition, the rate was maintained at about 0.20 Å/s during the deposition by adjusting the current value to 40-45 A.

For C_{70} films are 6.7×10^2 eV/Å (S_e), ~1.14 eV/Å (S_n) and ~19.05 μm (projected range). In both cases the projected range is about 19 μm, hence all the ions will pass through the film (thickness ~150 nm) and therefore all the ions after passing through the film are buried into the substrate. UV-visible absorption spectra of pristine and Ni ion irradiated samples on quartz have been recorded by using U-3300 UV-visible spectrometer (Hitachi make at IUAC, New Delhi). Raman spectra of the pristine and 90 MeV Ni ion irradiated thin films were measured using LABRAM Raman spectrometer in a range of 200-1800 cm^{-1} at room temperature. AFM images were recorded by Bruker AFM analyzer for morphological study.SEM images were recorded on MIRA II LMH Field Emission Scanning Electron Microscope (TESCAN for particle size approximation before and after irradiation, at a resolution of 1.5 nm at 25 kV.

4.2.1.4 Methods of preparation, irradiation by 125 MeV Au ion and characterization of C_{70} thin film

The vacuum before deposition was about 7×10^6 mbar and during deposition was about 3.7×10^5 mbar, respectively. The deposition was carried out at a uniform rate of ~ 0.2 Å s^{-1}. The as deposited fullerene C_{70} thin films were irradiated with 125 MeV Au ion beam. For 125 MeV Au ions, the value of electronic (S_e) and nuclear (S_n) energy losses in C_{70} are 1.39×10^{-3} eV/Å and 1.57×10^{-1} eV/Å, respectively and the range of Au ions is 16.9 μm.

The fullerene C_{70} thin films of thickness ~150 nm were deposited using thermal resistive method of thickness 150 nm. The detailed description of synthesis and irradiation is presented in chapter 3. Structural properties of pristine and irradiated samples, were studied my Micro-Raman spectroscopy in AIRIX STR 500 Raman spectrograph at room temperature in Ar ion laser excitation at 532 nm (~1 mW, 50 × objective). The optical absorption of pristine and irradiated films was recorded using Hitachi 3300 UV-visible Spectrometer.

4.2.2 Results and discussion:

4.2.2.1 C_{70} thin film irradiated by 90 MeV Si ion beam:

4.2.2.1.1 Raman analysis:

Figure 4.11 depicts Raman spectra of the pristine C_{70} along with the 90 MeV Si ion beam irradiated samples at different fluences (1×10^{12}, 3×10^{12}, 1×10^{13}, 3×10^{13} and 6×10^{13} ions/cm^2), recorded in the range of 200- 1800 cm^{-1}. Inset of figure 4.12(a) represents the position of Raman peaks for pristine C_{70} thin films. The corresponding modes are compatible to those assigned in a previous report [22-23] and matches well with the theoretical predicted modes.
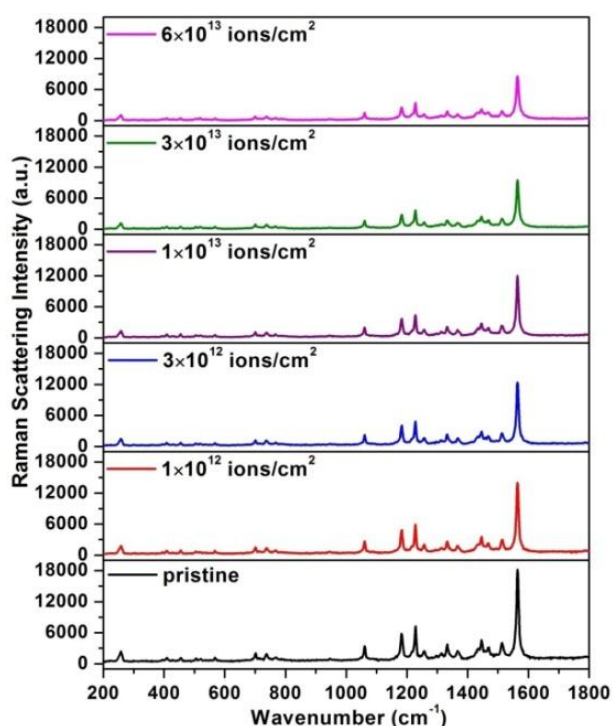
Figure 4.11 Raman spectra of pristine and 90 MeV Si ion irradiated fullerene C_{70} films.

It has been observed that Raman peaks decline with increase in fluence of the ion beam but not completely diminished even at higher fluence (6×10^{13} ions/cm^2). The decrease in intensity of Raman peaks with ion fluence reveals that the C_{70} fullerene molecules are breaking as a result of energy deposition by the ion beam. Higher the fluence more is the energy deposited and thus results in larger number of breaking of C_{70} molecule. But C_{70} fullerene is not completely transformed into amorphous Carbon (a-C) at a fluence of 6×10^{13} ions/cm^2. This is because the electronic energy loss ($\sim$ 2.26×10^2 eV/Å) deposited by 90 MeV Si ion is low enough to transform C_{70} fullerene

into a-C. The breakage of C_{70} molecules is explained on the basis of Thermal Spike Model.

According to this, when an ion with high energy enters the material, it transfers its energy to the atoms of the material by electron–electron (e-e) and electron–phonon (e-p) coupling in 10^{-13}-10^{-12} sec, and this leads to rise in the temperature of the lattice. When the temperature is considerably higher than the melting temperature of the material, a molten state is produced within limited area, typically of a diameter of few nm for a short time ($t \geq 10^{-11}$ s).
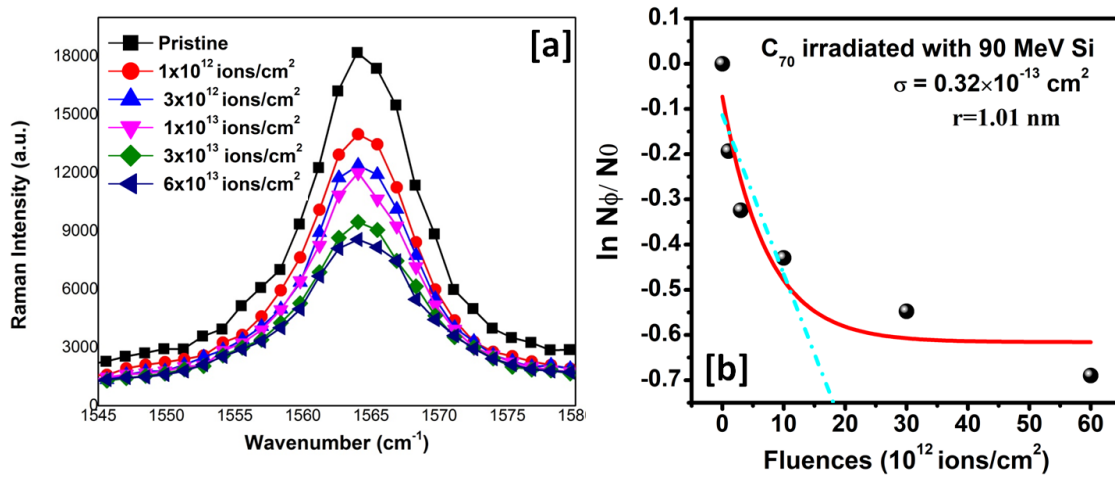
Figure 4.12 (a) Irradiation-induced damage of the most intense Raman mode 1564 cm^{-1} at different fluences of 90 MeV Si ions. (b) Curves between normalized integral area and different fluences of 90 MeV Si ion beam.

Finally, the material is quenched by thermal conduction at a very high rate of 10^{14} K/s; and results in formation of a cylindrical region (latent tracks) known as ion tracks [29-30].Now to examine in more details the effect of energy deposition by ion beam on the C_{70} fullerene, the most intense Raman peak centered at 1564 cm^{-1} is chosen. Figure 4.12 (a) represents the spectra of the most intense Raman peak (1564 cm^{-1}) from 1545 to 1585 cm^{-1} wave number for pristine and ion irradiated samples. The peak intensity reduces with ion fluence. Hence this peak is investigated in detail to analyze the effect of 90 MeV Si ion energy deposition.

Following the method described in section 4.1.3.2.3, damage cross section is calculated with use of relation

$$N(\phi) = N_o exp(-\sigma \phi) \qquad (4.5)$$

Where, N (ϕ) = areal density of fullerene C_{70} molecules remaining after ion irradiation at a fluence of ϕ, N_0 = areal density of pristine fullerene C_{70} and σ = cross section of damage in fullerene by ion irradiation for a single ion impact.

The plot of ln (N (φ)/N_0) as a function of fluence is shown in figure 4.12 (b), the curve in the plot has two slopes; one slope for the effect at low fluence and the other due to the effect at high fluence. To avoid the overlapping of tracks that takes place at higher fluences, the slope value is taken up to the fluence (1×10^{13} ions/cm^2) where the overlapping of the tracks starts.

The slope of the figure 4.12 (b) gives the value of damage cross-section (σ) and is approximated to be ~0.32 $\times 10^{-13}$ cm^2 and the value of the radius of ion track (r) calculated by equation (3) comes out to be ~1.01 nm.

4.2.2.1.2 Surface Analysis

Atomic Force Microscopy (AFM) has been performed to analyze the change in the surface morphology of the sample because of the irradiation effect. Figure 4.13(a) represents the 2-D micrographs for the pristine as well as 90 MeV Si ion irradiated C_{70} thin films.
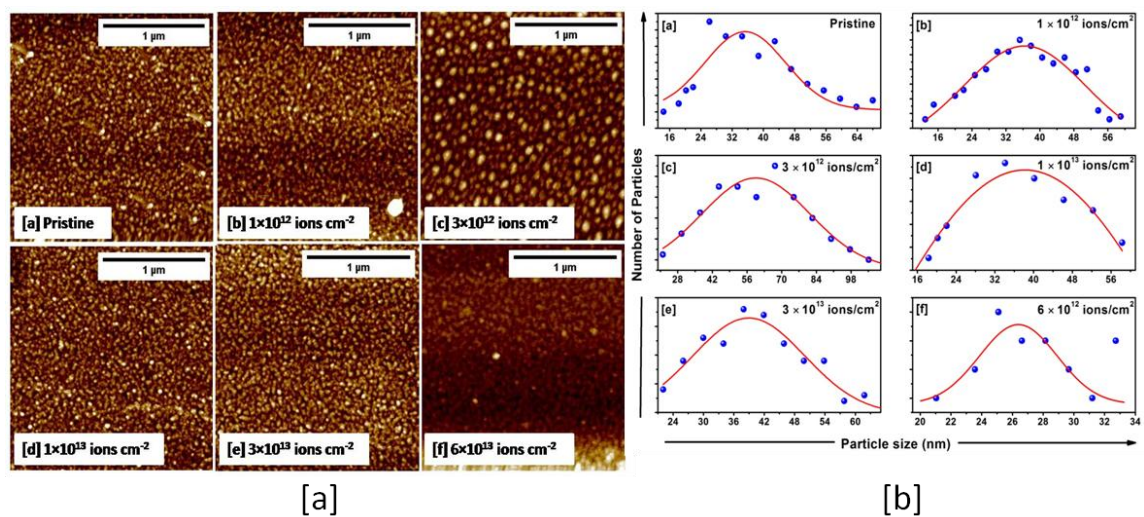
Figure 4.13 (a) 2-D AFM images of pristine and 90 MeV Si ion irradiated films at different fluences (b) represents the corresponding distribution of particle size fitted with Gaussian function of fullerene C_{70} pristine and irradiated thin films.

The approximated value of the average particle size and roughness calculated from AFM analysis are tabulated in table 4.3. The roughness is observed to increase with increasing fluence. This can be explained on the basis of the fact that as the fluence is increased it produces more defects and hence results in increase of roughness. Figure 4.13(b) represents the corresponding distribution of particle size fitted with Gaussian function of the pristine and 90 MeV Si ion irradiated at fluence 1×10^{12}, 3×10^{12}, 1×10^{13}, 3×10^{13} and 6×10^{13} ions/cm^2 on fullerene C_{70} thin films. From table 4.3, it is observed that the average particle size becomes larger after irradiation. This is due to

the agglomeration of smaller particles into larger ones; since the smaller particles have higher surface free energy there is an urge for its agglomeration to form bigger particles which decreases surface free energy owing to lower specific surface area of larger particles. The average particle size at highest fluence (6×10^{13} ions/cm^2) is reduced to a value of 26.3nm, which is attributed to the large overlapping of ion tracks at this fluence.

Table 4.3 Represents the variation of average particle size, roughness and contact angle of fullerene C_{70} thin films with increasing fluences of 90 MeV Si ion.

Fluence (ions/cm^2)	Average Particle Size (nm)	Roughness (nm)	Contact Angle (degree)
Pristine	35.3	1.25	99.6
1×10^{12}	36.4	1.38	106.0
3×10^{12}	59.8	3.51	108.0
1×10^{13}	36.5	1.60	106.8
3×10^{13}	38.1	1.63	96.4
6×10^{13}	26.3	2.77	88.1

4.2.2.1.3 Contact angle measurement:

The contact angle of water droplet with the film surface act as a primary data that specifies the degree of wettability during a solid and liquid interaction. The wetting characteristic of a solid surface calculated on the basis of contact angle is based on a fundamental parameter, i.e. intermolecular forces which are responsible for contraction of the surfaces called surface tension. Figure 4.14(a) shows a liquid drop placed on a flat horizontal solid surface. The contact angle θ_c is defined as the angle formed by the intersection of the liquid/solid and liquid/vapour interfaces, geometrically acquired by applying a tangent line from the contact point along the liquid/ vapour interface in the droplet profile.
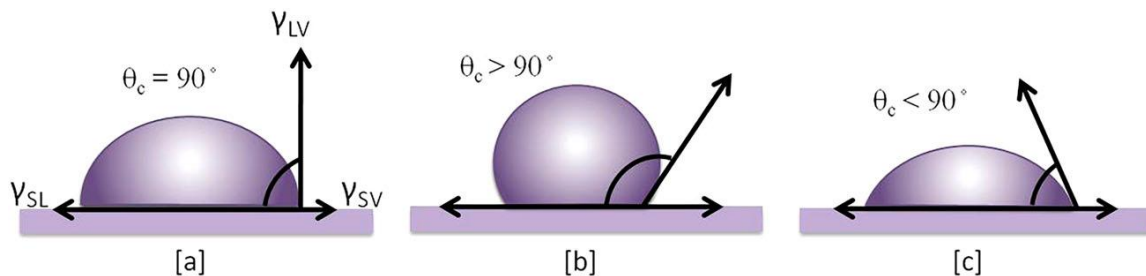
Figure 4.14 Schematic shows the formation of contact angle formed by liquid drop.

The interface where all the three phases (solid, liquid and vapour) co-exist is referred as the three phase contact line. Theoretically, the contact angle (θ_c) can be explained

by the Young's Equation (Thomas Young Model) based on the mechanical equilibrium of the drop under the action of three interfacial tensions.

$$\gamma_{LV} cos\theta_c = \gamma_{SV} - \gamma_{SL} \qquad (4.6)$$

$\gamma_{LV}, \gamma_{SV}, \gamma_{SL}$ are the interfacial tensions of liquid/vapour, solid/vapour and solid/liquid interfaces, respectively. θ_c is Young's contact angle. This model is based on the assumption that the surface is flat and homogenous and also neglects the external forces such as gravity which deforms the droplet. The gravity force can be neglected by considering the size of droplet to be very small [27].

Figure 4.14(b) is shown the droplet spread over a small area on the film surface when $\theta_c > 90°$) and it defines the surface hydrophobic (wettability unfavourable) in nature. Figure 4.14(c) shows that the droplet is spread over a large area on the surface for $\theta_c < 90°$ and the surface is defined as hydrophilic (wettability favourable) in nature [28]. Further to include roughness factor of the film we have to make corrections in the above model that given by Wenzel equation

$$cos\,\delta = rcos\,\theta_c \qquad (4.7)$$

Where r is roughness factor and δ is modified contact angle after including roughness factor. The wettability can be modified with a slight change in roughness and chemical composition of the surface by using several methods but among these methods SHI irradiation tool plays a vital role in altering the surface wettability. In the present work, the main focus is on the ion irradiation effect on fullerene C_{70} thin films. It appears interesting to see the effect of ion irradiation on wettability of fullerene C_{70} thin films. Measurements of contact angle has been made, in order to analyze the hydrophilic or hydrophobic character of the pristine and 90 MeV Si ion irradiated fullerene C_{70} thin films. The contact angle measurement technique is static contact angle measurement method in which the contact area between the liquid and solid does not change externally during the measurement. The angle was estimated using Sessile drop fitting method.

Figure 4.15 (a) shows the snapshots of the contact angle measurement for pristine as well as 90 MeV Si ion irradiated fullerene C_{70} thin films at different fluence. The contact angle first increases and then decreases with fluence as shown in figure 4.15(b) and tabulated in table 4.3.
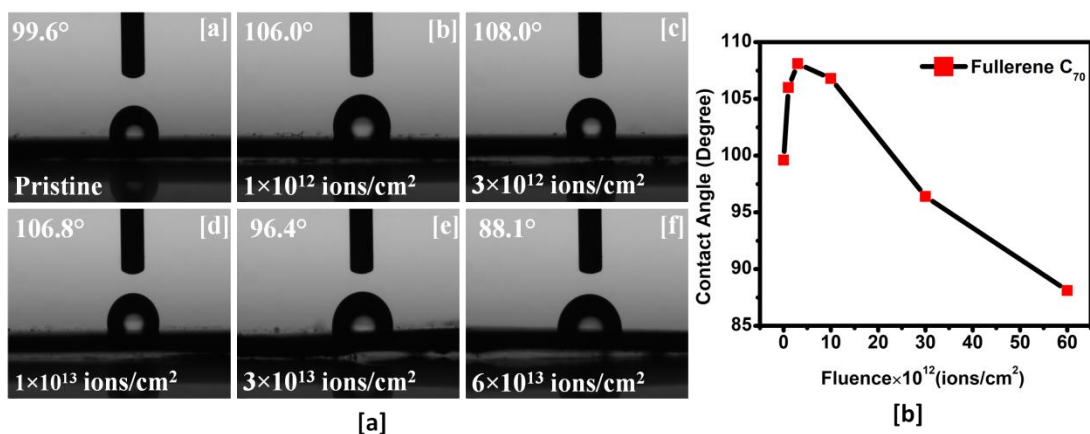
Figure 4.15 (a) The snapshots of the contact angle measurement for the pristine and 90 MeV Si ion irradiated thin films (b) variation of contact angle with fluence of 90 MeV Si ion beam.

This demonstrates that the hydrophobic nature of fullerene C_{70} increases with fluence up to 3×10^{12} ions cm^{-2} and as the fluence reaches to 1×10^{13} ions cm^{-2} it starts decreasing. From AFM studies it is clear that the roughness of the film enhances up to this fluence and after that it decreases. As the roughness increases the hydrophobic surface becomes more hydrophobic and hydrophilic surface becomes more hydrophilic [28]. Although there is an increase in the roughness values at highest fluence, the contact angle show lower value (~88.1°) as compared to pristine film (~99.64°), which is due to the fact that, at this particular fluence (6×10^{13} ions cm^{-2}) the transformation of fullerene C_{70} into amorphous carbon takes place, which is hydrophilic in nature [29]. The resultant hydrophilic nature of the film will be beneficial in application area of biosensors due to enhancement of adsorption [30].

4.2.2.2 C_{70} thin film irradiated by 55 MeV Si ion beam:

4.2.2.2.1 Raman analysis:

Raman study has enabled to observe the modification in fullerene C_{70} thin films caused by ion irradiation. It is known that fullerene C_{70} is rich in 53 Raman active modes ($12 A_1' + 22 E_2' + 19 E_1''$) [27]. Hence assigning different Raman active modes appears to be quite complicated. Figure 4.16 represents the Raman spectra of pristine and irradiated thin film samples with different fluences 1×10^{12}, 3×10^{12}, 1×10^{13} and 3×10^{13} ions/cm^2. The modes observed in the spectra corroborate with the reports available in literature [19-20].

From the spectra in figure 4.16, it is observed that, the intensity of Raman peaks decreases with increasing fluence. This observation implies that increasing fluence enhances the breakage of fullerene C_{70} molecules. However, even at higher fluence (~

3×10^{13}ions/ cm^2) the Raman peaks have not completely disappeared This signifies that fullerene C_{70} thin film has not been entirely transformed into amorphous carbon at these fluences; the present observation is supported by the results of previous study [90 MeV Si].
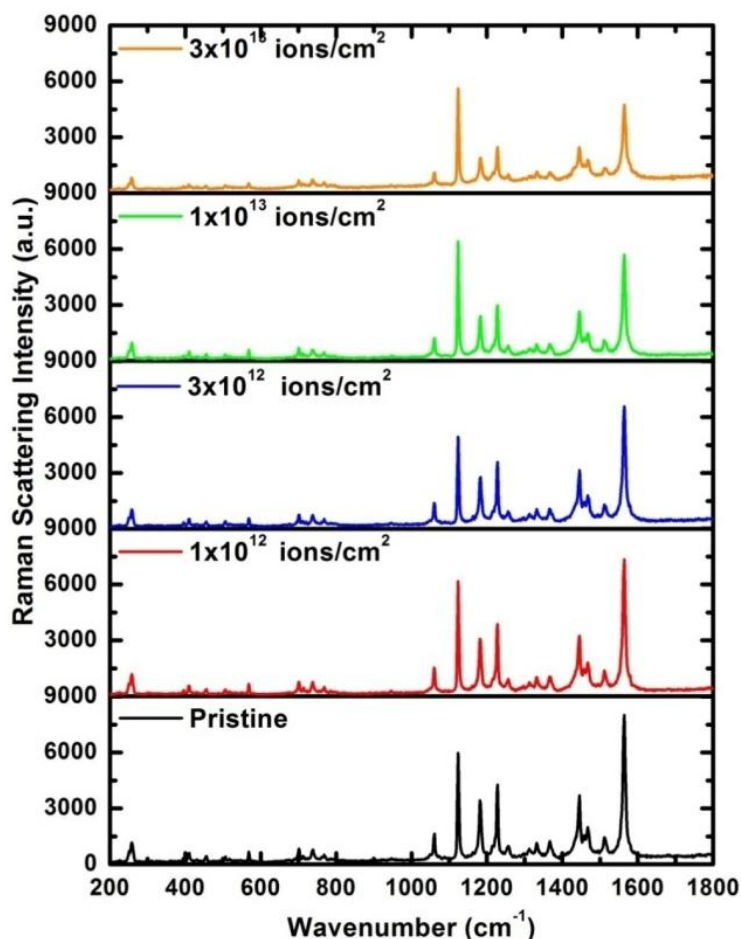
Figure 4.16 Raman spectra of pristine and 55 MeV Si ion irradiated fullerene C_{70} films.

The breakage of C_{70} molecules is explained on the basis of Thermal Spike Model. In accordance with the model, when the temperature exceeds the melting temperature of the material, a molten state is produced, typically of a diameter of few nm for a short time ($t \geq 10^{-11}$ s).

The material is subsequently quenched by thermal conduction at a very high rate of 10^{14} K/s and these results in formation of a cylindrical region known as ion tracks [21-22]. Analysis of the effect of ion irradiation on Raman peaks is done with the most intense peak centered at 1564 cm^{-1}. No evidence of extra fragmentation has been observed as there is no extra peak observed after irradiation. In figure 4.17(a), the most intense peak (at 1564 cm^{-1}) is observed in the range between 1550-1580 cm^{-1} for

the pristine and the irradiated fullerene C_{70} thin films. It is seen that the most intense Raman vibrational peak diminishes in intensity with increasing ion fluences.
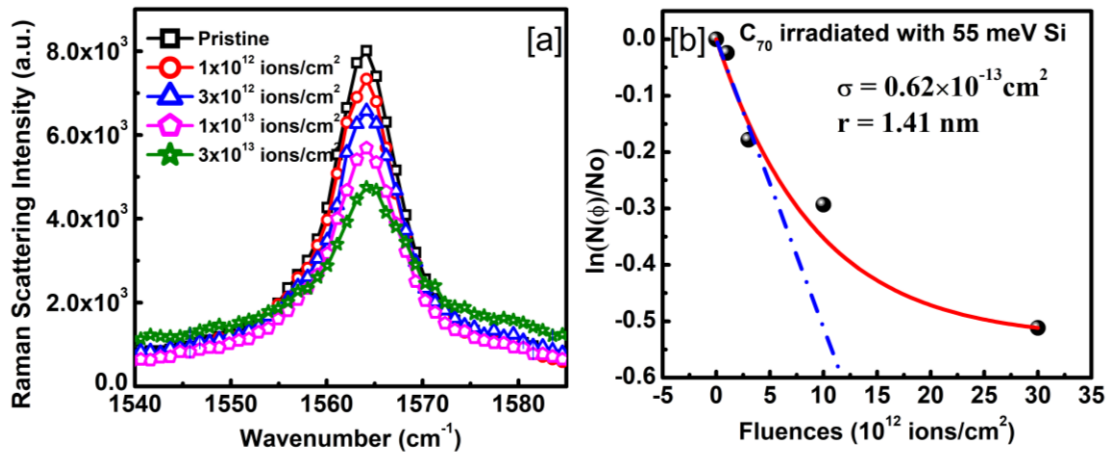
Figure 4.17 (a) The most intense Raman mode for different fluences (b) Relation between normalized integral area vs. fluences of 55 MeV Si ion beam.

By using the classical formula as obtained from the existing literature, damage cross section obtained by 55 MeV Si ion beam irradiation has been calculated. Following the method, described in the previous section. Figure 4.17 (b) is drawn which shows the plot of ln $N(\phi)/N_0$ as a function of fluence. It is interesting to note from figure 4.17(b) that an exponential curve has resulted in place of expected straight line as per classical formula $ln\left(\frac{N(\phi)}{N_o}\right) = -\sigma\,\phi$ with notation having usual meaning; hence it is apparent that the classical relation advocated elsewhere [11] is not adequate to explain the results of present experiment on C_{70}. This inadequacy can be explained by the phenomenological model for damage cross-section provided by Bajwa et al.[11]. In this model, they have described the interaction of ion with fullerene in terms of differential equations. On the basis of that model one can explain Figure 4.17(b). In this plot two slopes can be drawn which result due to two ways of deposition of energy, one at low fluence where the ion tracks formed due to ion irradiation are distinct from each other and the other is at high fluence where the overlapping of ion tracks takes place. Thus a change in slope ($\sim 3\times10^{12}$ ions/ cm^2 fluence) is observed at the start of overlapping of ion tracks formed by the irradiation of 55 MeV Si ion beam.

From the figure 4.17(b), 0.6 $\times10^{-13}$ cm^2 comes out to be value of the damage cross-section (σ) (from the slope of the curve in figure 4.17(b)). The value of the radius of ion track (r) is calculated to be around ~1.41nm.

4.2.2.2.2 UV-visible absorption spectroscopy:

Figure 4.18 depicts the UV-visible absorption spectrum of pristine within (300 -700 nm) on glass substrates at room temperature. From the UV-visible absorption spectroscopy, several weak peaks centered at ~ 661, ~ 638, ~ 614, ~ 569, ~ 533 and ~ 494 nm can be observed. The most intense peak (higher in intensity) is observed at ~ 387 nm. Further, this most intense absorption peak is followed by two weak peaks at ~ 359, ~ 336 nm respectively.
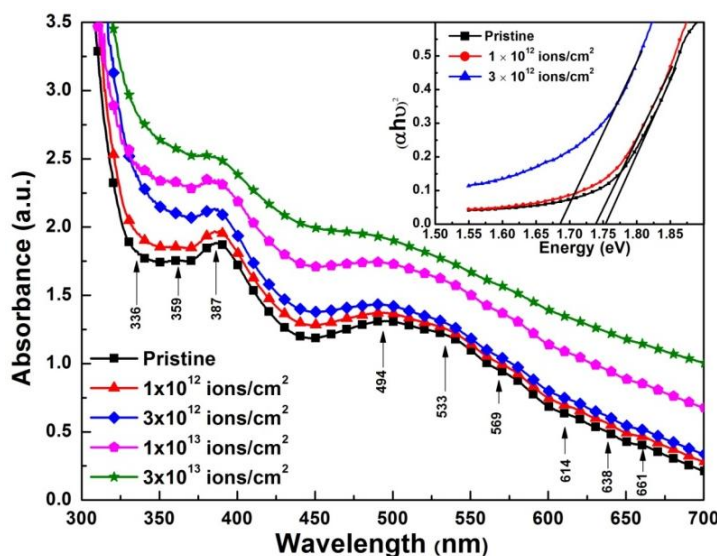
Figure 4.18 UV-visible absorption spectra of pristine and irradiated fullerene C_{70} films. Concerned Tauc plots are shown in inset.

These peaks are attributed to different transition. As C_{70} molecule has D_{5h} point group symmetry, this lower symmetry makes the electronic energy levels of fullerene C_{70} molecule a structure of abundant distribution. Hence it is very complicated to assign its transition. On the basis of literature, some of the transitions are assigned as peak 387 nm (3.20 eV), 494 nm (2.50 eV) and 533 nm (2.32 eV), respectively corresponding to the $A_2', E_1'' \rightarrow E_1', A_2'' \rightarrow A_1'$ and $A_2' \rightarrow A_1''$ of the fullerene C_{70} [28-29].

Figure 4.18 represents the UV- visible absorption spectra of pristine and 55 MeV Si ion beam irradiated fullerene C_{70} thin films at different fluences 1×10^{12}, 3×10^{12}, 1×10^{13} and 3×10^{13} ions/cm². This figure has shown the irradiation effect on the UV-visible absorption spectrum of fullerene C_{70} thin film due to increasing fluence. As the fluence is increased, the absorption peaks characteristic of fullerene C_{70} (336 nm, 359 nm, 387 nm, 494 nm, 553 nm, 569 nm, 614 nm, 638 nm and 661 nm) are reduced. At

the highest fluence 3×10^{13} ions/cm^2, these peaks are significantly reduced; this is indicative of the transformation of fullerene C_{70} into amorphous carbon.

Table 4.4 Represents the variation in band gap, average particle size and roughness of fullerene C_{70} thin films with increasing fluences of 55 MeV Si ion.

Fluence (ions/cm^2)	Bandgap (eV)	Average Particle Size (nm)	Roughness (nm)
Pristine	1.75	26±0.5	3.37
1×10^{12}	1.73	50±0.7	3.22
3×10^{12}	1.68	53±0.4	3.07
1×10^{13}	-	61±0.5	2.60

From the absorption spectra the band gap of the pristine and the ion irradiated fullerene C_{70} thin films has been calculated. The direct band gap (E_g) and linear absorption coefficient (α) are related by the well-known Tauc relation:

$$(\alpha h\nu)^{1/n} = A(h\nu - E_g) \tag{4.8}$$

Where, h: Planks constant, ν: frequency of vibration, A: proportionality constant, α: absorption coefficient, E_g: band gap. For fullerene C_{70} we consider direct band transition. Hence the value of n has been taken ½. The above Tauc relation may be written as:

$$(\alpha h\nu)^2 = A(h\nu - E_g) \tag{4.9}$$

Further the effect of ion irradiation on band gap can be observed in the inset of figure 4.18 which shows a plot (αhν)^2 as a function of energy (hν), α being the absorption coefficient. The value of the band gap (E_g) is estimated by extrapolating the linear fitted region. The point on the energy axis, at which the extrapolated line meets with (αhν)^2 = 0, corresponds to the direct band gap of the fullerene C_{70}. The band gap from this plot has been approximated as 1.75 eV for pristine and for the irradiated fullerene C_{70} thin film with fluences 1×10^{12} and 3×10^{12} ions/cm^2 as 1.73 and 1.68 eV, respectively (table 4.4).

4.2.2.2.3 Surface analysis:

Surface morphology of the fullerene C_{70} pristine and 55 MeV Si ion beam irradiated thin films is analyzed by atomic force microscopy. Three dimensional images of pristine C_{70} and 55 MeV Si ion beam irradiated films at fluences 1×10^{12}, 3×10^{12} and 1×10^{13} ions/cm^2 are shown in figure 4.19 (a). A two-dimensional AFM image is

shown in the inset of figure 4.19 (a) for 1×10^{13} ions/cm^2. With increasing fluence of 55 MeV Si ion, particles, are seen to be developing in size. Roughness values calculated for pristine and for irradiated films at fluences 1×10^{12}, 3×10^{12} and 1×10^{13} ions/cm^2 are tabulated in table 4.4.

The decrease in the roughness value with increasing fluence is explained by the fact that the ion loses its energy to the target material, thereby resulting in the release of stress in film and hence the roughness of the film also gets decreased. Figure 4.18 (b) represents the corresponding distribution of particle size fitted with Gaussian function for the pristine and 55 MeV Si ion irradiated fullerene C$_{70}$ thin films at fluences 1×10^{12}, 3×10^{12} and 1×10^{13} ions/cm^2.
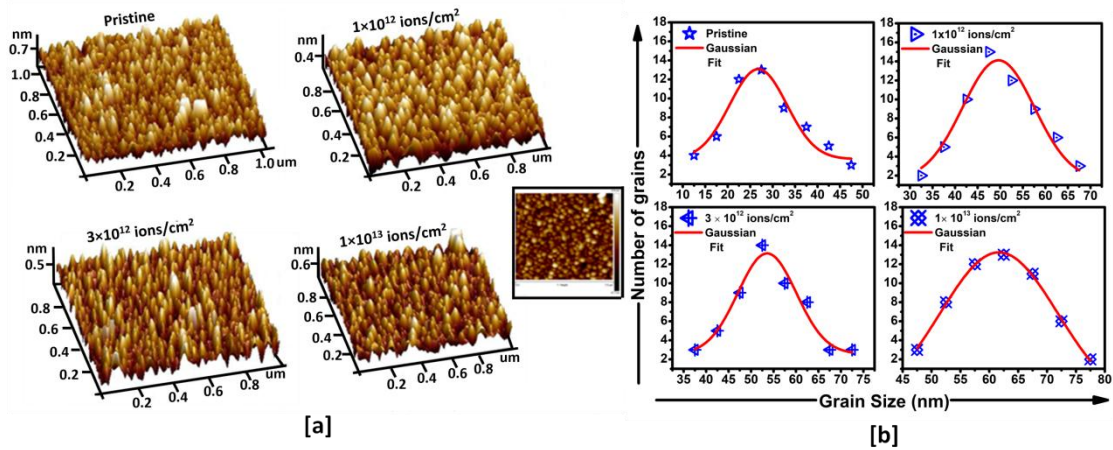
Figure 4.19 3-D AFM images of pristine and 55 MeV Si ion irradiated films at fluences 1×10^{12}, 3×10^{12} and 1×10^{13} ions/cm^2; a two dimensional AFM image is shown in inset for fluence 1×10^{13} ions/cm^2.

The approximated values of the average particle size from the Gaussian fit are tabulated in table 4.4. From the table, it is observed that the average particle size is increased with increase in fluence. This may be due to the agglomeration of smaller particles into larger ones; since the smaller particles have higher surface free energy there is at urge for its agglomeration to form bigger particles which decreases surface free energy owing to lower specific surface area of larger particles.

4.2.2.3 C$_{70}$ thin film irradiated by 90 MeV Ni ion beam:

4.2.2.3.1 UV-visible absorption spectroscopy:

Optical absorption spectra of the pristine and 90 MeV Ni ion irradiated fullerene C$_{70}$ films on quartz substrate was measured from 300 to 700 nm.
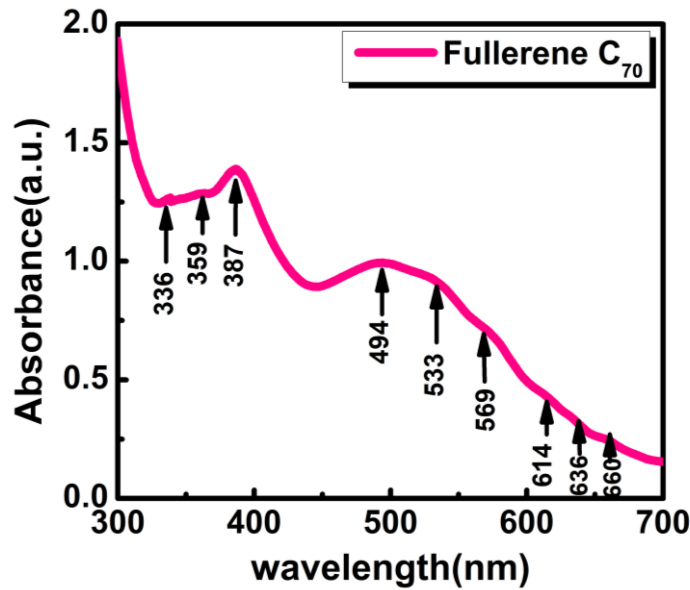
Figure 4.20 UV-visible absorption spectrum of fullerene C_{70} pristine thin film on quartz.

The absorption spectrum of the pristine film is shown in figure 4.20 and is consistent with the reports already available in the literature [19-20]. The spectrum consists of many peaks, starting with a weak band at 660 nm (1.87 eV). This weak band is then followed by a number of very weak peaks 636 nm (1.94 eV), 614 nm (2.01 eV), 569 nm (2.17 eV), 533 nm (2.32 eV), and 494 nm (2.50 eV). The highest peak (maximum in intensity) is observed at 387 nm (3.20 eV). After this, there are two weak peaks observed at 359 (3.45 eV) and 336 nm (3.68 eV). The assignment of the peaks is done identically with that in the previous section [28]. Peak 387 nm (3.20 eV), 494 nm (2.50 eV) and 533 nm (2.32 eV) corresponds to the A_2', $E_1''{\rightarrow}E_1'$, $A_2''{\rightarrow}A_1'$ and $A_2'{\rightarrow}A_1''$ of the fullerene C_{70}.

The effect of SHI irradiation with increasing fluence on fullerene C_{70} is well illustrated in figure 4.21, which clearly demonstrates a decrease in the intensity of optical absorption peaks with an increase in ion fluence along with the fading of the above features. Now to analyze the irradiation effect on the optical band gap of the fullerene C_{70}, Tauc plots (inset of figure 4.21) are constructed for pristine and irradiated fullerene C_{70} films at $1{\times}10^{12}$ and $3{\times}10^{12}$ ions/cm^2 fluences. The direct band gap calculated by Tauc plot for pristine film is ~1.87 eV and for the sample irradiated at a fluence of $1{\times}10^{12}$ ions/cm^2 is about ~1.83 eV which decreases up to ~1.80 eV for the sample irradiated at a fluence of $3{\times}10^{12}$ ions/cm^2 (table 4.5).
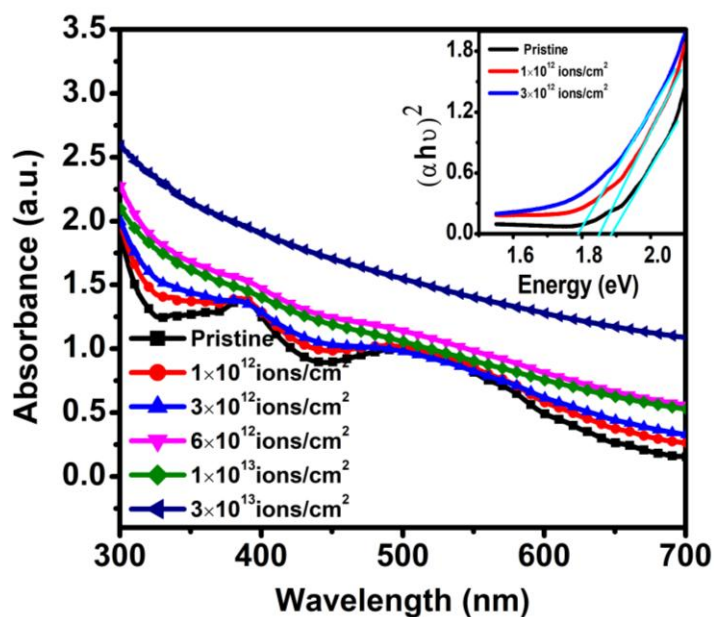
Figure 4.21 UV-visible absorption spectra of pristine and irradiated fullerene C_{70} thin films with inset of Tauc plot.

For higher fluences ($>1\times10^{13}$ ions/cm^2) band gap cannot be calculated by Tauc plot as absorption edge cannot be obtained for higher fluences. This is due to the transformation of fullerene C_{70} into a-C at higher fluences.

*4.2.2.3.2 Raman Analysis***:**

Since fullerene is comprised of carbon-carbon bonds and Raman spectroscopy is the most sensitive to highly symmetric covalent bonds with little or no natural dipole moment, Raman spectroscopy is highly suitable for fullerene characterization. Hence, in order to estimate the damage occurred in fullerene C_{70} due to 90 MeV Ni ion beam irradiation, Raman spectroscopy has been performed on pristine and irradiated films.

It is known that fullerene C_{70} vibrational spectrum results in numerous bands. As stated earlier, there are 53 Raman active modes ($12 A_1' + 22 E_2' + 19 E_1''$) predicted in the pure fullerene C_{70} at room temperature according to group theory and various first principle theories [18]. Figure 4.22 represents the Raman spectrum of the pristine fullerene C_{70} film deposited on quartz substrate. The bands observed in figure 4.22 are consistent with those available in the literature [19-20] and are ascribed to the internal modes of C_{70} molecule.
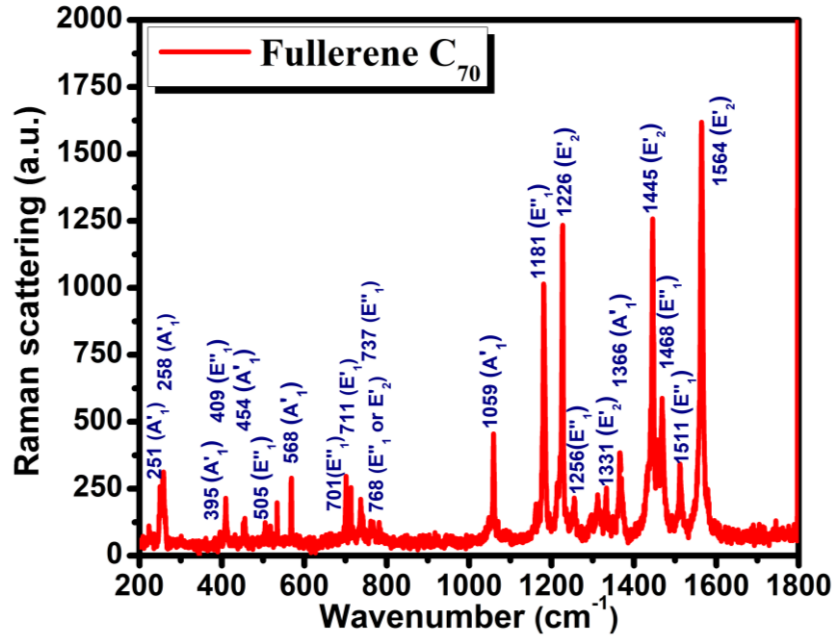
Figure 4.22 Raman spectrum of pristine fullerene C_{70} film.

The different modes are assigned [32] as ($251 cm^{-1} \rightarrow A_1'$), ($258 cm^{-1} \rightarrow A_1'$), ($395 cm^{-1} \rightarrow A_1'$), ($409 cm^{-1} \rightarrow E_1''$), ($454 cm^{-1} \rightarrow A_1'$), ($505 cm^{-1} \rightarrow E_1''$), ($568 cm^{-1} \rightarrow A_1'$), ($701 cm^{-1} \rightarrow E_1''$), ($711 cm^{-1} \rightarrow E_1'$), ($737 cm^{-1} \rightarrow E_1''$), ($768 cm^{-1} \rightarrow E_1''$ or E_2'), ($1059 cm^{-1} \rightarrow A_1'$), ($1181 cm^{-1} \rightarrow E_1''$), ($1226 cm^{-1} \rightarrow E_2'$), ($1256 cm^{-1} \rightarrow E_1'$), ($1331 cm^{-1} \rightarrow E_1''$), ($1366 cm^{-1} \rightarrow A_1'$), ($1445 cm^{-1} \rightarrow E_2'$), ($1468 cm^{-1} \rightarrow E_1''$), ($1511 cm^{-1} \rightarrow E_1''$), ($1564 cm^{-1} \rightarrow E_2'$). Figure 4.23 depicts the Raman spectra of pristine and 90 MeV Ni ion beam irradiated fullerene C_{70} thin films deposited on quartz substrate at different fluences 1×10^{12}, 3×10^{12}, 6×10^{12}, 1×10^{13} and 3×10^{13} ions/cm^2.

After ion irradiation, the intensity of the Raman bands decreases as the fluence is increased. This reduction in peak intensity with fluence is due to the damage caused by the ion beam irradiation. Because the films are exposed to ion beam, this ion irradiation leads to breakage of C_{70} fullerene molecules. As a result, the intensity of all the Raman bands starts declining with increasing fluence. At higher fluence 3×10^{13} ions/cm^2 the peaks are completely disappeared, which is an evidence of complete transformation of fullerene C_{70} film into amorphous carbon (a-C). In addition, no extra peak or shifting in the Raman bands has been observed after ion irradiation; this suggests that no intermediate fragments of fullerene C_{70} in any significant quantity have been formed. The transformation of fullerene C_{70} into amorphous carbon is due

to track formation by incoming ion in fullerene C_{70}, which can be explained on the basis of Thermal Spike Model [30-31] as described in previous section.
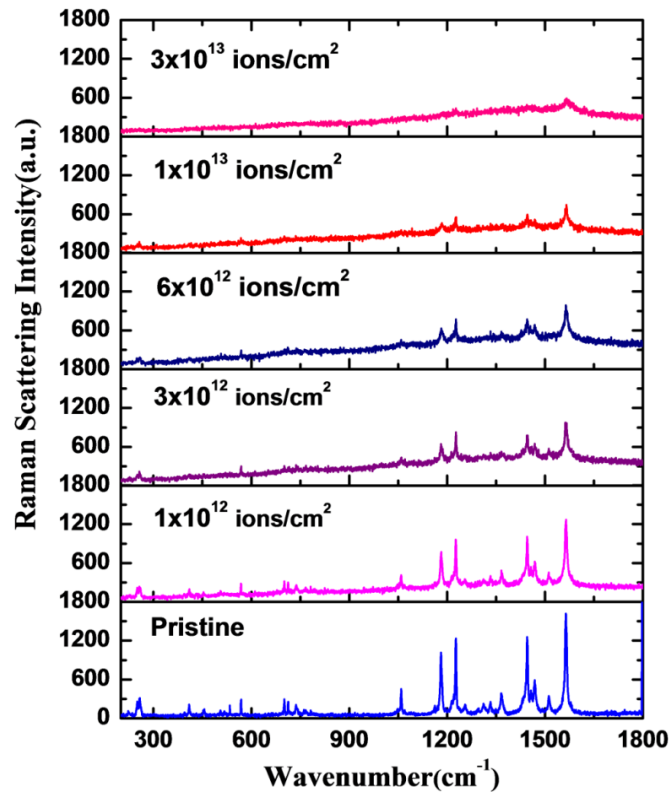
Figure 4.23 Raman spectra of pristine and 90 MeV Ni ion irradiated fullerene C_{70} films.

The film gets completely amorphized at higher fluences due to the reason that at lower fluence, there is no overlapping of ion tracks as they are distant apart. In contrast, at higher fluence, the cylindrical zones (ion tracks) start overlapping with one another resulting in the formation of more ion tracks in the film. At the stage when almost all the cylindrical zones get overlapped, the complete amorphization of fullerene C_{70} thin film takes place [11]. This is verified by figure 4.24 where the plot between ln N (ϕ) /N_0 and the fluence for the selected peak, 1564 cm^{-1}, has two slopes. The change in slope occurs after the fluence at which overlapping starts to occur.The most intense peak in the fullerene C_{70} (pristine sample) is observed at 1564 cm^{-1}. In figure 4.24 this most intense peak (1564 cm^{-1}) of pristine and irradiated films is shown in the range 1545-1585 cm^{-1}.
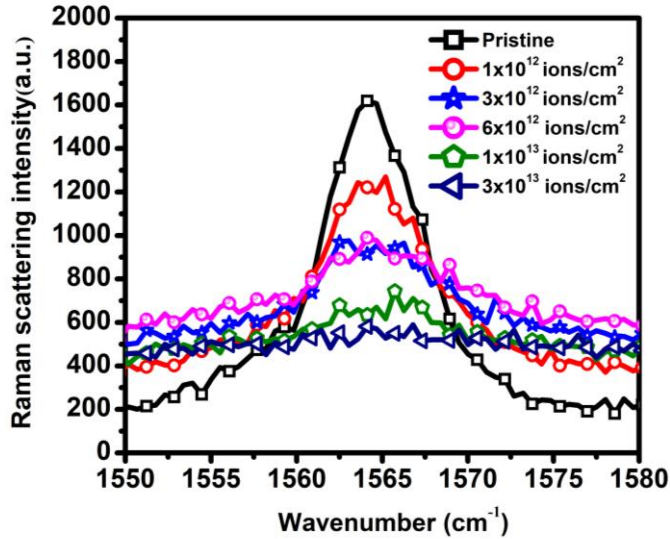
Figure 4.24 Irradiation-induced damage of the most intense Raman mode 1564 cm^{-1} at different fluences of 90 MeV Ni ion.

This figure 4.24 represents the detailed picture of diminishing of peak intensity with increasing fluence. This damage of C_{70} molecule with increasing fluence can be elaborated by calculating damage cross-section, using a classical formula with the assumption that a single ion can produce damage in the form of amorphization track.

$$N\ (\phi)\ =\ N_o exp(-\sigma\ \phi) \hspace{2cm} (4.10)$$

Here N (ϕ) is the areal density of the fullerene C_{70} molecules remaining after ion irradiation with fluence ϕ, N_0 is the areal density of fullerene C_{70} pristine and σ is the cross section of damage in fullerene by ion irradiation.
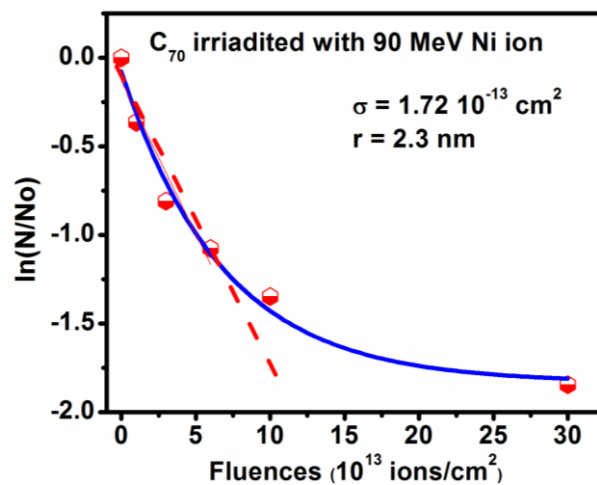
Figure 4.25 Curves between normalized integral area and fluences of 90 MeV Ni ions.

Figure 4.25 represents the plot between ln N (ϕ) /N_0 and the fluence for the selected peak (1564 cm^{-1}). The plot has two slopes one at lower fluences (0-6×10^{12}ions/cm^2)

and the other at higher fluences (1×10^{13}-3×10^{13} ions/cm^2) signifying two different ways for distribution of energy in the films.

As stated before, this stems from the fact that at low fluence the cylindrical zone remain far apart from each other, whereas at high fluence, the overlapping of ion tracks takes place resulting in more conducting zones in the fullerene C_{70} film, and so smaller damage cross section. The radius of damage cross section is calculated to be ~ 2.3 nm of fullerene C_{70} for 90 MeV ion irradiation.

4.2.2.3.3 SEM analysis:

SEM images have been recorded in order to determine the particle size of the pristine as well as of 90 MeV Ni ion beam irradiated fullerene C_{70} films at different fluences. The two dimensional SEM images of the pristine and irradiated films are presented in figure 4.26(a). The particle size distributions of the pristine and irradiated films are also shown in figure 4.26(b). The average particle size was approximated to be ~ 40 nm for the pristine and ~ 47 nm, ~ 48 nm and ~ 57 nm for the films irradiated with a fluence of 1×10^{12}, 6×10^{12} and 1×10^{13} ions/cm^2, respectively (table 4.5).
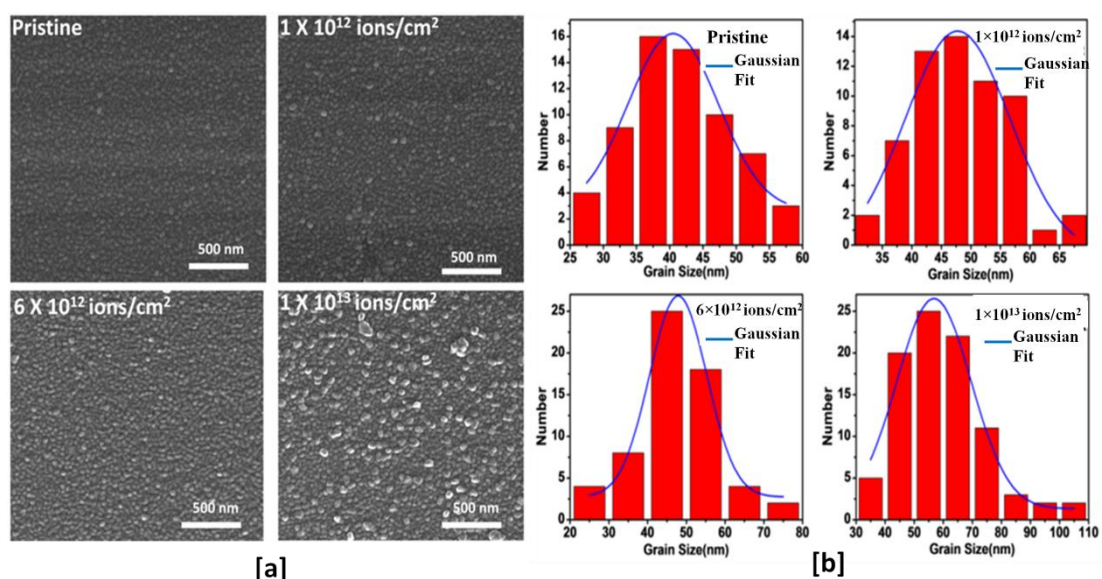
Figure 4.26 (a) Two dimensional SEM images and (b) particle size distribution of pristine and 90 MeV Ni ion irradiated films.

It can be clearly seen in figure 4.26 (b) that after irradiation, the particle size increases with increase in fluences. This indicates agglomeration of the smaller particles to bigger particles, which is due to the presence of molten state owing to thermal spike produced by the ion for a very short duration of time (~ pico seconds) during irradiation which helps in diffusion of particles.

4.2.2.3.4 AFM analysis:

Surface morphology and average particle size of the fullerene C_{70} pristine and 90 MeV Ni ion beam irradiated films deposited on glass substrate were analyzed by Atomic Force Microscopy (AFM). Three dimensional (3D) images of pristine C_{70} and 90 MeV Ni ion beam irradiated films at fluences 3×10^{12} and 3×10^{13} ions/cm^2 are shown in figure 4.27.
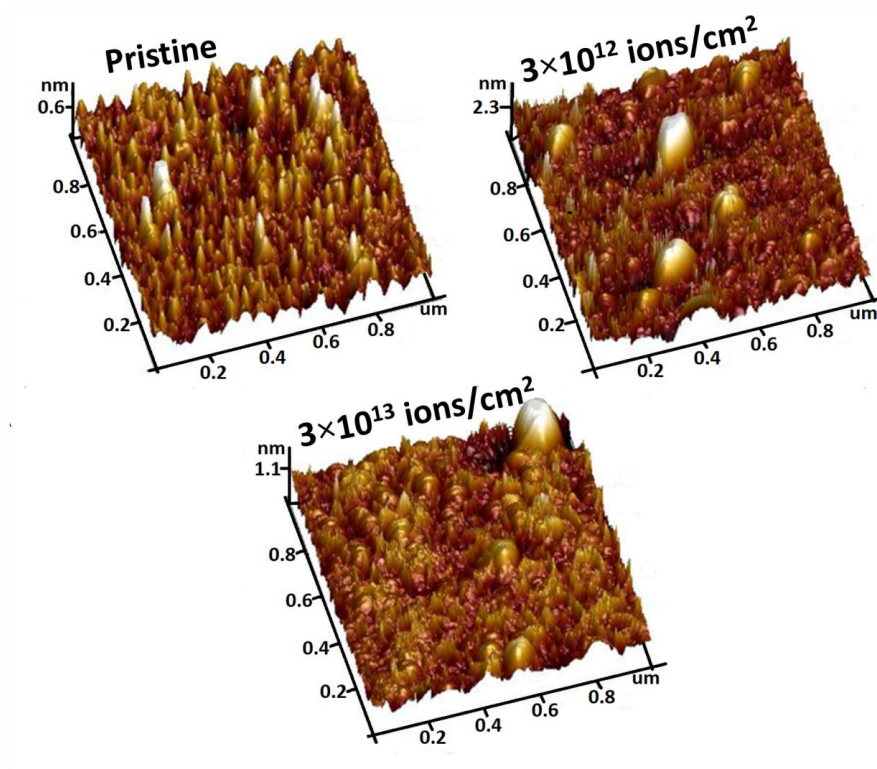
Figure 4.27 3-D AFM images of pristine and 90 MeV Ni ion irradiated films at fluence 3×10^{12} and 3×10^{13} ions/cm^2.

Roughness calculated for pristine and irradiated films at fluences 3×10^{12} and 3×10^{13} ions/cm^2 has been tabulated in table 4.5. The increase in the roughness with fluence is due to the ion impact which produces more damages at higher fluence. The average particle size of the pristine and the irradiated fullerene C_{70} thin film with fluences 3×10^{12} and 3×10^{13} ions/cm^2 has been approximated to be ~ 40 nm, ~ 63 nm and ~ 67 nm respectively (table 4.5).

Table 4.5 Band gap, the average particle size (calculated with SEM and AFM analysis) and roughness of fullerene C_{70} pristine and irradiated at different fluences of 90 MeV Ni ion.

Fluence (ions/cm^2)	Bandgap (eV) *UV-visible Absorption Analysis*	Average Particle size (nm) *SEM Analysis*	Average Particle size (nm) *AFM Analysis*	Roughness (nm) *AFM Analysis*
Pristine	1.87	40	39	1.98
1×10^{12}	1.83	47	--	--
3×10^{12}	1.80	--	63	3.49
6×10^{12}	--	48	--	--
1×10^{13}	--	57	--	--
3×10^{13}	--	--	67	3.88

An increase in particle size has been observed with increasing fluence, which is in agreement with SEM results. It has also been found from the table 4.5 that the particle size and the roughness of the films increase monotonically.

4.2.2.4 C_{70} thin film irradiated by 125 MeV Au ion beam:

4.2.2.4.1 UV- visible absorption spectroscopy:

Figure 4.28 shows the absorption spectra of pristine and irradiated fullerene C_{70} thin films with 125 MeV Au ions at different fluences.
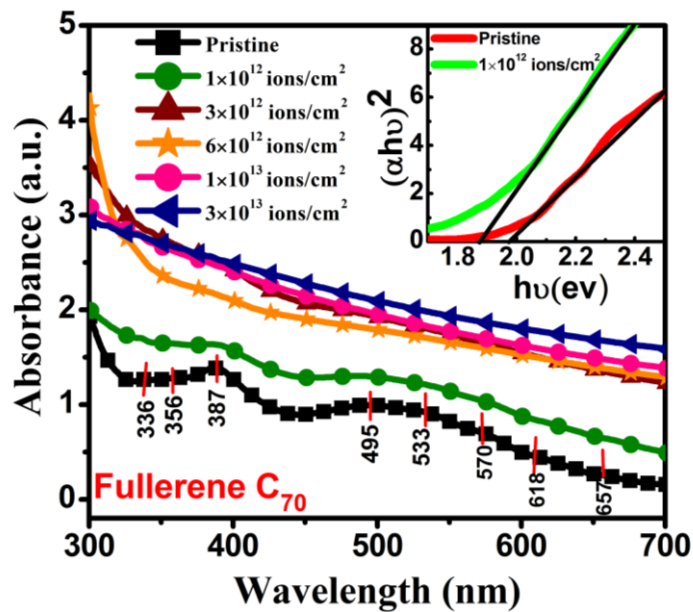
Figure 4.28 UV-visible absorption spectra of pristine and irradiated fullerene C_{70} thin films. Inset shows Tauc's plot of pristine and irradiated films.

Pristine fullerene C_{70} spectra exhibit a number of peaks. The highest peak is observed at 387 nm which is followed by two weak peaks at 356 and 336 nm. Since fullerene C_{70} has complex structure (followed by lower symmetry) [1], it is difficult to assign exact transitions. Some peaks are assigned from literature. Figure 4.28 depicts the

effect of SHI irradiation which clearly shows the increasing absorption and diminishing intensity of absorbance with increasing ion fluence. From inset in figure 4.28 the optical band gap of films are found to be 1.97 eV and 1.87 eV for pristine and irradiated fullerene C_{70} film at 1×10^{12} ions/cm^2, respectively.

4.2.2.4.2 Raman analysis:

Raman spectra demonstrated that the intensity of peaks is diminishing with an increase in fluence because of interaction of ion beam which tends to cause breakage in fullerene molecules. This confirms the transformation of fullerene C_{70} into amorphous carbon as usual at higher fluences and no shifting of peaks is the evidence of absence of intermediate fragmentation of C_{70} molecules under ion irradiation by 125 MeV Au ion beam.
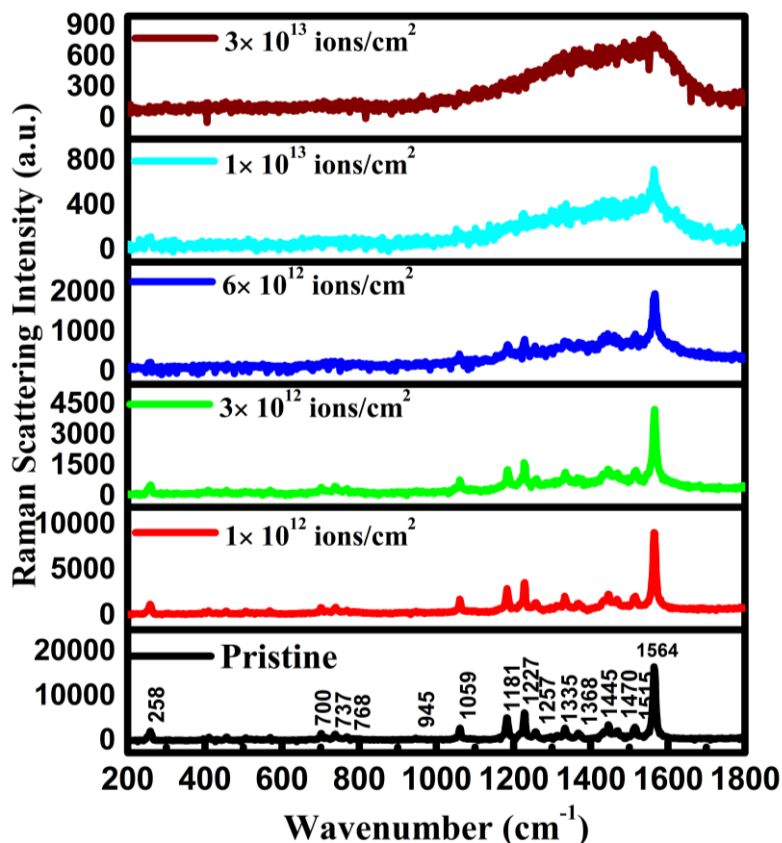
Figure 4.29 Raman spectra of pristine and 125 MeV Au ion irradiated C_{70} thin films

In figure 4.30, the most intense peak (1564 cm^{-1}) of pristine C_{70} is selected to see the kinetics of damage with fluence, which is vanished after fluence of 6×10^{12} ions/cm^2.
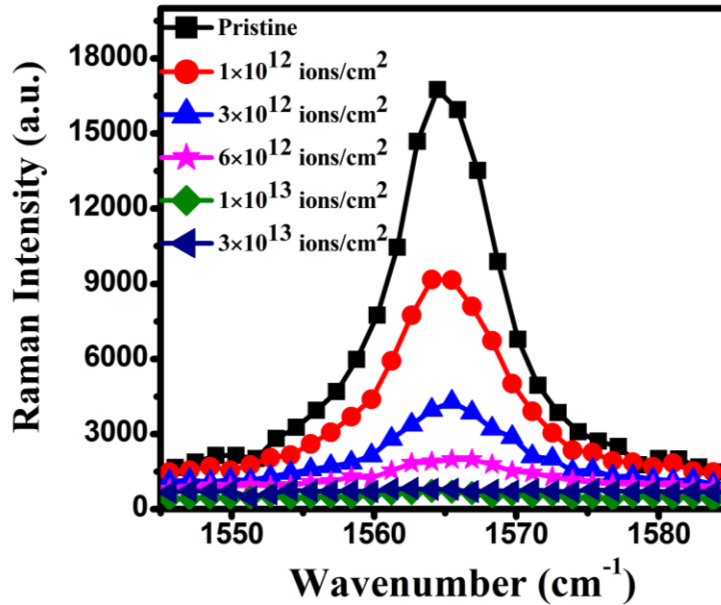
Figure 4.30 Irradiation-induced damage of the most intense Raman mode of pristine C_{70} thin film irradiated with 125 MeV Au ions at different fluences.

However, the broad peaks at 1350 cm^{-1} and 1550 cm^{-1} correspond to D and G bands of amorphous carbon The damage cross-section (track formation) of fullerene C_{70} molecules was estimated by following the previous method (section *4.2.3.1.1*).
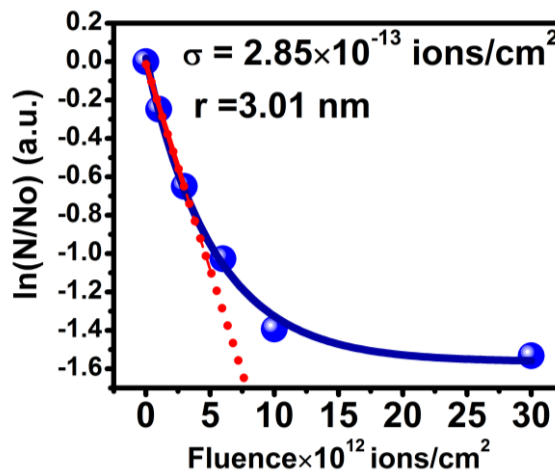
Figure 4.31 Curve between normalized integral area at different fluences of 125 MeV Au ion.

The value of damage cross-section may be approximated to be 2.8×10^{-13} cm^2 with measured radius of ion track ~ 3.01 nm.

4.2.2.5 Ion track radius in fullerene C_{70} : Dependence of electronic energy loss

Till now, it has been reported that fullerene C_{70} thins films (~150 nm thick) prepared by thermal deposition technique are irradiated with different ions (Au, Ni, Si) having different energies in order to vary the electronic energy loss (S_e). These

samples are irradiated within the fixed range of fluence i.e. 1×10^{12} ions/cm^2 to 3×10^{13} ions/cm^2 for each of energetic ion beam. Following technique described elsewhere (ref), the damage cross sections due to ion beam irradiation of different energies viz., 90 MeV Si, 55 MeV Si, 90 MeV Ni and 125 MeV Au are determined with the aid of Raman spectroscopy. The electronic energy loss (S_e) due to each irradiation and the corresponding damage cross section (σ) are mapped to obtain gainful information about the potential damage cross section for any arbitrary electronic energy loss. Additionally, radius (r) of ion track may be approximated for any S_e value.

4.2.2.5.1 Raman analysis:

As mentioned in the previous paragraph, the damage cross sections (σ) due to different ion beam irradiation of different energetic ions viz. 90 MeV Si, 55 MeV Si, 90 MeV Ni and 125 MeV Au causing different electronic energy losses (226 eV/Å, 274 eV/Å, 672 eV/Å and 1393 eV/Å respectively) are determined with the help of results from Raman spectroscopy and then ion track is calculated.
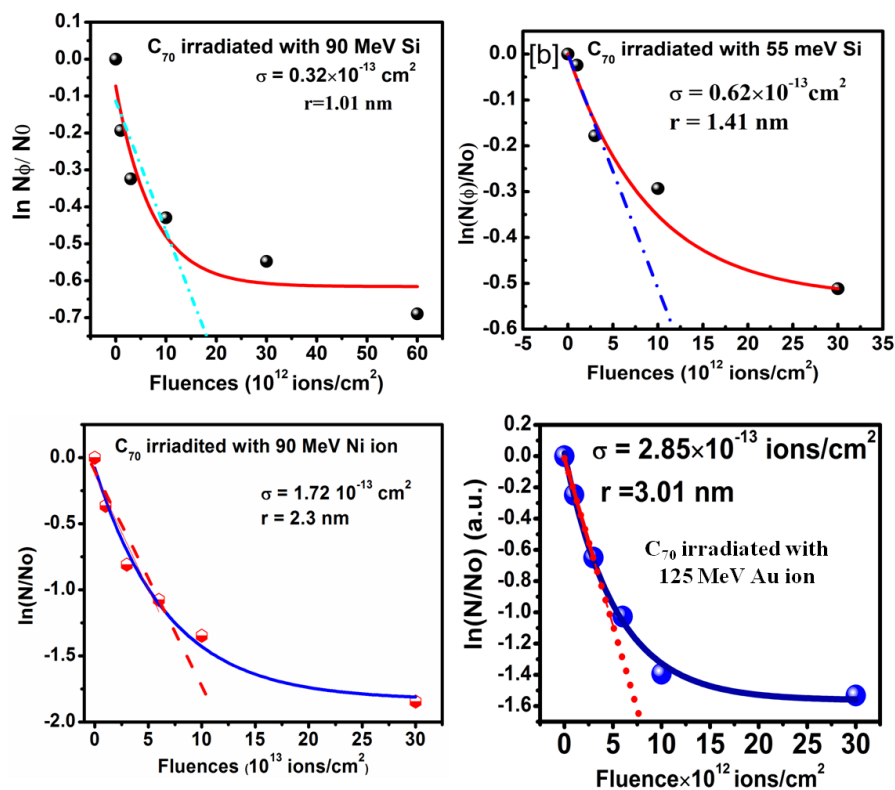
Figure 4.32 Curve between normalized integral area at different fluences of (a) 90 MeV Si ion (b) 55 MeV Si ion, (c) 90 MeV Ni ion and (d) 125 MeV Au ion irradiated C_{70} thin films.

Figure 4.32 shows the values of damage cross-sections against the corresponding electronic energy loss (S_e); this helps to give a qualitative picture of the value of

obtainable damage cross section for an arbitrary value of electronic energy loss value. The conjecture advocated here differs conceptually from the proposition of Bajwa et al. [11]. Admittedly, the electronic energy loss as determined by the common technique of use of SRIM may be varied for the same ion of different energies and accordingly a relationship with corresponding damage cross section (σ) could be developed. It is to be noted that electronic energy loss manifests in determining the damage cross section in the fullerene thin films.

The electronic energy loss can be varied by i) using same type of ions of different energies, ii) varying the fluence value for a specific ion beam with a definite energy, iii) using different types of ions iv) material under irradiation. In the instant case, the approach is slightly different from the previous one. It is hypothesized that damage cross section of a fullerene is solely dependent upon the electronic energy loss notwithstanding the quality of ions bringing about such loss
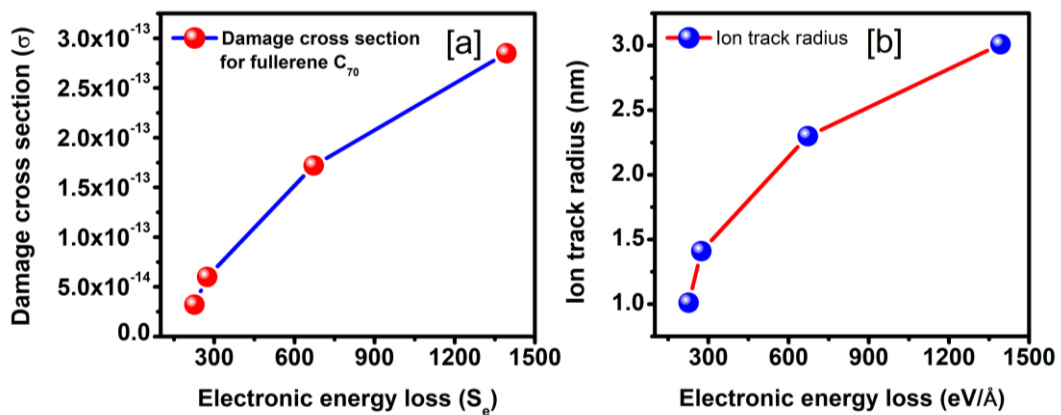
Figure 4.33 (a) Curve between electronic energy loss (S_e) and damage cross section (b) Curve between electronic energy loss (S_e) and ion track radius.

Moreover, there is no data available for the response of C_{70} fullerene to irradiation by an ion beam which can relate the damage cross section with the electron energy loss. The curve drawn in figure 4.33(a) is unique in the sense that it can be made quite helpful to estimate the damage cross section in fullerene C_{70} for any electronic energy loss. Thus, increasing value of S_e (226 eV/Å, 274 eV/Å, 672 eV/Å and 1393 eV/Å) results in increased value of damage cross section (Table 4.6) and hence an increasing radius of ion track (figure 4.32- b) is noted from 1nm to 3nm. It may be noted that due to experimental limitation the number of data points are rather small in the present experimentation and there is a chance of higher degree of misfit with the real-life data for certain intermittent electron energy loss not covered under the present experimental results; nevertheless, the approach has the novelty that it makes use of

different types of ions of different energies and hence bears the scope of yielding a globally optimized relationship between the electronic energy loss and the damage cross section.

Table 4.6 Represents the parameters of different ion beam and calculated damage cross section and ion track radius for respective beam.

Swift Heavy Ion	S_n (eV/Å)	S_e (eV/Å)	Projected Range	σ (cm^2)	r (nm)
90 MeV Si	0.16	226	33.33μm	0.32×10^{-13}	1.01
55 MeV Si	0.25	274	19.25μm	0.60×10^{-13}	1.41
90 MeV Ni	1.14	672	19.05μm	1.72×10^{-13}	2.30
125 MeV Au	15.73	1393	16.98μm	2.85×10^{-13}	3.01

From the results in figure 4.33 it is observed that increasing electronic energy loss leads a consistent increase in damage cross section and in this regard the results are in qualitative agreement with those reported earlier for C_{60} fullerene [11]; this tends to indicate that the difference in bonding and or stability between the two important fullerenes, C_{70} and C_{60} does not alter the quality of relationship between electronic energy loss and damage cross section although there is a genuine quantitative variation. This has the implication that phenomenological aspects determining the damage cross sections in irradiated fullerene are identical at least in C_{70} and C_{60}.

4. 3 Conclusions:

A comprehensive study of fullerene C_{60} from polymerization to amorphization by 90 MeV Ni ions is demonstrated. The Raman studies reveal that a new mode of spectra appears in the lower fluence range which is suggestive of polymerization of C_{60} fullerene whereas at higher fluence the disappearance of peaks verifies the transformation of fullerene to a-C due to overlapping of ion tracks. The radius of the ion track is calculated to be ~ 3.03 nm. The UV-visible absorbance peaks intensity declines with fluence. Also, the optical band gap decreases with increase in fluence. The increase in conductivity of the fullerene at higher fluence confirms the transformation of fullerene into a-C (a-C is more conducting than fullerene).

C_{70} thin films are grown on different substrates by resistive heating method. Ion track has been formed by irradiating the thin films with different energy ion 90 MeV Si, 55 MeV Si, 90 MeV Ni and 125 MeV Au causing different electronic energy losses (226 eV/Å, 274 eV/Å, 672 eV/Å and 1393 eV/Å respectively). UV-visible absorption

spectroscopy results lead one to infer that the absorption bands declines with increasing fluences. In addition, the author also concludes that the band gap values decrease with increase in fluence. The author infers that agglomeration of the smaller particles takes place due to irradiation of fullerene C_{70} thin films. The damage cross section and radius of the track is determined with the help of Raman spectroscopy. Singhal et al. [23] have reported the effective radius r of ion track for damage of fullerene molecules to be 3.5 nm for C_{60} and 2.5 nm for C_{70} upon irradiation by 120 MeV Ag ion. On the same line, irradiating with 90 MeV Ni ion beam, ion track radius is estimated to be ~ 3.03 nm for C_{60} and ~2.30 nm for C_{70}. These studies confirm the effect of molecular and inter-molecular configurations of the interacting fullerenes on the damage caused by the incoming ion. It can be seen from the results of the present study that increasing Se leads to an increase in damage cross section and the radius of ion track. On comparison of the results of present investigation for C_{60} with that observed by Singhal et.al. [23] a very good consistency is noted. Similar correspondence could be observed for C_{70} too. It is concluded that there is a defined relationship between electronic energy loss and damage cross section and that the potential of the relationship may be harnessed to understand an unknown situation. This will enable ion track engineering for production of nanowires with least number of trials.The relation is phenomenologically identical in both C_{60} and C_{70}.

REFERENCES

[1] C. Talbot, Fullerene and nanotube chemistry: an update, *School Science Review*, 81(1999) 37-48.

[2] D.K. Avasthi, Y.K. Mishra, R. Singhal, D. Kabiraj, S. Mohapatra, B. Mohanta, N.K. Gohil and N. Singh, Synthesis of Plasmonic Nanocomposites for Diverse Applications, *Journal of Nanoscience and Nanotechnology*,10 (2010) 2705–2712.

[3] R. Singhal, J.C. Pivin and D.K. Avasthi, Ion beam irradiation-induced tuning of SPR of Au nanoparticles in fullerene C_{70} matrix: dependence of energy loss, *J Nanopart Res*, 15 (2013) 1641.

[4] R. Singhal, J.C. Pivin, R. Chandra, D.K. Avasthi, Ion irradiation studies of silver/amorphous carbon nanocomposite thin film, *Surface & Coatings Technology*, 229 (2013) 50-54.

[5] R. Singhal, D.C. Agarwal, Y.K. Mishra, D. Kabiraj, G. Mattei, J.C. Pivin, R. Chandra and D.K. Avasthi, Synthesis, characterizations, and thermal induced structural transformation of silver fullerene C_{60} nanocomposite thin films for applications in optical devices, *J. Appl. Physics*, 107 (2010) 103504.

[6] R. Singhal, D. Kabiraj, P.K. Kulriya, J.C. Pivin, R. Chandra and D.K. Avasthi, Blue-Shifted SPR of Au Nanoparticles with Ordering of Carbon by Dense Ionization and Thermal Treatment, *Plasmonics*, 8 (2013) 295-305.

[7] A. Kumar, D.K. Avasthi, A. Tripathi, D. Kabiraj, F. Singh and J.C. Pivin, Synthesis of confined electrically conducting carbon nanowires by heavy ion irradiation of fullerene thin film, *J. Appl. Physics,* 101 (2007) 014308.

[8] N. Bajwa, A. Ingale, D.K. Avasthi, R. Kumar, K. Dharamvir and V.K. Jindal, Substrate effect on structural modification of C_{60} induced by 110 MeV Ni ion, *Nucl. Instrum. Methods Phys. Res. B*, 212 (2003) 233-237.

[9] D.K. Avasthi, A. Kumar, R. Singhal, A. Tripathi and D.S. Misra, Studies on carbon nanotubes and fullerenes under extreme conditions, *J. Nanosci. Nanotechnology*, 10 (2010) 3767-3779.

[10] S. Lotha, A. Ingale, D.K. Avasthi, V.K. Mittal, S. Mishra, K.C. Rustagi A. Gupta, V.N. Kulkarni and D.T. Khathing, Effect of heavy ion irradiation on C_{60}, *Solid State Communications*,111 (1999) 55-60.

[11] N. Bajwa, A. Ingale, D.K. Avasthi, R. Kumar, A. Tripathi, K. Dharamvir and V.K. Jindal, Role of electron energy loss in modification of C_{60} thin films by swift heavy ions, *J. Appl. Physics*, 104 (2008) 054306.

[12] Y. Maeyoshi , A. Saeki, S. Suwa , M. Omichi , H. Marui , A. Asano , S. Tsukuda , M. Sugimoto , A. Kishimura , K. Kataoka and S. Seki, Fullerene nanowires as a versatile platform for organic electronics, *Scientific Reports*, 2 (2012) 1-6.

[13] H. Kumar, Y.K. Mishra, S. Mohapatra, D. Kabiraj, J.C. Pivin, S. Ghosh and D.K. Avasthi, Compositional analysis of atom beam co-sputtered metal–silica nanocomposites by Rutherford backscattering spectrometry, *Nucl. Instr. and Meth. in Phys. Res. B*, 266 (2008) 1511-1516.

[14] L.R. Doolittle, Algorithms for the rapid simulation of Rutherford backscattering spectra, *Nucl. Instr. and Meth. in Phys. Res. B*, 9 (1985) 344-351.

[15] J. Kastner, H. Kuzmany, L. Palmetshofer, Damage and polymerization by ion bombardment of C_{60}, *Appl. Phys. Letter*, 65 (1994) 543-545.

[16] J. Mort, R. Ziolo, M. Machonkin, D.R. Huffman and M.I. Ferguson, Electrical conductivity studies of undoped solid films of $C_{60/70}$, Chemical Physics Letters, 186(1991) 284-286.

[17] A.F. Hebard, M.J. Rosseinsky, R.C. Haddon, D.W. Murphy, S.H. Glarum, T.T.M. Palstra, A.P. Ramirez and A.R. Kortan, Superconductivity at 18 K in potassium-doped C_{60}, *Nature*, 350(1991) 600.

[18] N. Bajwa, K. Dharamvir and V.K. Jindal, A. Ingale, D.K. Avasthi, R. Kumar, A.Tripathi, Swift heavy ion induced modification of C_{60} thin films, *J. Appl. Physics*, 94 (2003) 326.

[19] D.K. Avasthi, Effects and uses of ion beams with diamond, DLC and fullerene films, *Vacuum*, 47 (1996) 1249-1258.

[20] A. Kumar, F. Singh, D.K. Avasthi and J.C. Pivin, Infrared studies of swift heavy ion irradiated C_{60} thin films, *Nuclear Instruments and Methods in Physics Research B*, 244 (2006) 221–224.

[21] M.S. Dresselhaus, G. Dresselhaus and R. Satio, Carbon fibers based on C_{60} and their symmetry, *Phys. Rev. B*, 45 (1992) 6234-6242.

[22] R.A. Jishi, R.M. Mirie, M.S. Dresselhaus, G. Dresselhaus, P.C. Eklund, Phys. Rev.B 48 (1993) 5634-5642

[23] R. Singhal, F. Singh, A. Tripathi and D. K. Avasthi, A comparative study of ion-induced damages in C_{60} and C_{70} fullerenes, *Radiation Effects & Defects in Solids,* 164 (2009) 38-48.

[24] R. Singhal, A. Kumar, Y.K. Mishra, S. Mohapatra, J.C. Pivin and D.K. Avasthi, Swift heavy ion induced modifications of fullerene C_{70} thin films, *Nuclear Instruments and Methods in Physics Research B,* 266 (2008) 3257–3262.

[25] D.K. Avasthi and G.K. Mehta, Swift heavy ions for materials engineering and nanostructuring, Springer Science & Business Media, Springer-Netherland, (2011) ISBN 978-94-007-1229-4.

[26] S.K. Srivastava, D.K. Avasthi, W. Assmann, Z.G.Wang, H. Kucal, E. Jacquet, H.D. Carstanjen and M. Toulemonde, Test of the hypothesis of transient molten state diffusion for swift-heavy-ion induced mixing, *Phys. Rev. B*, 71 (2005) 193405.

[27] U.B. Singh, R.P. Yadav, R.K. Pandey, D.C. Agarwal, C. Pannu and A.K. Mittal, Insight mechanisms of surface structuring and wettability of ion-treated Ag thin films, *J. Phys. Chem. C*, 120 (2016) 5755-5763.

[28] U.B. Singh, D.C. Agarwal, S.A. Khan, M. Kumar, A. Tripathi, R. Singhal, B.K. Panigrahi and D.K. Avasthi, Engineering of hydrophilic and plasmonic properties of Ag thin film by atom beam irradiation, *Appl. Surf. Science*, 258 (2011) 1464-1469.

[29] Y. Zhou, B. Wang, X. Song, E. Li, G. Li and S. Zhao, Control over the wettability of amorphous carbon films in a large range from hydrophilicity to super-hydrophobicity, *Appl. Surf. Science*, 253 (2006) 2690-2694.

[30] G.B.V.S. Lakshmi and D.K. Avasthi, Tuning of wettability of PANI-GNP composites using keV energy ions, *Nuclear Instruments and Methods in Physics Research B*, 379 (2016) 152-155

Chapter 5

Study the Effect of Low and High Energy Ion Beam Irradiation on Copper-Fullerene C$_{60}$ Nanocomposite Thin Films

5.1 Effect of Low Energy Ion Beam Irradiation on Copper-Fullerene C$_{60}$ Nanocomposite Thin Films

It is known that enhancement of surface plasmon resonance (SPR) is an exciting research question to address [1-4]. It is possible to induce SPR if noble metal nanoparticles (Au, Ag and Cu) are embedded in a suitable matrix [5-7]. Exploration of the use of noble metal particles embedded in the matrix materials in the fields of sensors, optical waveguides, photonic devices and surface enhanced spectroscopes are reported elsewhere [8-10]. Most noble metal clusters are characterized by a SPR band lying in the visible region.

Fullerene has been widely chosen as a host matrix for metal reinforced nanocomposites because of its diverse applications such as in solar cells due to its high electron affinity property, fullerene based inters digitated (IDCs) circuits and molecular wires based on its electron accepting property [11-14]. Fullerene material is considered as a good acceptor material in organic solar cells which is due primarily to its high electron affinity. In general, P3HT as donor material is used with fullerenes in active layer of organic solar cells. Implicitly, broad absorption band of active layer materials is a necessity for the effective utilization of sunlight and hence it is the challenge to material scientists to discover means for increasing the absorption band of the suitable active material [15]. Research on induced SPR in fullerene metal nanocomposite has already been reported by early workers [16-18]. Singhal et al. [19-20] have elegantly demonstrated the usefulness of inducing SPR by incorporating nanoparticles of noble metals (Au, Ag) in fullerene C$_{60}$ and C$_{70}$ matrices.

A number of means to enhance the magnitude and tune the position of SPR are reported to be varying atomic fraction of nanoparticles to embed, annealing temperature of thin film, alteration of refractive index of matrix material and also chemical composition of the thin films [21-25]. Recently heavy ion irradiation has also emerged as means to enhance and tune SPR spectra of fullerene noble metal nanocomposites. The energies of irradiating ions and the fluence of irradiation bring about changes in position of SPR band (tuning).

5.1.1 Effect of 100 keV Ag Ion Irradiation on SPR of Cu-C$_{60}$ Nanocomposite Thin Film

The present study is to induce SPR in such a way that most of visible region can be utilized for further use in optoelectronic applications especially for organic solar cell. To achieve this, nanoparticles of group 11 elements viz. Cu and Ag with respective SPR peak positions within ~ 410 – 450 nm and ~ 550 - 600 nm [26] are chosen such that a wide area of visible region can be covered. Fullerene C$_{60}$ being an excellent electron acceptor is a natural choice as the major constituent of matrix material for fabrication of organic solar cells. Cu nanoparticles are known to exhibit a relatively weak SPR band in the range of ~550 - 600 nm. In contrast, SPR peaks due to Ag and Au occur reportedly within occur 410 - 450 nm and 500-550 nm, respectively. It therefore appears that implantation of Ag ion (whose SPR peak lies at the lowest wavelength among these three elements) in Cu-C$_{60}$ nanocomposite would have a wide coverage within the visible band for SPR to take place. Thus the present approach of exploring synergistic SPR in C$_{60}$nancomposites with binary and ternary reinforcement of nanoparticles of group 11 elements appears to open a new vista in plasmonic research. In the present study, a methodology has been so evolved that Cu-C$_{60}$ film will be irradiated concurrently with implantation of Ag nanoparticles in SiO$_2$ substrate. Therefore we have chosen 100 keV Ag ion beam which gives ~ 61.4 nm of projected range. The motivation with this is two-folded; one is to induce SPR due to Cu nanoparticles in fullerene C$_{60}$ thin film and second is to implant Ag nanoparticles in SiO$_2$ substrate so that combined SPR effect due to Cu as well as Ag nanoparticles in the same sample can be achieved.

5.1.1.1 Experimental Details:

In this synthesis, fullerene C$_{60}$ powder was taken in one boat and in another boat copper C$_{60}$ powder has been taken. Before starting deposition, vacuum is kept at ~ 6.2×10^{-6} mbar and maintained at ~ 5.7×10^{-6} mbar during deposition. To obtain 20% copper in fullerene C$_{60}$ thin films, the deposition rate were set in such a way that fullerene is deposited four times than copper. The deposition rates were set at ~ 0.025 Å/s and ~ 0.1 Å/s for copper and C$_{60}$, respectively. Combined rate for deposition of Cu and fullerene C$_{60}$ simultaneously is taken about ~ 0.13Å/s. The thickness measured through the quartz crystal was 40 nm. Rutherford backscattering was performed to determine the metal to fullerene C$_{60}$ ratio in the films and thickness of

the film as well; it is that there has been ~13 % of copper in fullerene C_{60} and thickness of the film is about ~28 nm.

The deposited nanocomposite thin films in section 3.3.2.1, $Cu(13\%)C_{60}$ were irradiated with 100 keV Ag ion beam in IUAC, New Delhi with fluence 1×10^{14}, 1×10^{15}, 1×10^{16} and 3×10^{16} ions/cm^2. For 100 keV Ag ions, the electronic (S_e) and nuclear (S_n) energy losses as calculated by the SRIM (The Stopping and Range of Ions in Matter) program in nanocomposites film of Cu (13%) C_{60} are ~ 42 and ~1.5×10^2 eV/Å, respectively. The projected range of Ag ions in the respective films was found to be ~ 61.4 nm by the same software.

TRIM simulation has been done in order to see the energy loss and vacancies produced by the 100 keV Ag ion in $Cu-C_{60}$ nanocomposite thin films. Figure 5.1 (a) represents the curve between the energy loss and thickness of the film. From the figure it is seen that loss of energy of ions is more at the surface and decreases slowly with increase in thickness of the thin films. Figure 5.1(b) shows the vacancies per angstrom with thin film depth. The number of vacancies increased with target depth and the maximum vacancies are observed around 450 Å i.e. in the SiO_2 layer.
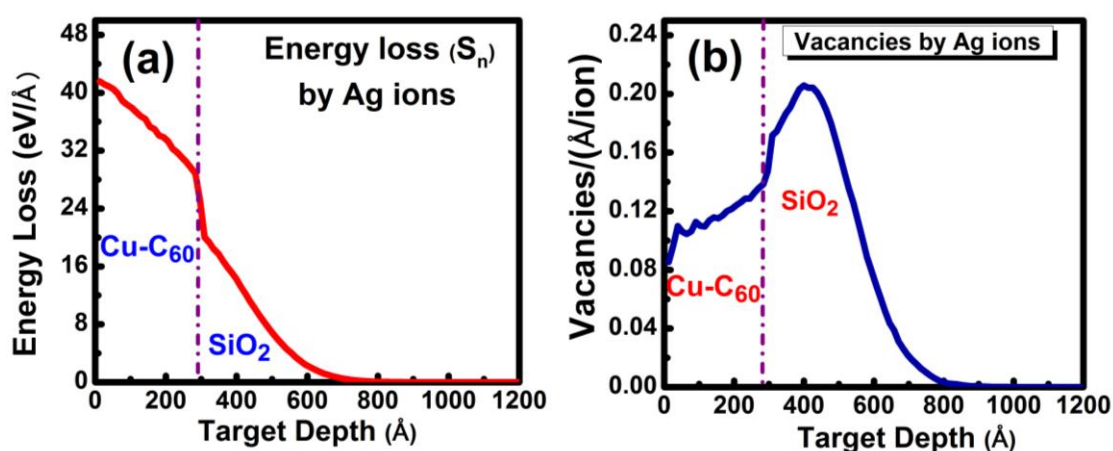
Figure 5.1 Simulation of 100 keV Ag ion in $Cu-C_{60}$ nanocomposite film on SiO_2 substrate (a) Defect production by incoming ions; (b) Vacancies produced per angstrom in the entire thickness of the film..

UV-visible absorption spectra of pristine and irradiated films of $Cu-C_{60}$ on the glass substrates were recorded using a UV-3300 Hitachi spectrometer. TEM images of pristine and irradiated with 3×10^{16} ions/cm^2 fluence films of $Cu-C_{60}$ nanocomposite deposited on carbon coated Cu grids were captured using a Tecnai G^2 20 (FEI) S-Twin TEM. Raman spectra of pristine and irradiated films of $Cu-C_{60}$ nanocomposite on the glass substrates were recorded using an AIRIX STR 500 by following the

procedure as described in section 3. XPS data has been recorded with Omicron nanotechnology XPS system from Oxford instruments (model- ESCA+) consisting of an ultra-high vacuum chamber attached with a monochromatic Al-Kα radiation source of energy 1486.7 eV and a 124 mm hemispherical electron analyzer.

5.1.1.2 Result and Discussion:

5.1.1.2.1 RBS analysis:

To determine the exact film thickness, atomic species and their concentration Rutherford backscattering (RBS) spectrometry was used using a 2.0 MeV He^{++} beam. To cross verify the film thickness determined by RBS technique, AFM or profilometer could also be used. However, the author feels that RBS technique can yield most accurate value of film thickness. That is collaborated by previous reports. A typical RBS spectrum of a Cu-C_{60} nanocomposite pristine sample on Si substrate along with Rutherford Universal Manipulation Program (RUMP) simulated spectrum (continuous line) is shown in figure 5.2.
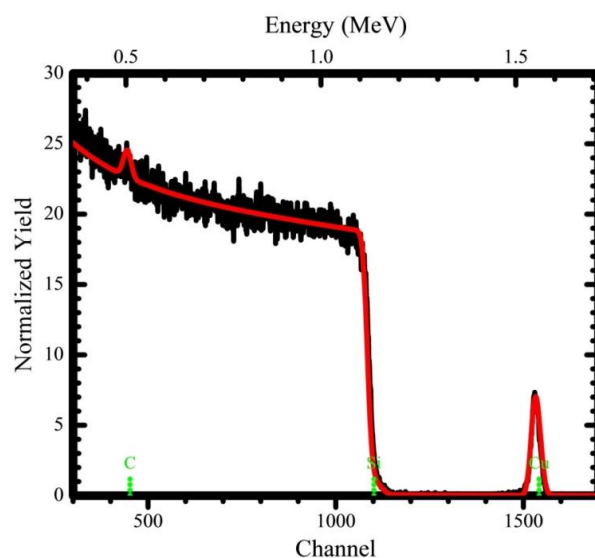
Figure 5.2 RUMP simulated (continuous line), Rutherford backscattering spectrum of Cu-C_{60} nanocomposite film on Si substrate.

The plateau region in spectrum represents the Si substrate which is overridden by the C hump. The film thickness, estimated by RUMP simulation was found to be ~ 28 nm with ~ 13 at.% Cu composition in fullerene C_{60}.

5.1.1.2.2 Raman analysis:

Figure 5.3 shows the Raman spectrum of pristine and 100 keV Ag ion irradiated thin films characteristic peaks of fullerene C_{60} are observed in pristine sample (Cu-C_{60}) at wave numbers of 265, 493, 1423, 1467 cm^{-1}. These modes are consistent with

previous reports on UV-visible absorption modes of fullerene C_{60} [27]. From Raman spectroscopy study, it is observed that as the fluence increases, the intensity of the modes is diminished and finally they can no more be resolved. From this, it is confirmed that the fullerene C_{60} in Cu-C_{60} nanocomposite thin film is converted into a-C beyond certain fluence. This is in accordance with the previously reported results of converting fullerene into amorphous carbon on irradiation [17, 28]. Hence refractive index of the film has also been reduced to that of amorphous carbon, ~1.6, which is lower than pure fullerene C_{60} (~ 2.1) [17].

This change in refractive index is further responsible of shift in SPR wavelength position.
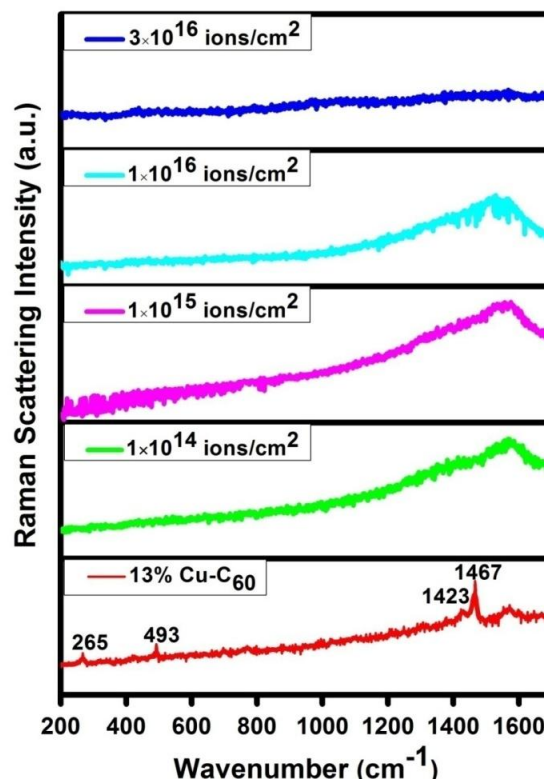
Figure 5.3 Raman spectra of pristine and 100 keV Ag ion irradiated Cu-C_{60} nanocomposite thin films.

5.1.1.2.3 UV-visible absorption spectroscopy analysis:

Figure 5.4 shows UV- visible absorption spectra of Cu-C_{60} nanocomposites pristine and 100 keV Ag ion irradiated thin films. It appears from the figure 5.4 (a) that the pristine Cu-C_{60} thin film is amorphized which is not the case. In order to do away with this apparent anomaly, the optical spectrum of pristine Cu(13%)C_{60} has been separately shown; this authenticates the crystallinity of C_{60} thin film as the characteristic optical bands are present in the nanocomposite thin film where Cu

nanoparticles are incorporated in fullerene C_{60} thin film, Moreover, the high concentration of copper has led to much stronger absorption peak and in comparison, the concerned absorption peak is such weak that it is masked in figure 5.4 (a); once drawn differently in a separate scale the due peaks are revealed figure 5.4 (c).
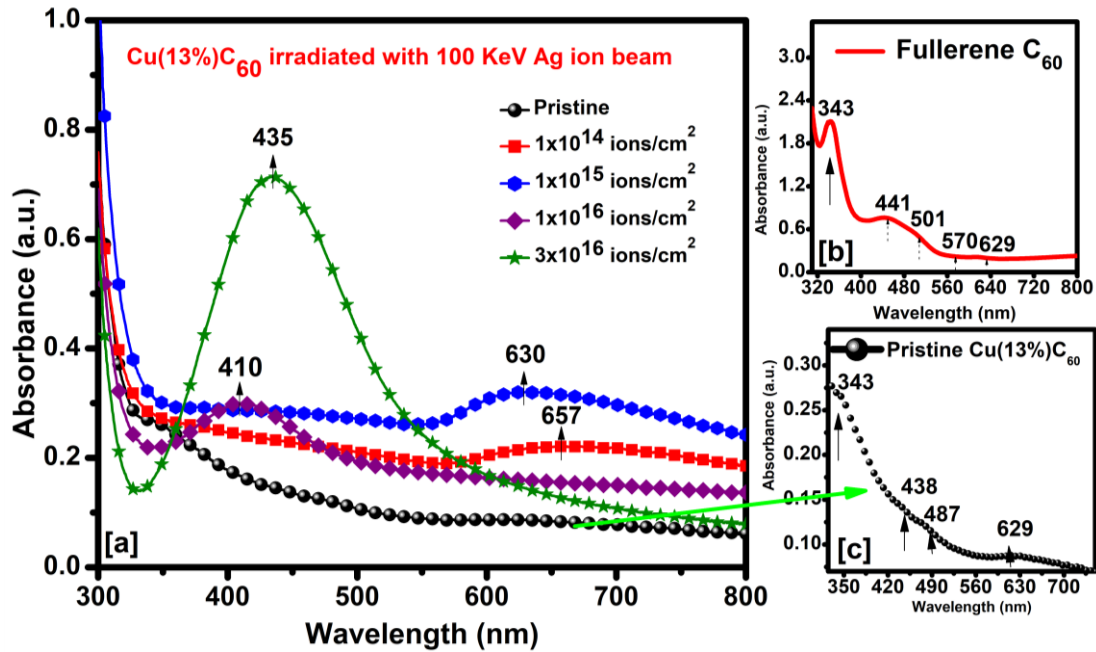
Figure 5.4 UV-visible absorption spectra of pristine and 100 keV Ag ion irradiated Cu-C_{60} nanocomposite thin films (b) UV-visible absorption spectrum of fullerene C_{60} thin film (c) UV-visible absorption spectrum of Cu(13%)C_{60} thin film.

From the figure, it is clear that in pristine Cu-C_{60} nanocomposite, there is no evidence for a characteristic SPR band for copper. This is explained on the basis that the particle size of copper is very small in pristine sample. Upon irradiation, Cu nanoparticles starts to increase in size and a weak SPR band arises at ~667 nm for the fluence 1×10^{14} ions/cm^2. The SPR peak for Cu nanocomposites are reported to be ~570 nm [29], the observed shift in SPR peak may be explained by the matrix effect. With further increase in fluence, the same band becomes narrow (~ 630 nm) with a blue shift of ~ 20 nm. This blue shifting in SPR peak may be due to a change in refractive index of fullerene C_{60} matrix [30], as explained by Raman spectroscopy analysis which shows there fullerene C_{60} starts converting into amorphous carbon at the fluence, 1×10^{14} ions/cm^2

The energy position of the SPR peak can be predicted by using the following equation of Mie theory [31]. As per Mie theory, extinction cross-section coefficient (σ_{ext}) for

spherical particles is enough low, such that they don't polarize each other; it is expressed by the equation

$$\sigma_{ext} = 9\frac{\omega}{c}\varepsilon_m^{3/2}V_o\left[\frac{\varepsilon_2(\omega)}{\{\varepsilon_1(\omega)+2\varepsilon_m\}^2+\varepsilon_2^{\ 2}(\omega)}\right] \quad (5.1)$$

Where, V_o is the volume fraction and ω is the applied optical frequency. $\varepsilon(\omega) = \varepsilon_1(\omega) + i\epsilon_2(\omega)$ is the dielectric constant of metal and $\varepsilon_m(\omega)$, dielectric constant of embedding matrix.

In the present study fullerene is the host matrix, which has complex dielectric constant given by

$$\epsilon_m = \epsilon_m' - j\epsilon_m'' \quad (5.2)$$

Where ϵ_m' is real part and ϵ_m'' is imaginary part of dielectric constant of fullerene. According Kataura's optical data, imaginary part of the dielectric constant in the visible and near IR region is related to the absorption. So it is very important to consider this; it however, makes the calculation for dielectric constant very complex. But the complex part approaches to zero for the wavelength range above 420 nm. Hence, in the present case, the imaginary part has negligible influence on the absorption in the visible and IR region. So this imaginary is neglected and the dielectric constant is taken to result from the real part only.

Now, the complex dielectric function of metal can be expressed by Drude free carrier contribution for $(\omega\tau \gg 1)$ and an interband contribution:

$$\varepsilon(\omega) = 1 - \frac{\omega_p^2}{\omega^2} + i\frac{\omega_p^2}{\omega^2\tau} + \varepsilon_{inter} \quad (5.3)$$

Where ω_p is Drude bulk plasma frequency which is given by $\omega_p = \sqrt{\dfrac{ne^2}{\varepsilon_o m_e}}$, n = free electron density of metal, e is electronic charge, m_e is the mass of e and ε_{inter} denotes interband transition term

With the replacement, $\omega = \dfrac{2\pi c}{\lambda}$, it follows

$$\varepsilon_1(\lambda) = 1 + \varepsilon_{inter} - \frac{\omega_p^2}{4\pi^2 c^2}\lambda^2 \quad (5.4)$$

$$\varepsilon_2(\lambda) = \frac{\omega_p^2}{8\pi^3 c^3 \tau}\lambda^3 \qquad (5.5)$$

Here λ is the free space wavelength of light. From the above expression $\varepsilon_1(\lambda)$ is seen to vary linearly with λ^2, and the same occurs for $\varepsilon_2(\lambda)/\lambda$. Here $\varepsilon_2(\lambda)$ has dependency on relaxation time (τ) hence it will rise with temperature as relaxation time is anticipated to decline with temperature.

From above discussion it seems that the SPR energy not only depends on the shape and size but also depends on the dielectric constant of the matrix. For the maximum value of the σ_{ext}, the denominator of equation (1) has to be minimum and this gives $\varepsilon_1(\omega) + 2\varepsilon_m = 0$; this is known as Frohlich condition which, when coupled with dipole mode presents its maximum.

By considering the Drude free electron term andabove condition, the resonance frequency is given:

$$\omega = \frac{\omega_p}{\sqrt{(1 + 2\varepsilon_m)}} \qquad (5.6)$$

The above equation clearly indicates that with the decrease of dielectric constant of host matrix (ε_m), the resonance frequency (ω) increases and so there is a blue shift in the UV-visible absorption studies.

Although the use of Mie theory explains the experimental observation quite satisfactorily, it is not out of context to mention that there are opinions which advocate that the use of Maxwell-Garnet theory in case of high metal concentration in a fullerene-based nanocomposite is a better proposition. It is anticipated that there could be optical interaction between metal nanoparticles when the concentration is quite high and the size is very small; this implies a high particle density and hence less interparticle distance. This may lead to intense optical interaction and can produce misleading information regarding the energy position. However, there was other experimental evidence that confirms that SPR of copper may not appear at its low concentration; however, it is felt that use of Maxwell-Garnet theory to compare with the existing prediction can be an interesting area of future study. Moreover, use of a lower copper concentration to develop SPR of copper to acceptable strength can also be a scientific challenge.

With further increase in fluence, a different SPR peak at ~ 410 nm is observed. This SPR peak is attributed to the peak of silver because its position is same as that of silver nanoparticles in SiO_2 matrix [28]. It is found that the appearance of the SPR peak of Ag in silica (in pristine nanocomposite) is slightly out of expected position (about 410 nm); but one cannot see the characteristic copper peak. However, in any case the Cu-related SPR should still be visible; it is surmised that it might have reinforced with other peaks probably due to the larger size of Cu nano particle radius at its high concentration. Moreover, as can be seen from the figure 5.4 (c), there is a wide band positioned at 629 nm and it is hard to say if it is due to fullerene itself or due to the presence of Cu nanoparticles in pristine sample, because the other bands of fullerene are still present. Therefore, the absence of copper peak in pristine is not a tenable proposition. Since SPR due to copper takes place between 550- 650 nm it is conjectured that copper peak in pristine is not visible in Fig. 5.4 because the scale in which the plots are drawn to delineate the strong Ag peak with a reasonable height has been such that it has not allowed the weaker copper peak in pristine to become visible. However, such invisibility does not preclude the real occurrence of copper related peak. This is supported by the fact that when irradiated, the SPR enhancement due to copper makes it clearly visible even amidst the much stronger Ag peak (figure 5.4). At fluence 3×10^{16} ions/cm^2, a wide and higher intensity SPR band arises at wavelength ~ 435 nm. A red shift of ~25 nm observed in SPR peak may be attributed to nucleation of silver particles within the substrate. Red shift in Ag- SPR peak confirms the presence of Ag particles in glass substrate which is further evidenced in TEM analysis.

This broad SPR band covers a wide visible region around 350 to 640 nm. This is the resultant of Ag SPR peaks riding over the copper SPR peak spectrum and finally, results in broad SPR spectrum within the visible region.

5.1.1.2.4 TEM Analysis:

To see the effect of low energy heavy ion irradiation on the morphology and crystallinity of the thin films, TEM and HRTEM studies are done for both pristine and 100 keV Ag ion irradiated samples for 3×10^{16} ions/cm^2 fluence. Figure 5.5 (A) and figure 5.6(A) show the bright field TEM images for the pristine and ion irradiated thin films with fluence 3×10^{16} ions/cm^2. Nearly spherical morphology of the particles is observed from the above photographs.
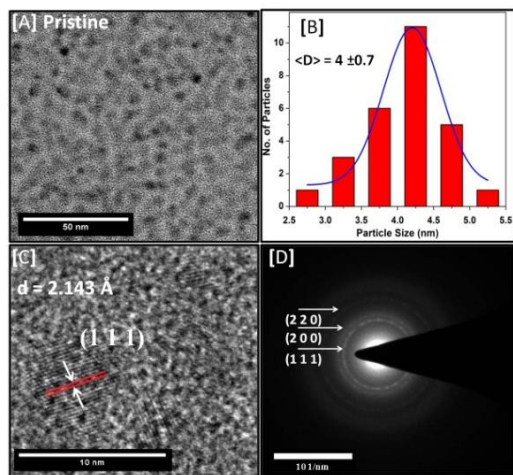
Figure 5.5 (A) TEM image, (B) particle size distribution, (C) HRTEM image and (D) SAED pattern of Cu-C$_{60}$ pristine thin film.
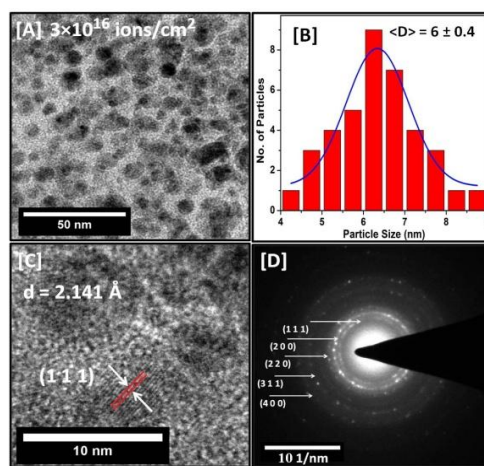
Figure 5.6 (A) TEM image, (B) particle size distribution, (C) HRTEM image and (D) SAED pattern of Cu-C$_{60}$ thin film irradiated at 3×10^{16} ions/cm^2 fluence.

The size distribution of the particles is shown in figure 5.5 (B) and figure 5.6(B) for pristine and ion irradiated thin films. A variation in particle distribution is observed with average particle size of 4±0.7 nm and 6±0.4 nm for pristine and ion irradiated thin films, respectively, as determined by the statistical analysis. The increase in particle size after irradiation is due to agglomeration of the particles [26,27,32]. The HRTEM image of the pristine and ion irradiated thin films are shown in figure 5.5 (C) and figure 5.6(C). The distance between the two adjacent lattice planes is calculated and found to be 2.143 Å, which corresponds to the value of interpanar distance of (111) plane of cubic copper. Moreover, the selected area electron diffraction (SAED) patterns shown in figure 5.5 (D) and figure 5.6(D) for the pristine and ion irradiated thin films corroborate the HRTEM results.

Table 5.1 Presents average particle size calculated by TEM, SEM and AFM analysis, respectively. Roughness is also tabulated calculated from AFM images.

Fluence (ions/cm^2)	Average Particle Size(nm) TEM Analysis	Average Grain Size(nm) SEM Analysis	Average Grain Size(nm) AFM Analysis	Roughness (nm)
Pristine	4±0.7	9±0.1	9±0.3	1.76
1×10^{15}	--	10±0.1	12±0.1	2.10
3×10^{16}	6±0.4	20±0.3	15±0.5	2.83

The lattice spacings calculated from SAED pattern are found to be 2.141 Å, 1.843 Å, 1.283 Å, 1.116 Å, 0.914 Å for (111), (200), (220), (311) and (400) planes of the cubic

phase of the copper. This confirms the presence of cubic phase of copper in pristine and ion irradiated thin films.

5.1.1.2.5 Surface analysis:

To study the effect of irradiation on surface morphology of Cu-C$_{60}$ nanocomposite thin film, atomic force microscopy has been performed. Figure 5.7 (a) shows 2D AFM image of pristine Cu-C$_{60}$ thin film and images of nanocomposite irradiated with 100 keV Ag ion beam at fluences 1×10^{15} ions/cm^2 and 3×10^{16} ions/cm^2 are shown in figure 5.7 (b) and (c), respectively.

Roughness and average grain size values calculated by AFM analysis are tabulated in table 5.1. It is observed from table 5.1 that, as the fluence is increased surface roughness increases with increasing fluence. This increment in surface roughness with increasing fluence is due to higher number of ion bombardment on the nanocomposite thin films. As the films are irradiated with ion beam, it goes through small surface changes that are due to sputtering on a surface thus, resulting in increased roughness.
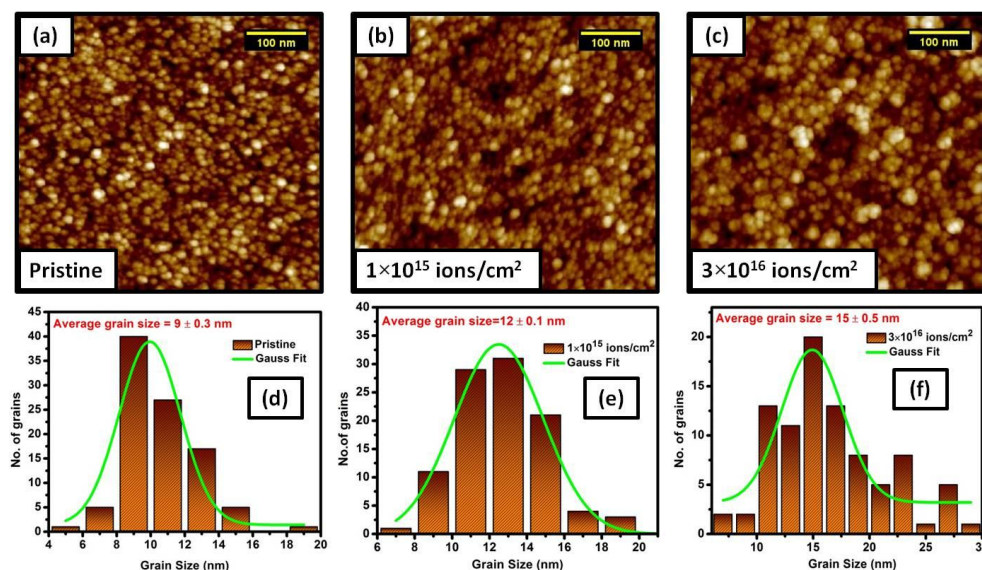
Figure 5.7 (a), (b) and (c) show the 2D AFM images and (d), (e) and (f) represents the corresponding grain size distribution of pristine and irradiated Cu-C$_{60}$ nanocomposite thin films with 1×10^{15} ions/cm^2 and 3×10^{16} ions/cm^2, respectively.

The average grain size of pristine thin film is 9 nm (table 5.1) and increases to 15 nm at fluence 3×10^{16} ions/cm^2; this is also shown in grain size distribution plots in Fig. 5.7(d), (e) and (f). This increased grain size can be explained on the basis of agglomeration of smaller grains. In view of the fact that the smaller grains have higher surface free energy, there is an urge for its coarsening to form bigger grain which decreases the overall free energy of the system.
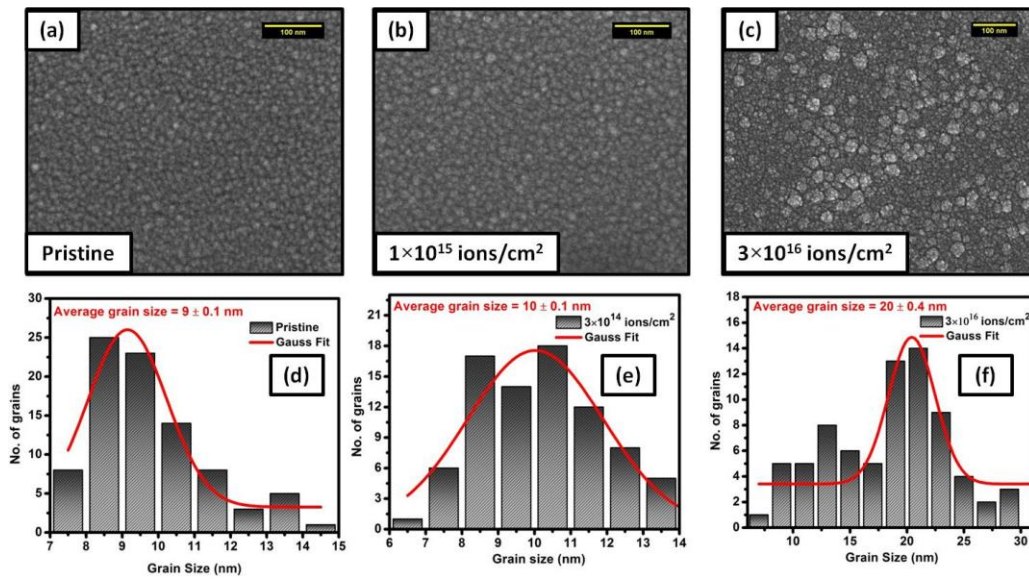
Figure 5.8 (a), (b) and (c) show the SEM images and (d), (e) and (f) represents the corresponding grain size distribution of pristine and irradiated Cu-C$_{60}$ nanocomposite thin films with 1×10^{15} ions/cm^2 and 3×10^{16} ions/cm^2, respectively.

Figure 5.8 represents the Scanning electron microscopy images of pristine and irradiated nanocomposite thin films with grain size distribution. From the images it is quite apparent that irradiation at higher fluence leads to grain coarsening with decrease in surface free energy being the driving for such growth under high energy input during irradiation. The average grain size is calculated and tabulated in table 5.1; the results obtained from SEM study support the results obtained from AFM study.

5.1.1.2.6 X-ray photoelectron spectroscopy (XPS):

XPS study is employed to acquire detailed information of the chemical composition and to determine the elemental states of the samples, particularly that of the Cu. Figure 5.9 represents the survey scan spectrum of the pristine Cu-C$_{60}$ nanocomposite thin films.

The spectrum has certain peaks corresponding to the binding energy C, Cu and O, and confirms the presence of these elements on the surface of the thin film. For detailed investigation, the core level scans were analyzed for each of the element present on the surface. Core-level spectrum for C 1s peak is presented in figure 5.10(a).The spectrum is fitted to three peaks positioned at 285.01 eV, 287.83 and 288.98. The main peak at 285.01 is identified as C-C bonding present in C$_{60}$, whereas the other two peaks at 287.83 and 288.98 are attributed to the C=O and -O-C=O bonding, respectively [33].
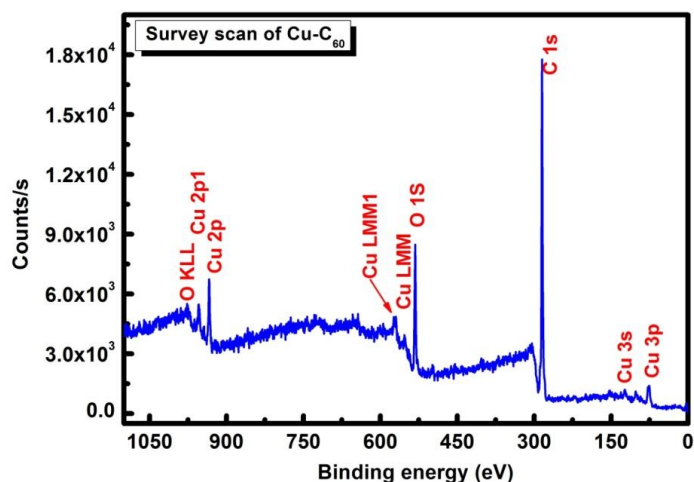
Figure 5.9 Survey scan spectrum of Cu-C$_{60}$ pristine nanocomposite thin film.

Figure 5.10(b) shows the O1s core-level spectrum. The spectrum has one peak at 531.4 ascribed to the C-O bonding [34].
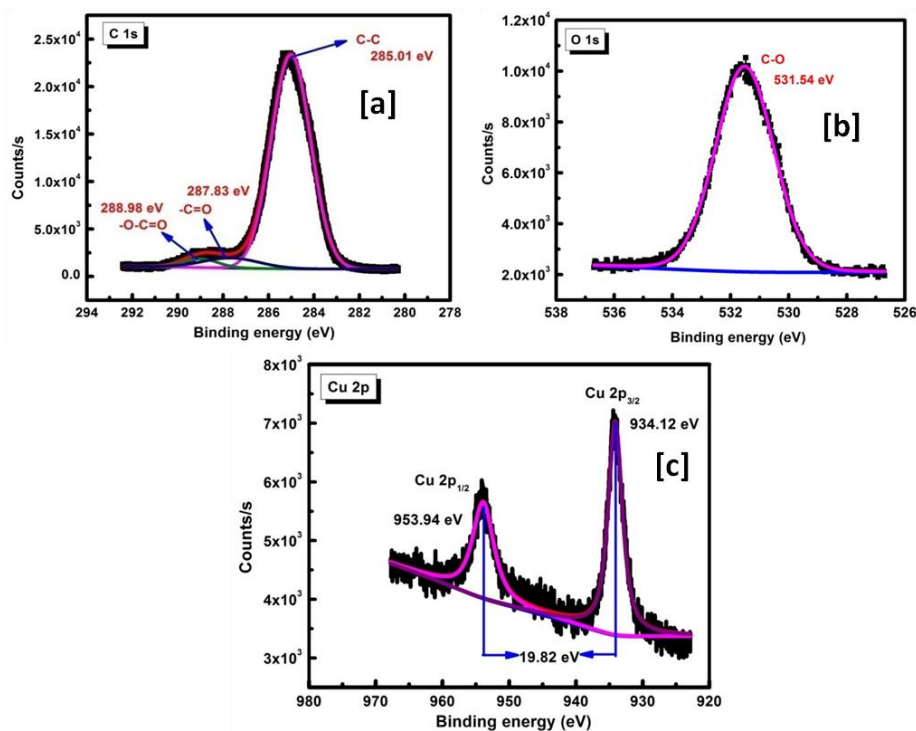
Figure 5.10 (a) Core-level spectrum for C 1s peak (b) core-level spectrum for O 1s peak (c) core-level spectrum for Cu 2p peak.

The core-level Cu 2p spectrum is shown in Figure 5.10(c) The spectrum has two intense peaks located at 934.12 and 953.94 eV, which can be assigned as Cu 2p3/2 and Cu 2p1/2 spin-orbital components, respectively.

The difference between the two peak position is $\Delta = 19.82$, which is in agreement with the literature. Incidentally XPS study has not given evidence of bonding between Cu and oxygen. The most important point here is that we have not observed any

satellite peak corresponding to Cu^{2+} species ruling out the presence of CuO in our samples, even though we have O in our sample, it was probably confined on the top most layer of the surface due to environmental exposure [35].

5.1.2 Effect of 350 keV Ag Ion Irradiation on SPR of Cu-C$_{60}$ Nanocomposite Thin Film

Study on the irradiation of fullerenes by ion beam of different energies is well documented in literature [36-42]. In general the interaction of high energy ions in fullerene C_{60} and C_{70} are expected to form ion tracks through the destruction of fullerene molecules into amorphous carbon (a-C) [36-43]. These high conducting ion tracks can be meant to be employed as nanowires with potential applications in solar cell [44]. Notionally amorphization of fullerenes are taken to be realized during high energy ion beam irradiation; while the research report give evidence of polymerization of C_{60} molecules at low doses, the amorphization has been usually envisaged at higher fluences [45].

In this context, it remains a question if irradiation of fullerene by low energy heavy ions can have identical impact on to the structural transformation as observed in the case of high energy ion beam irradiation That irradiation of C_{60} by low energy heavy ion can lead to amorphization of fullerene C_{60} is already reported by few researchers [36-39].

Report on influence of low energy ion beam irradiation on Au-C$_{70}$ nanocomposite thin film has demonstrated fascinating observation by the earlier workers [20]. It is surmised that at higher doses of low energy heavy ion, the nuclear collision can become quite perceptible and may ultimately lead to the formation of amorphized carbon [46]. On the contrary, at low doses the nuclear collisions may lead to photopolymerization of fractal molecules produced by disintegration of fullerene molecules during interaction with irradiating heavy ions [46]. In contrast, electronic energy deposition may lead to statistically distributed ion impacts with the fullerene molecules [46-48]. The series of collisions having been exponentially related with the fluence tantamount to collision cascade, the density of which might not be that high at low doses as to completely destroy all the molecules of fullerenes [48]. A partial destruction by nuclear collision forms amorphous carbon which remain admixed with photopolymerized fullerenes at low fluence [48-49].

This being the scenario of fullerene molecule under irradiation by low energy heavy ions, it appears quite interesting to investigate the modification in structural properties

of a nanocomposite where metal nanoparticles are deliberately embedded in fullerene C_{60} matrix. While SPR behavior in noble metal (Au, Ag) embedded fullerene based composites after being irradiated by high energy ion beam have been widely studied [17-18], the effect of low energy ion beam irradiation on the characteristics of Cu metal reinforced fullerene based nanocomposites is yet to be documented in literature. It is known that SPR behavior due to reinforcing noble metal is significantly influenced by the characteristics of host matrix. Therefore, it may be anticipated that the above stated structural changes in C_{60} due to irradiation by low energy heavy ions might have interesting bearing onto the SPR behavior due to copper in a copper-C_{60} nanocomposite thin film. Hence, in the present investigation attempts are made to study the modifications in structure and optical properties of Cu-C_{60} nanocomposites after irradiation by 350 keV Ar ion beam.

5.1.2.1 Experimental Details:

Thin films of Cu-C_{60} nanocomposite films were grown on glass, quartz, silicon and TEM grids by Physical Vapour Deposition (PVD) technique based on co-evaporation. The deposition was done through simultaneously evaporating fullerene C_{60} powder (99.9% Alfa Aesar) and copper powder in two tungsten boats. The respective weight of fullerene C_{60} and Cu powder was 0.04 g and 0.10g, respectively. Circular holder was used for the substrate mounting and there was no heating given to substrates during deposition. Collective rate for deposition of Cu and fullerene C_{60} simultaneously is taken about ~0.4Å/s and deposition was stopped on reaching a thickness about 50 nm. Before starting deposition, vacuum is kept at ~ 8.7×10^{-6} mbar and on completion of deposition it was recorded to be 9.2×10^{-6} mbar. The as-deposited thin films were irradiated with 350 keV Ar ion beam using LEIBF facility at Inter University Accelerator Centre (IUAC), New Delhi. The projectile range of the 350 keV Ar ions through the Cu(18%)-C_{70} nanocomposite thin films. For Cu (18%)-C_{60} nanocomposite thin films, the values of S_e and S_n are about 7.41×10^1 eV/Å and 3.27×10^1 eV/Å, respectively with projected range about 299 nm. RBS characterization (facility at IUAC) delineates the atomic percentage of Cu in fullerene C_{60} is found to be ~ 18% with thickness of the film, ~ 32 nm. The irradiation is performed with 350 keV Ar ion beam in IUAC, New Delhi at different fluences from 1×10^{12} to 3×10^{13} ions/cm^2.

Hitachi spectrometer was used to record the UV-visible absorption spectra of the nanocomposite thin films on quartz substrate. Tecnai G^2 20 (FEI) S-Twin TEM

microscope operating at 200 kV was used to capture the TEM images of pristine and irradiated thin film. AIRIX STR 500 Raman spectrograph fixed with Ar ion laser excitation wavelength at 532 nm was used to record the Raman spectra of pristine and irradiated films.

5.1.2.2 Results & Discussions:

5.1.2.2.1 RBS analysis:

Figure 2 illustrates the schematic diagram of RBS technique. The $4He^{2+}$ (alpha particles) beam of energy 2.000 MeV with charge ~15μC is used to record the spectrum.
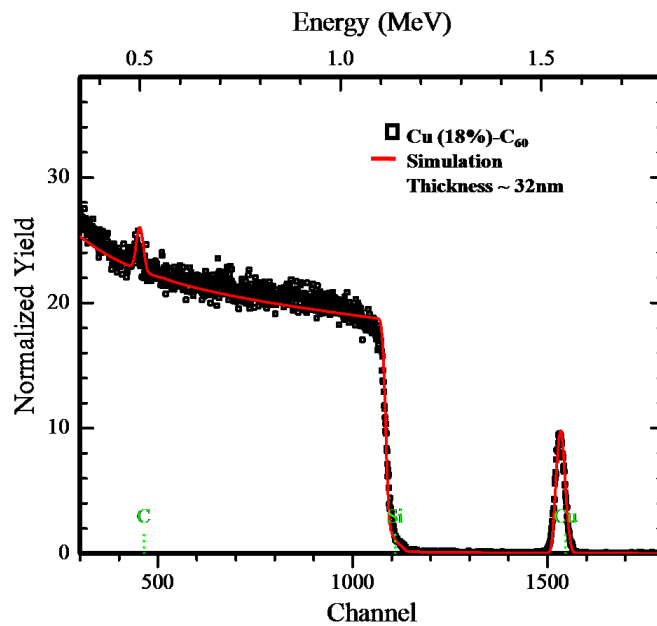
Figure 5.11 Rutherford backscattering spectrum of Cu-C_{60} nanocomposite film on Si substrate.

The RBS spectrum of Cu-C_{60} nanocomposite thin film is shown in figure 5.11 and is represented by square symbols. The Red line (solid) represents the Rutherford Universal Manipulation Program (RUMP) simulated spectrum [50].

In figure 5.11 the position of each element C, Cu and Si is marked. The plateau in the spectrum shows the silicon substrate that was overridden with a hump of carbon. RUMP simulation code is used for simulation of RBS spectrum which estimates the atomic percentage of Cu ~18% in fullerene C_{60} matrix and thickness around 32 nm.

5.1.2.2.2 UV-visible absorption spectroscopy:

UV-visible absorption spectra of the nanocomposite thin films are shown in figure 5.12. It appears from the figure that SPR band in pristine occurs at ~ 622 nm. It is observed from the same figure that with increasing fluence, SPR band has undergone a red shift attaining a value of 644 nm at a high fluence of 3×10^{16} ions/cm^2 with a

significant increase in intensity. Such a shift of SPR band towards higher wavelength owes its origin to the enhancement of particle size at higher fluences.
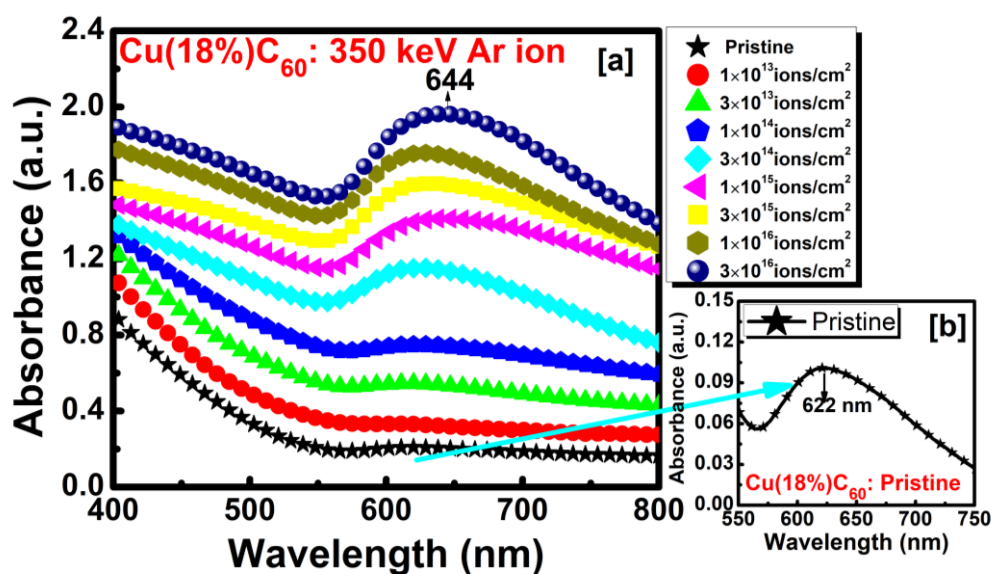
Figure 5.12 UV-visible absorption spectra of pristine and 350 keV Ar ion irradiated Cu-C$_{60}$ nanocomposite thin films.

It may be noted that the low energy irradiation by 350 keV Ar ion has given rise to a partial amorphization of the matrix and hence the overall change in the refractive index of region surrounding copper nanoparticles might have been somewhat lower. It is known that amorphization of fullerene is associated with lowering of refractive index and that this phenomenon causes a blue shift of SPR band of noble metal nanoparticles surrounded by irradiated fullerene matrix. In this particular case fullerene C$_{60}$ having highest stability in the fullerene group has undergone more of polymerization of fractal group formed due to nuclear collisions in preference to complete amorphization due to inadequacy in the strength of collision cascades created at low energy heavy ion irradiation [48-49].

The enhancement of its intensity corroborates the earlier observation [17-20] and is attributed to increase in particle size of copper nanoparticles at increasing fluence of irradiation. It is conjectured that the effect of particle size has dominated over that due to the change in refractive index of the matrix. Following irradiation, this has been responsible for the observed red shift of SPR band of copper (figure 5.12). It may be contextual to mention that high concentration of the copper (18%) in the nanocomposite thin film has also accentuated particle growth due to the small interparticle distance within the matrix.

5.1.2.2.3 Raman analysis:

Raman study reveals the transformation of the host matrix into amorphous carbon and confirms the decreased refractive index of the host matrix.
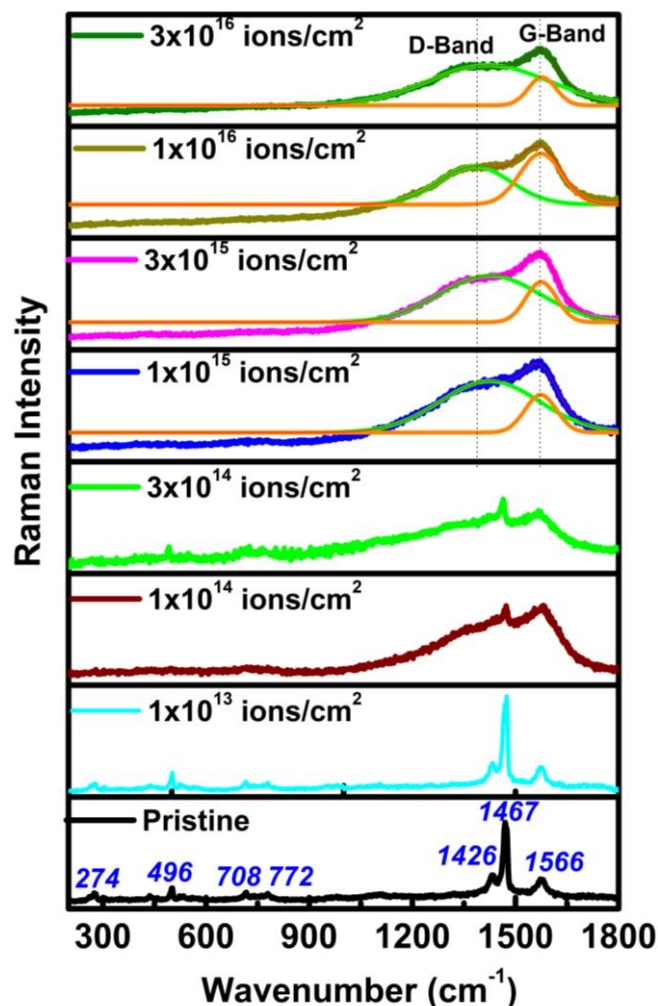
Figure 5.13 Raman spectra of pristine and 350 keV Ar ion irradiated Cu-C_{60} nanocomposite thin films.

Raman spectrum of pristine Cu-C_{60} thin film shows (figure 5.13) the Raman bands at the positions 274, 496, 708,772, 1426, 1467 and 1566 cm^{-1} which are consistent with the characteristic bands of icosahedra C_{60}films [28].

With increasing fluence, the characteristic Raman bands tend to disappear. This tendency of diminution in intensity followed by the disappearance of these Raman bands at higher fluence is indicative of the destruction of C_{60} fullerene molecule.

It is further noted that the D and G bands starts appearing at 1×10^{15} ions/cm^2 fluence which, with further increase in fluence shows appreciable changes in shape and positions. A gradual widening of G-band characterizes amorphization and it is

observed from the result of the present experiment that appreciable amorphization of the matrix has taken place at the fluence of 3×10^{16} ions/cm^2. This structural damage has significant influence on the position of SPR band due to copper nanoparticles.

5.1.2.2.4 TEM analysis:

The effect of low energy heavy ion irradiation on the characteristics of Cu-C$_{60}$ nanocomposite thin film has been studied by high resolution transmission electron microscopy. Representative results for pristine and thin film irradiated at 3×10^{16} ions/cm^2 fluence are shown in figure 5.14.
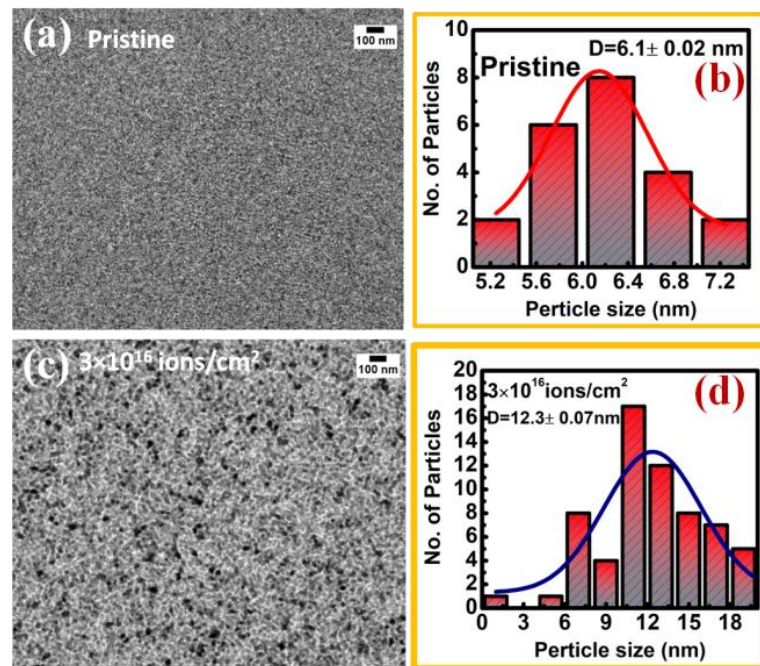
Figure 5.14 (a) TEM image (b) particle size distribution of pristine thin Cu-C$_{60}$ thin film. (c) TEM image (d) particle size distribution of Cu-C$_{60}$ thin film irradiated with 350 keV Ar ion at 3×10^{16} ions/cm^2 fluence.

The shape of copper nanoparticles is found to be nearly spherical for both pristine and after irradiation at fluence 3×10^{16} ions/cm^2 with 350 keV Ar ion (figure 5.14 a and c), the average particle size of the pristine nanocomposite thin film is measured as 6.1 nm (5.14(b)). The particle size distribution of the ion irradiated thin film with fluence 3×10^{16} ions/cm^2 is shown in figure 5.14(d). From this statistical analysis of particle size distribution, it is observed that the average particle size has increased from 6.1±0.02 nm in pristine to 12.3 ± 0.7 nm for irradiated thin film. The increase in particle size after irradiation is attributed to coarsening of the particles [26-27]. The appreciable particle coarsening is responsible for shift of SPR band position to a longer wavelength. It is not out of place to mention that the irradiated matrix

surrounding nanoparticles has undergone change in refractive index so that it impacts a blue shift of SPR band; the overall red shift as observed in the case of thin film irradiated with fluence 3×10^{16} ions/cm^2 against the pristine verifies that particle coarsening have overridden the matrix effect in respect of shift of SPR band for copper embedded C$_{60}$ nanocomposites irradiated with low energy heavy ions viz. 350 keV Ar ion.

5.2 To Observe the Effect of High Energy Ion Beam Irradiation on Copper-Fullerene C_{60} Nanocomposite Thin Films

Metal based fullerene nanocomposites is taken as an important area of research in plasmonics due, primarily to the improved absorption characteristics in the visible region as a result of SPR of metal nanoparticles. Reportedly, fullerene can be utilized in various fields of applications especially in organic solar cells [51-52]. SPR of plasmonic nanostructures is known to enhance the solar light harvesting by several ways. Various reports are available in the literature about choosing different metal nanoparticles in the different matrices at different composition [53-59]. Enhancement of optical properties in metal-reinforced fullerene nanocomposites is reported by Singhal et al. [16-20]. The same research group reported the enhancement of SPR band frequency and its tuning by the employment of different methods such as swift heavy ion irradiation and thermal treatment. The tuning or shifting of SPR peak is attributed to the change in interparticle distance between the nanoparticles which takes place due to particle growth by ion irradiation or thermal treatment. Ion irradiation is the finest technique to tune different properties of materials [19-20]. Ion irradiation and ion implantation are both very useful methods for achieving the enhanced and modified properties of fullerene nanocomposites for different application areas.

In addition, plenty of reports are available in literature about the modification in the properties of fullerene for application in organic solar cell [51-52,60]. Maeyosh et al. reported the formation of fullerene-based nanowires by irradiating it at high fluence which might aid in the enhancement in power conversion efficiency (PCE) of organic solar cells [50]. Using fullerene as a matrix to incorporate metal nanoparticles makes it a bi-functional nanocomposite, in which the properties of matrix that is fullerene and metal nanoparticles can be utilized concurrently [16-20]. The most suited electron acceptor material for organic solar cell is fullerene and absorption can be increased within the visible region by incorporating the metal nanoparticles. This increased absorption is one of the fundamental factors that can be engaged for further enhancement of efficiency of organic solar cells [15].

In present study, Cu nanoparticles embedded fullerene C_{60} matrix is studied for monitoring the variation in the optical, structural and electrical properties of the nano composites under the effect of high energy heavy ion, i.e. 120 MeV Ag ion beam at different fluences 1×10^{12}, 3×10^{12}, 6×10^{12}, 1×10^{13} and 3×10^{13} ions/cm^2. The present

work aiming to study the SPR response of copper-C_{60} nanocomposites under the influence of irradiation bears the significance that the overall system may become cost effective when compared with the Au or Ag metal nanoparticles.

5.2.1 Experimental Details:

Cu-C_{60} nanocomposite films were grown on different substrates such as glass, quartz, silicon and TEM grids with the aid of thermal resistive co-deposition method. The detailed process is described in section 5.1.2.2. The irradiation is performed with 120 MeV Ag ion beam in IUAC, New Delhi at different fluences from 1×10^{12} to 3×10^{13} ions/cm^2. The deposited Cu (18%) C_{60} nanocomposite thin films were irradiated with 120 MeV Ag ion beam. The SRIM (The Stopping and Range of Ions in Matter) program is used to determine the value of the electronic (S_e) and nuclear (S_n) energy losses in nanocomposites film of Cu (18%) C_{60} and are found to be $\sim 1.39\times10^3$ eV/Å and ~ 5.80 eV/Å, respectively, with projected range ~ 14.75 µm.

Hitachi spectrometer was used to record the UV-visible absorption spectra of the nanocomposite thin films in wavelength range from 200 to 800 nm. TEM images of pristine and of thin film irradiated at highest fluence (3×10^{13} ions/cm^2) are recorded with Tecnai G^2 20 (FEI) S-Twin TEM microscope. Raman spectra were taken with the aid of AIRIX STR 500 Raman spectrograph fixed with Ar ion laser excitation wavelength at 532 nm. Omicron nanotechnology XPS system from Oxford instruments (model- ESCA+) with a monochromatic Al-K$_\alpha$ radiation source of energy 1486.7 eV was used to record XPS spectra. Bruker D8 Diffractometer was used to record the diffraction pattern of pristine and irradiated thin films. Agilent Semiconductor device analyzer was utilized in recording I-V measurements for determining the resistivity variation under the influence of irradiation.

5.2.2 Results & Discussions:

5.2.2.1 RBS analysis:

Following the same RBS technique for similarly synthesized C_{60} thin films, the estimated percentage of copper has been found to be 18% with a film thickness of 32nm. The detail of RBS experiments are already described in section5.2.

5.2.2.2 Raman analysis:

Raman spectroscopy is performed to analyze the structure and property changes taking place due to irradiation of Cu-C_{60} nanocomposite thin films. For proper study of the effect of irradiation on Raman bands of Cu-C_{60} nanocomposite thin film, in a particular area, 1000-1900 cm^{-1}is given the major attention (figure 5.15).

Figure 5.15 illustrates the variation of Raman bands positioned at 1422, 1467and 1566 cm^{-1}under the effect of ion irradiation. Figure 5.15 shows that due to breaking of fullerene molecule, the intensity of Raman bands continuously decrease up to fluence 3×10^{12} ions/cm^2.
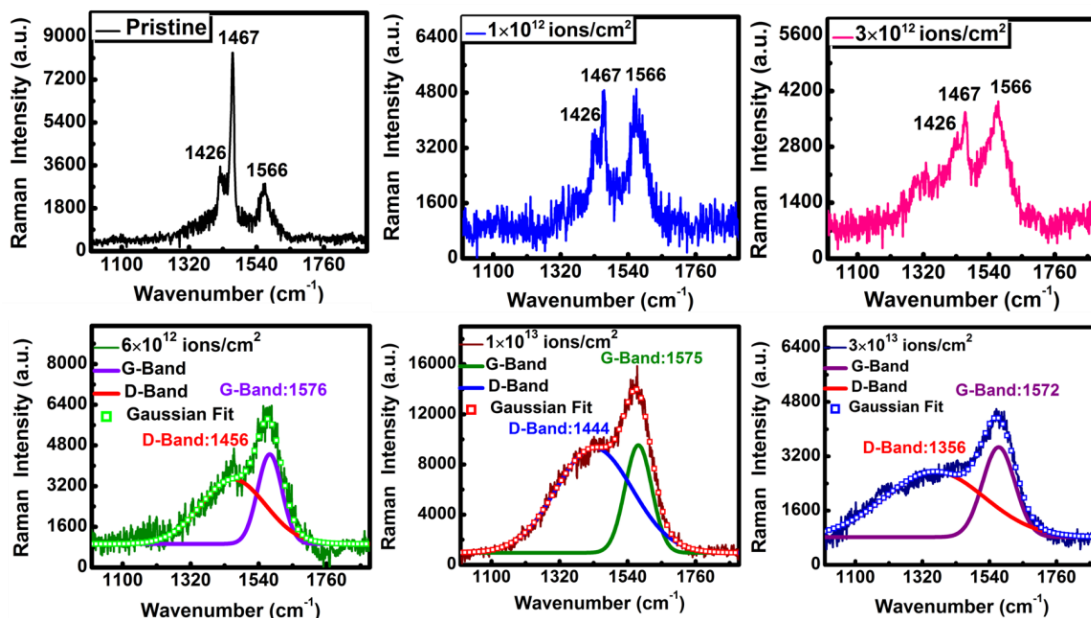
Figure 5.15 Raman spectra of pristine and 120 MeV Ag ion irradiated Cu-C$_{60}$ nanocomposite thin films.

At fluence 6×10^{12} ions/cm^2, these bands convert into two broad bands and further deconvolution of the band confirms that the bands cantered at 1456 and 1576 cm^{-1} are the D and G bands of a-C. Here D stands for disorder and corresponds to A$_{1g}$ symmetry which arises due to breathing vibrations of rings at K zone boundary whereas G stands for graphite correspond to E$_{2g}$ symmetry arising from bond stretching vibrations in both rings and chains. It is remarkable to note that most of disordered carbon are dominated by these two graphite modes (D-band and G-band) even when the carbon do not have particular graphite ordering [61-62]. The variation in D-band and G-band position is visualized with increasing fluence and final position of these come out to be ~ 1356cm^{-1} and 1572 cm^{-1} at 3×10^{13} ions/cm^2 fluence. From the above observation, it is conjectured that the presence of D-band and G-band at highest fluence confirms the conversion of C$_{60}$ into amorphous carbon.

5.2.2.3 TEM analysis:

The crystanllity and the size of embedded Cu nanoparticles in nanocomposite thin film are determined by transmission electron microscopic measurements. Figure 9 (a, b and c) depicts the bright field TEM image, SAED (selected area electron

diffraction) pattern and particle size distribution, respectively of pristine film. Figure 5.16 (a) confirms that the morphology of the nanoparticles to be nearly spherical. Figure 5.16 (b) shows the SAED pattern of pristine film with marked planes that confirms the cubic phase of Cu.

Figure 5.16 (c) represents the particle size distribution of copper nanoparticles. The particle size calculated for pristine film comes around 4.1 ± 0.03 nm. In order to observe the effect of 120 MeV Ag ion irradiation on nanocomposite thin film, TEM measurements are also done for the 3×10^{13} ions/cm^2 fluence irradiated samples. Figure 5.16 (c, d and e) shows similarly the TEM image, SAED pattern and particle size distribution, respectively for 120 MeV Ag ion irradiated with fluence 3×10^{13} ions/cm^2 sample.
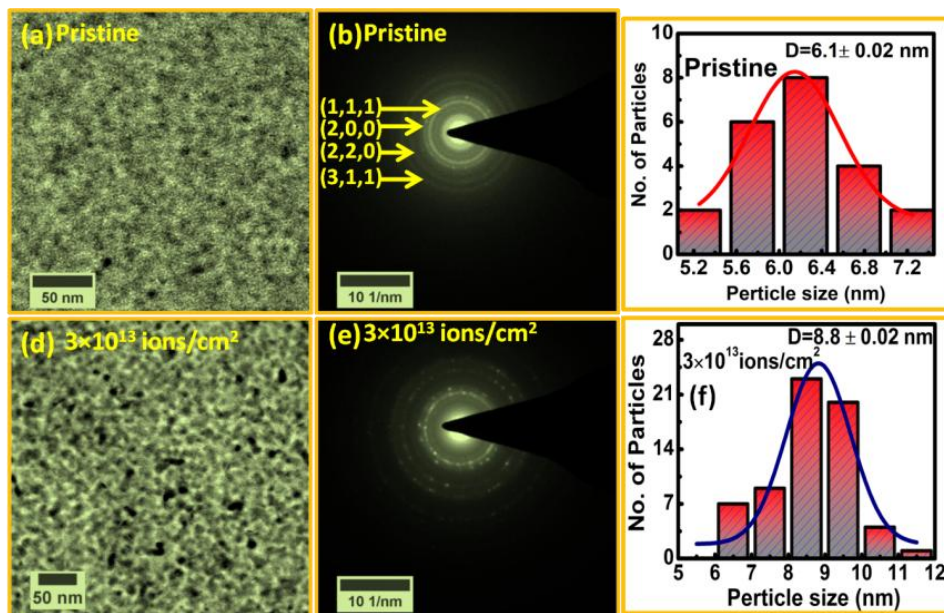
Figure 5.16 (a) TEM image, (b) SAED pattern (c) particle size distribution, of Cu-C$_{60}$ pristine nanocomposite thin film. (d) TEM image, (e) SAED pattern (f) particle size distribution, of Cu-C$_{60}$ nanocomposite thin film irradiated at fluence 3×10^{13} ions/cm^2.

As in pristine sample, nearly spherical morphology of the particles is retained at higher fluence. The SAED pattern further confirms the enhancement in the crystallinity of the Cu-C$_{60}$ thin films. The particle size distribution is represented in Figure 5.16 (c) and statistically determined average particle size comes out to be about 8.8 ± 0.02 nm. This increase in particle size is due to agglomeration of smaller particles to make up the bigger particles [26-27].

5.2.2.4 UV-visible absorption spectroscopy:

Figure 5.17 represents the effect of irradiation on absorption spectrum of nanocomposite film. From figure 5.17 it is clear that in pristine there is a SPR band at around 622 nm which is seemingly induced due to the presence of copper nanoparticles in fullerene matrix. The irradiated thin films represent the increased intensity of the SPR band. This trait is also existent in case of gold and silver nanoparticles embedded in fullerene matrix [13-14, 24]. As represented in the inset of figure 4 the intensity of absorption band increases as the number of ion/cm^2 of the ion beam are increased.
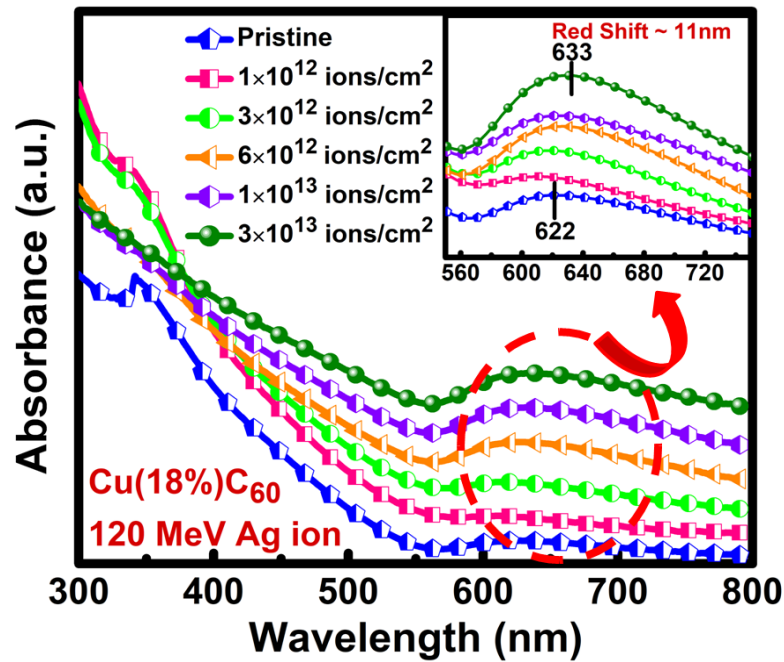
Figure 5.17 UV-visible absorption spectra of pristine and 120 MeV Ag ion irradiated Cu-C$_{60}$ nanocomposite thin films.

In comparison to the SPR peak position of pristine film, a red shift of ~11 nm in SPR peak is observed in the irradiated thin film at highest fluence (3×10^{13} ions/cm^2). This red shift is attributed to the variation in size of the copper nanoparticles at a wider size distribution due to the effect of irradiation.

The size effect on SPR width in metal nanoparticles results in the broadening of the SPR band for very small and large nanoparticles. According to Drude approximation, dielectric function of the material that is dependent on frequency is given by [63]

$$\epsilon_m = 1 - \frac{\omega_p^2}{(\omega^2 + i\gamma\omega)} \qquad (5.7)$$

Where ω_p denotes Drude bulk plasma frequency and can be represented by the relation $\omega_p = \sqrt{\dfrac{ne^2}{\varepsilon_o m_e}}$, here n, ε_0, e and m_e are the symbolic representations of free electron density, vacuum permittivity, electron charge and effective mass of electron, respectively. In equation (1), γ denotes the damping constant that depends upon the radius of nanoparticles and defines the width of the SPR as

$$\gamma(r) = \gamma_0 - \frac{Av_f}{r} \qquad (5.8)$$

Here A, v_f, rand γ_0 are the symbols defining the constant specifies the scattering details, Fermi velocity of the electrons, radius of the metal nanoparticles and bulk damping constant, respectively.

According to this equation, the SPR width represents two kinds of behavior on the basis of particle size distribution. For smaller nanoparticles whose radius is smaller than 25 nm, intrinsic size effect dominates and gives dependency of nanoparticle radius (r) as 1/r, hence the SPR width increases with decrease in the nanoparticle size (r) [64]. In contrast, for larger particles with radius greater than 25 nm, extrinsic size effect plays role and affects the bandwidth of the nanoparticles which is directly proportional to the size of nanoparticles,(r). This implies that the width SPR band increases as the particle size increases. Further, the dual behavior can be explained on basis of the surface of nanoparticles where the scattering of conduction electrons takes place. This results in increase of the SPR width with decrease of the nanoparticle size and radiation damping due to which the SPR band broadens again when nanoparticle size increases [65].

Optical band gap (E_g) Calculation:

The optical transitions can be explained on the basis of the band gap of the material. Apart from this, electrical conductivity of a material is directly dependent on the band gap of the material.

Smaller value of band gap of a particular material makes it more electrical conductive and vice versa. In order to determine the value of the optical band gap of the films, Tauc Plot is used (figure 5.18).

It can be seen from figure 5.18 that the band gap values come out to be 2.7 eV for pristine Cu-C$_{60}$ nanocomposite thin film and it decreases to a value of 2.2 eV for irradiated CuC$_{60}$ nanocomposite at fluence 6×10^{12} ions/cm^2.The incessant increase in

fluence results in consistent decrease in the value of optical band up to a value of 2.0 eV for the thin film irradiated with highest fluence i.e. 3×10^{13} ions/cm^2. Hence, copper nanoparticles are found to play a vital role in altering the electrical properties by varying optical band gap values of nanocomposite thin films. This can be understood by the creation of localized electronic states in between of HOMO-LUMO gap due to the presence of Cu nanoparticles.
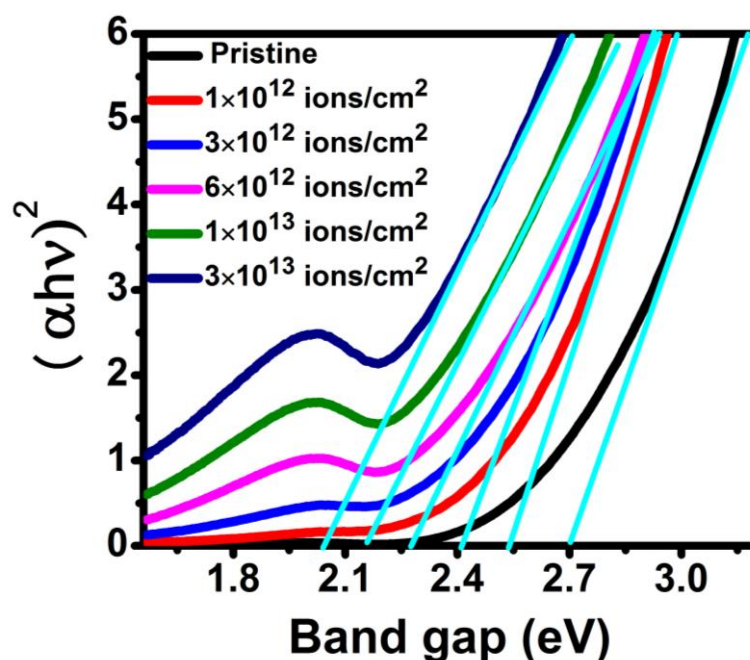
Figure 5.18 Tauc plots of pristine and irradiated Cu-C$_{60}$ nanocomposite thin films.

The optical and electrical properties are highly dependent on the localized electronic states [66]. These states are liable for recombination centers and trapping centers and results in enhancement of the low energy transitions that is responsible for the overall change observed in band gap values.

Table 5.2 Represents the calculated average particle size using XRD and TEM analysis.

Fluence (ions/cm^2)	Average Particle Size XRD Analysis (nm)	Average Particle Size TEM Analysis (nm)
Pristine	3.7±0.03	4.1±0.03
6×10^{12}	4.4±0.06	--
1×10^{13}	5.5±0.02	--
3×10^{13}	7.1±0.06	8.8±0.02

5.2.2.5 XRD analysis:

The presence of Cu nanoparticles in the fullerene C_{60} matrix is further confirmed by X-ray diffraction analysis. Figure 5.19 illustrates the XRD pattern of pristine and irradiated films. The prominent peak at 2θ values of about 43.2^0 represent the (111) Bragg's reflection of FCC structure of copper and the peak at 35. 4^0 represent the Cu_2O (111).
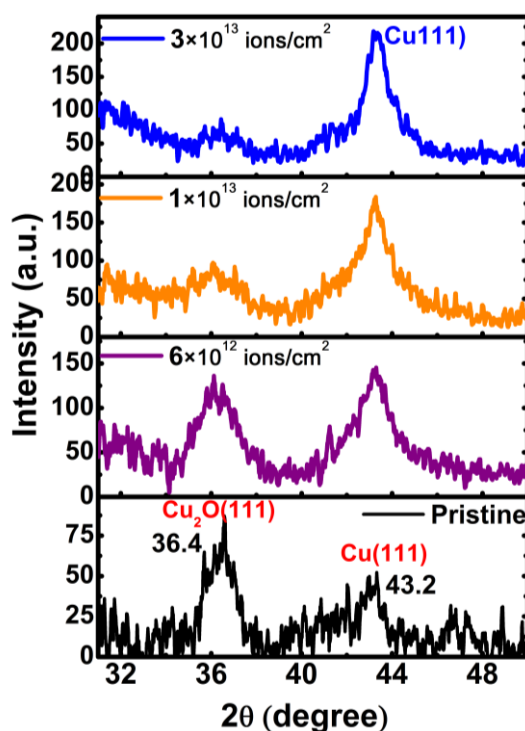
Figure 5.19 XRD patterns of pristine and 120 MeV Ag ion irradiated Cu-C_{60} nanocomposite thin films.

With increasing fluence the Cu_2O peak is seen to diminish with simultaneous increase in Cu metal peak intensity. At a particular fluence 3×10^{13} ions/cm^2, Cu_2O peak becomes very faint and the peak of Cu becomes very strong in XRD pattern. This confirms the removal of oxygen under the effect of ion irradiation of higher fluence. This observation is further confirmed by XPS analysis. The crystallite size measurements were also carried out using the Debye Scherrer formula [67].

The average values of particle size of pristine and irradiated films calculated with the help of Scherrer formula are tabulated in table 5.2 Average particle size is seen to increase with increasing fluence and this observation is consistent with the previous results of TEM and UV- absorption.

5.2.2.6 Conductivity measurement:

As optical band is decreased with irradiation and so it is important to analyze the change in electrical conductivity of the Cu-C$_{60}$ nanocomposite thin films due to ion irradiation. Two probe method has been used due to high resistance of the films. Figure 5.20 (a-f) shows the graphs between current (A) and voltage (V) for pristine and irradiated thin films.
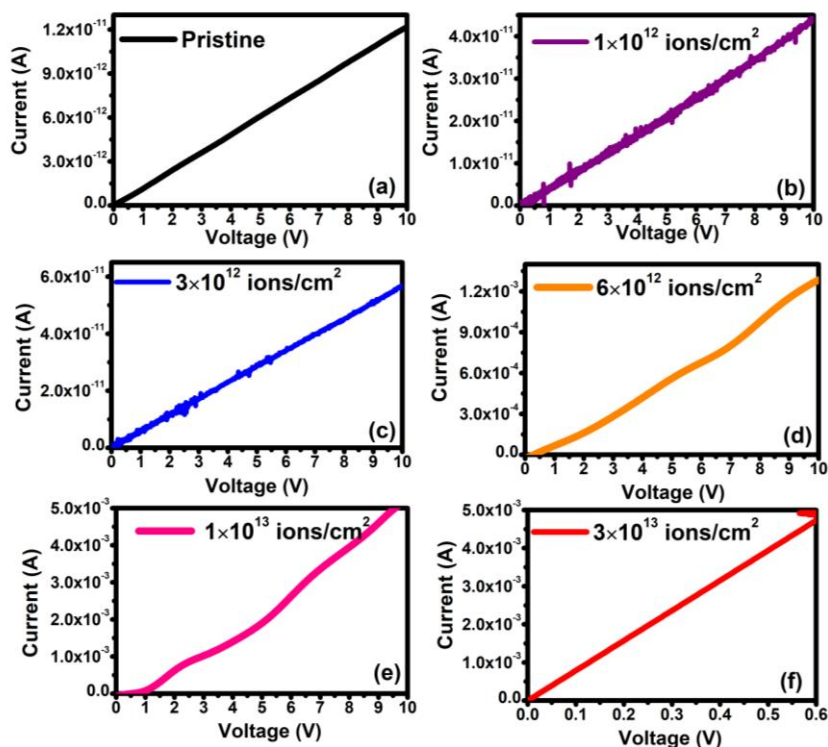
Figure 5.20 (a-f) Plot between current (I) and voltage (V) for pristine and 120 MeV Ag ion irradiated Cu-C$_{60}$ nanocomposite thin films.

The reciprocal of the slope gives the value of resistance between two points. The estimated resistivity values for pristine and irradiated films are tabulated in table 5.3.

Table 5.3 Represents the variation of band gap and resistivity with 120 MeV Ag ion irradiation.

Fluence (ions/cm^2)	Band gap (eV)	Resistivity (ohm-cm)
Pristine	2.7	2.6×10^6
1×10^{12}	2.5	5.6×10^5
3×10^{12}	2.4	7.2×10^5
6×10^{12}	2.2	2.3×10^{-1}
1×10^{13}	2.1	5.7×10^{-2}
3×10^{13}	2.0	4.0×10^{-4}

It is observed that resistivity decreases with increasing fluence. This is ascribed to the conversion of C_{60}, into a-C with increasing fluence; since a-C has a higher conductivity than C_{60} the decrease in resistivity with increasing fluence is obvious.

The transformation of C_{60} into a-C has been verified by Raman spectroscopy and the results of Raman spectroscopy are inconsistent with conductivity results. The initial resistivity value of pristine Cu-C_{60} nanocomposite film is very much less than the value of the C_{60} matrix thin films; there has been a wide decrease in resistivity from 10^6 Ω-cm to 10^{-4} Ω-cm is observed for the nanocomposite.

This is presumably due to the presence of copper nanoparticles in the nanocomposite film which enhance the conductivity of the films with increasing size of nanoparticles with 120 MeV Ag ion beam as verified by XRD and TEM results.

5.2.2.7 Surface analysis:

Atomic force microscopy (AFM) characterization has been performed to analyze the effect of irradiation on the surface morphology of Cu-C_{60} films. Figure 5.21 (a-e) shows 2-D AFM images of Cu-C_{60}pristine nanocomposite thin film and irradiated thin films. Table 5.4, shows that the increasing fluence leads to an increase in surface roughness. Ion bombardment is the reason of increased roughness. The sputtering effect creates small changes on the surface of the film and the resultant is the increased roughness of the film.
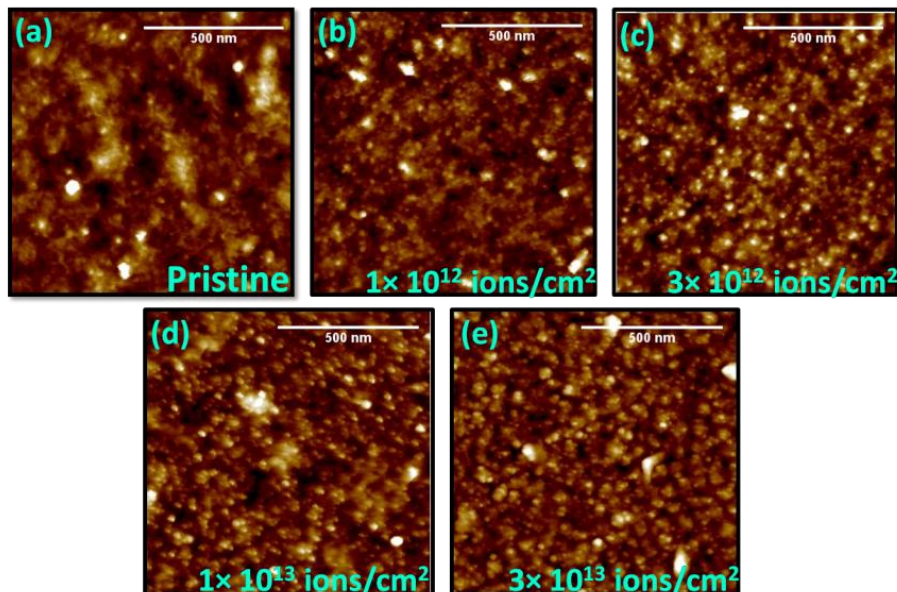
Figure 5.21 2-D AFM images of Cu-C_{60} pristine nanocomposite thin film and irradiated with 120 MeV Ag ions.

It can be seen that as the fluence is increasing, the grain size of the film also increases; this can be explained on the basis of the fact that agglomeration takes place to reduce the surface free energy of smaller grains by forming bigger grains. This increased grain size is consistent with TEM results also.

Scanning electron microscopy (SEM) characterization has also been performed to analyze the particle morphology under irradiation effect. Figure 5.22 (a-c) shows the SEM images for pristine irradiated for fluence of 3×10^{12} and 3×10^{13} ions/cm^2 thin films.
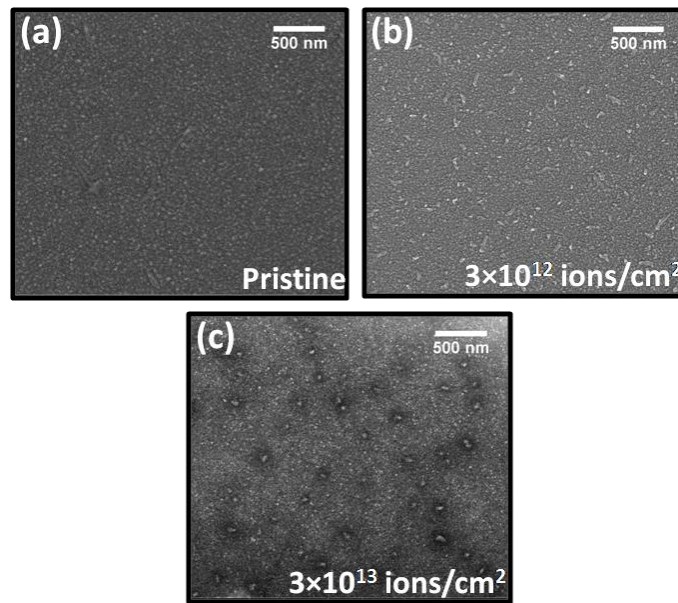
Figure 5.22 SEM images of Cu-C$_{60}$ pristine and irradiated nanocomposite thin film with 120 MeV Ag ions.

From the SEM images it is revealed that as the fluence is increased the average particle size is also increases. Figures 5.22(c), gives clear evidence of the particles agglomeration. This is consistent with AFM results too.

Table 5.4 Represents the variation of roughness with 120 MeV Ag ion irradiation.

Fluence (ions/cm^2)	Roughness (nm)
Pristine	1.98
1×10^{12}	2.05
3×10^{12}	2.43
6×10^{12}	3.01
1×10^{13}	2.88
3×10^{13}	2.54

5.2.2.8 XPS analysis:

In order to support the interpretations drawn from the above studies, X-ray photoelectron spectroscopy is also employed to examine the Cu-C_{60} nanocomposite thin films before and after irradiation. Figure 5.23 depicts the survey scans of pristine and ion irradiated Cu-C_{60} nanocomposite films, where the later one has been conducted at a fluence of 3×10^{13} ion/cm^2. The spectra have definite peaks consistent with the binding energies of C, Cu and O, along with Auger peaks. These peaks confirm the presence of the said elements at the surface of ~~the~~ thin films.
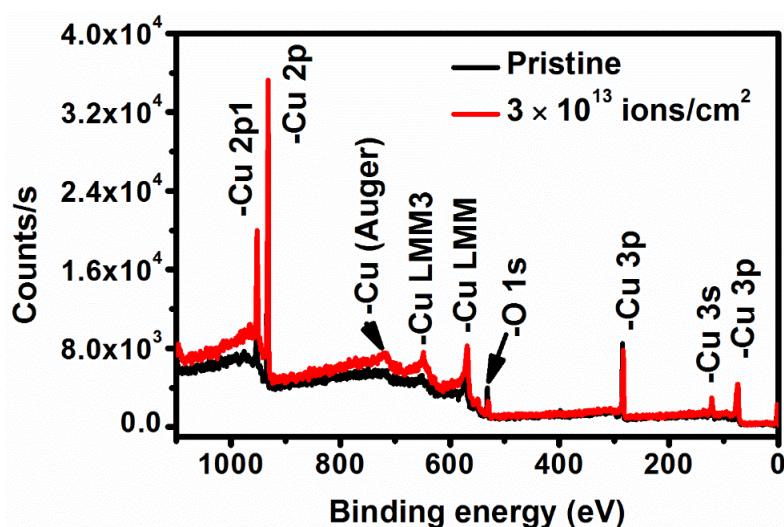
Figure 5.23 Survey scan spectra of Cu-C_{60} nanocomposite thin films before and after irradiation.

The core level spectrum of Cu is also investigated to confirm the growth of Cu particles. Figure 5.24(a) displays the Cu-$2p$ core level spectrum showing doublets with two possible peaks due to spin-orbital splitting. The peaks in pristine film situated at ~953.15 and 933.32 eV has been assigned to Cu $2p_{1/2}$ and Cu $2p_{3/2}$ components [68].

The core level peak of Cu $2p_{3/2}$ has further been deconvoluted into two peaks located at ~933.68 and 933.12 eV, mainly associated with the copper oxides (CuO/Cu_2O) and pure Cu (figure 5.24b), respectively. For ion beam irradiated films (5.23c), these peaks are found to be originated at ~952.12 eV (Cu $2p_{1/2}$) and ~932.15 eV (Cu $2p_{3/2}$). Deconvolution of the Cu $2p_{3/2}$ peak with two peaks at ~934.54 and 932.12 eV, corresponds to the copper oxide (CuO) and copper metallic bonding, respectively. To find the amount of copper oxide present in the thin films, the area under each peak is calculated and found that the amount of copper oxide is ~27.1 at.% in the pristine film, which is reduced to 6.3 %, after irradiation. This confirms the transformation of

copper oxide to copper. The transformation of copper oxide to copper is also suggested by the observed small shift of ~1.02 eV towards lower binding energy as shown in figure 5.24(a).
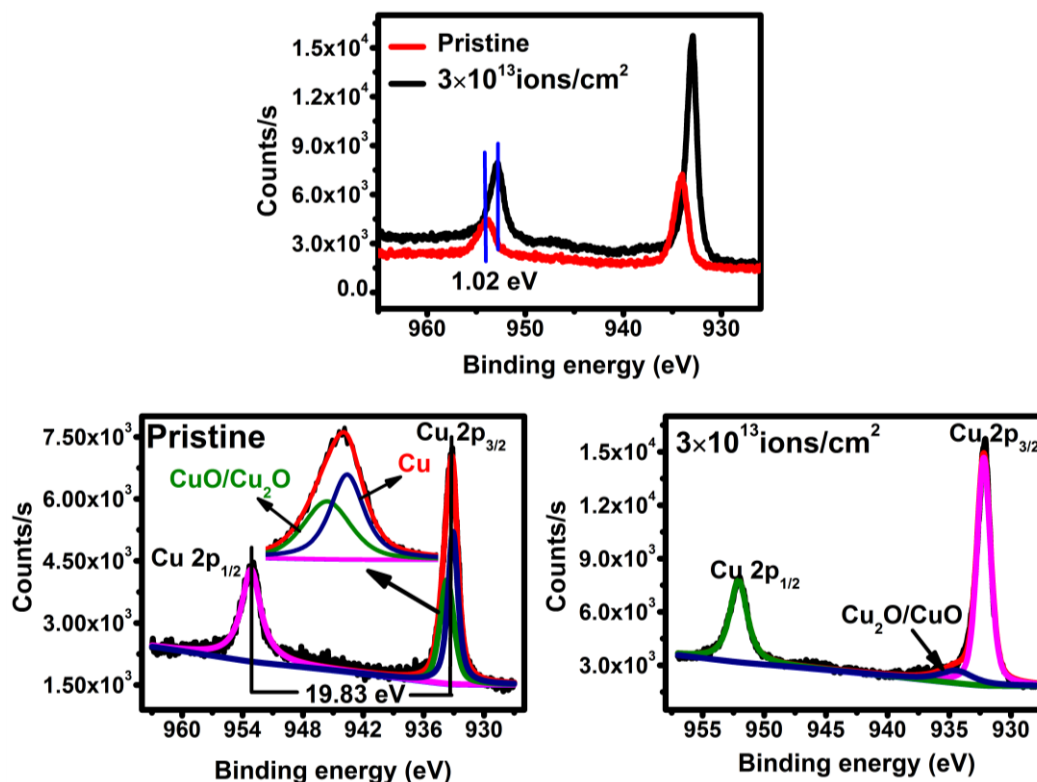
Figure 5.24 (a) Core level scan of Cu 2p peak before and after irradiation (b) core level scan of Cu peak before irradiation (c) core level scan of Cu peak after irradiation.

Supporting to XRD results, XPS results do authenticate the presence of Cu_2O in pristine samples; however, the signature of presence of cu-oxide is rather faint and this is ascribed to the sputtering and etching steps involved in XPS characterization. Moreover, figure 5.24(b) further confirms the presence of oxygen in pristine thin film. These observations are corroborated by results of deconvolution of the same figure thereby ensuring consistency in observations made by various techniques (fig.5.19). It is understood that post deposition oxidation of copper is inevitable. Copper is highly affinitive to oxygen and although deposition is carried out under high vacuum, post deposition exposure to ambient condition is quite conducive to effect oxidation of copper present at the surface layer of the thin film; high surface area to volume ratio is also aiding to such oxidation which however gets devoid of oxygen upon reduction during irradiation for reasons narrated in the current discussion section.

5.3 Conclusions:

Cu(13%)C_{60} nanocomposite thin films can be successfully synthesized on different substrates (glass, silicon and TEM grid substrates) and irradiated by 100 keV Ag ion beam with different fluences from 1×10^{14} ions/cm^2 to 3×10^{16} ions/cm^2. Raman study confirms the transformation of fullerene C_{60} into a-C. UV-visible absorption spectrum shows the SPR around 630 nm for copper and around 435 nm for Ag. At a particular fluence 3×10^{16} ions/cm^2, a broad SPR band is observed.

It is concluded that low energy heavy ion irradiation of Cu (18%)C_{60} nanocomposite thin film causes a shift of SPR band from 622 nm to 644 nm in irradiated sample at the fluence 3×10^{16} ions/cm^2 with concurrent enhancement of intensity. Destruction of fullerene C_{60} takes place due to irradiation and the signature of the amorphization becomes prominent at the fluence 3×10^{16} ions/cm^2. Moreover, there is an appreciable increase in size of copper nanoparticles after irradiation which results in enhancement of the SPR band intensity. Cu (18%) C_{60} nanocomposite irradiated with high energy 120 MeV Ag ion beam. SPR band induced due to presence of copper nanoparticles in fullerene matrix get further enhanced by irradiation. Decrease in band gap with increased conductivity is the result due to transformation of C_{60} into amorphous carbon, increase in average particle size of nanoparticles in irradiated sample is confirmed by XRD and TEM study. XRD and XPS results further confirm the presence of Cu_2O in pristine sample. However, the amount of oxygen component in irradiated samples decrease with increasing fluence. Copper nanoparticles retain the spherical morphology even after irradiation.

REFERENCES

[1] D.K. Avasthi, Y.K. Mishra, R. Singhal, D. Kabiraj, S. Mohapatra and B. Mohanta, Synthesis of plasmonic nanocomposites for diverse applications, *J. Nanosci. Nanotechnol.*, 10 (2010) 2705-2712.

[2] R. Singhal, J.C. Pivin, R. Chandra and D.K. Avasthi, Ion irradiation studies of silver/amorphous carbon nanocomposite thin film, *Surf. Coat. Tech.*, 229 (2013) 50-54.

[3] D.K. Avasthi, Y.K. Mishra, D. Kabiraj, N.P. Lalla and J.C. Pivin,, Synthesis of metal–polymer nanocomposite for optical applications, *Nanotechnology,* 18 (2007) 125604.

[4] A. Liang, Q. Liu, G. Wen and Z. Jiang, The surface-plasmon-resonance effect of nanogold/silver and its analytical applications, TrAc trends in Analytical Chemistry, 37(2012) 32.

[5] Y.K. Mishra, F. Singh, and D.K. Avasthi, Synthesis of elongated Au nanoparticles in silica matrix by ion irradiation, *App. Phys. Lett.*, 91 (2007) 063103-1-3.

[6] Y.K. Mishra, S. Mohapatra, D. Kabiraj, B. Mohanta, N.P. Lalla, J.C. Pivin and D.K. Avasthi, Synthesis and characterization of Ag nanoparticles in silica matrix by atom beam sputtering, *Scripta Materialia*, 56 (2007) 629-632.

[7] J. Hu, P. Liu and L. Chen, Comparison of surface plasmon resonance responses to dry/wet air for Ag, Cu, and Au/SiO2, *App Opt*, 51 (2012) 1357-1360.

[8] E. Ozbay, Plasmonics: Merging photonics and electronics at nanoscale dimensions, *Science*, 311(2006) 189.

[9] H.J. Lezec, A. Degiron, E. Devaux, R.A. Linke, K. Martin-Moreno, F.J. Garcia-Vidal, T.W. Ebbeson, Beaming light from a subwavelength aperture, *Science*, 297 (2002) 820.

[10] M.V. Roldan, A. Frattini, O.D. Sanctis, H. Troiani and N. Pellegri, Characterization and applications of Ag nanoparticles in waveguides, *Appl. Surf. Sci*. 254 (2007) 281-285.

[11] D.R. Mckenzie, C.A. Davis, D.J.H. Cockaynet, D.A. Muller and A.M. Vassallo, The structure of the C_{70} molecule, *Nature*, 355 (1992) 622-624.

[12] K.M. Chen, K. Wu, Y. Chen, Y.Q. Jia, S.X. Jin, C.Y. Li, Z.N. Gu and X.H. Zhou, Heterojunctions of solid C_{70} and crystalline silicon: Rectifying properties and barrier heights, *Appl. Phys. Lett.*, 67 (1995) 1683-1685.

[13] A.W. Jensen, S.R. Wilson and D.I. Schuster, Biological applications of fullerenes, *Bioorg. Med. Chem.*, 4 (1996) 767-779.

[14] A.A. Mohamad and A.W. Allaf, Fullerene-60 thin films for electronic applications, *Synth. Met.* 104 (1999) 39-44.

[15] J. Hou, X. Guo, Active Layer Materials for Organic Solar Cells, Organic Solar Cells. Green Energy and Technology, Springer, London (2013) 17-42.

[16] R. Singhal, D.C. Agarwal, Y.K. Mishra, D. Kabiraj, G. Mattei, J.C. Pivin, R. Chandra and D.K. Avasthi, Synthesis, characterizations, and thermal induced structural transformation of silver-fullerene C_{60} nanocomposite thin films for applications in optical devices, *J. Appl. Phys.* 107 (2010) 2-7.

[17] R. Singhal, DC. Agarwal, YK. Mishra *et al.,* Swift heavy ion induced modifications of optical and microstructural properties of silver–fullerene C_{60} nanocomposite, *Nuclear Instruments and Methods in Physics Research Section B,* 267 (2009) 1349-1352.

[18] R. Singhal, D.C. Agarwal, Y.K. Mishra, F. Singh, J.C. Pivin, R. Chandra, D.K. Avasthi, Electronic excitation induced tuning of surface plasmon resonance of Ag nanoparticles in fullerene C_{70} matrix, *J. Phys. D: Appl. Physics*, 42(2009) 155103

[19] R. Singhal, D.C. Agarwal, S. Mohapatra, Y.K. Mishra, D. Kabiraj, F. Singh, D.K. Avasthi, A.K. Chawla, R. Chandra, G. Mattei and J.C. Pivin*,* Synthesis and characterizations of silver fullerene C_{70} nanocomposite, *Applied Physics Letters,* 93 (2008) 103114.

[20] R. Singhal, J.C. Pivin and D.K. Avasthi, Ion beam irradiation-induced tuning of SPR of Au nanoparticles in fullerene C_{70} matrix: dependence of energy loss, *J Nanopart Res*, 15 (2013) 1641.

[21] C.S. Sundar, A. Bharathi, Y. Hariharan, J. Janaki, V.S. Sastry, T.S. Radhakrishnan, Thermal decomposition of C_{60}, *Solid State Commun.,* 84 (1992) 823.

[22] T. Lee, Min, N.K. Lee HW, J.N. Jang, D.H. Lee, M.P. Hong, K.H. Kwon, The deposition of amorphous carbon thin films for hard mask applications by

reactive particle beam assisted sputtering process, *Thin Solid Films*, 517 (2009) 3999.

[23] J.W. Arbogast, A.P. Darmanyan, C.S. Foote, Y. Rubin, F.N. Diederich, M.M. Alvarez, J. Anz and R.L. Whetten, Photophysical properties of sixty atom carbon molecule (C_{60}), *J. Phys. Chem.*, 95 (1991) 11-12.

[24] G. Chambers, A.B. Dalton, C.M. Evans, H.J. Byrne, Observation and identification of the molecular triplet in C_{60} thin films, *Chem. Phys. Lett.,* 345(2001) 361-366.

[25] G. Xu, M. Tazawa, P. Jin and S. Nakao, Surface plasmon resonance of sputtered Ag films: substrate and mass thickness dependence, *Appl. Phys. A: Mater. Sci. Process.*, 80 (2005) 1535.

[26] Z. Kaminskiene, I. Prosycevas, J. Stonkute and A. Guobiene, Evaluation of Optical Properties of Ag, Cu, and Co Nanoparticles Synthesized in Organic Medium, *Acta Physica Polonica A,* 123 (2013) 111-114.

[27] P.C. Eklund, A.M. Rae, Y. Wang, P. Zhou, K.A. Wang, J.M. Holden, M.S. Dresselhaus, G. Dresselhaus, Optical properties of C_{60} and C_{70} based solid films, *Thin Solid Films*, 257(1995) 211-232.

[28] R. Singhal, F. Singh, A. Tripathi and D. K. Avasthi, A comparative study of ion-induced damages in C_{60} and C_{70} fullerenes, *Radiation Effects & Defects in Solids,* 164 (2009) 38-48.

[29] J. Hu, P.S. Liu, L. Chen, Comparison of Surface Plasmon Resonance Responses to Dry/Wet Air for Ag, Cu, and Au/SiO_2, *Appl. Optics*, 51(2012) 9.

[30] O. Kvítek, J. Siegel, V. Hnatowicz and V. Svorlík, Noble Metal Nanostructures Influence of Structure and Environment on Their Optical Properties, *Journal of Nanomaterials*, 743684(2013) 1-15.

[31] U. Kreibig and M. Vollmer, Optical Properties of Metal Clusters, Springer Series in Materials *Science*, 25 (1995).

[32] U.B. Singh, D.C. Agarwal, S.A. Khan, M. Kumar, A. Tripathi, R. Singhal, B.K. Panigrahi and D.K. Avasthi, Engineering of hydrophilic and plasmonic properties of Ag thin film by atom beam irradiation, *Appl. Surf. Science*, 258 (2011) 1464-1469.

[33] S. Roy, T. Das, Y. Ming, X. Chen , C.Y. Yue, X. Hu, Specific functionalization and polymer grafting on multiwalled carbon nanotubes to fabricate advanced nylon 12 composites, *J. Mater. Chem. A*, 2 (2014) 3961-3970.

[34] K. Spyrou, L. Kang , E.K. Diamanti , R.Y. Gengler, D. Gournis, M. Prato, P. Rudolf, A novel route towards high quality fullerene-pillared graphene, *Carbon*, 61 (2013) 313-320.

[35] Yu S, Liu J, Zhu W, Hu ZT, Lim TT, Yan X, Facile room-temperature synthesis of carboxylated graphene oxide-copper sulfide nanocomposite with high photodegradation and disinfection activities under solar light irradiation, *Scientific Reports,* 5 (2015) 16369.

[36] S. Lotha, A. Ingale, D.K. Avasthi, V.K. Mittal, S. Mishra, K.C. Rustagi, Gupta, V.N. Kulkarnif and D.T. Khathinga, Effect of Heavy Ion Irradiation on C_{60}, *Solid State Communications*, 111 (1999) 55-60.

[37] K. Narumi and H. Naramoto, Modification of C_{60} thin films by ion irradiation *Surface and Coatings Technology*, 158-159 (2002) 364-367.

[38] S. Ghosh, D.K. Avasthi, A. Tripathi, S.K. Srivastava, S.V.S. Nageswara Rao, T. Som, V.K. Mittal, F. Gr€uner and W. Assmann, Studies of electronic sputtering of fullerene under swift heavy ion impact, *Nuclear Instruments and Methods in Physics Research B*, 190 (2002) 169-172.

[39] F.C. Zawislak, D.L. Baptista, M. Behar, D. Fink, P.L. Grande and J.A.H. da Jornada, Damage of ion irradiated C_{60}, *Nuclear Instruments and Methods in Physics Research B*, 149 (1999) 336-342.

[40] K.L. Narayana, M.Yamaguchi, N. Dharmarasu, N. Kojima and D. Kanjilal, Low Energy Ion Implantation and High Energy Heavy Ion Irradiation in C_{60} Films, *Nuclear Instruments and Methods in Physics Research B*, 178 (2001) 301-304.

[41] A. Kumar, F. Singh, R. Kumar, A. Tripathi, D.K. Avasthi and J.C. Pivin, Electrical transport study of structural phase transitions in C_{60} films and the effect of swift heavy ion irradiation, *Solid State Communications*, 138 (2006) 448-451.

[42] A. Kumar, D.K. Avasthi and J.C. Pivin, Electromagnetic properties of ion irradiated C_{60} films, *Surface & Coatings Technology*, 203 (2009) 2703-2706.

[43] A. Kumar, Fouran Singh, D.K. Avasthi and J.C. Pivin, Infrared studies of

swift heavy ion irradiated C_{60} thin films, *Nuclear Instruments and Methods in Physics Research B*, 244 (2006) 221-224.

[44] Y. Maeyoshi , A. Saeki, S. Suwa , M. Omichi , H. Marui , A. Asano , S. Tsukuda , M. Sugimoto , A. Kishimura , K. Kataoka and S. Seki, Fullerene nanowires as a versatile platform for organic electronics, *Scientific Reports*, 2 (2012) 1-6.

[45] N. Bajwa, A. Ingale, D.K. Avasthi, R. Kumar, A. Tripathi, K. Dharamvir and V.K. Jindal, Role of electron energy loss in modification of C_{60} thin films by swift heavy ions, *J. Appl. Physics*, 104 (2008) 054306.

[46] J. Kastner, H. Kuzmany and L. Palmetshofer, Damage and polymerization by ion bombardment of C_{60}, *Appl Phys Lett*, 65 (1994) 543-545.

[47] D. Fink, R. Klett, P. Szimkovick, J. Kastner, L. Palmetshofer, L.T. Chadderton, L. Wang and H. Kuzmany, Ion beam radiation damage of thin fullerene films, *Nuclear Instruments and Methods in Physics Research B,* 108 (1996) 114–124.

[48] D. Fink, L.T. Chadderton, J. Vacik, V. Hnatowicz, F.C. Zawislak, M. Behar and P.L. Grande, Damage and sputtering of fullerene by low energy medium and heavy ions. *Nuclear Instruments and Methods in Physics Research B*, 113 (1996) 244-247

[49] S. Prawer, R. Kalish, M. Adel and V. Richter, Effects of heavy ion irradiation on amorphous hydrogenated (diamond like) carbon films, *J Appl Phys.*, 61 (1987) 4492-4500.

[50] L.R. Doolittle, Algorithms for the rapid simulation of Rutherford backscattering spectra, *Nucl. Instr. and Meth. in Phys. Res. B*, 9 (1985) 344-351.

[51] M. T. Rispens, A. Meetsma, R. Rittberger, C.J. Brabec, N.S. Sariciftci and J.C. Hummelen, Influence of the solvent on the crystal structure of PCBM and the efficiency of MDMO-PPV:PCBM 'plastic' solar cells, *Chem. Commun.*,17 (2003) 2116 – 2118

[52] W. Ma, C. Yang, X. Gong, K. Lee, A. J. Heeger, Thermally Stable, Efficient Polymer Solar Cells with Nanoscale Control of the Interpenetrating Network Morphology, Adv. Funct. Mater. 2005, 15, 1617-1622.

[53] K. Kelly, E. Coronado, L.L. Zhao, and G.C. Schatz, The optical properties of metal nanoparticles: The influence of size, shape, and dielectric environment, *J. Phys. Chem. B* 107 (2003) 668-677.

[54] E. Hutter and J.H. Fendler, Exploitation of Localized Surface Plasmon Resonance, *Adv. Mater.*, 16 (2004) 1685-1706.

[55] L.L. Beecroft and C.K. Ober, Nanocomposite Materials for Optical Applications, *Chem. Mater.*, 9 (1997) 1302-17.

[56] K.C. Lee, S.J Lin, C.H. Lin, C.S. Tsai, Y.J. Lu, Size effect of Ag nanoparticles on surface plasmon resonance, *Surface & Coatings Technology*, 202 (2008) 5339-5342.

[57] V. Amendola, R. Pilot, M. Frasconi1, O. M Marago, M.A. Iatì, Surface plasmon resonance in gold nanoparticles: a review, *J. Phys.: Condens. Matter*, 29 (2017) 203002.

[58] H. Takele, H. Greve, C. Pochstein, V. Zaporojtchenko and F. Faupe, Plasmonic properties of Ag nanoclusters in various polymer matrices, *Nanotechnology*, 17 (2006) 3499–3505

[59] J. Rozra, I. Sain, A. Sharma, N. Chandak, S. Aggarwal, R. Dhiman and P.K. Sharma, Cu nanoparticles induced structural, optical and electrical modification in PVA, *Materials Chemistry and Physics*, 134 (2012) 1121-1126.

[60] P. Ling, Z. Ran, C. Shufen, Z. Qin, D. Lingling, F. Xiaomiao and H. Wei, Highly efficient dual-plasmon polymer solar cell incorporating Au@SiO$_2$ core–shell nanorods and Ag nanoparticles, *RSC Adv.*, 6 (2016) 90944-9095.

[61] A.C. Ferrari and J. Robertson, Interpretation of Raman spectra of disordered and amorphous carbon, *Physical Review B*, 61(2000) 14095.

[62] J. Robertson, Diamond-like amorphous carbon, *Material Science and Engineering R Reports*, 37 (2002) 129-281.

[63] V.N. Rai and A.K. Srivastava, Correlation between optical and morphological properties of nanostructured gold thin film, *JSM Nanotechnol Nanomedicine*, 4 (2016) 1039.

[64] S. Link and M.A. El-Sayed, Spectral Properties and Relaxation Dynamics of Surface Plasmon Electronic Oscillations in Gold and Silver Nanodots and Nanorods, *J. Phys. Chem. B*, 103 (1999) 4212-4217.

[65] O.A. Yeshchenko, I.M. Dmitruk, A.A. Alexeenko, A.V. Kotko, J. Verdal and A.O. Pinchuk, Size and Temperature Effects on the Surface Plasmon Resonance in Silver Nanoparticles, *Plasmonics*, 7 (2012) 685-694.

[66] C.U. Devi, A.K. Sharma and V.V.R.N. Rao, Electrical and optical properties of pure and silver nitrate-doped polyvinyl alcohol films, *Mater. Lett.,* 56 (2002) 167.

[67] B.D. Cullity, Elements of X-Ray Diffraction, Addison Wesley Pub.Co., (1978).

[68] S. Yu, J. Liu, W. Zhu, Z.T. Hu, T.T. Lim and X. Yan, Facile room-temperature synthesis of carboxylated graphene oxide-copper sulfide nanocomposite with high photodegradation and disinfection activities under solar light irradiation, *Scientific Reports,* 5 (2015)16369.

Chapter 6

Study the Effect of Low and High Energy Ion Beam Irradiation on Copper-Fullerene C_{70} Nanocomposite Thin Films.

6.1 To Observe the Effect of Low Energy Ion Beam Irradiation on Copper-Fullerene C_{60} Nanocomposite Thin Films

Among the different kinds of nanocomposites synthesized so far, noble metal nanoparticles encapsulated in fullerenes yield a good combination of optical properties with electrical conductivity and chemical inertia. [1]. Among the many potential applications of fullerenes [2-5], the use of fullerene as "organic photovoltaic" is of interest in the present study. It is known that, fullerene C_{60} and C_{70} exhibit the capacity to be reversibly reduced with up to six electrons. This high electron affinity is the resultant of triply-degenerate low-lying LUMOs (lowest unoccupied molecular orbital). Although, fullerene C_{60} is the most common derivative used in photovoltaic, the power conversion efficiency of C_{70} is 25% higher than that of C_{60}. Moreover, the efficiency of organic solar cells based on fullerene matrix can be further enhanced by incorporating noble metal nanoparticles. These nanoparticles are in use since pre-historic times for coloring glasses, the phenomenon originating from optical absorption in some range of wavelength by way of surface plasmon resonance (SPR). This interesting property (SPR) comes in picture as the nanoparticles diameter becomes comparable or smaller than the wavelength of the incident light. Earlier workers have investigated SPR of Ag, Au and Cu particles embedded in C_{60} or in C_{70}, with different compositions and precipitation processes including ion irradiation [6-10]. R. Singhal et al. have reported the tuning of the SPR in fullerene based metal nanocomposites by means of swift heavy ion irradiation [6-7]. This induced and tuned SPR has been explained on the basis of the dependence of SPR band on different factors such as size of nanoparticles, structure and refractive index of the surrounding matrix [11-14].

The motivation behind the present study is to achieve improved absorption of light by incorporating metal nanoparticles in fullerene C_{70} matrix for application in plasmonic organic solar cells. More the absorption of light more becomes the number of charge carriers and hence there is improved efficiency and better performance of solar cells. In plasmonic technology Au and Ag have so far been preferred because of their strong absorption but the present study is based on incorporation of Cu metal in fullerene C_{70} matrix because copper is less expensive, abundant, and possesses high thermal and

electrical conductivity and exhibits similar absorption behavior (SPR) to Ag and Au. Ion irradiation by 350 keV Ar ion beam produces atomic displacements and atomic defects which are likely to promote diffusion; this is expected to give rise to enhance precipitation of Cu particles. It is important to note that the present study involves low energy ion irradiation with electronic energy loss (S_e) and nuclear energy loss (S_n) being about ~71.37 eV/Å and ~28.36 eV/Å respectively. However, the Se for 350 keV Ar ion irradiation appears to be smaller than the threshold for ion track creation; therefore, the expected modifications to be produced in the fullerene C_{70}-copper nanocomposite thin films, will be mainly determined by nuclear energy loss S_n leading to collision cascade. Hence attempts are made to qualify the influence of low energy heavy ion irradiation on the changes in structure and properties of a C_{70}-10at% Cu nanocomposite thin film.

6.1.1 Experimental Details:

Thin films of Cu-C_{70} nanocomposite have been deposited by thermal co-evaporation technique in a high vacuum chamber, on different types of substrates such as glass, silicon and TEM grids. Copper (Cu) powder and fullerene C_{70} powder were taken in two different tungsten (W) boats, weighing 0.14g and 0.07 g, respectively. Separate deposition rates set for fullerene C_{70} and Cu powder evaporation were 0.45 Å/sec and 0.05 Å/sec, respectively. The deposition was started with the combined rate at ~0.5 Å/sec. To maintain low contamination, deposition is done in high vacuum at a pressure of 8.4×10^{-6} mbar.

The as-deposited Cu (10%)-C_{70} thin films were irradiated with 350 keV Ar ion beam using Low energy ion beam facility (LEIBF) at Inter University Accelerator Centre (IUAC), New Delhi. The projectile range of the 350 keV Ar ions through the Cu(10%)-C_{70} nanocomposite thin films is ~ 334.6 nm as determined by the Stopping and Range of Ions in Matter (SRIM) program, which is larger than the thickness (~ 30 nm) of the Cu(10%)-C_{70} nanocomposite thin films. It confirms that all the Ar ions are embedded into the substrate after passing through the nanocomposite thin films. The corresponding electronic energy loss (S_e) and nuclear energy loss (S_n) are ~ 7.13×10^1 eV/Å and ~ 2.83×10^1 eV/Å, respectively. The films were irradiated at fluences of 1×10^{13}, 3×10^{13}, 1×10^{14}, 3×10^{14}, 1×10^{15}, 3×10^{15}, 1×10^{16} and 3×10^{16} ions/cm^2.

The composition and thickness of the deposited films were determined by means of Rutherford Backscattering Spectrometry (RBS) as per details given in Chapter 3. Optical characterization is done by the UV-visible absorbance spectra with a U-3300 UV-visible spectrometer of Hitachi Company. Raman spectra of the pristine and irradiated films were recorded AIRIX STR 500 confocal micro Raman spectrograph (Airix make). Atomic force microscopy (AFM) images were recorded with a Bruker AFM Analyzer before and after irradiation; SEM study was with the aid of Nova Nano FE-SEM 450 Field Emission Scanning Electron Microscope (FEI make). Conductivity measurements were performed by using two probe methods with an Agilent Semiconductor device. XPS analyses of the chemical structure were studied by an Omicron nanotechnology device (model- ESCA+).

6.1.2 Result & Discussions:

6.1.2.1 RBS analysis:

A typical RBS spectrum of a film containing Cu and C (supposed to be a composite of Cu nanoparticles embedded in fullerene C_{70} matrix) on Si substrate is shown in figure 6.1.
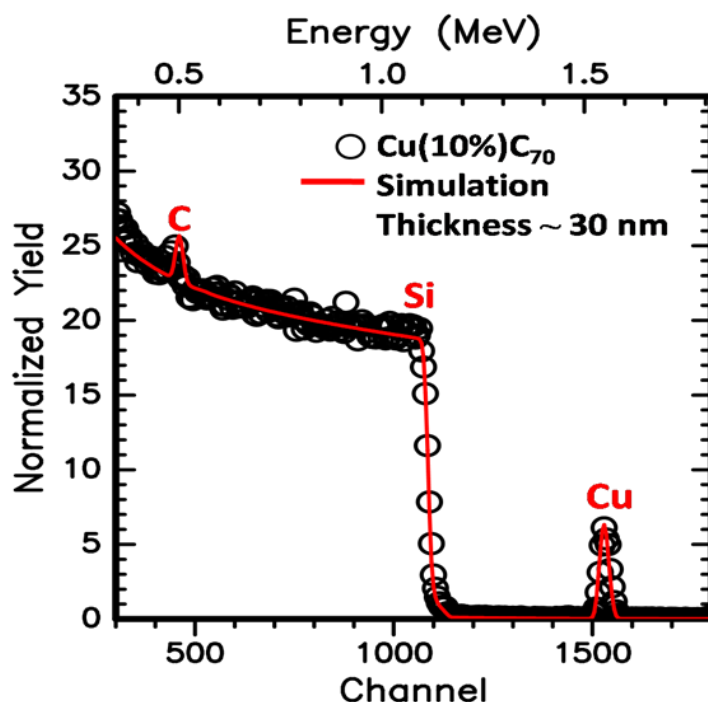
Figure 6.1 Rutherford backscattering spectrum of Cu-C_{70} nanocomposite film on Si substrate.

A fit of the experimental data by a simulation using the RUMP code [16-17] is also shown. The increase of scattering yield below 300 keV in the spectrum is due to the occurrence of multiple scattering structures when the ion energy becomes too low.

The observed decrease in the spectrum around channel 400 is presumably due to the non-Rutherford scattering cross-section from Si atoms. The scattering cross section of C atoms is known to be less than that of Si substrate atoms (as it varies as the square of atomic number) and the ions scattered by C atoms produce only a small peak around 500 keV imposed over the plateau, which corresponds to scattering of ions by Si atoms. Nevertheless, the thickness of C+Cu deposited on the Si substrate is given with an accuracy of 1nm by the shift of the threshold k_{Si} , which is due to the electronic energy loss of ions in the film before being scattered by Si atoms. The thickness of the film can also be checked from the width of the Cu peak at around 1500 keV (threshold of scattering by Cu atoms k_{Cu}) , whose area gives the exact number of Cu atoms. The concentration of Cu is estimated to be of 10 at% and the thickness of the film to 30 nm assuming that it has the atomic density of bulk fullerene C_{70}.

6.1.2.2 UV-visible absorption spectroscopy:

The representative UV-visible absorption spectra of pristine C_{70} and Cu (10%) C_{70} are shown in figure 6.2. It can be seen that the features in absorbance spectrum of Cu (10%) C_{70} nanocomposite thin film is qualitatively similar to the spectrum of pristine C_{70}. But all absorbance bands of Cu (10%) C_{70} nanocomposite thin film is broader than pristine C_{70} thin film. This is due to the presence of Cu nanoparticles into fullerene C_{70} matrix.

It can be seen that pristine Cu-C_{70} nanocomposite thin film showed no strong absorption band of the Cu nanoparticles which is around 550 nm-650 nm. This may be attributed to the low metal (Cu) concentration in fullerene C_{70} matrix [10].

Figure 6.3 shows the UV-visible absorption spectrum of pristine film and those irradiated at different fluences 1×10^{13}, 3×10^{13}, 1×10^{14}, 3×10^{14}, 1×10^{15}, 3×10^{15}, 1×10^{16} and 3×10^{16} ions/cm^2. With increasing fluence, the shallow absorption bands observed in the pristine film is seen to gradually disappear due to irradiation by 350 keV Ar ion beam; this may be ascribed to the amorphization of fullerene C_{70} matrix. This

observation persists till a fluence of 3×10^{14} when a very flat curve is seen. This indicates amorphization of matrix and is typical of any organic material as also semiconductors under any kind of irradiation.
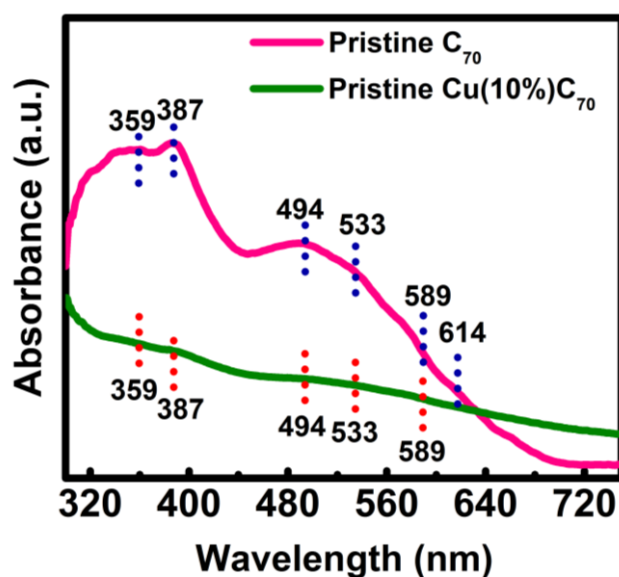
Figure 6.2 UV-visible absorption spectra of fullerene C_{70} thin film and Cu (10%)-C_{70} nanocomposite thin films.

With further increase in fluence (1×10^{15} ions/cm^2), a new absorption band arises at around 627 nm, which corresponds to SPR oscillations in Cu nanoparticles embedded in C_{70} matrix of refractive index of 2.3. The absorption bands for copper nanoparticles has been reported to be in the range of 550-650 nm depending on the surrounding environment i.e. matrix [18-19].

The precipitation of Cu nanoparticles is confirmed by TEM analysis. With further increase in fluence, the SPR absorption band becomes more intense and blue shifted. At particular highest fluence, the Cu nanoparticles SPR shifted to lower wavelength at ~ 603 nm. The position of SPR bands depends on various factors among which the type of metal and dielectric constant of matrix are very important. The size of nanoparticles also affects this position of SPR band but more specifically it increases the width of the band; it becomes minimum when valency electrons are delocalized in bulk metal and particles behave as dipoles in Maxwell equations (radii of 10 to 30 nm). The other important factor affecting the SPR position and width is the mutual polarization of the particles when their volume concentration becomes noticeably

higher, typically above 5%. Now to examine the variation in the size of nanoparticles with irradiation, the average particle size is calculated from absorption spectra. As there is no SPR in case of pristine Cu-C$_{70}$ nanocomposite thin film due to low concentration of Cu metal, the average particle size in the nanocomposite can be calculated for the films irradiated with fluence 1×10^{15} ions/cm^2 and higher fluence.
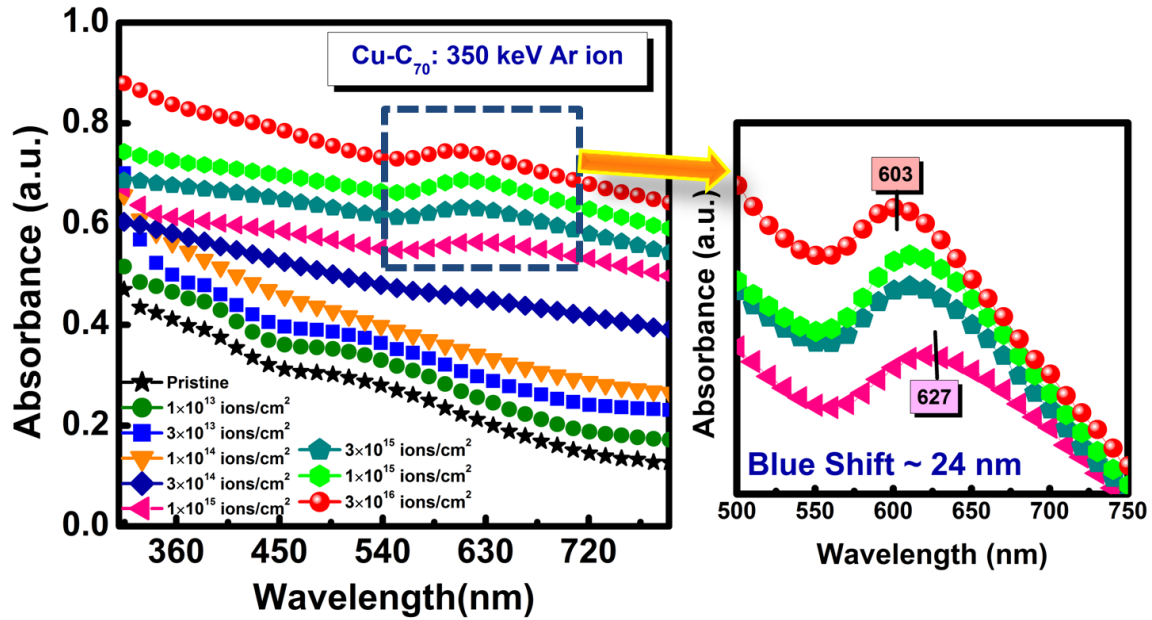
Figure 6.3 UV-visible absorption spectra of pristine and 350 keV Ar ion irradiated Cu (10%)-C$_{70}$ nanocomposite thin films.

Now from the absorption spectra, the average particle size can be estimated with a consideration that conduction electron is behaving as free particles with the following formula [20].

$$R_{NP} = v_F \Delta\tau \tag{6.1}$$

Here R$_{NP}$ is the average radius of nanoparticles (in present case Cu nanoparticles), $\Delta\tau$ is the mean free time of the conduction electrons in the nano-sized metal particles and v_F is the Fermi velocity of electrons in bulk copper (for Cu = 1.57×10^6 m/s). Above equation can be further modified with the application of Heisenberg Uncertainty principle relation as

$$\Delta\tau = \frac{\hbar}{\Delta E} \tag{6.2}$$

Here $\hbar$ is the Planks constant; energy spread ΔE can be calculated from the FWHM of the optical absorption band of UV-visible absorption graph between absorbance and energy (eV)

Hence equation (i) can be written as

$$R_{NP} = v_F \frac{\hbar}{\Delta E} \qquad (6.3)$$

The average particle size of nanoparticles can be calculated from the following equation

$$D = 2R_{NP} = 2v_F \frac{\hbar}{\Delta E} \qquad (6.4)$$

Here, D is the average diameter of the nano-sized particles [21]. The variation of average particle size of Cu nanoparticles estimated with the above formula is tabulated in table 6.1. The average particle size increases from 4.75 nm (at fluence 1×10^{15} ions/cm^2) to 5.94 nm (at fluence 3×10^{16} ions/cm^2). This increase in particle size is due to agglomeration of nanoparticles at higher fluences. The shift (red or blue) in SPR peak is attributed to the change in refractive index of matrix and size and shape of nanoparticles. In the present study, there is a slight change in the size of nanoparticles (confirmed from TEM analysis in section 3.4) which is generally responsible for red shift; but complete transformation of fullerene to amorphous carbon is also observed. Thus, the phase change of host matrix appears to have dominated over the change in size of nanoparticles. This has caused the observed blue shift of ~24 nm in SPR peak of Cu nanoparticles.

6.1.2.3 Raman analysis:

Figure 6.4 (a-i) shows the Raman spectra of pristine and irradiated thin films at different fluences 1×10^{13}, $3 \times 10^{13,}$ 1×10^{14}, 3×10^{14}, 1×10^{15}, 3×10^{15}, 1×10^{16} and 3×10^{16} ions/cm^2, respectively. Figure 6.4 (a) shows Raman spectrum of pristine Cu-C$_{70}$ nanocomposite thin film with Raman bands at 266, 459, 569, 738, 1066, 1179, 1230, 1333, 1467 and 1569 cm^{-1}, respectively which corroborates the observation made by other researchers [22-24]. Despite the lack of well defined absorption bands in the UV-visible absorption spectra, the occurrence of C$_{70}$ Raman scattering bands attest

the signature of the existence of fullerene balls and their semi crystalline packing. 10% Cu dispersed in the matrix does not affect much the vibration bands of matrix.
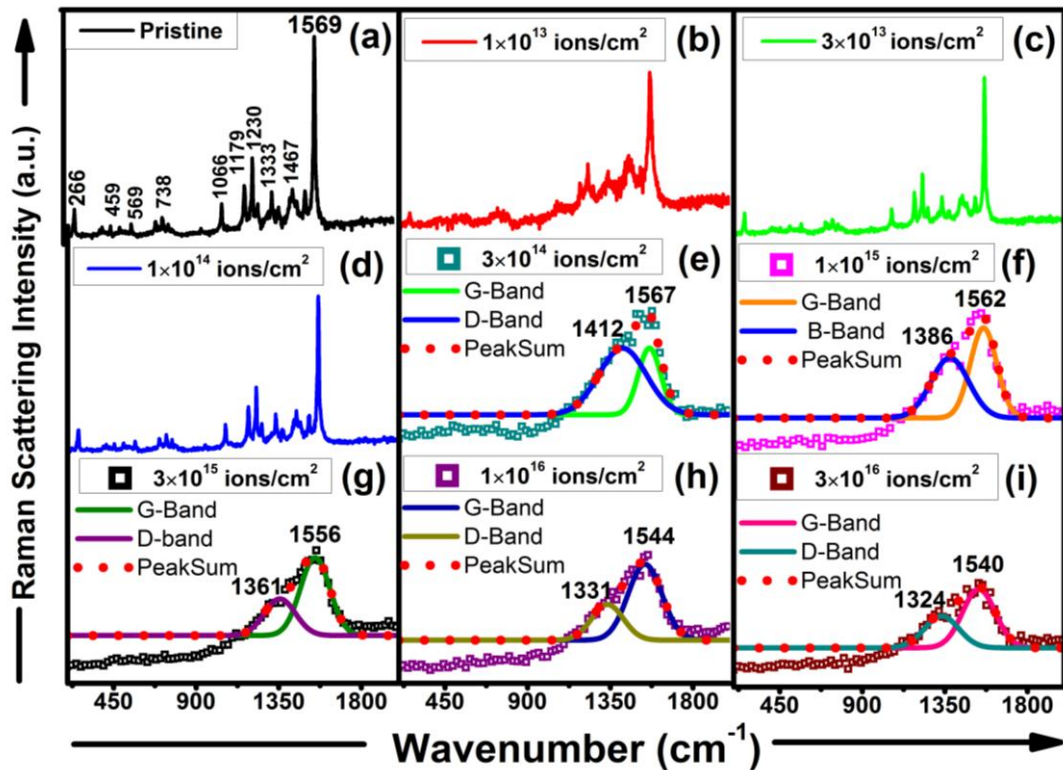
Figure 6.4 Raman spectra of pristine and 350 keV Ar ion irradiated Cu (10%)-C_{70} nanocomposite thin films.

Upon irradiation the intensity of Raman active bands appears to decrease first (not significantly up to fluence 1×10^{14} ions/cm^2).

Further increase in fluence produces new vibration modes as characterized by two broad bands, at 1412 cm^{-1} and 1567 cm^{-1}; these are typical of amorphous carbon and are called D band (as disorder) and G band (as graphite like). Sp^3 bonded carbons have a much lower scattering cross section with excitation in the visible band and produce a narrow band at 1350 cm^{-1}. The position and width of G and D bands depends mainly on the size of sp^2 rings or chains (purely sp2 clusters): in diamond like carbon they are well separated whereas in evaporated carbon with about 20% of sp3 bonds they merge at 1500 cm^{-1} and in the case of nanocrystalline graphite the G peak occurs at 1610 cm^{-1}.

In the present case the centre of D and G bands seems to have shifted to 1324 and 1540 cm^{-1} at the highest fluence of 3×10^{16} ions/cm$^{2.}$ in accordance with Gaussian fit; however strong overlapping of bands is accountable to random packing of molecules [25-26].

6.1.2.4 TEM analysis:

The crystallinity of the nanocomposite thin film has been determined with the aid of *Transmission Electron Spectroscopy*. Figure 6.5 (a-d) depicts the TEM image, particle size distribution, selected area electron diffraction (SAED) pattern and HRTEM micrograph of pristine Cu (10%)-C$_{70}$ nanocomposite thin film.

Figure 6.5 (a) and inset in figure 6.5(a) confirms that the morphology of the nanoparticles is nearly spherical. Figure 6.5 (b) represents the particle size distribution of copper nanoparticles embedded in fullerene C$_{70}$ thin film. The average size calculated for pristine Cu-C$_{70}$ nanocomposite thin film comes out to be ~ 2.4 nm. Figure 6.5 (c) shows the SAED pattern of pristine Cu-C$_{70}$ nanocomposite thin film with marked planes suggesting the presence of cubic Cu phase. HRTEM images in figure 6.5(d) confirms the presence of copper nanoparticles within the matrix.
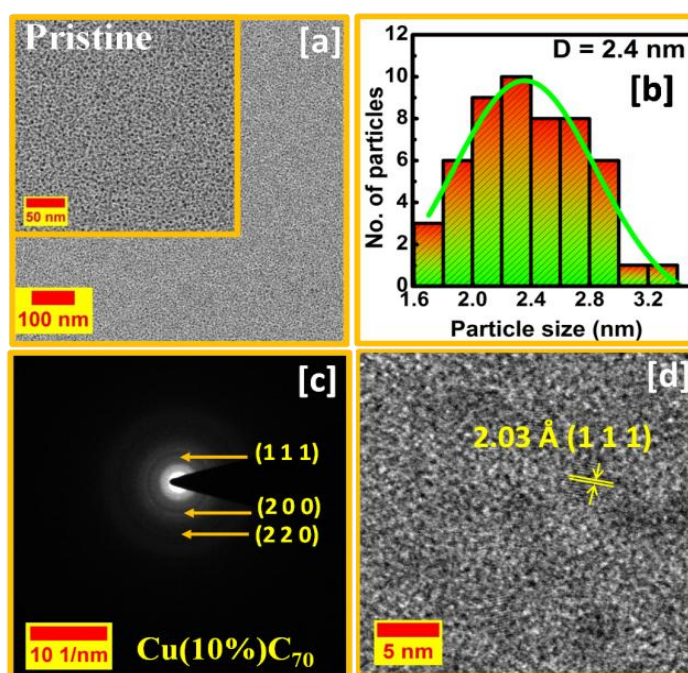
Figure 6.5 (a) TEM image, (b) particle size distribution, (c) SAED pattern and (d) HRTEM image of pristine Cu (10%)-C$_{70}$ nanocomposite thin film.

In order to see the effect of low energy 350 keV Ar ion irradiation on the morphology and crystallinity of the nanocomposite thin film, TEM measurements are also performed on the sample irradiated with highest fluence 3×10^{16} ions/cm^2. Figure 6.6 (a-d) shows the TEM image, particle size distribution, SAED pattern and HRTEM
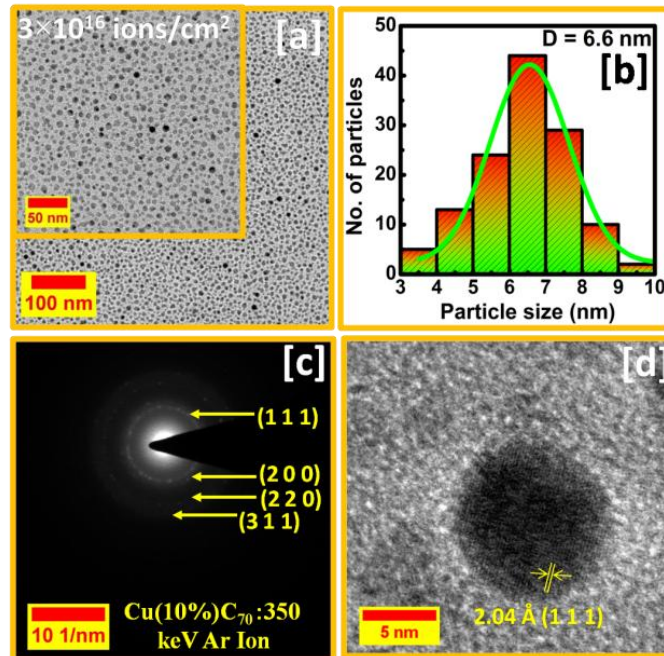
Figure 6.6 (a) TEM image, (b) particle size distribution, (c) SAED pattern and (d) HRTEM image of 350 keV Ar ion irradiated Cu (10%)-C$_{70}$ nanocomposite thin film.

image for 350 keV Ar ion irradiated at a fluence of 3×10^{16} ions/cm^2. As in pristine sample, nearly spherical morphology of the particles is retained at higher fluence.

Table 6.1 Represents the variation of average particle size calculated with UV-visible absorption spectroscopy and TEM analysis.

Fluence (ions/cm^2)	Average particle size (nm) (UV-visible absorption spectroscopy analysis)	Average particle size (nm) (TEM analysis)
Pristine	--	2.4
1×10^{15}	4.75	
3×10^{15}	5.21	--
1×10^{16}	5.77	--
3×10^{16}	5.94	6.6

The particle size distribution is shown in figure 6.6 (c) and statistically determined average particle size is found to be about 6.6 nm (table 6.1). The increase in particle

size after irradiation is due to agglomeration of the particles [27-28]. Both SAED and HRTEM images in figure 6.6(c) and (d) confirm the presence of copper.

6.1.2.5 Surface analysis:

To study the irradiation effects on the surface morphology of Cu (10%)-C_{70} nanocomposite thin films, atomic force microscopy has been performed and presented in Figure 6.7 (a-i) which show two dimensional (2-D) AFM images of Cu (10%)-C_{70} nanocomposite thin film and irradiated with 350 keV Ar ion at different fluences (1×10^{13}, 3×10^{13}, 1×10^{14}, 3×10^{14}, 1×10^{15}, 3×10^{15}, 1×10^{16} and 3×10^{16} ions/cm^2).

Table 6.2 Represents the variation of roughness with 350 keV Ar ion irradiation.

Fluence (ions/cm^2)	Roughness (nm)
Pristine	2.88
1×10^{13}	2.62
3×10^{13}	3.31
1×10^{14}	3.76
3×10^{14}	4.28
1×10^{15}	4.36
3×10^{15}	2.03
1×10^{16}	1.89
3×10^{16}	1.64

These 2-D AFM images depict the surface modification in different ways at different fluence which usually happens in case of low energy ion irradiation, as because the damage takes place mostly over the surface. Since there is surface modification for each of fluence, there is also variation in roughness of the Cu (10%)-C_{70} nanocomposite thin films. The calculated roughness values for pristine and 350 keV Ar ion irradiated Cu (10%)-C_{70} nanocomposite thin film are tabulated in table 6.2 and shown in figure 6.8. From table 6.2 it is clear that, with the increase in fluence, roughness of the nanocomposite thin films also increases up to a fluence of 1×10^{15} ions/cm^2.

As stated earlier, this increment in roughness with fluence is due to ion bombardment on the nanocomposite thin films that results in sputtering of the film. Apart from this, it is clear from figure 6.7 that up to a particular fluence of 3×10^{14} ions/cm^2 there are discrete modifications in surface morphology over the whole surface of nanocomposite thin film. This is the reason for such increase in roughness. Apart

from this, the sputtering that takes place at the initial fluences leads to enhancement in surface roughness. With further increase in the fluence, the roughness of the film is seen to have decreased.
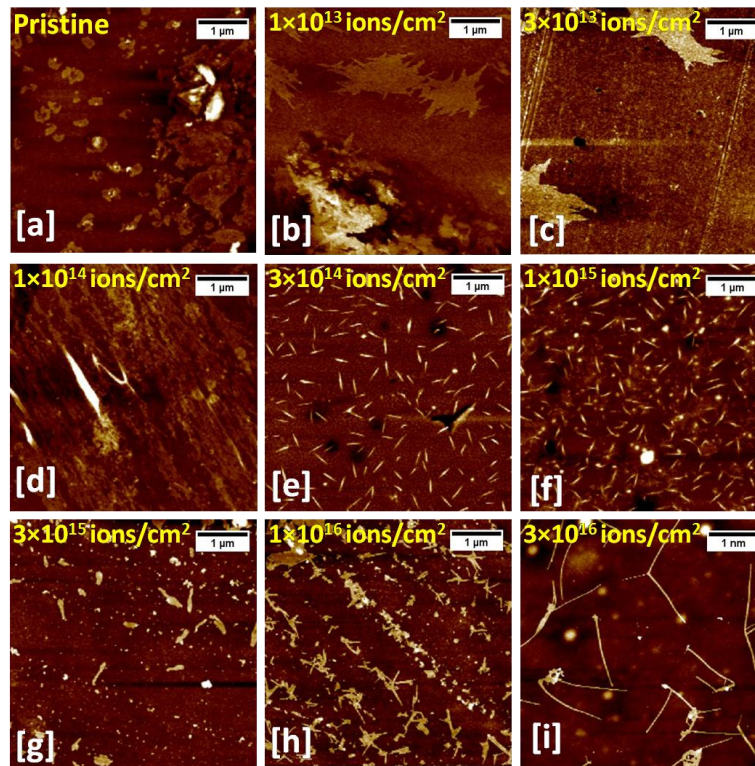
Figure 6.7 2-D AFM images of pristine and 350 keV Ar ion irradiated Cu (10%)-C_{70} nanocomposite thin films.

The change in surface morphology is discontinuous at lower fluence and becomes continuous at higher fluences, thereby making the films smoother.
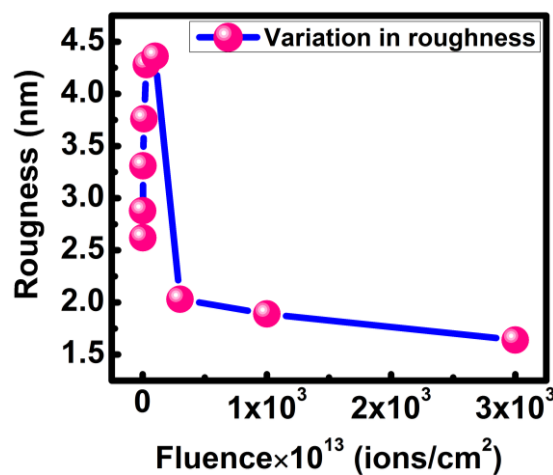
Figure 6.8 Variation of roughness of Cu (10%)-C_{70} nanocomposite thin films with ion irradiation.

The features which are evolved with irradiation on the surface of nanocomposite thin film are further investigated with scanning electron microscope (SEM) characterization.

Figure 6.9 (a-i) represents the SEM images of pristine and 350 keV Ar ion irradiated nanocomposite thin films at different fluences from 1×10^{13} to 3×10^{16} ions/cm^2. From the SEM images, almost same surface features are observed in thin films irradiated at different fluences. This observation is harmonious with AFM results.
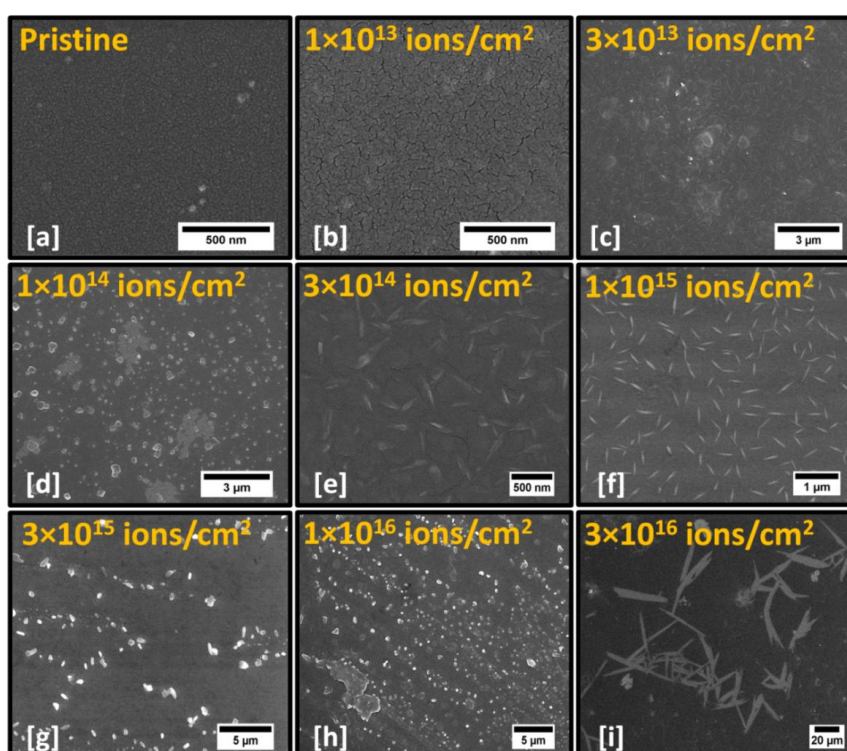
Figure 6.9 SEM images of pristine and 350 keV Ar ion irradiated Cu (10%)-C$_{70}$ nanocomposite thin films.

6.1.2.6 Conductivity measurements:

In the present study, two probe I-V measurements have been performed to analyze the change in resistivity of Cu-C$_{70}$ nanocomposite thin films irradiated with 350 keV Ar ion. Figure 6.10 (a-i) represents the IV graph for pristine and low energy 350 keV Ar ion irradiated Cu-C$_{70}$ nanocomposite thin films with fluences as 1×10^{13}, 3×10^{13} 1×10^{14}, 3×10^{14}, 1×10^{15}, 3×10^{15}, 1×10^{16} and 3×10^{16} ions/cm^2, respectively. The estimated values of resistivity for pristine and irradiated films are tabulated in table 6.3.
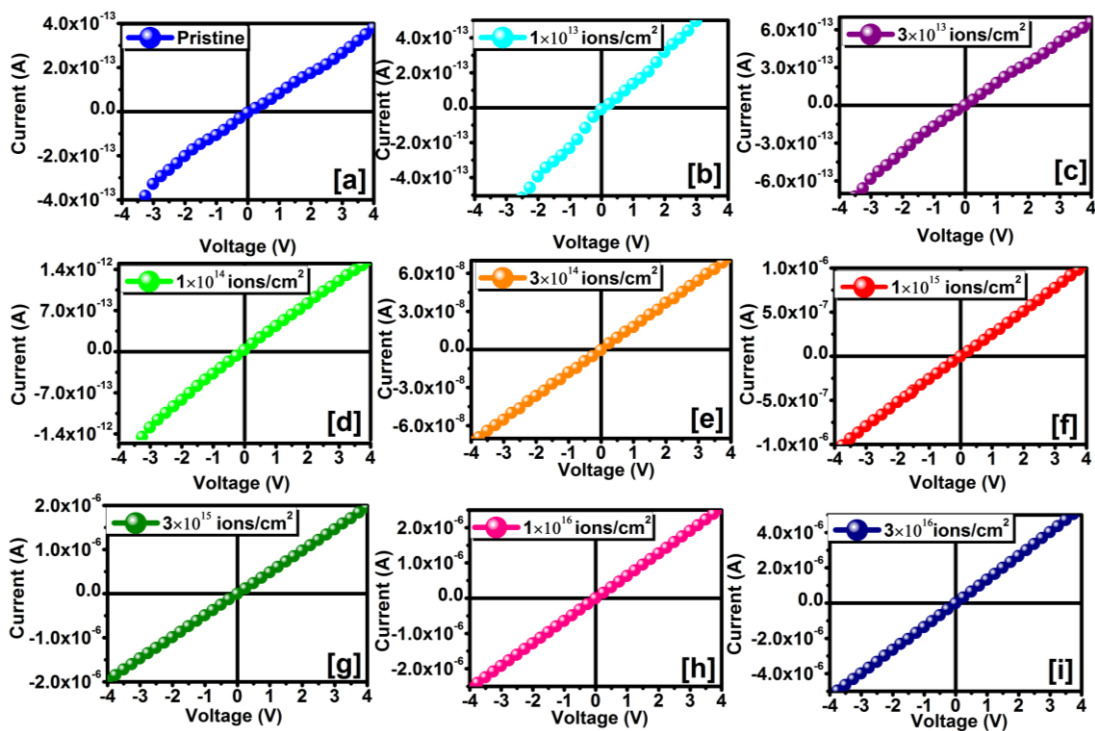
Figure 6.10 (a-i) Plot between current (I) and voltage (V) for pristine and 350 keV Ar ion irradiated Cu (10%)-C$_{70}$ nanocomposite thin films.

The reinforcement of copper nanoparticles makes Cu-C$_{70}$ nanocomposite thin film more conductive as compared to pure C$_{70}$ thin films. From table 6.3 it is observed that resistivity decreases with increase in fluence in the irradiated samples.

Table 6.3 Represents the variation of resistivity with 350 keV Ar ion irradiation.

Fluence (ions/cm^2)	Resistivity (Ω-cm)
Pristine	2.7×10^7
1×10^{13}	1.6×10^7
3×10^{13}	1.5×10^7
1×10^{14}	6.9×10^6
3×10^{14}	1.6×10^2
1×10^{15}	1.1×10^2
3×10^{15}	6.1×10^1
1×10^{16}	4.6×10^1
3×10^{16}	2.3×10^{-2}

Since the conductivity of a-C is higher as compared to fullerene C$_{70}$, the transformation of fullerene C$_{70}$ matrix into a-C makes the films more conductive [29]. This also supports the Raman spectroscopy results indicating the transformation of fullerene into amorphous carbon. The decrease in resistivity from 10^7 Ω-cm to 10^{-2} Ω-

cm as observed in the present study, due to the presence of copper nanoparticles of increasing size with 350 keV Ar ion beam irradiation as verified by TEM.

6.1.2.7 XPS analysis:

XPS study is carried out with pristine and irradiated samples in order to acquire detailed information about the modification effected by low energy ions at surfaces. The survey scan spectra of the pristine and irradiated Cu-C$_{60}$ composite films at a fluence of 3×10^{16} ion/cm^2 are illustrated in figure 6.11. The spectra confirm the presence of all the major elements (C, Cu, and O,) of the deposited composite films corresponding to their binding energy. Also Auger peaks of Cu LMM3 and LMM are also observed. However absence of any peak corresponding to any impurity or contamination suggests that the films are free from impurities or any contamination.
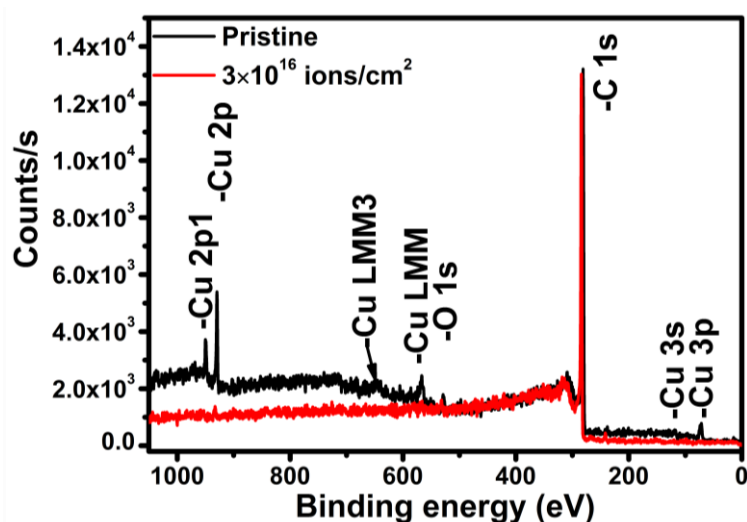
Figure 6.11 Survey scan spectra of pristine and 350 keV Ar ion irradiated Cu-C$_{70}$ nanocomposite thin films.

Further, core level scan of the Cu 2p peak is done in order to see if any modification takes place by ion beam. Figure 6.12 (a-c) shows the core level scan for the pristine and irradiated Cu-C$_{60}$ composite films at a fluence of 3×10^{16} ion/cm^2. The spectrum for pristine thin film has two intense peaks located at 934.16 and 954.13 eV and can be allocated to Cu2p$_{3/2}$ and Cu2p$_{1/2}$ spin-orbital components, respectively [30-31].

For the irradiated thin film the peak positions is shifted a little bit towards lower binding energy which may be due to the change in the host environment after irradiation. Furthermore, no satellite peak could be observed in the pristine as well

as irradiated thin film, corresponding to Cu^{2+} species which is indicative of the absence of CuO in the thin films.
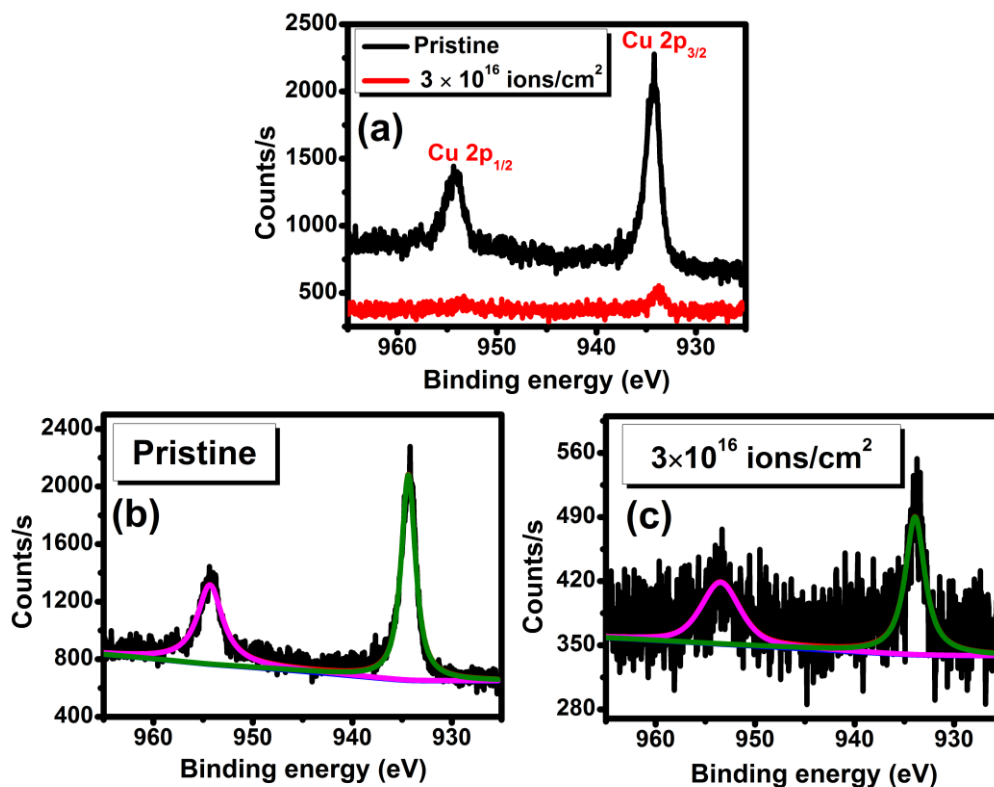
Figure 6.12 Core level scans for Cu 2p of Cu-C_{70} nanocomposite thin films before and after irradiation.

The survey scan spectra of the pristine films and that irradiated at a fluence of 3×10^{16} ion/cm^2 are displayed in Figure 6.12. The spectra confirm the presence of all the major elements (including O which is always present on surfaces). Spectra of Cu 2p core level (Figure 6.12 (a-c)) show the usual spin orbit splitting as Cu $2p_{3/2}$ and Cu $2p_{1/2}$, with main binding energies of 934.16 and 954.13 eV for the pristine and irradiated thin film at fluence 3×10^{16} ion/cm^2 which corroborate to the values available in handbooks for Cu metal.

6.2 To Observe the Effect of High Energy Ion Beam Irradiation on Copper-Fullerene C_{60} Nanocomposite Thin Films

The effects of high energy ion irradiation on the behavior of noble metal–C_{60}/C_{70} are well documented in literature [6-10]. However the copper–C_{60}/C_{70} nanocomposites under irradiation by high energy ion beam are yet to be studied in details. In chapter 5, the results of high and low energy ion beam on the modifications in structural properties of copper C_{60} nanocomposites are critically analyzed. The observations in there stimulated further research on irradiation of Cu-C_{70} by ion beam of different energy range. As a token of accomplishing the task, the discussion on the results of experiments with low energy ion beam irradiated (350 keV Ar) Cu-C_{70} nanocomposite thin films has been presented in previous section i.e. 6.1. In the line of observations on the appearance of SPR only at higher fluences, it is a matter of scientific interest to explore if high energy heavy ion beam (120 MeV Ag) irradiation produces any other interesting results. Moreover, it is important to understand the effect of such irradiation on characteristic growth of nanoparticles and the concurrent change in refractive index of fullerene C_{70}. This is because the size of nanoparticles and the properties of surrounding host matrix are the deciding factors for the intensification and positioning of SPR band. It is for these reasons the present section deals with the study on the effect of 120 MeV Ag ion irradiation on Cu-C_{70} nanocomposite thin films.

6.2.1 Experimental Details:

Cu-C_{70} nanocomposite films were grown on different substrates such as glass and TEM grids with the aid of thermal resistive co-deposition method. The detailed process is described in section 6.1. The irradiation is performed with 120 MeV Ag ion beam in IUAC, New Delhi at different fluences from 1×10^{12} to 3×10^{13} ions/cm^2. For Cu (10%)-C_{70} nanocomposite thin films, the values of S_e and S_n are about 1.24×10^3 eV/Å and 5.13 eV/Å, respectively with projected range about 16.50 μm.

Hitachi spectrometer was used to record the UV-visible absorption spectra of the nanocomposite thin films in wavelength range from 200 to 800 nm. TEM images of pristine and of thin film irradiated at highest fluence (3×10^{13} ions/cm^2) are recorded with Tecnai G^2 20 (FEI) S-Twin TEM microscope. Raman spectra were taken with

the aid of AIRIX STR 500 Raman spectrograph fixed with Ar ion laser excitation wavelength at 532 nm.

6.2.2 Results & Discussions:

6.2.2.1 RBS analysis:

Following the same RBS technique for similarly synthesized C_{70} thin films the estimated percentage of copper has been 10% and the film thickness was 30 nm. The detail of RBS experiments are already described in section *6.1.3.1*.

6.2.2.2 UV-visible absorption spectroscopy:

The UV-visible absorption spectra of pristine and 120 MeV Ag ion irradiated Cu (10%)-C_{70} nanocomposite thin films at different fluences 1×10^{12}, $3\times10^{12,}$ 6×10^{12}, 1×10^{13} and 3×10^{13} ions/cm^2. are shown in figure 6.13. The pristine Cu (10%) C_{70} nanocomposite thin film exhibits the characteristic fullerene C_{70} bands in the UV-visible absorption spectrum. It can be seen that irradiation of the nanocomposite thin film by 120 MeV Ag ion leads to gradual disappearance of the characteristic optical bands due to fullerene C_{70} with increasing fluence.
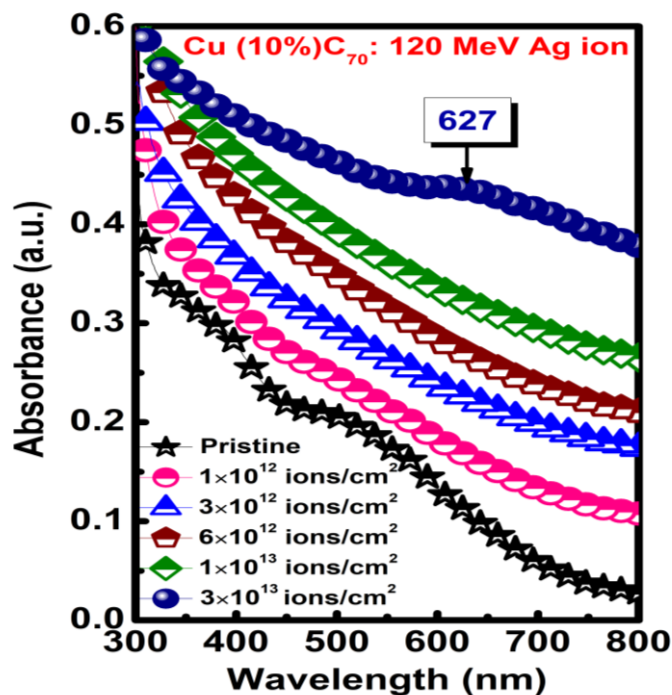

Figure 6.13 UV-visible absorption spectra of pristine and 120 MeV Ag ion irradiated Cu (10%)-C_{70} nanocomposite thin films.

This trend continues till 1×10^{13} ions/cm^2 fluence; it can be explained on the basis of transformation of C$_{70}$ molecule to amorphous carbon. It is to be noted that the irradiation phenomenon creates a lot of crystal defects which help in local transport of atoms leading thereby to the coarsening of Cu nanoparticles.

It can be modeled other way by considering that imposition of high energy into the system, leads to local melting of materials which intensifies mass transport and differential densities between copper and the surrounding matrix aids in agglomeration of copper particles due to lowering of surface free energy. The UV-visible absorption spectrum of the nanocomposites for the fluence 3×10^{13} ions/cm2 discerns a visible absorption peak at 627 nm. This peak is assigned as the SPR band due to copper nanoparticles. From these observations it is clear that appearance of SPR band of copper due to irradiation is conditioned by the attainment of threshold particle size. So long as, this nanocomposites of low copper content has not envisaged sufficient particle growth by increasing the fluence, the SPR band does not become appreciable.

6.2.2.3 Raman analysis:

The results of Raman spectroscopy of the pristine and irradiated nanocomposite thin films are presented in figure 6.14. In case of increasing fluence under irradiation by 120 MeV Ag ion, the Raman spectra of experimental nanocomposite thin films record gradual diminution and disappearance of characteristic Raman bands of fullerene C$_{70}$ as fully observed in the spectrum of pristine.

This has its origin to the destruction of fullerene molecules with gradual amorphization. Transformation of fullerene C$_{70}$ molecule to amorphous carbon tantamount to final emergence of graphitic bond in the material. It is expected in the metal reinforced nanocomposites that the presence of metal nanoparticles would locally create structural disturbance for which all the characteristics band might not be observable in the corresponding Raman spectrum. However, in the instant case one can observe the occurrence of all the characteristics peaks due to fullerene C$_{70}$ in the Raman spectrum of pristine.
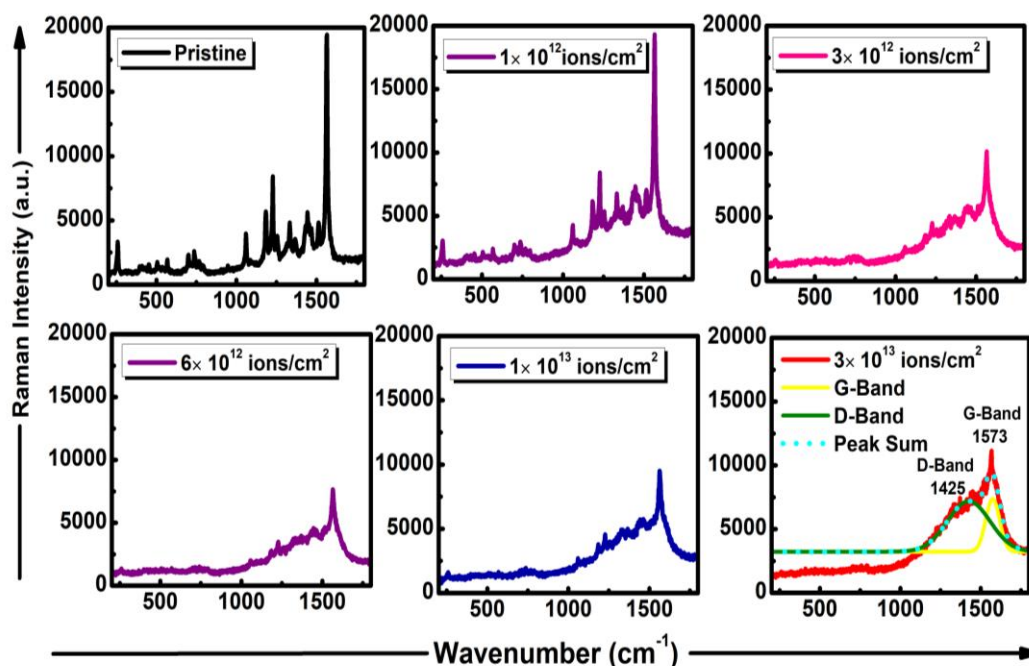
Figure 6.14 Raman spectra of pristine and 120 MeV Ag ion irradiated Cu (10%)-C_{70} nanocomposite thin films.

This is due to the presence of small quantity of copper (10 at. %) within the nanocomposite. Raman spectrum of the nanocomposite for the fluence 3×10^{13} ions/cm^2, clearly shows the existence of D and G bands. The presence of these bands suggests that there has been appreciable amorphization of fullerene C_{70}. This observation corroborate with the result of UV-visible absorption spectrum.

6.2.2.4 TEM analysis:

The crystallinity of the nanocomposite thin film is studied with the aid of Transmission electron microscopy. Figure 6.16 (a-d) depicts the bright field TEM image, particle size distribution, selected area electron diffraction (SAED) pattern and HRTEM micrograph of pristine Cu (10%)-C_{70} nanocomposite thin film.

Figure 6.16 (a) and inset in figure 6.16(a) confirms that the morphology of the nanoparticles is nearly spherical. Particle size distribution of copper nanoparticles embedded in fullerene C_{70} thin film is shown in Figure 6.16 (b). The calculated average particle size comes out to be ~ 2.4 nm for pristine Cu-C_{70} nanocomposite thin film. The SAED pattern of pristine Cu-C_{70} nanocomposite thin film shown in figure 6.16(c) gives clear evidence of the presence of cubic copper.
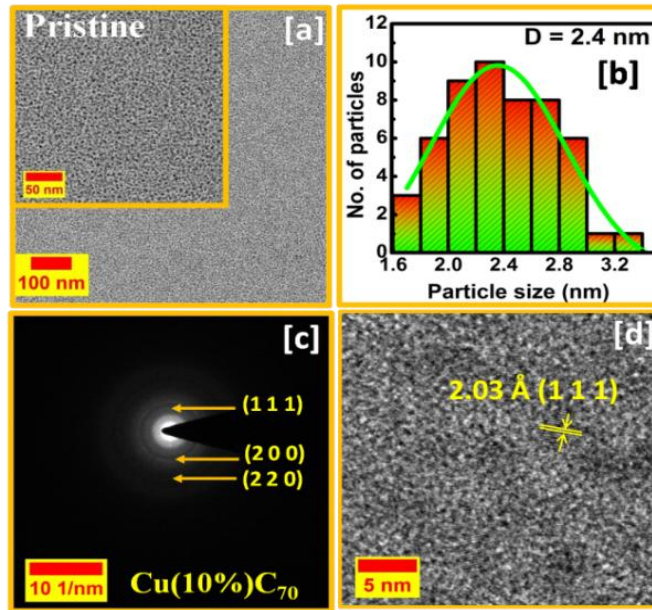
Figure 6.15 (a) TEM image, (b) particle size distribution, (c) SAED pattern and (d) HRTEM image of pristine Cu (10%)-C$_{70}$ nanocomposite thin film.

The high resolution image in figure 6.16(d) resolves the lattice fringes; the interplaner distance measured from the HRTEM image is found to be 2.03A which corresponds to (111) plane of FCC copper.

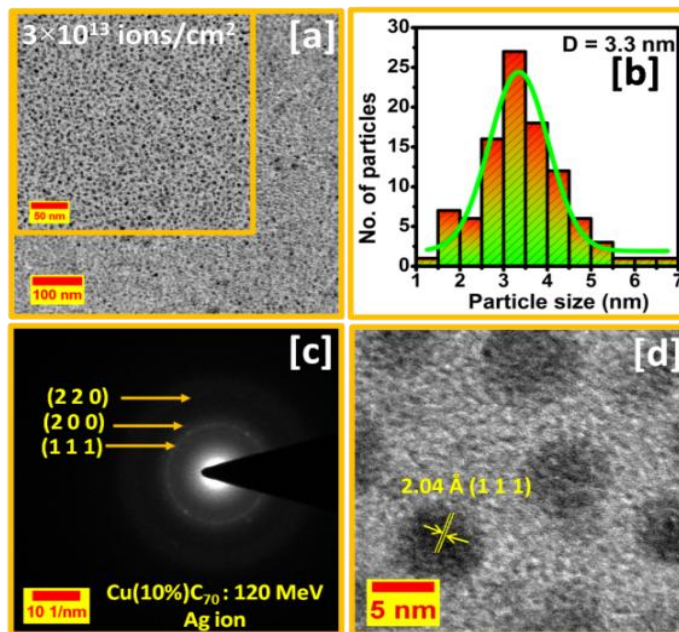**Figure 6.16** (a) TEM image, (b) particle size distribution, (c) SAED pattern and (d) HRTEM image of 120 MeV Ag ion irradiated Cu (10%)-C$_{70}$ nanocomposite thin film.

In order to study the effect of irradiation by high energy 120 MeV Ag ion on the morphology and crystallinity of the nanocomposite thin film, TEM measurements are also performed on the sample irradiated with the highest fluence 3×10^{13} ions/cm^2. Figure 6.17 (a-d) shows the bright field TEM image, particle size distribution, SAED pattern and HRTEM image for 120 MeV Ag ion irradiated sample. Alike pristine sample, a nearly spherical morphology of Cu particles is also retained even at higher fluence. The particle size distribution shown in figure 6.16(c) verifies that statistically determined average particle size is around 3.3 nm. This increase in particle size after irradiation stems from the agglomeration of nano particles [25-26]. The SAED pattern analysis indicates the occurrence of FCC copper in the matrix. This observation is confirmed by the lattice spacing measurement in HRTEM image of the concerned sample (figure 6.17 d). The interplaner spacing is measured to be 2.04A which again confirms to (111) plane of copper.

6.1.3 Conclusions:

C$_{70}$ thin films containing particles of Cu metal can be successfully synthesized using thermal co-deposition method. RBS analysis confirms the percentage of copper metal around 10% and thickness of th film ~30 nm. The SPR of Cu in metal state can be promoted by irradiation which produces displacements and atomic diffusion. Moreover, upon irradiation by low energy 350 keV Ar ion, the SPR band can be blue shifted due to the change in refractive index of the host matrix arising out of structural transformation. The particle size increases from 2.4 nm to 6.6 nm with increasing fluence of 350 keV Ar ion beam. Connectively, the conductivity of the film is increased, and lends scope for further study to extend the applications of Cu-C$_{70}$ nanocomposite thin films.

Irradiation by 120 MeV Ag ion leads to amorphization of Cu (10%)C$_{70}$ nanocomposite thin films at higher fluences. The intensity of SPR due to copper becomes appreciable only at a fluence of 3×10^{13} ions/cm^2 so as to depict a visible band in UV-visible absorption spectra at 627 nm. Appearance of D and G band at higher fluence confirms that transformation of fullerene to amorphous carbon appreciably occurs due to 120 MeV Ag ion irradiation for 3×10^{13} ions/cm^2 fluence. Irradiation brings about a marginal increase in particle size concurrent with

amorphization of adjoining fullerene C_{70} matrix. Both these are responsible for the emergence of SPR band due to copper induced at a fluence 3×10^{13} ions/cm^2.

REFERENCES

[1] M Z. Krolow, C.A. Hartwig, G.C. Link, C.W. Raubach, J.S.F. Pereira, R.S. Picoloto, M.R.F. Gonçalves, N.L.V. Carreno and M.F. Mesko, Synthesis and Characterisation of Carbon Nanocomposites, In: Avellaneda C. (eds) NanoCarbon 2011. Carbon Nanostructures, Springer, Berlin, Heidelberg, 3 (2013).

[2] E. Ulloa, Fullerenes and their Applications in Science and Technology, Introduction to Nanotechnology Spring, (2013).

[3] B.C. Yadav and R. Kumar, Structure, properties and applications of fullerenes, *International Journal of Nanotechnology and Applications*, 2 (2008) 15-24.

[4] M. Prato, J. Mater. Chem., 1997, 7, 1097-1109.

[5] S. Margadonnan and K. Prassidesw, Recent advances in fullerene superconductivity, *Journal of Solid State Chemistry*, 168 (2002) 639-652.

[6] R. Singhal, J.C. Pivin and D.K. Avasthi, Ion beam irradiation-induced tuning of SPR of Au nanoparticles in fullerene C_{70} matrix: dependence of energy loss, *J Nanopart Res*, 15 (2013) 1641.

[7] R. Singhal, D.C. Agarwal, Y.K. Mishra, D. Kabiraj, G. Mattei, J.C. Pivin, R. Chandra and D.K. Avasthi, Synthesis, characterizations, and thermal induced structural transformation of silver-fullerene C_{60} nanocomposite thin films for applications in optical devices, *J. Appl. Phys.* 107 (2010) 2-7.

[8] P. Sharma, R. Singhal, R. Vishnoi, D.C. Agarwal, M.K. Banerjee, S. Chand, D. Kanjilal and D.K. Avasthi, Effect of Ag Ion Implantation on SPR of Cu-C60 NanocompositeThin Film, *Plasmonics*, 13 (2018) 669.

[9] R. Singhal, P. Sharma, R. Vishnoi and D. K. Avasthi, Synthesis and characterizations of Au-C60 nanocomposite, *Journal of Alloys and Compounds*, 696 (2017) 9-15.

[10] H. Inani, R. Singhal, P. Sharma, R. Vishnoi, S. Channd ,Vacuum, 2017, **142**, 5-12

[11] Y.K. Mishra, S. Mohapatra, R. Singhal, D.K. Avasthi, D.C. Agarwal and S.B. Ogale, Au-ZnO: A tunable localized surface plasmonic nanocomposite, *Appl. Phys. Lett.*, 92 (2008) 043107.

[12] Y.K. Mishra, D.K. Avasthi, P.K. Kulriya, F. Singh, D. Kabiraj, A. Tripathi and J. C. Pivin, I. S. Bayer and A. Biswas, Appl. Phys. Lett., Controlled growth of gold nanoparticles induced by ion irradiation: An *in situ* x-ray diffraction study, **90** (2007) 073110.

[13] M.C. Ridhway, R. Giulian, D.J. Sprouster, P. Kluth, L.L. Araujo, D.J. Llewellyn, A. P. Byrne, F. Kremer, P.F.P. Fichtner, G. Rizza, H. Amekura, M. Toulemonde, Role of Thermodynamics in the Shape Transformation of Embedded Metal Nanoparticles Induced by Swift Heavy-Ion Irradiation, Phys. Rev. Lett., **106** (2011) 095505.

[14] U. Kriebig, M. Vollmer, Optical Properties of Metal Clusters, Springer (1995).

[15] L.R. Doolittle, Algorithms for the rapid simulation of Rutherford backscattering spectra, *Nucl. Instr. and Meth. in Phys. Res. B*, 9 (1985) 344-351.

[16] H. Kumar, Y.K. Mishra, S. Mohapatra, D. Kabiraj, J.C. Pivin, S. Ghosh and D.K. Avasthi, Compositional analysis of atom beam co-sputtered metal–silica nanocomposites by Rutherford backscattering spectrometry*, Nucl. Instr. and Meth. in Phys. Res. B*, 266 (2008) 1511-1516.

[17] J. Rozra, I. Saini, A. Sharma, N. Chandak, S. Aggarwal, R. Dhiman and P.K. Sharma, Cu nanoparticles induced structural, optical and electrical modification in PVA, *Materials Chemistry and Physics*, , 134 (2012) 1121-1126.

[18] A. Sharma, S. Bahniwal, S. Aggarwal, S. Chopra and D. Kamnjilal, Synthesis of copper nanoparticles in polycarbonate by ion implantation, Bull. Mater. Sci., 34 (2011) 645-649.

[19] G.W. Arnold, Near-surface nucleation and crystallization of an ion-implanted lithia-alumina-silica glass, *J. App Phys.*, 46 (1975) 4466.

[20] C. Kittel, Introduction to Solid State Physics, eighth ed., Wiley Eastern, India, 2007..

[21] M.S. Dresselhaus, G. Dresselhaus and R. Satio, Carbon fibers based on C_{60} and their symmetry, *Phys. Rev. B*, 45 (1992) 6234-6242.

[22] R.A. Jishi, R.M. Mirie, M.S. Dresselhaus, G. Dresselhaus and P.C. Eklund, Force-constant model for the vibrational modes in C_{70}, *Phys. Rev. B*, 48 (1993) 5634–5642.

[23] A.C. Ferrari and J. Robertson, Interpretation of Raman spectra of disordered and amorphous carbon, *Physical Review B*, 61(2000) 14095.

[24] J. Robertson, Diamond-like amorphous carbon, *Material Science and Engineering R Reports*, 37 (2002) 129-281.

[25] Z. Kaminskiene, I. Prosycevas, J. Stonkute and A. Guobiene, Evaluation of Optical Properties of Ag, Cu, and Co Nanoparticles Synthesized in Organic Medium, *Acta Physica Polonica A,* 123 (2013) 111-114.

[26] P.C. Eklund, A.M. Rae, Y. Wang, P. Zhou, K.A. Wang, J.M. Holden, M.S. Dresselhaus and G. Dresselhaus, Optical properties of C_{60} and C_{70} based solid films, *Thin Solid Films*, 257(1995) 211-232.

[27] R. Singhal, A. Kumar, Y. K. Mishra, S. Mohapatra, J. C. Pivin and D. K. Avasthi, Swift heavy ion induced modifications of fullerene C70 thin films, *Nucl. Instr. and Meth. in Phys. Res. B*, 266 (2008) 3257-3262.

[28] K. Spyrou, L. Kang , E.K. Diamanti , R.Y. Gengler, D. Gournis, M. Prato and P. Rudolf, A novel route towards high quality fullerene-pillared graphene, *Carbon*, 61 (2013) 313-320.

[29] S. Yu, J. Liu, W, Zhu, Z.T. Hu, T.T. Lim, X. Yan, Facile room-temperature synthesis of carboxylated graphene oxide-copper sulfide nanocomposite with high photodegradation and disinfection activities under solar light irradiation, *Scientific Reports,* 5 (2015) 16369.

Chapter 7

Conclusions and Future Scope

7.1 Conclusions:

Given that the absorbance of irradiated metal-fullerene nanocomposites is increased due enhancement of SPR band, the concerned light harvesting capacity can be gainfully utilized if conditions are created to insure production of electron – hole pair upon absorptions of photons. Dissipation in phonons upon plasmonic absorption is certainly a risk so far as meaningful application in plasmonic solar cells are concerned. It is therefore of paramount importance to tune the SPR band by suitable processes; as already stated, host matrix and quality of metal nanoparticles are of paramount importance in this regard. Favorable change in host matrix can be accomplished by ion irradiation. Knowing that irradiation is a very important means of tuning the SPR band and that copper is a prospective nanomaterial due to its favorable SPR position, the present study is designed.

In fact, to talk about solar cell application the electronic band gap and optical band gap are often considered. Basically, this involves distinguishing the difference in the methods applied to measure them. Optical band gap measurement as done here is essentially an excitation spectroscopy, where the charge state of materials remains unchanged. This means that the number of electrons before and after transition between valency and conduction remains unaltered. In contrast, measurement of band position by electron spectroscopy, leads to either injection of extra electrons or withdrawing electrons from the solid. In order to realize this, one must overcome the barrier due to Culomb repulsion. Thus, electronic band gap is higher by this amount than the optical band gap. Normally in solids with overlapping of states, this difference is negligible; on the contrary, it is large in organic solar cells as the system comprises of spatially localized conduction and valency band. In device engineering, this difference is matter of great significance. In solar cells, optical band gap value is quite important because one has to excite by photons to produce electro-hole pair. This calls for the use of suitable bias in design of devices.

In the light of above, the author draws the following conclusions:

❍ The importance of studying the fullerene C_{60} and fullerene C_{70} thin films under the effect of irradiation lies in its' potential for their further use as a matrix for the reinforcement of metal nanoparticles. Fullerene C_{60} thin film irradiated with 90 MeV Ni ion beam over a wide range of fluences from 1×10^9 to 3×10^{13} ions/cm^2. Raman spectroscopy reveals the appearance of new mode of Raman spectrum in

the lower fluence range. Also, it suggests that the polymerization of C_{60} fullerene takes place under irradiation of fullerene C_{60} by 90 MeV Ni ion beam at lower fluences (1×10^9 to 1×10^{11} ions/cm^2). At higher fluence (1×10^{12} to 3×10^{13} ions/cm^2) the formation of ion tracks takes place due to the passage of ion beam through the fullerene C60 thin films. The radius of these ion tracks is calculated about 3.03 nm. At a particular fluence 3×10^{13} ions/cm^2, the transformation of fullerene to amorphous carbon (a-C) takes place along with overlapping of these ion tracks. The variation in optical properties of fullerene C_{60} thin films under the effect of ion irradiation has been studied by UV-visible absorption spectroscopy and it is observed that the intensity of absorbance peaks of fullerene C_{60} thin films declines with the increasing fluence of 90 MeV Ni ion beam. Decrement in optical band gap of fullerene C_{60} thin film with fluence of 90 MeV Ni ion beam also observed. From the conductivity measurement, increment in the resistivity of fullerene C_{60} thin films is observed. This also confirms the transformation of fullerene into a-C. From the surface analysis, the roughness of the fullerene C_{60} changes with the ion irradiation.

○ Fullerene C_{70} thin films of thickness about ~150 nm deposited on different substrates (glass, quartz and silicon) by thermal resistive heating method were irradiated with different ion beams of different electronic energy loss values 226 eV/Å, 274 eV/Å, 672 eV/Å and 1393 eV/Å for 90 MeV Si, 55 MeV Si, 90 MeV Ni and 125 MeV Au ion beam, respectively. It is concluded from the UV-visible absorption spectroscopy that the absorption bands decline with increasing fluences. For each ion beam, Raman spectroscopy confirms the transformation of fullerene C_{70} into amorphous carbon with increasing fluence of the respective ion beam. In case of 90 MeV Si and 55 MeV Si ion beam, the Raman bands are still visible at highest fluence 3×1^{13} ions/cm^2, that confirms the dependency of the Raman bands intensity on electronic energy loss values of the ion beam and fluence of the ion beam. Further, the damage cross section and radius of the ion track for each ion beam (90 MeV Si, 55 MeV Si, 90 MeV Ni and 125 MeV Au ion beam) are determined with the help of Raman spectroscopy. It has been observed that the value of damage cross section is increasing with increasing value of the electronic energy loss of the ion beam. Hence, it is concluded that a definite relationship exists between the electronic energy loss and the damage cross section in ion beam irradiated fullerene C_{70} thin films; the damage cross section

increases with increasing electron energy loss (S_e). This relation can help to understand an unknown situation and enables ion track engineering for production of nanowires with least number of trials. The relation is phenomenologically identical in both C_{60} and C_{70}.

○ Cu-C_{60} nanocomposite thin films can be successfully synthesized on different substrates (glass, silicon and TEM grid substrates). The percentage of copper metal and thickness of Cu-C_{60} nanocomposite thin films estimated with RBS characterization were found to be ~ 13% and 28 nm. Cu(13%)C_{60} thin films irradiated by low energy 100 keV Ag ion beam at different fluences from 1×10^{14} ions/cm^2 to 3×10^{16} ions/cm^2. Raman spectroscopy confirms the decline of Raman bands intensity with the increasing fluence of 100 keV Ag ion and at a particular fluence 3×10^{16} ions/cm^2, transformation of fullerene C_{60} into a-C takes place. UV-visible absorption spectra show the SPR is not present in the pristine Cu(13%)C_{60} nanocomposite thin film. By increasing the fluence of 100 keV Ag ion beam two separate SPR bands arises at positions ~ 410 nm (For Ag nanoparticles) and ~ 630 nm (for Cu nanoparticles). At the highest fluence 3×10^{16} ions/cm^2, a broad SPR band at position around 435 nm is observed. Transmission electron micrographs proves that particle coarsening of Cu takes place due to irradiation and particle size increases from 4 ±0.7 nm in pristine to 6 ± 0.4 after irradiation.

○ Cu nanoparticles embedded in fullerene C_{60} matrix thin films are synthesized. From the RBS analysis the thickness of the film is about 32 nm and atomic concentration of Cu nanoparticles is about 18%. The deposited Cu (18%)C_{60} nanocomposite thin films are irradiated with low energy 350 keV Ar ion beam at different fluences from 1×10^{13} ions/cm^2 to 3×10^{16} ions/cm^2. From UV-visible absorption spectroscopy, SPR band due to copper nanoparticles hase been observed at about 622 nm in pristine Cu (18%) C_{60} nanocomposite thin film. The intensity of this SPR band increases with irradiation. Low energy heavy ion (350 keV Ar) irradiation of Cu (18%)C_{60} nanocomposite thin film causes a shift of SPR band from 622 nm to 644 nm at the fluence 3×10^{16} ions/cm^2. There is a concurrent enhancement of intensity of SPR band with the observed red shift. Destruction of fullerene C_{60} takes place due to irradiation with the signature of the amorphization being prominent at fluence 3×10^{16} ions/cm^2. Appreciable increase in size of

copper nanoparticles results after irradiation and this increase in particle size leads to enhancement of the SPR band intensity.

Cu (18%) C_{60} nanocomposite thin films are also irradiated with high energy 120 MeV Ag ion beam at different fluences from 1×10^{12} ions/cm^2 to 3×10^{13} ions/cm^2. SPR band induced due to presence of copper nanoparticles (~ 622 nm) is enhanced by high energy ion beam irradiation. At the highest fluence of 120 MeV Ag ion beam 3×10^{13} ions/cm^2, the SPR band shift to position ~ 633 nm due to increased particle size of copper nanoparticles. This increase in average particle size of nanoparticles is responsible for the enhancement of SPR intensity. Copper nanoparticles retain the spherical morphology even after irradiation. From the UV-visible absorption spectroscopy, the optical band gap of Cu (18%) C_{60} nanocomposite thin films decrease with increase in fluence of 120 MeV Ag ion beam. Raman spectroscopy confirms the transformation of fullerene C_{60} into amorphous carbon. The diminution of oxygen component upon irradiation present in pristine Cu (18%) C_{60} nanocomposite thin film is confirmed by XPS and XRD characterizations.

○ C_{70} thin films containing nanoparticles of Cu metal were successfully synthesized using thermal co-deposition method. Rutherford backscattering (RBS) analysis confirms the thickness of the film 30 nm and concentration of Cu is about 10 %. The Cu (10%) C_{70} nanocomposite thin films have been irradiated by low energy 350 keV Ar ion beam at different fluence (1×10^{13} ions/cm^2 to 3×10^{16} ions/cm^2). There is no SPR band present in the pristine Cu (10%) C_{70} nanocomposite thin film due to lower concentration of Cu nanoparticles. The SPR of Cu metal state can be promoted by low energy ion irradiation. The intensity of SPR band increases with increase in fluence of the ion beam. At fluence 1×10^{15} ions/cm^2, SPR band is observed at position about 627 nm. With further increase in fluence, enhances this band intensity and blue shift of about 24 nm is also observed. This blue shift is due to the change in refractive index of the host matrix. Both UV visible absorption and TEM analysis confirm the increased size of Cu nanoparticles with fluence. The conductivity of the film is increased and lends scope for further study to extend the applications.

○ Cu (10%)C_{70} nanocomposite thin films are irradiated with 120 MeV Ag ion beam at different fluences (1×10^{12} ions/cm^2 to 3×10^{13} ions/cm^2) to analyse the variation

of the Cu (10%)C_{70} nanocomposite thin films under the effect of high energy ion beam irradiation. Irradiation by 120 MeV Ag ion leads to amorphization of Cu (10%)C_{70} nanocomposite thin films at higher fluences. Appearance of D and G band due to 120 MeV Ag ion irradiation confirms the transformation of fullerene into amorphous carbon that appreciably occurs at 3×10^{13} ions/cm^2 fluence. The intensity of SPR band (~627 nm) due to copper nanoparticles becomes appreciable only at a fluence of 3×10^{13} ions/cm^2. Irradiation brings about a marginal increase in particle size concurrent with amorphization of adjoin fullerene C_{70} matrix.

7.2 Scope of Future Work:

There are several issues which need to be focused in the field of nanocomposites. Also new ideas related to these nanocomposites are required to be explored so that one can extend the study in future along the following lines:

❍ SPR band intensity is dependent on the composition of the metal nanocomposites. So it appears important to observe the effect of irradiation on different concentration of metal in nanocomposites.

❍ In present study, the effect of two beams were studied (350 keV Ar ion and 120 MeV Ag ion) on Cu nanoparticles reinforced fullerene C_{60} and C_{70} nanocomposite thin films. There is scope for studying the effect of ion irradiation on Cu-C_{60} and Cu-C_{70} nanocomposite thin films with different ion beams of different energies.

❍ Due to inherent electron affinity property of fullerenes, they are considered to be quite suitable as acceptor material in solar cells. By incorporating metal nanoparticles (Au, Ag and Cu) in fullerene matrix, the absorption can be enhanced due to SPR of nanoparticles; hence this can be utilized for solar energy harvesting. Attempts can be made to fabricate efficient solar cells.

❍ Effect of dual surface plasmon resonance by incorporating two metal nanoparticles such as Ag and Cu in fullerene matrix can be studied to explore if the whole visible region of the spectrum can be utilized for efficient optical devices applications.

❍ SPR tuning at different fluences of the incident ion beam with spatial selectivity may result in a single sample with different regions of different SPR band intensity and wavelength. Hence multiple SPR bands may be possible for a single sample.

❍ Non linear optical properties of fullerenes will be quite interesting to study in fullerene based metal nanocomposites. The non linearity in optical property may depend on the different metal nanoparticles embedded in fullerene C_{60} and C_{70} matrices. Hence in future the variation of non linear properties in case of fullerene based metal nanocomposites can be studied.

List of publication from research work

[1] **Sharma P**, Singhal R, Vishnoi R, Sharma GD, Kulriya P, Ojha S, Banerjee MK & Chand S (2019) Evolution of SPR in 120 MeV Silver Ion Irradiated Cu(18%)C_{60} Nanocomposites Thin Films. *Journal of Materials Science: Materials in Electronics (JMSE)*, 30: 8301.

[2] **Sharma P** & Singhal R (2019) Ion Irradiation (Low & High Energy Ion) Induced Surface Plasmon Resonance in Cu(10%)C_{70} Nanocomposite Thin Films. *Materials Research Express*, 6, 085626.

[3] **Sharma P**, Singhal R, Vishnoi R, Agarwal DC, Banerjee MK, Chand S, Kanjilal D & Avasthi DK (2018). Effect of Ag Ion Implantation on SPR of Cu-C_{60} Nanocomposite Thin Film. *Plasmonics*, *13*(2), 669-679.

[4] **Sharma P**, Singhal R, Vishnoi R, Banerjee MK & Avasthi DK (2017). A comprehensive study of SHI irradiated fullerene C_{60} thin films: Polymerization to amorphization. *Synthetic Metals*, *227*, 93-99.

[5] **Sharma P**, Singhal R, Vishnoi R, Kaushik R, Banerjee MK, Avasthi DK & Ganesan V (2016). Ion track diameter in fullerene C_{70} thin film using Raman active vibrational modes of C_{70} molecule. *Vacuum*, *123*, 35-41.

[6] **Sharma P**, Singhal R, Banerjee MK, Vishnoi R, Kaushik R & Singh F (2016) Electronic excitation induced modification in fullerene C_{70} thin films. *Nuclear Instruments and Methods in Physics Research Section B: 379*, 188-194.

[7] **Sharma P**, Singhal R, Vishnoi R, Banerjee MK, Kaushik R, Kamma KV, Lakshmi GBVS, Tripathi A & Avasthi DK (2016) Surface and structural studies of fullerene C_{70} under ion irradiation. *Surface Engineering*, 32(11), 846-852.

[8] **Sharma P**, Singhal R, Vishnoi R & Banerjee MK (2017) Ion Track in Fullerene C_{70} Thin Film: Dependence of Electronic Energy Loss. *AIP Conference Proceedings*, 1832, 050158.

CURRICULUM VITAE

Ms. Pooja Sharma

Research Scholar
Department of Physics
Malaviya National Institute of Technology
Malviya Nagar, J.L.N. Marg, Jaipur, Rajasthan
📞 **+919799628795**
✉ **poojamnit2014@gmail.com**

Pooja Sharma's research area includes **metal-fullerene (C_{60}, C_{70}) nanocomposite thin films** synthesized by thermal co-evaporation techniques. By incorporating metal nanoparticles (Au, Ag and Cu) in fullerene matrix absorbance is increased due to induced Surface Plasmon Resonance (SPR) by noble metals (Au, Ag and Cu) which bears application potential in organic solar cells. Currently she is working on polymer-fullerene bulk heterojunction organic solar cell device fabrication. During her BASE internship period she worked on Perovskite solar cells fabrication and inter layer modifications for enhancement in efficiency of Perovskite solar cells in **National Renewable Energy Laboratory (NREL), Colorado, USA.**

Research interest: Deposition of films and characterization, Carbon nanostructures; Metal based carbon (fullerene, amorphous carbon) nanocomposite thin film; Ion irradiation and implantation; Polymer-fullerene bulk heterojunction organic solar cell; Perovskite Solar Cell

Skills Acquired:

- **Expertise in:** Thermal coating Unit, Tube Furnace, Spin coater, Pelletiser, Keithley Sourcemeter, UV-visible spectrometer, RF-DC sputtering, CVD and PVD techniques.
- **Characterization skills:** XRD; TEM, SEM, AFM, XPS, Raman spectroscopy, FTIR, Photoluminescence, UV-Visible, Two / Four probe method, RBS, I-V Measurement etc.
- **Analytical Skills**: Band gap calculation TEM micrographs and SAED, and other analyses of results of sophisticated instruments
- **Software skills:** SRIM, TRIM, ORIGIN, Image J, Nanoscope Analyzer, X-RUMP, XPS Peak Fit.

Academic Qualifications: **10th Examination**: First Division (85.33%); **12th Examination**: First Division (8.20 CGPA); **B.Sc. Exam**: First Division (68.68%); **M.Sc. Exam**: First Division (77.47%); **Ph. D. Course Work:** First Division (8.6 CGPA)

Research Activities: Attended a number of conferences as oral presenter and more seven Scientific Workshops/ Schools/Course Modules. Participated in experiment at **Elettra Beam line Synchrotron Trieste**, **Italy;** Participated in experiment at **DESY Research Lab Hamburg, Germany.**

Award: Bhaskara Advanced Solar Energy **(BASE)** Fellowship-2017

Exams Qualified: **GATE-2013** with score 461, AIR 340; **GATE-2014** with score 379, AIR 845

Title of Thesis: **Synthesis, Characterization and Irradiation of Fullerene Based Metal Nanocomposites**

Number of publications: **17**

Some Important Publications:

- P. Sharma et al. (2019) *J Mater Sci: Mater Electron* 30, 8301
- P. Sharma et al. (2019) Mater. Res. Express 6,085626
- P. Sharma et al. (2018) *Plasmonics* 13(2), 669-679.
- P. Sharma et al. (2018) *Synthetic Metals* 227, 93-99.
- P. Sharma et al. (2017) *Vacuum* 123, 35-41.
- P. Sharma et al. (2017) *Surface Engineering* 32(11), 846-852.
- P. Sharma et al. (2017) *Nuc. Inst. and Meth. in Phys. Res.Sec. B:* 379,188-194.